INVESTIGATION OF THE EFFECT OF NACA 4416 AEROFOIL SHAPED FUSELAGE ON THE PERFORMANCE OF AN UNMANNED AIR VEHICLE

BY

G.M. JAHANGIR ALAM

A THESIS

SUBMITTED TO THE DEPARTMENT OF MECHANICAL ENGINEERING, BANGLADESH UNIVERSITY OF ENGINEERING AND TECHNOLOGY (BUET) IN PARTIAL FULFILLMENT OF THE REQUIREMENTS FOR THE DEGREE OF DOCTOR OF PHILOSOPHY (Ph.D).

BANGLADESH UNIVERSITY OF ENGINEERING AND TECHNOLOGY (BUET) DHAKA

DECEMBER, 2013

COMPUTATIONAL RESULTS

4.1 Software and Data used for Computational Result

NACA 4416 cambered aerofoil has been used during design aerofoil shaped fuselage and conventional cylindrical shaped fuselage UAV models and investigation of their aerodynamic characteristics. The numerical data have been obtained by using Computational Fluid Dynamics (CFD) software. The flow of air through the aerofoils is considered to be incompressible and subsonic. The chord length of the aerofoil during theoretical design has been kept 10 cm. Volume of both the models have been kept same, which is 534.102 cm^3 during computational design. The free stream airflow has been kept as 20 m/s and 40 m/s respectively and the effect of temperature has been neglected. The density of air has been considered as ρ_o = 1.225 kg/m^3, operating pressure as 1.01 bar or 14.7 psi and absolute viscosity as μ_a = 1.789 $x10^{-5}$ kg/m-s. The Reynold's Number has been considered as 1.37 x 10^5 (for 20 m/s) and 2.74 x 10^5 (for 40 m/s) respectively. The data have been obtained at different angles of attack from -3° to 18° with 3° steps. Fifteen tapping points have been made computationally on each surface of the aerofoil to study the surface Pressure at each point. Finally, the computational results obtained from the CFD analysis for both the designs, would be investigated and analyzed.

4.2 Purpose of 3D UAV Models and Design of 2D NACA 4416 Aerofoil Profile

The designed UAVs will be used for aerial photography, surveillance, reconnaissance or similar purposes. It could also be used for many versatile purposes by incorporation of different types of sensors. Lift, drag force coefficients and lift-to-drag ratio for both the designs will be determined from CFD software. Point surface pressure on upper and lower surfaces of each wing of the designed UAV will also be determined and analyzed with this software. However, this design will not give any idea on engine thrust. A 2D NACA 4416 aerofoil profile has been designed by utilizing CFD software before designing the 3D conventional

cylindrical and aerofoil shaped fuselage UAV models. The chord length of the aerofoil is 10 cm. The free stream airflow has been kept 20 and 40 m/s respectively. All other parameters like viscosity, operating pressure, Reynold's Numbers have been kept same as mentioned in section 4.1 for designing the 2D NACA 4416 profile. The final total computational domain including 2D NACA 4416 profile after meshing is shown in Figure 4.1a and b respectively.

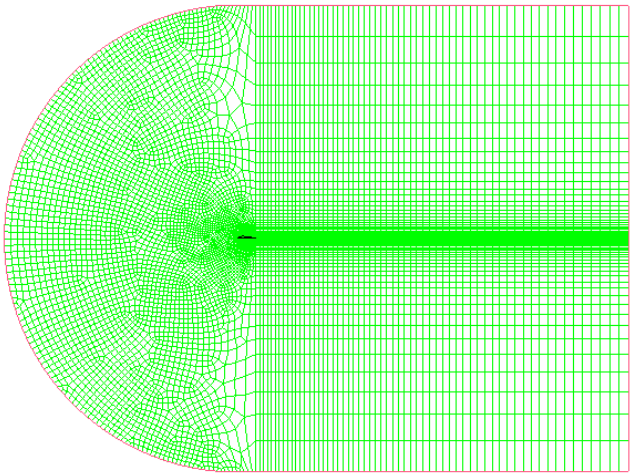

Figure 4.1a: Total Computational Domain including 2D NACA 4416 Profile after Meshing.

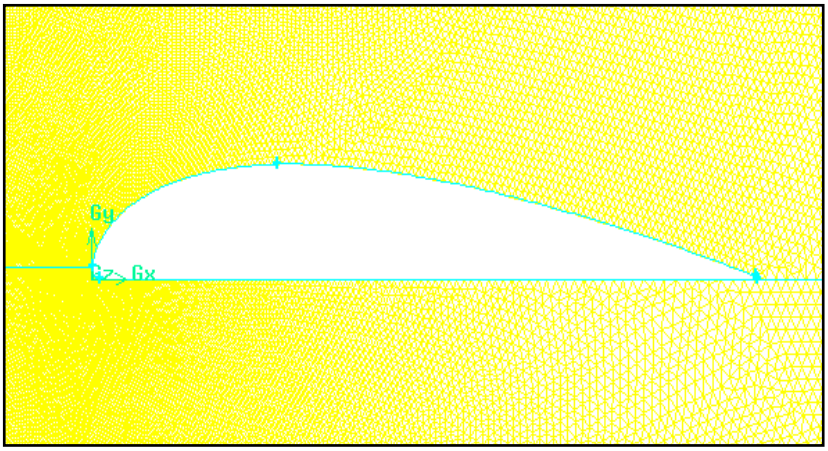

Figure 4.1b: 2D NACA 4416 Profile after Meshing (zoom effect).

4.3 Configuration Layout for Design of Conventional Cylindrical Shaped Fuselage UAV Model

Four major parts of a typical conventional cylindrical shaped fuselage model are wing, fuselage, horizontal stabilizer and vertical stabilizer. Up wing type conventional model has been selected. Total volume of this model is 534.102 cm^3. The left and right wings have been designed by using NACA 4416 aerofoil. Major features which have used during designing the wings of this model are as follows:

a. Aerofoil type : NACA 4416 (cambered aerofoil).
b. Chord Length : 10 cm.
c. Tip to tip length of both wing : 44 cm.
d. Center section diameter of fuselage : 4 cm.
e. Root to tip length of each wing (span) : 20 cm.
f. Maximum thickness between upper and lower surface : 1.186 cm.
g. Taper Angle : Zero.

The shape of the designed conventional fuselage is cylindrical. It's nose to tail length is 20 cm. It has mainly three parts - divergent part, middle part and convergent part. Detail features which have been used during designing the conventional cylindrical shaped fuselage UAV model are as follows:

a. <u>Divergent part (1st section)</u>
   - Length : 2.8 cm.
   - Nose radius : Approx 0.25 cm.
   - Divergent angle : 25 degree.
b. <u>Middle part (2nd section)</u>
   - Length : 13 cm.
   - Diameter : 4 cm (over the whole length).
c. <u>Convergent part (3rd section)</u>
   - Length : 4.2 cm.
   - Tail radius : Approx zero.
   - Convergent angle : 22 degree.

Total length, width and thickness of horizontal stabilizer are 14 cm, 3 cm and 0.4 cm respectively. It has been placed in a suitable position at the rear side of the fuselage. Total length, width and thickness of vertical stabilizer are 6 cm, 3 cm and 0.8 cm respectively. It has also been placed in a suitable position at the rear side of the fuselage. The isometric and wireframe views of the conventional cylindrical shaped fuselage model are shown in Figure 4.2 and 4.3 respectively.

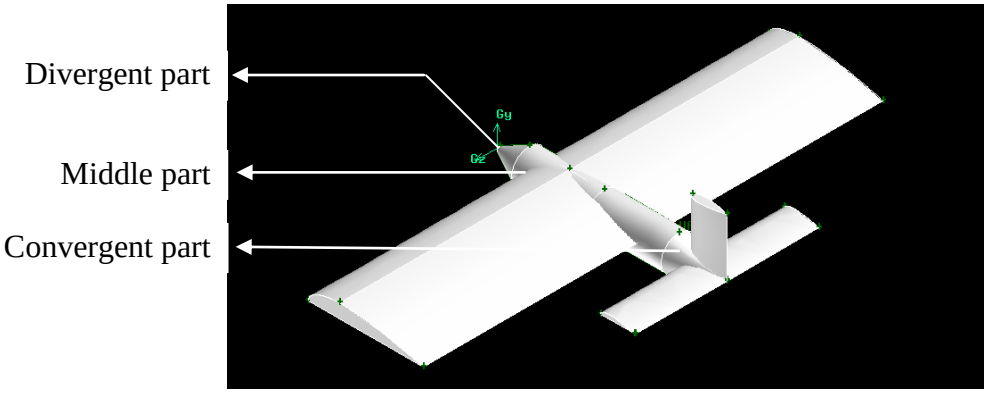

Figure 4.2: Isometric View of Cylindrical Shaped Fuselage Model.

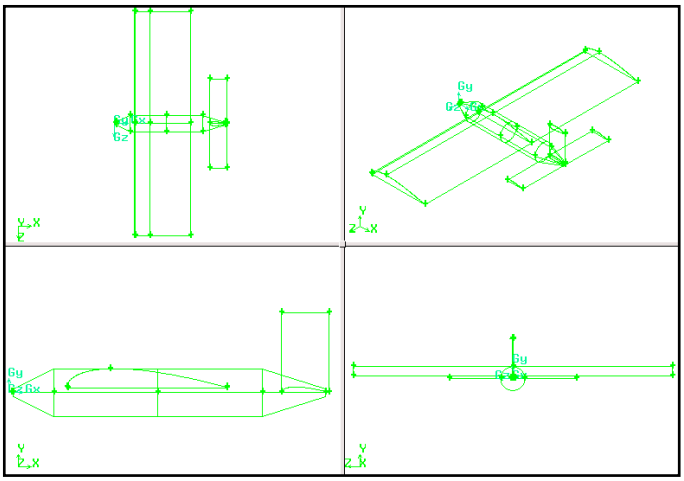

Figure 4.3: Different Wire-frame Views of Cylindrical Shaped Fuselage Model.

4.4 Configuration Layout for Design of Aerofoil Shaped Fuselage UAV Model

Four major parts of the proposed aerofoil shaped fuselage model are wing, fuselage, horizontal stabilizer and vertical stabilizer. Up wing type model has been selected.

The volume of the model is 534.102 cm^3. The left and right wings have been designed by using NACA 4416 aerofoil. Major features which have been used during designing the wings are as follows:

a. Aerofoil type : NACA 4416 (cambered aerofoil).
b. Chord Length : 10 cm.
c. Thickness of fuselage : 8 cm.
d. Tip to tip length of both wing : 48 cm.
e. Root to tip length of each wing (span) : 20 cm.
f. Maximum thickness between upper and lower surface : 1.186 cm.
g. Taper Angle : Zero.

The designed fuselage is of aerofoil shaped. It's chord length is 20 cm. The left and right fuselages have been designed by using NACA 4416 aerofoil. Major features which have been used during designing the fuselages are as follows:

a. Aerofoil type : NACA 4416 (cambered aerofoil).
b. Chord Length : 20 cm.
c. Tip to tip length of both fuselage : 8 cm.
d. Root to tip length of each fuselage (span) : 4 cm.
e. Maximum thickness between upper and lower surface : 2.26 cm.
f. Taper Angle : Zero.

Total length, width and thickness of horizontal stabilizer are 14 cm, 3 cm and 0.4 cm respectively. It has been placed in a suitable position at the rear side of the fuselage. Total length, width and thickness of vertical stabilizer are 6 cm, 3 cm and 0.8 cm respectively. It has been also placed in a suitable position at the rear side of the fuselage. The isometric and wireframe views of the aerofoil shaped fuselage UAV model are shown in Figure 4.4 and 4.5 respectively.

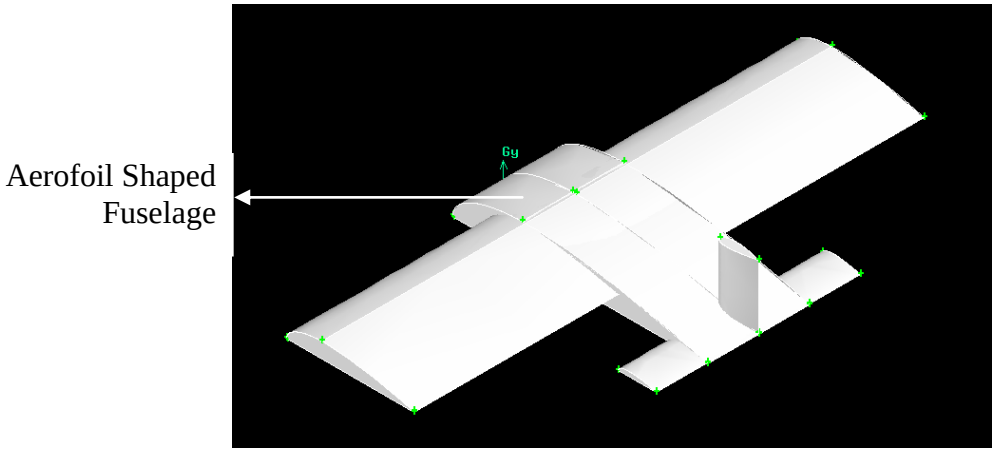

Figure 4.4: Isometric View of Aerofoil Shaped Fuselage Model.

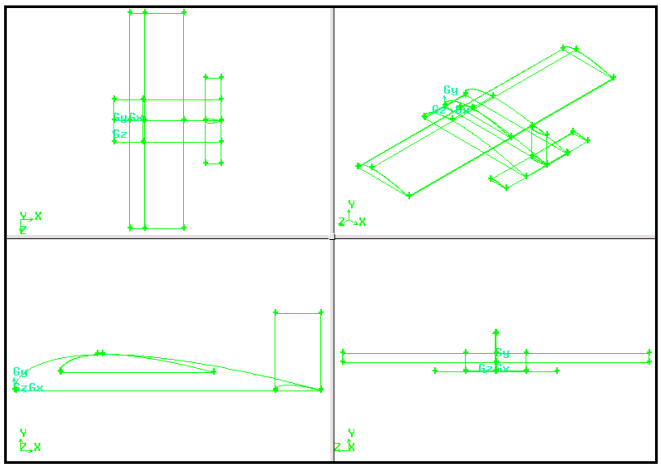

Figure 4.5: Different Wire-frame Views of Aerofoil Shaped Fuselage Model.

4.5 Finalization of Design

The finalization of design of two 3D models (cylindrical and aerofoil shaped) involves lot of trial and errors at different stages of the design. Modification of both the design have been carried out in different steps during creation of geometry and adjustment of far field boundary, meshing of geometry, setting up operation and boundary condition, setting up of different factors etc. Then, the variables of both the design have been initialized and checked for convergence. After analyzing the

result, the designed geometry has been further re-fined or re-meshed to obtain the accuracy as far as possible. As such, lot of trial and errors are involved before finalization of those design. The finalized cylindrical and aerofoil shaped fuselage UAV models have been converged through iteration. The finalized total computational domain of 3D UAV models and close view of 3D UAV models after meshing (zoom effect) are shown in Figure 4.6 to 4.9 respectively.

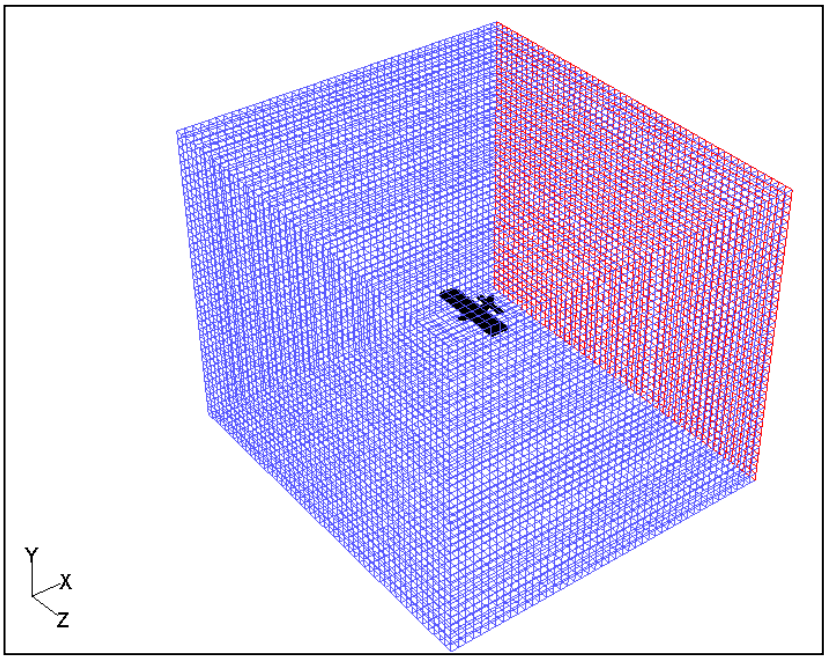

Figure 4.6: Total Computational Domain of Cylindrical Shaped UAV Model.

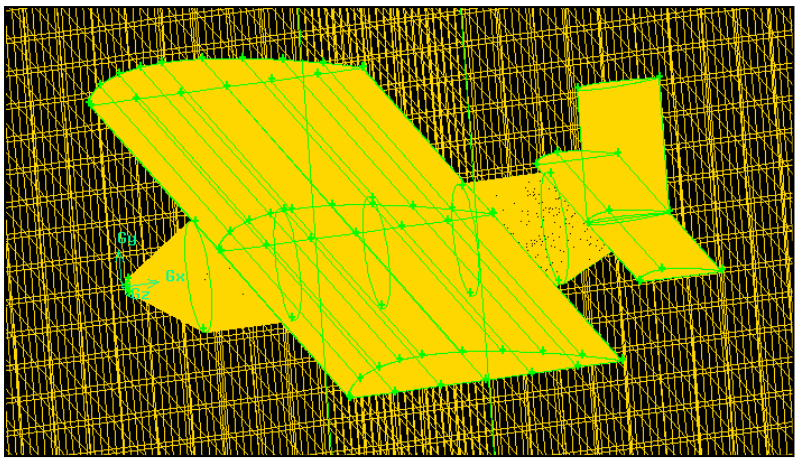

Figure 4.7: 3D Cylindrical Shaped UAV Model after Meshing (zoom effect).

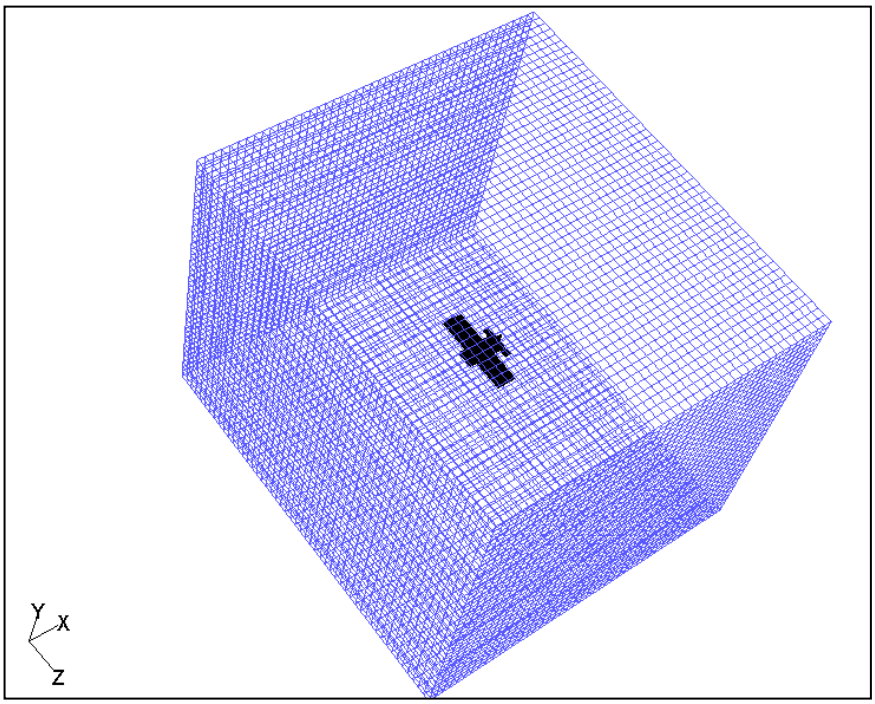

Figure 4.8: Total Computational Domain of Aerofoil Shaped UAV Model.

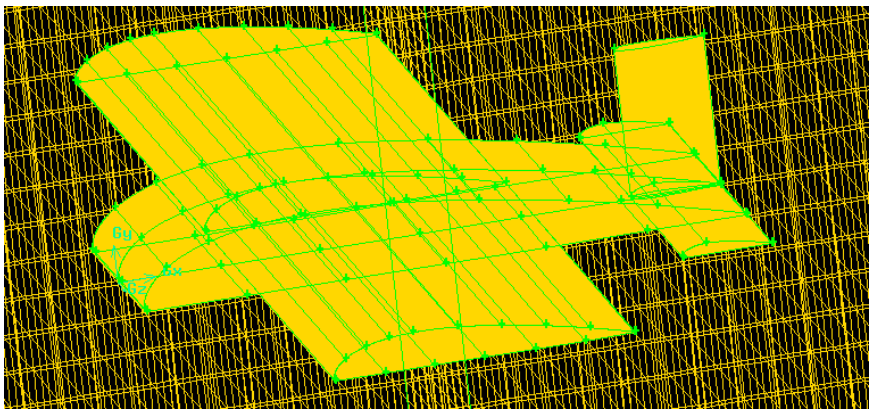

Figure 4.9: 3D Aerofoil Shaped UAV Model after Meshing (zoom effect).

4.6 Grid Independency Test

Grid independency test has been carried out for NACA 4416 profile among coarser, finer and main grid. The cells and nodes of main grid are 5,62,133 and 2,02,049 respectively. The coarser grid has been chosen 10% less than the main grid i.e. 5,05,920 cells and 1,81,844 nodes respectively. The finer grid has been chosen 10% more than the main grid i.e. 6,18,346 cells and 2,22,254 nodes respectively. Three graphs regarding variation of lift coefficient at different angle of attack have been plotted in same scale and results have been compared and analyzed. The grid independency test (for coarser grid, main grid and fine grid) for 2D NACA 4416 Profile is shown in Figure 4.10. The result of lift coefficient vs angle of attack for main and finer grid has been found almost same. But the result of coarser grid is found different than that of the main or finer grid.

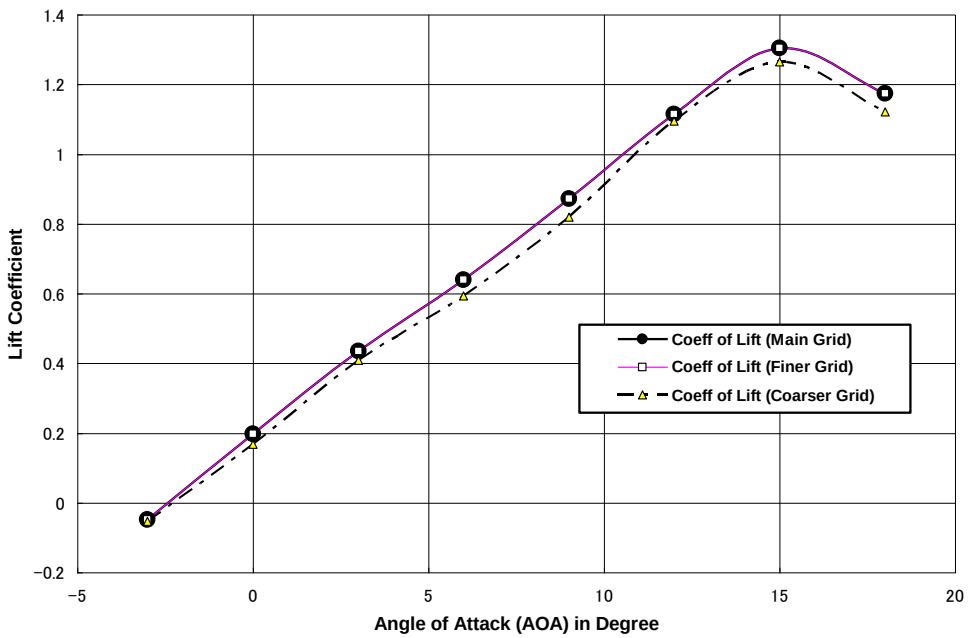

Figure 4.10: Grid Independency Test for 2D NACA 4416 Profile.

4.7 Aerodynamic Characteristics of 2D NACA 4416 Aerofoil Profile at 20 m/s

The variation of lift coefficient with angle of attack at 20 m/s for 2D NACA 4416 Profile at different angle of attack is shown in Figure 4.11. The zero lift angle has been found at -3° angle of attack. Then the lift coefficient increases almost linearly with the increase of angle of attack up to approximately 15° [Abbott and Doenhoff,

1959]. In other wards, the lift coefficient increases linearly with the increase of angle of attack up to 15°. After wards, the lift coefficient decreases with the further increase of angle of attack. As such, the stalling angle of 2D NACA 4416 profile is found at about 15˚. It is also observed that the maximum lift coefficient, C_{Lmax} for this profile is approximately 1.3.

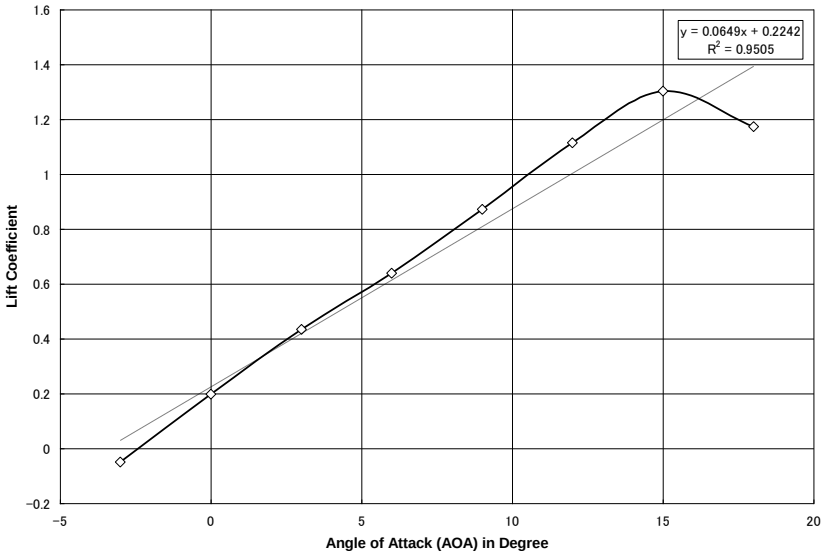

Figure 4.11: Variation of Lift Coefficient with Angle of Attack for 2D NACA 4416 Profile at 20 m/s.

The variation of drag coefficient with angle of attack at 20 m/s for 2D NACA 4416 Profile at different angle of attack is shown in Figure 4.12. The shape of the drag coefficient vs angle of attack curve is found parabolic nature. As such, the drag coefficient increases with the increase of angle of attack. The value of drag coefficient for this profile at 15° angle of attack is found 0.124.

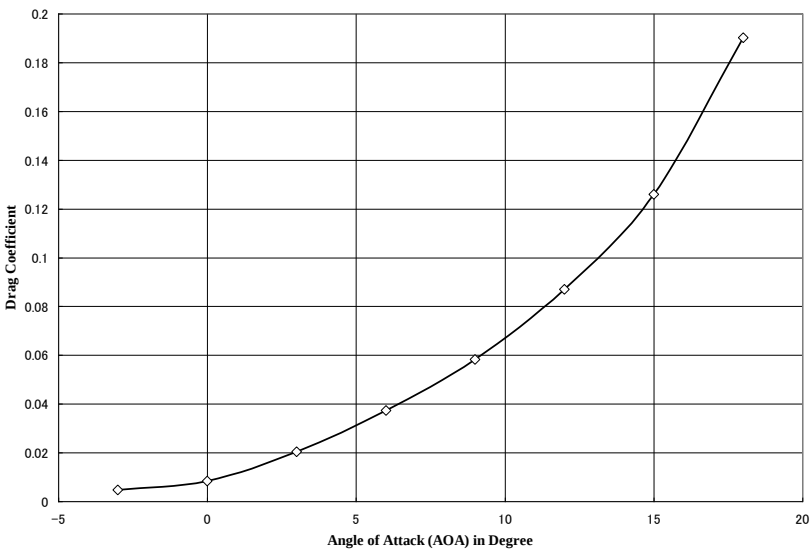

Figure 4.12: Variation of Drag Coefficient with Angle of Attack for 2D NACA 4416 Profile at 20 m/s.

4.8 Aerodynamic Characteristics of Conventional Cylindrical Shaped Fuselage at 20 m/s

The variation of lift coefficient with angle of attack at 20 m/s for conventional cylindrical shaped fuselage model at different angle of attack is shown in Figure 4.13. The zero lift angle has been found at -3º angle of attack. Then the lift coefficient increases almost linearly with the increase of angle of attack up to approximately 15°. In other wards, the lift coefficient increases linearly with the increase of angle of attack up to 15° [Abbott and Doenhoff, 1959]. After wards, the lift coefficient decreases with the further increase of angle of attack. As such, the stalling angle of conventional model is found at about 15˚. It is also observed that the maximum lift coefficient, C_{Lmax} for this type of model is approximately 0.946.

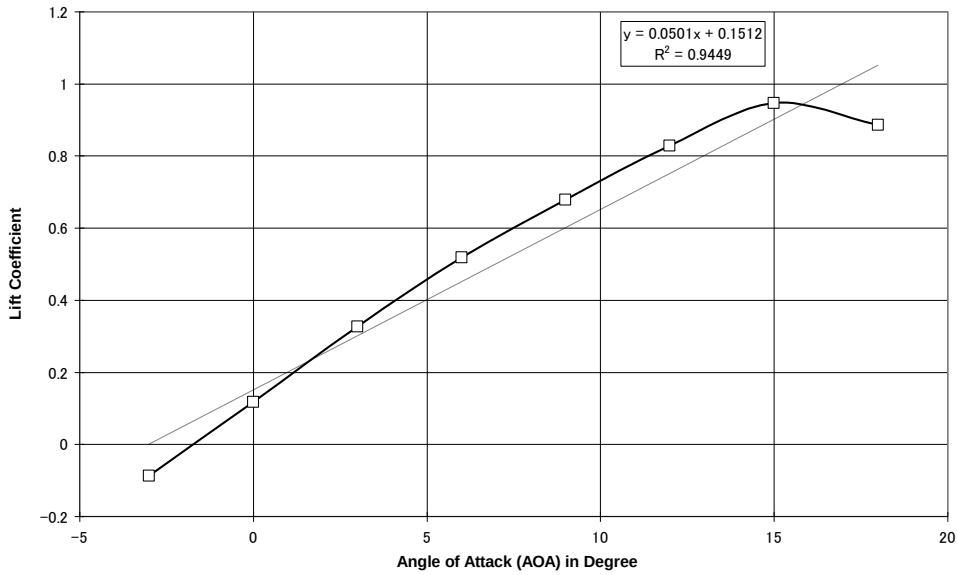

Figure 4.13: Variation of Lift Coefficient with Angle of Attack for Conventional Cylindrical Shaped Fuselage UAV Model at 20 m/s.

The variation of drag coefficient with angle of attack at 20 m/s for conventional cylindrical shaped fuselage model at different angle of attack is shown in Figure 4.14. The shape of the drag coefficient vs angle of attack curve is found parabolic

nature. As such, the drag coefficient increases with the increase of angle of attack. The value of drag coefficient for this conventional model at 15° angle of attack is found 0.144.

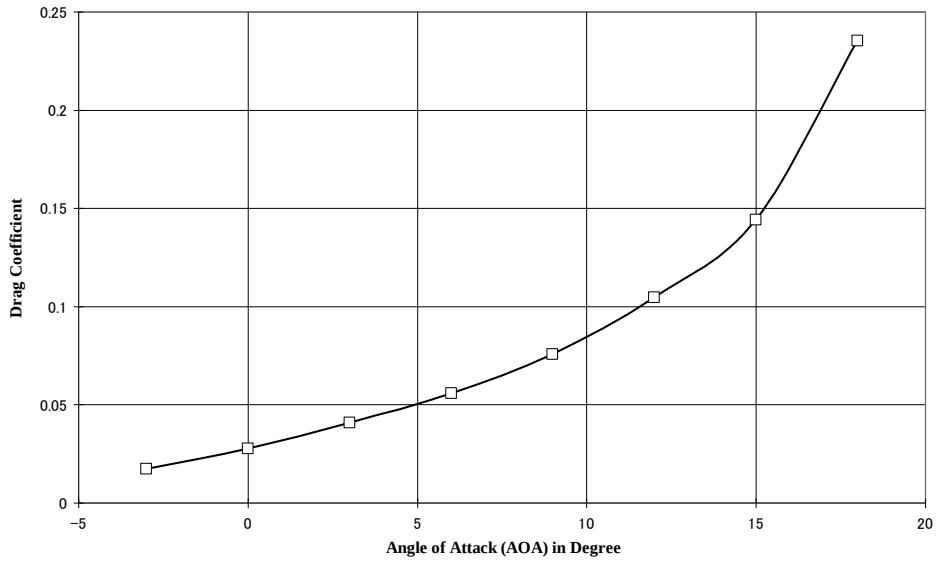

Figure 4.14: Variation of Drag Coefficient with Angle of Attack for Conventional Cylindrical Shaped Fuselage UAV Model at 20 m/s.

4.9 Aerodynamic Characteristics of Aerofoil Shaped Fuselage at 20 m/s

The variation of lift coefficient with angle of attack at 20 m/s for aerofoil shaped fuselage model at different angle of attack is shown in Figure 4.15. The zero lift angle has been found at -3º angle of attack. Then the lift coefficient increases almost linearly with the increase of angle of attack up to approximately 15°. In other wards, the lift coefficient increases linearly with the increase of angle of attack up to 15°. After wards, the lift coefficient decreases with the further increase of angle of attack. As such, the stalling angle of aerofoil shaped fuselage UAV model is found at about 15˚. It is also observed that the maximum lift coefficient, C_{Lmax} for this type of model is approximately 1.20.

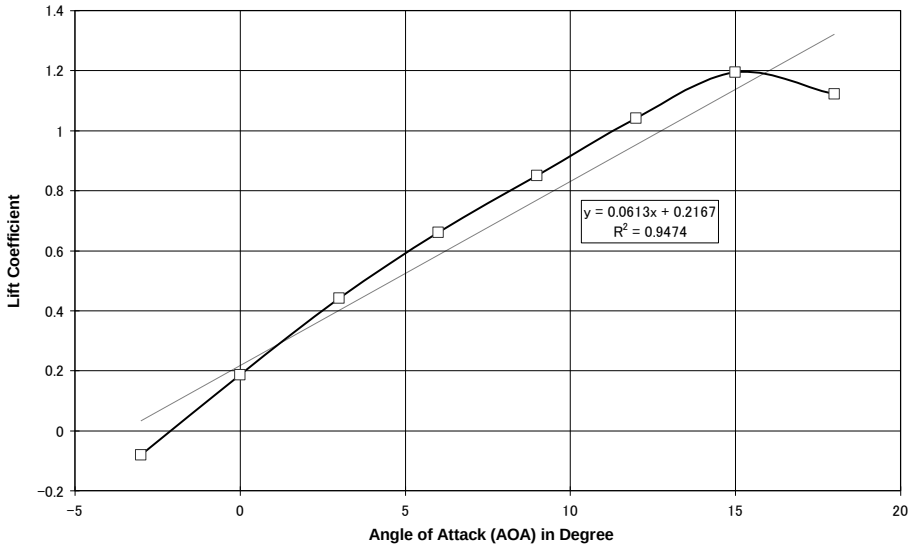

Figure 4.15: Variation of Lift Coefficient with Angle of Attack for Aerofoil Shaped Fuselage UAV Model at 20 m/s.

The variation of drag coefficient with angle of attack at 20 m/s for aerofoil shaped fuselage model at different angle of attack is shown in Figure 4.16. The shape of the drag coefficient vs angle of attack curve is found parabolic nature. As such, the drag coefficient increases with the increase of angle of attack. The value of drag coefficient for the aerofoil shaped fuselage UAV model at 15° angle of attack is found 0.166.

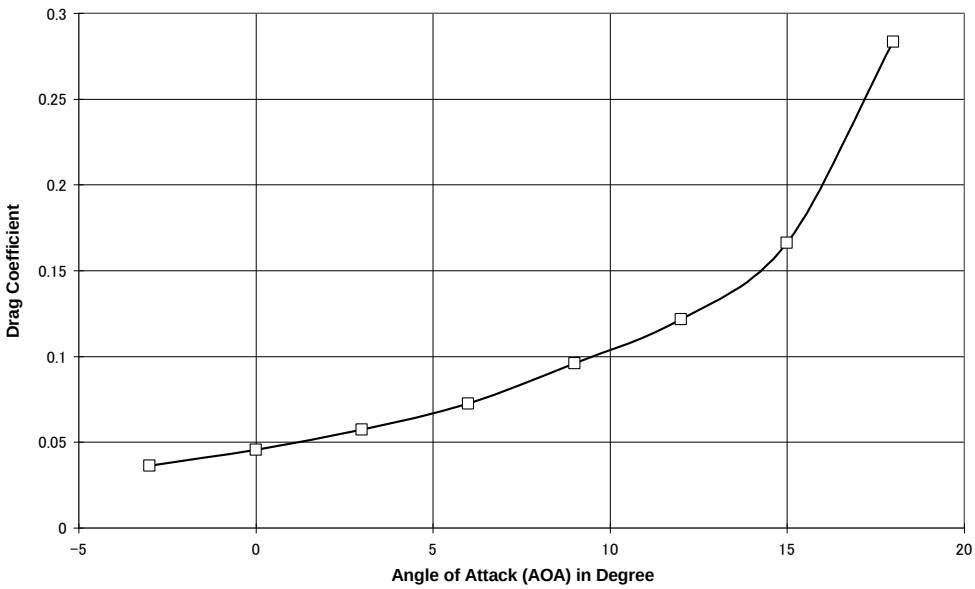

Figure 4.16: Variation of Drag Coefficient with Angle of Attack for Aerofoil Shaped Fuselage UAV Model at 20 m/s.

4.10 Aerodynamic Characteristics of 2D NACA 4416 Aerofoil Profile at 40 m/s

The variation of lift coefficient with angle of attack at 40 m/s for 2D NACA 4416 Profile at different angle of attack is shown in Figure 4.17. The zero lift angle has been found at -3º angle of attack. Then the lift coefficient increases almost linearly with the increase of angle of attack up to approximately 15º. In other wards, the lift coefficient increases linearly with the increase of angle of attack up to 15º. After wards, the lift coefficient decreases with the further increase of angle of attack. As such, the stalling angle of 2D NACA 4416 profile is found at about 15˚. It is also observed that the maximum lift coefficient, C_{Lmax} for this profile is approximately 1.52.

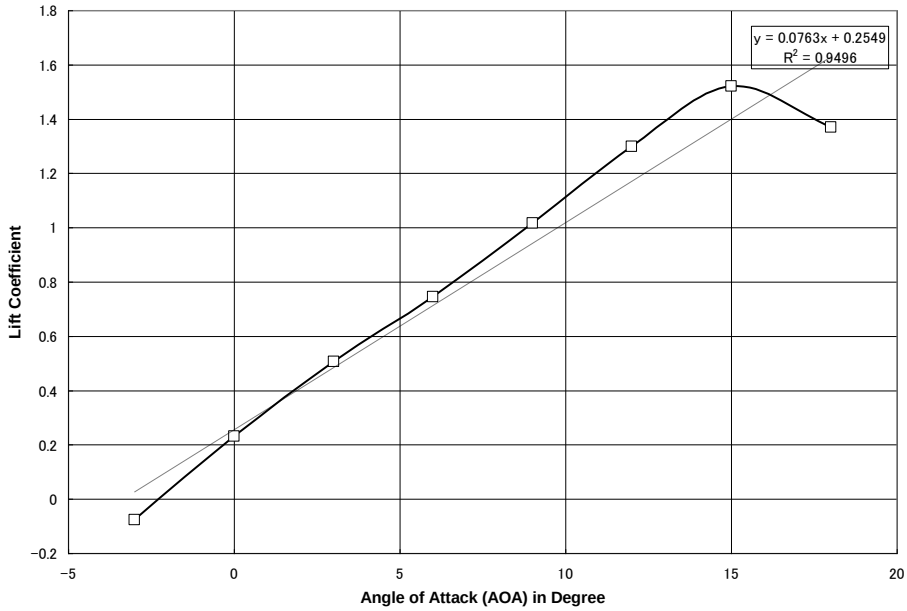

Figure 4.17: Variation of Lift Coefficient with Angle of Attack for 2D NACA 4416 Profile at 40 m/s.

The variation of drag coefficient with angle of attack at 40 m/s for 2D NACA 4416 Profile at different angle of attack is shown in Figure 4.18. The shape of the drag coefficient vs angle of attack curve is found parabolic nature. As such, the drag coefficient increases with the increase of angle of attack. The value of drag coefficient for this profile at 15º angle of attack is found 0.118.

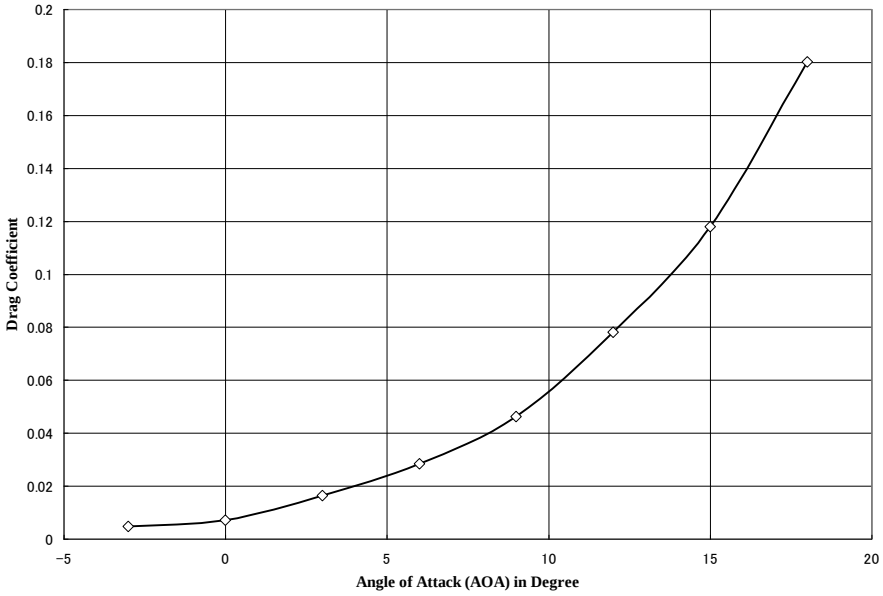

Figure 4.18: Variation of Drag Coefficient with Angle of Attack for 2D NACA 4416 Profile at 40 m/s.

4.11 Aerodynamic Characteristics of Conventional Cylindrical Shaped Fuselage at 40 m/s

The variation of lift coefficient with angle of attack at 40 m/s for conventional cylindrical shaped fuselage model at different angle of attack is shown in Figure 4.19. The zero lift angle has been found at -3° angle of attack. Then the lift coefficient increases almost linearly with the increase of angle of attack up to approximately 15°. In other wards, the lift coefficient increases linearly with the increase of angle of attack up to 15°. After wards, the lift coefficient decreases with the further increase of angle of attack. As such, the stalling angle of conventional model is found at about 15˚. It is also observed that the maximum lift coefficient, C_{Lmax} for this type of model is approximately 1.109.

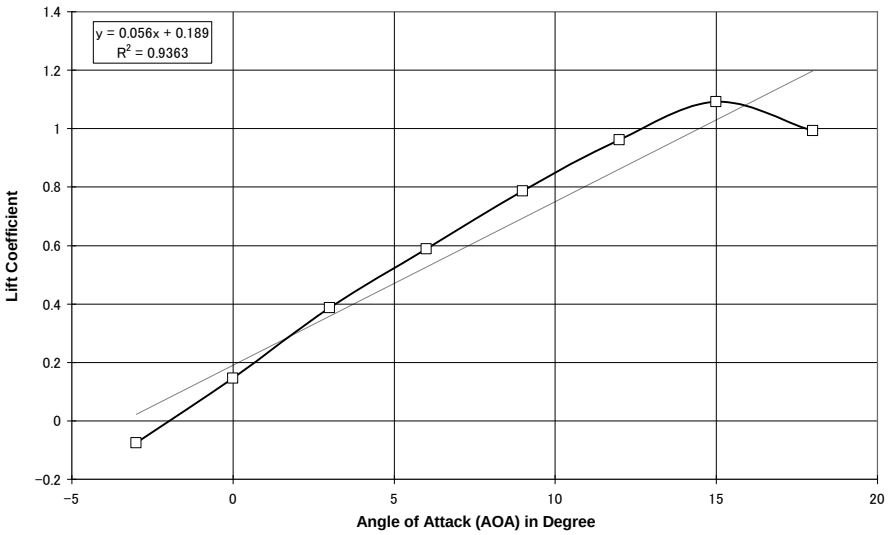

Figure 4.19: Variation of Lift Coefficient with Angle of Attack for Conventional Cylindrical Shaped Fuselage UAV Model at 40 m/s.

The variation of drag coefficient with angle of attack at 40 m/s for conventional cylindrical shaped fuselage model at different angle of attack is shown in Figure 4.20. The shape of the drag coefficient vs angle of attack curve is found parabolic nature. As such, the drag coefficient increases with the increase of angle of attack. The value of drag coefficient for this conventional model at 15° angle of attack is found 0.134.

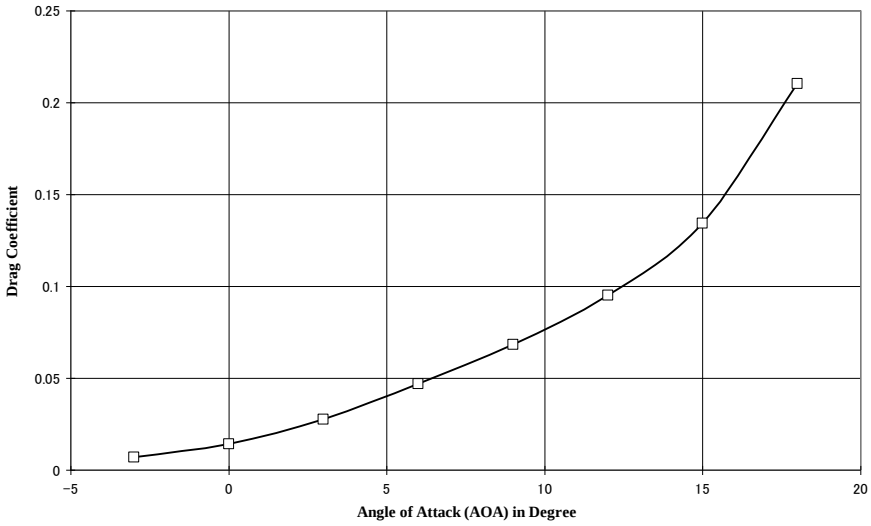

Figure 4.20: Variation of Drag Coefficient with Angle of Attack for Conventional Cylindrical Shaped Fuselage UAV Model at 40 m/s.

4.12 Aerodynamic Characteristics of Aerofoil Shaped Fuselage at 40 m/s

The variation of lift coefficient with angle of attack at 40 m/s for aerofoil shaped fuselage model at different angle of attack is shown in Figure 4.21. The zero lift angle has been found at -3º angle of attack. Then the lift coefficient increases almost linearly with the increase of angle of attack up to approximately 15º. In other wards, the lift coefficient increases linearly with the increase of angle of attack up to 15º. After wards, the lift coefficient decreases with the further increase of angle of attack. As such, the stalling angle of aerofoil shaped fuselage UAV model is found at about 15˚. It is also observed that the maximum lift coefficient, C_{Lmax} for this type of model is approximately 1.221.

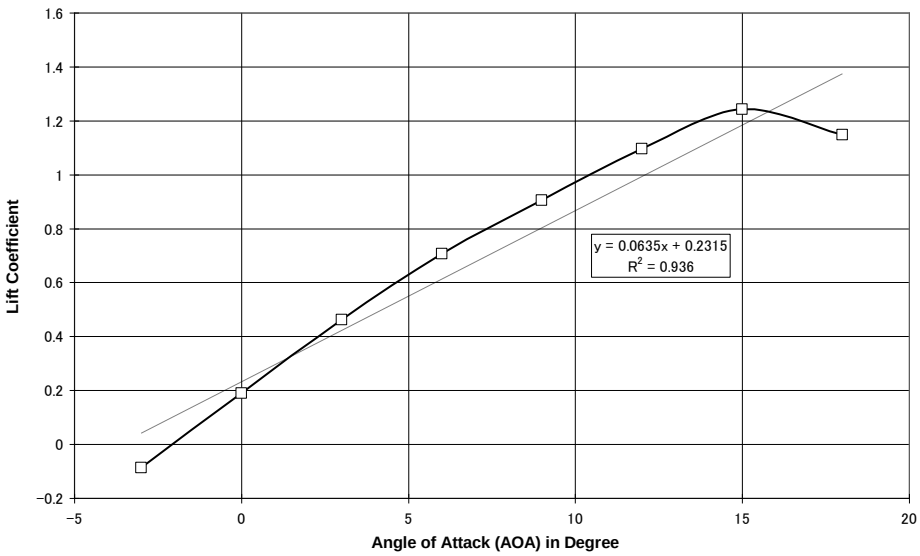

Figure 4.21: Variation of Lift Coefficient with Angle of Attack for Aerofoil Shaped Fuselage UAV Model at 40 m/s.

The variation of drag coefficient with angle of attack at 40 m/s for aerofoil shaped fuselage model at different angle of attack is shown in Figure 4.22. The shape of the drag coefficient vs angle of attack curve is found parabolic nature. As such, the drag coefficient increases with the increase of angle of attack. The

value of drag coefficient for the aerofoil shaped fuselage UAV model at 15° angle of attack is found 0.145.

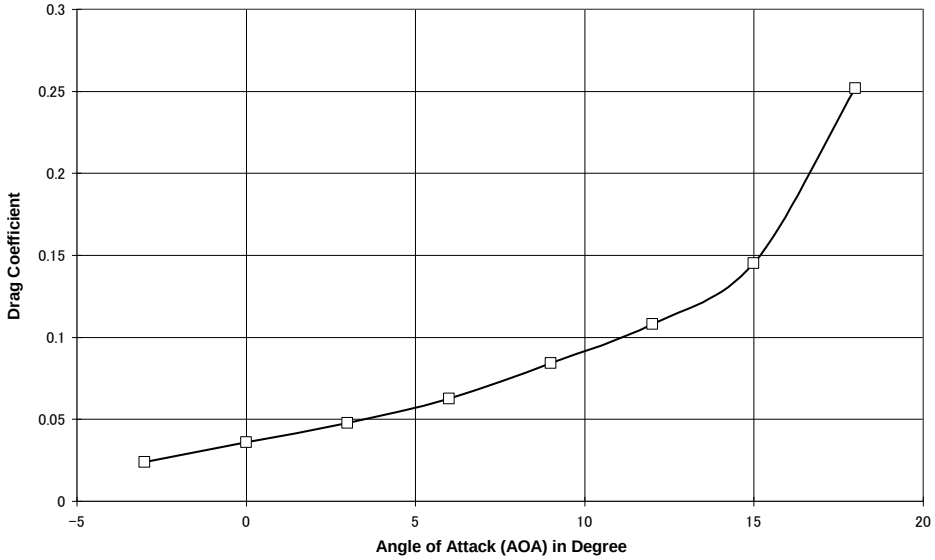

Figure 4.22: Variation of Drag Coefficient with Angle of Attack for Aerofoil Shaped Fuselage UAV Model at 40 m/s.

4.13 Surface Pressure of 2D NACA 4416 Aerofoil Profile at 20 m/s

Fifteen pressure tapping points have been made on the upper and lower surface of 2D NACA 4416 aerofoil profile to measure the surface Pressure. Figure 4.23 shows the 15 pressure tapping points made on both upper and lower surfaces of 2D NACA 4416 aerofoil profile. The variation of Pressure with chord length for 2D NACA 4416 aerofoil profile at 3°, 9°, 15° (stall angle) and 18° angle of attack for 20 m/s is shown in **Appendix – A** to Figure 4.24 (a, b, c and d). The difference of pressure between the lower surface pressure (pressure side) and the upper surface pressure (suction side) determines the amount of lift and drag force produced by this type of aerofoil. The height of the upper surface suction peak increases with the increase of angle of attack up to about 15°. Afterwards, separation starts due to sudden flattening of the upper surface pressure distribution (reduction of suction peak) with further increase of angle of attack. Furthermore increase of angle of attack will further reduce the lift.

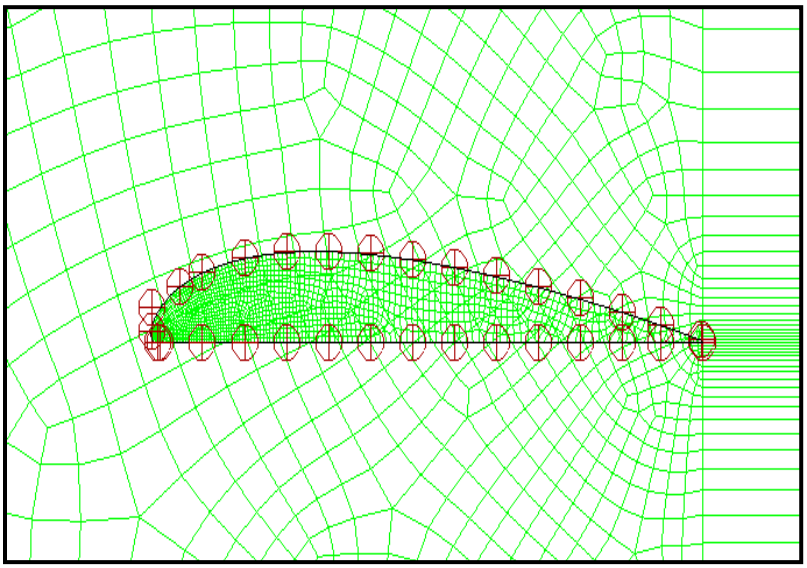

Figure 4.23: Point Surfaces of 2D NACA 4416 Profile.

4.14 Surface Pressure of Conventional Cylindrical Shaped Fuselage at 20 m/s

Fifteen pressure tapping points have been made on the upper and lower surface of 3D Conventional Cylindrical Shaped Fuselage UAV model at 25%, 50%, 75% and 90% from the root of left wing. Figure 4.25 shows the tapping points made on both upper and lower surfaces of left wing of 3D Conventional Cylindrical Shaped Fuselage UAV model. The variation of Pressure with chord length for Conventional Cylindrical Shaped Fuselage UAV model at 3°, 9°, 15° (stall angle) and 18° angle of attack for 20 m/s is shown in **Appendix – B** to Figure 4.26 (a, b, c and d), 4.27 (a, b, c and d), 4.28 (a, b, c and d) and 4.29 (a, b, c and d) respectively. The difference of pressure between the lower surface pressure (pressure side) and the upper surface pressure (suction side) determines the amount of lift and drag force produced by this type of aerofoil. The height of the upper surface suction peak increases with the increase of angle of attack up to about 15°. Afterwards, separation starts due to sudden flattening of the upper surface pressure distribution

(reduction of suction peak) with further increase of angle of attack. Furthermore increase of angle of attack will further reduce the lift.

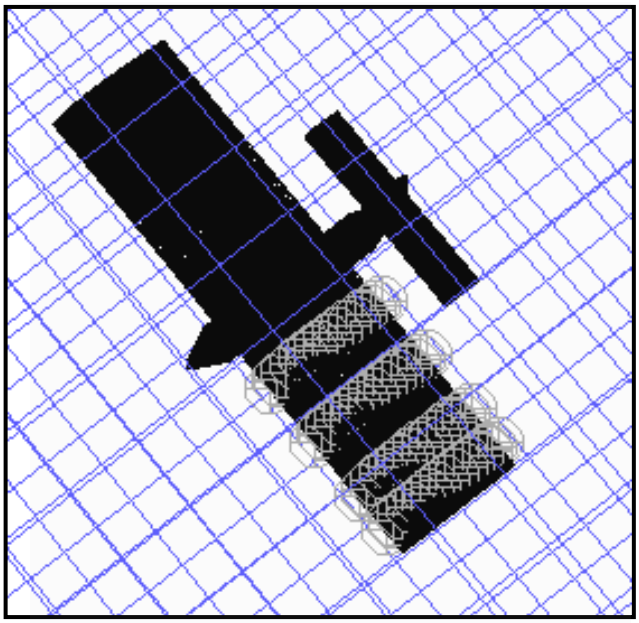

Figure 4.25: Tapping points on Left Wing of 3D Conventional Cylindrical Shaped Fuselage UAV model.

4.15 Surface Pressure of Aerofoil Shaped Fuselage at 20 m/s

Fifteen pressure tapping points have been made on the upper and lower surface of 3D Aerofoil Shaped Fuselage UAV model at 25%, 50%, 75% and 90% from the root of left wing. Figure 4.30 shows the tapping points made on both upper and lower surfaces of left wing of 3D Aerofoil Shaped Fuselage UAV model. The variation of Pressure with chord length for Conventional Cylindrical Shaped Fuselage UAV model at 3°, 9°, 15° (stall angle) and 18° angle of attack for 20 m/s is shown in **Appendix – C** to Figure 4.31 (a, b, c and d), 4.32 (a, b, c and d), 4.33 (a, b, c and d) and 4.34 (a, b, c and d) respectively. The difference of pressure between the lower surface pressure (pressure side) and the upper surface pressure (suction side) determines the amount of lift and drag force produced by this type of aerofoil. The height of the upper surface suction peak increases with the increase of angle of attack up to about 15°. Afterwards, separation starts due to sudden flattening of the upper surface pressure distribution (reduction of suction peak) with

further increase of angle of attack. Furthermore increase of angle of attack will further reduce the lift.

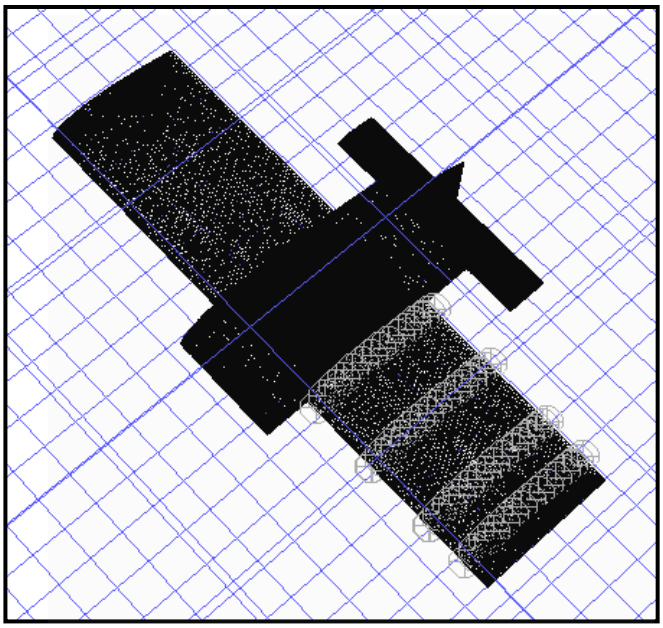

Figure 4.30: Tapping points on Left Wing of 3D Aerofoil Shaped Fuselage UAV model.

4.16 Surface Pressure of 2D NACA 4416 Aerofoil Profile at 40 m/s

Fifteen pressure tapping points have been made on the upper and lower surface of 2D NACA 4416 aerofoil profile to measure the surface Pressure. The variation of Pressure with chord length for 2D NACA 4416 aerofoil profile at 3°, 9°, 15° (stall angle) and 18° angle of attack for 40 m/s is shown in **Appendix – D** to Figure 4.35 (a, b, c and d). The difference of pressure between the lower surface pressure (pressure side) and the upper surface pressure (suction side) determines the amount of lift and drag force produced by this type of aerofoil. The height of the upper surface suction peak increases with the increase of angle of attack up to about 15°. Afterwards, separation starts due to sudden flattening of the upper surface pressure

distribution (reduction of suction peak) with further increase of angle of attack. Furthermore increase of angle of attack will further reduce the lift.

4.17 Surface Pressure of Conventional Cylindrical Shaped Fuselage at 40 m/s

Fifteen pressure tapping points have been made on the upper and lower surface of 3D Conventional Cylindrical Shaped Fuselage UAV model at 25%, 50%, 75% and 90% from the root of left wing. The variation of Pressure with chord length for Conventional Cylindrical Shaped Fuselage UAV model at 3°, 9°, 15° (stall angle) and 18° angle of attack for 40 m/s is shown in **Appendix – E** to Figure 4.36 (a, b, c and d), 4.37 (a, b, c and d), 4.38 (a, b, c and d) and 4.39 (a, b, c and d) respectively. The difference of pressure between the lower surface pressure (pressure side) and the upper surface pressure (suction side) determines the amount of lift and drag force produced by this type of aerofoil. The height of the upper surface suction peak increases with the increase of angle of attack up to about 15°. Afterwards, separation starts due to sudden flattening of the upper surface pressure distribution (reduction of suction peak) with further increase of angle of attack. Furthermore increase of angle of attack will further reduce the lift.

4.18 Surface Pressure of Aerofoil Shaped Fuselage at 40 m/s

Fifteen pressure tapping points have been made on the upper and lower surface of 3D Aerofoil Shaped Fuselage UAV model at 25%, 50%, 75% and 90% from the root of left wing. The variation of Pressure with chord length for Conventional Cylindrical Shaped Fuselage UAV model at 3°, 9°, 15° (stall angle) and 18° angle of attack for 40 m/s is shown in **Appendix – F** to Figure 4.40 (a, b, c and d), 4.41 (a, b, c and d), 4.42 (a, b, c and d) and 4.43 (a, b, c and d) respectively. The difference of pressure between the lower surface pressure (pressure side) and the upper surface pressure (suction side) determines the amount of lift and drag force produced by this type of aerofoil. The height of the upper surface suction peak increases with the increase of angle of attack up to about 15°. Afterwards, separation starts due to sudden flattening of the upper surface pressure distribution

(reduction of suction peak) with further increase of angle of attack. Furthermore increase of angle of attack will further reduce the lift.

4.19 Flow of Air on the Models

Air flows over the conventional cylindrical shaped fuselage and aerofoil shaped fuselage models at 20 m/s and 40 m/s respectively at different angle of attacks from -3º to 18º. Steam-line flow over the aerofoil sections of the wings of both the models as well as separation from the trailing edge could be visualized from Figure 4.44 to 4.49. It is found that all components (surfaces) of the aerofoil shaped fuselage contributed to the total lift. As such, the aerofoil shaped fuselage model is producing extra lift along with it's wing and this type of model might be a better option for designing the future UAV.

The aerofoil shaped fuselage model is also producing extra drag due to increased fuselage frontal area, fuselage-wing interference effect and trailing edge vortex. The effect of fuselage frontal area is not that much significant as the size of UAV is smaller. The fuselage-wing interference effect has been reduced by selecting the up wing type blended model. However, ways for reduction of the trailing edge vortex which leads to produce the induced drag from the aerofoil shaped fuselage might be a good option for future research.

As such, though the aerofoil shaped fuselage model would produce some extra drag than that of the conventional cylindrical shaped fuselage but in comparison of producing total amount of lift from all of it's components (surfaces), it is true that such type of fuselage might be more efficient for use in future than that of the conventional cylindrical shaped fuselage for designing the future UAV. More so, the concept of all body lifting structure would also open a good research arena in future. The visualization of air flow effect indicating the stream line flow over the models as well as flow separation from the trailing edges at the stall angle (15º angle of attack) are shown in Figure 4.44 to 4.49 respectively.

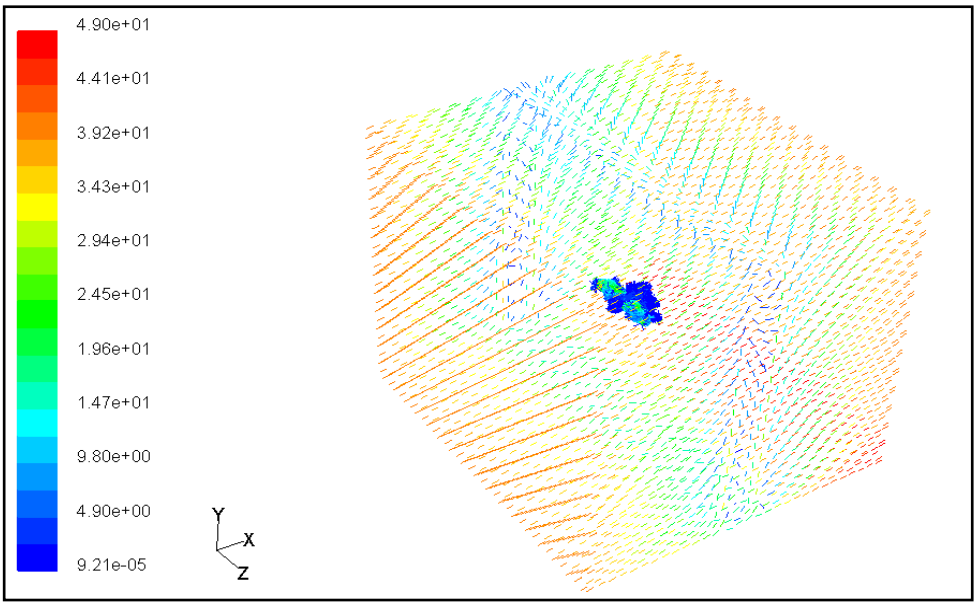

Figure 4.44: Flow of Air through Conventional Cylindrical Shaped Fuselage Model.

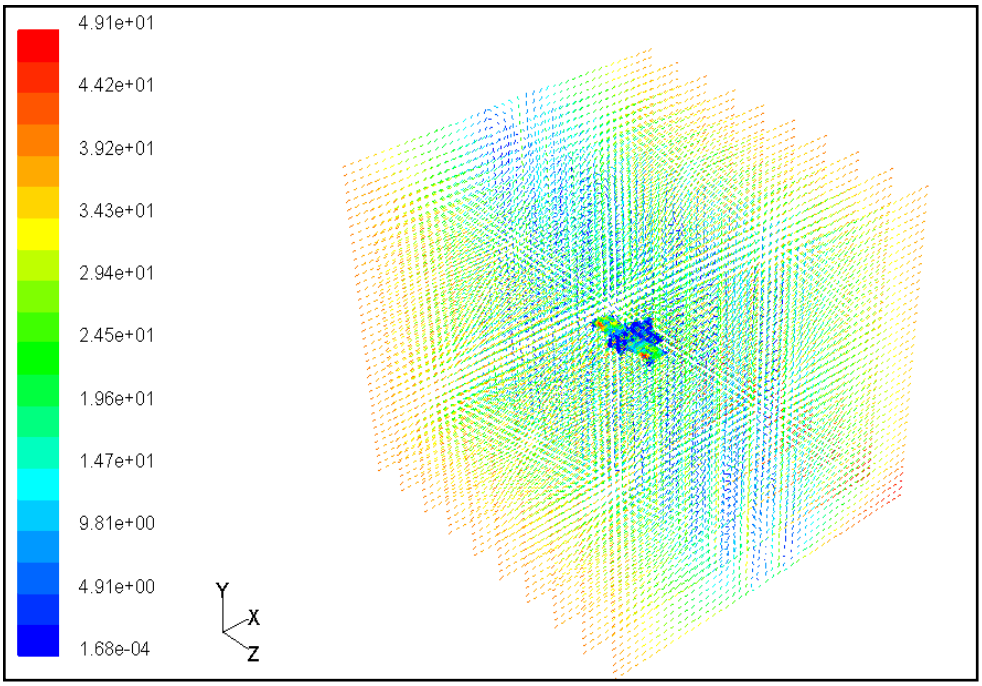

Figure 4.45: Flow of Air through Aerofoil Shaped Fuselage Model.

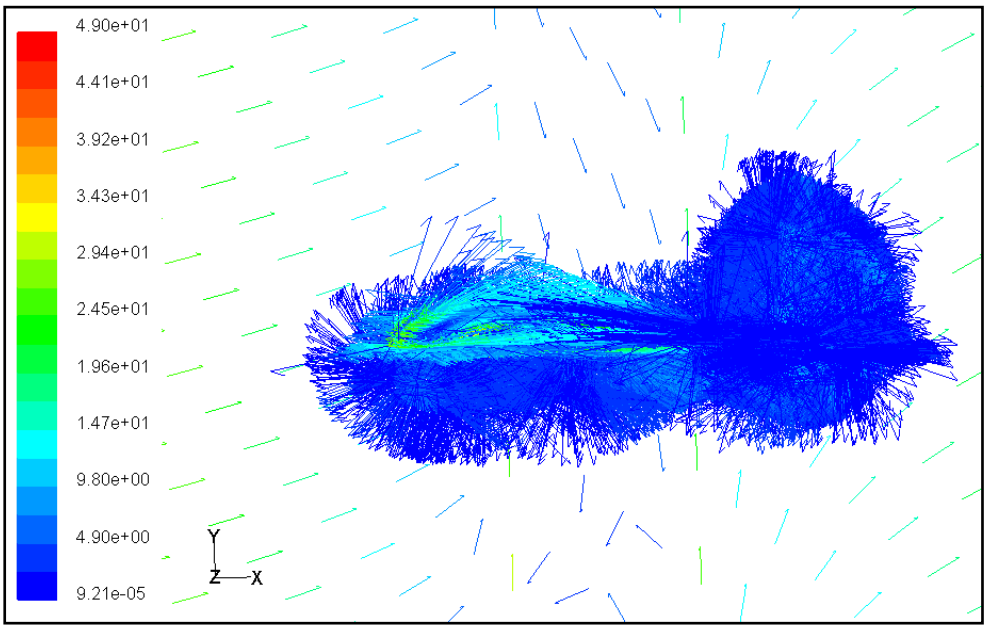

Figure 4.46: Flow of Air through Conventional Cylindrical Shaped Fuselage Model (Left Side View).

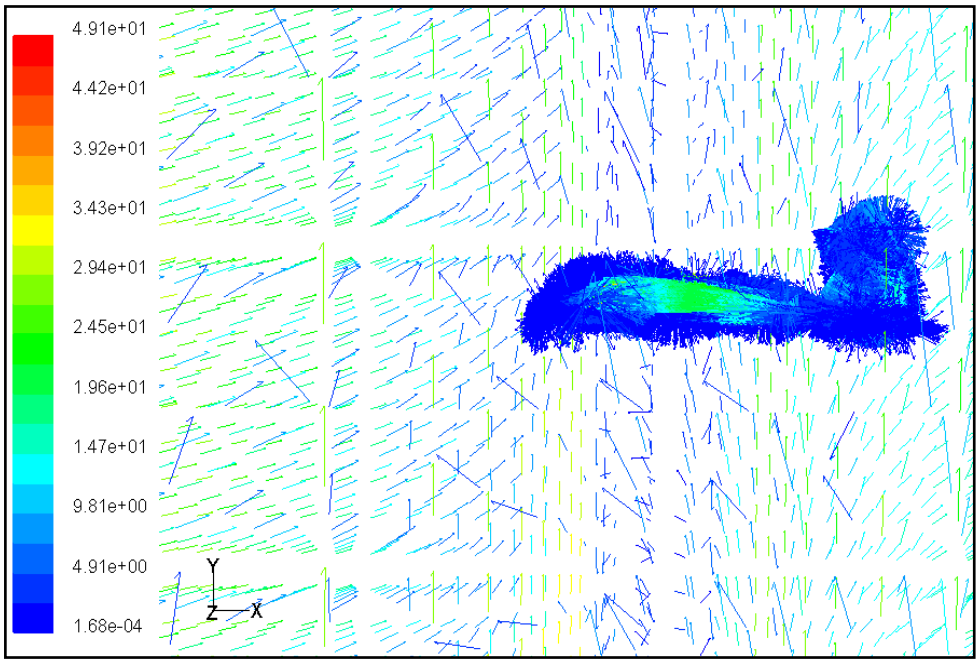

Figure 4.47: Flow of Air through Aerofoil Shaped Fuselage Model (Left Side View).

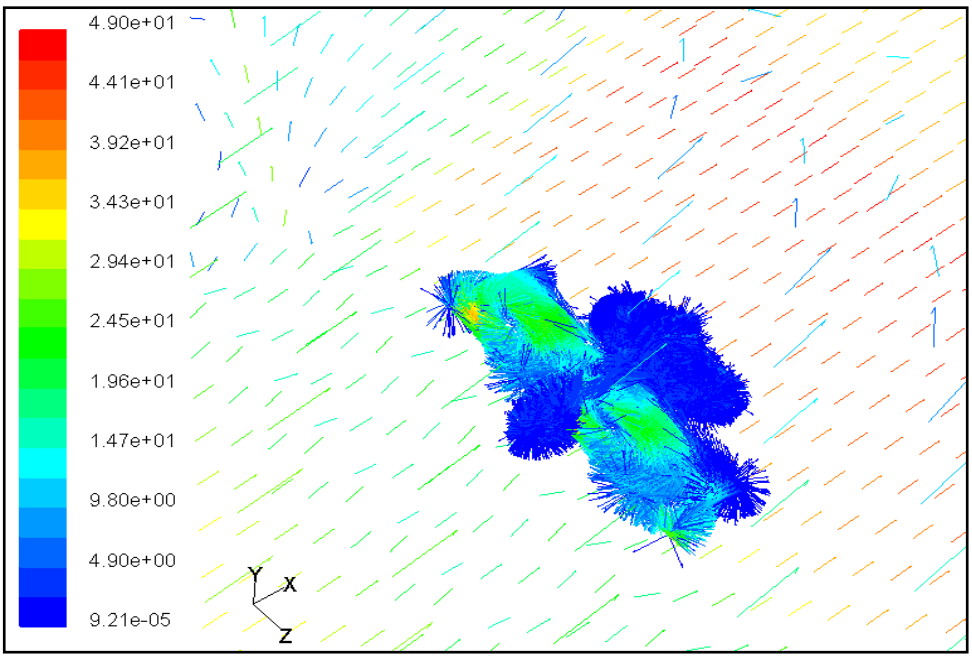

Figure 4.48: Flow of Air through Conventional Cylindrical Shaped Fuselage Model (Isometric View).

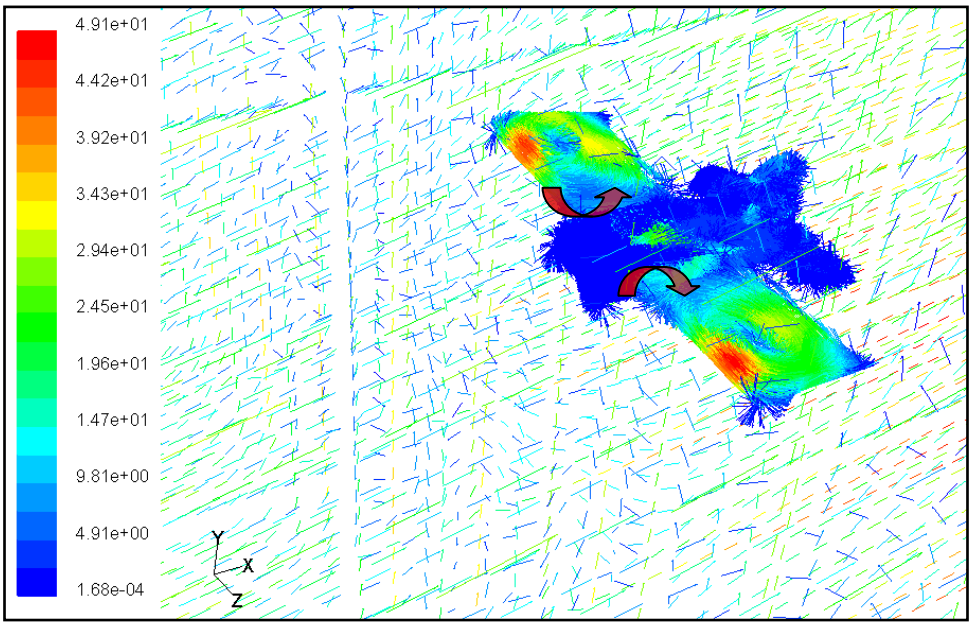

Figure 4.49: Flow of Air on the Aerofoil Shaped Fuselage Model

(Isometric View).

EXPERIMENTAL SETUP

5.1 Wind Tunnel Model AF 100

Open circuit subsonic wind tunnel model AF 100 has been used to test the UAV models of conventional cylindrical shaped fuselage and aerofoil shaped fuselage. This wind tunnel gives accurate result and is suitable to carry out tests of experimental models. Said wind tunnel is incorporated with a computer based data acquisition system. Wind tunnel model AF 100 is shown in Figure 5.1. Air enters the wind tunnel through an aerodynamically designed diffuser (cone) that accelerates the air linearly. A separate control and instrumentation unit controls the speed of axial fan (air velocity in the working section) from 0 to 40 m/s. AF 100 wind tunnel is associated with some special accessories like Versatile Dada Acquisition System (VDAS), 3-Component Balance, two differential pressure transducers, 32 Way Pressure display Unit, smoke generator etc. Tapping pressures from the models could be measured either from manometers or from the pressure transducers.

Figure 5.1: Photograph of Wind Tunnel Model AF 100.

5.2 Working Section

The working section of AF 100 wind tunnel is a square section whose dimensions are 60 cm (length) x 32 cm (width) x 30 cm (height). A pitot-static tube and a traversing pitot tube fit on the working section, upstream and downstream of any model. Working section of wind tunnel model AF 100 is shown in Figure 5.2.

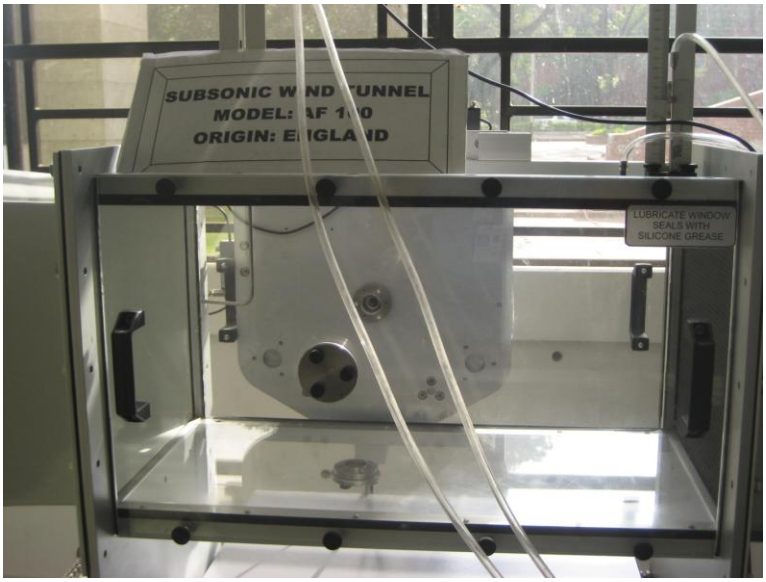

Figure 5.2: Photograph of Working Section of Wind Tunnel Model AF 100.

5.3 Versatile Data Acquisition System (VDAS).

It is a tool which has been incorporated with AF 100 model wind tunnel to read, record and save data automatically. It removes some human error and record lots of data in a short time, or automatically takes readings over several hours. A suitable computer is required to use with the VDAS system. The system has two parts – VDAS software and VDAS hardware (or computer interface module). The VDAS hardware connects the VDAS compatible sensors and instruments and converts the output signals into a format suitable for the VDAS software. Figure 5.3 shows the VDAS system.

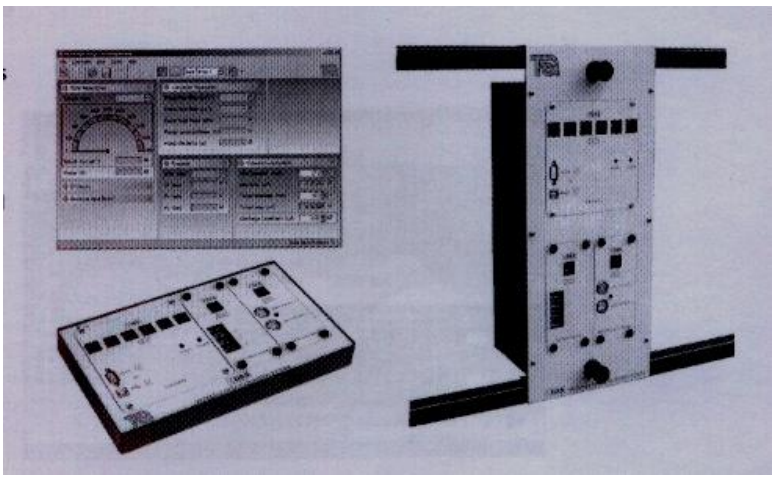

Figure 5.3: Photograph of VDAS System.

5.4 Three Component Balance (AFA 3).

The ‘Three Component Balance (AFA 3)’ is fitted with the working section of the wind tunnel model AF 100 to measure lift, drag and pitching moment exerted on the experimental models. The fabricated models are to be inserted through the equipment and it can be rotated 360 degrees freely in the force plate to allow adjustment of the angle of attack of the model. An incidence clamp could lock the models in position at a specific angle of attack. A dial graduated in degree on it’s periphery is fitted with this equipment which is used to measure the angle of attack of the models. This equipment is also incorporated with VDAS system to measure the lift and drag forces along with their coefficients automatically from the computer monitor through VDAS window. Photograph of ‘Three Component Balance (AFA 3)’ is shown in Figure 5.4.

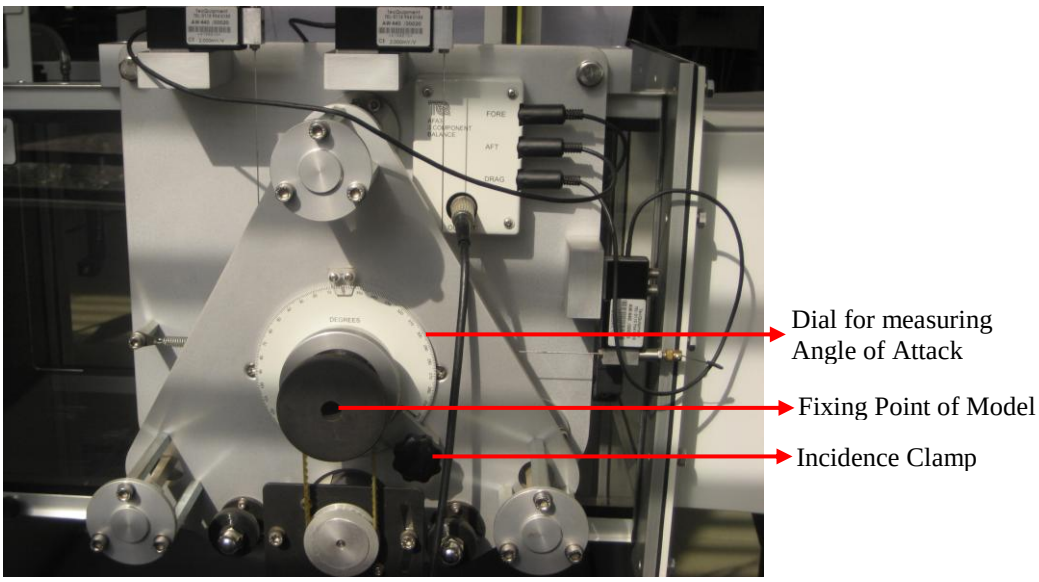

Figure 5.4: Photograph of Three Component Balance (AFA 3).

5.5 Differential Pressure Transducer (AFA 5).

Wind tunnel model AF 100 is fitted with two (02) pressure transducers rated at a maximum of $\pm$ 7 kPa pressure directly. It provides a means to measure and display a differential pressure from models, pitot static tubes and other devices fitted with the wind tunnel. The unit may also be used to measure pressure with respect to atmosphere or as a differential pressure measurement instrument. This equipment is also incorporated with VDAS system to measure differential pressure automatically from the computer monitor through VDAS window.

5.6 32-Way Pressure Display Unit (AFA 6).

Wind tunnel model AF 100 is fitted with one 32-Way Pressure Display Unit. This unit provides a means to measure and display 32 different point surface pressures from models, pitot static tubes and other devices fitted with the wind tunnel. The unit contains 32 calibrated pressure transducers rated at a maximum of $\pm$ 7 KPa

pressure. This module has an integral liquid crystal display with a scroll control which allows the user to read all 32 channels in group of 4 at any time. All pressures are measured by this unit with respect to atmosphere. This equipment is also incorporated with VDAS system to measure point surface pressure automatically from 32 tapping holes and displayed in the computer monitor through VDAS window.

5.7 Smoke Generator Unit.

A smoke generator unit could be fitted with the wind tunnel model AF 100 and operated to visualize the flow over the models. Smoke is created inside the unit by burning a special type of fuel with air. The generated smoke passes through a specialized nozzle fitted with the smoke generator. This nozzle is placed in front of the diffuser section of the wind tunnel. Smoke is sucked and flowed through the fabricated models. The stream line as well as separation of flow could be visualized easily by operating the smoke generator unit with incorporation of the wind tunnel.

5.8 Use of Adhesive and it's Effect.

Many types of adhesives are available to the woodworking industry. Most glues use in the woodworking industry is of liquid in nature. **S**everal factors affect the parts' assembly and the adhesive's curing. Some adhesives must be mixed immediately before applying and others are ready mixed. The quality of the surfaces to be glued together also affects the curing of glue. Generally, a smooth, un-sanded surface is needed to get good adhesion. If the surfaces are not smooth, the quality of the bond between the two wooden pieces is poor, leading to glue failure in use. The environment can also affect the bonding of the adhesive. The glue should be applied in a relatively dust-free area.

Epoxy resin are two-part adhesives that produce a strong, waterproof bond on wood, plastics, ceramics and practically any other material. Epoxies are good gap-fillers and can be readily used on non-porous surfaces. Epoxy is ideal for gluing ceramic tile to a table top or cabinet top or metal to wood. Here epoxy compound (m-seal) comprising of two tubes has been used as gap fillers between two wooden surfaces. M-seal is a general purpose epoxy compound which should not be used in items / areas which come into direct contact with flame, high temperature, drinking water and edible items. Both tubes of M-seal contain 25gm resin base and 25 gm of hardener, which are mixed together before apply to the wooden surfaces. After application on the wooden surface, varnish has been applied on all the objects to bring the surfaces of the object in the similar condition.

5.9 Experimental Set Up.

Four experimental set up have been fabricated by using NACA 4416 profile and utilizing the local resources. Among which, two set up of models have been fabricated to measure only the lift and drag forces and their coefficients. Another two set up of models have been used for measuring point surface pressures of upper and lower surfaces of the models from 36 tapping holes. Figure 5.5 and 5.6 show the two models for lift and drag force measurement and Figure 5.7 and 5.8 show half wing (only right wing) of another two models having 36 pressure tapping points. Figure 5.9, 5.10, 5.11 and 5.12 show different models fitted with the working section of the wind tunnel. The experimental set up for this thesis work consists of the following main features:

- Two models have been fabricated to measure lift and drag forces by using NACA 4416 profile. One model is of *'Conventional Cylindrical Shaped Fuselage'* and another one is of *'Aerofoil Shaped Fuselage'*.

    - The different dimensions of the wings of fabricated models (both cylindrical and aerofoil shaped fuselage) are: Chord Length, C = 55 mm;

Span, b = 114 mm (only left or right) and Maximum Thickness, t = 7 mm at 16% chord length from the root.

- The different dimensions of the cylindrical shaped fuselage of the fabricated model are: Diameter and length of middle portion = 21 mm and 66 mm respectively; Length and nose radious of divergent portion = 19 mm and 1.3 mm respectively, Divergent Angle = 25 Degree; Length of convergent portion = 23 mm, Nose radious of convergent portion = approximately zero and Convergent Angle = 22 Degree.

- The different dimensions of the aerofoil shaped fuselage of the fabricated models are: Chord Length, C = 108 mm; Span, b = 45 mm (Left + Right) and Maximum Thickness, t = 15 mm at 16% chord length from the root.

- Another two set up of models have been used for measuring point surface pressure of upper and lower surfaces of the models from 36 tapping holes. Only right side wing of both the models have been chosen as both the wings are identical. The different dimensions of the right wing of both the models are: Chord Length, C = 115 mm; Span, b = 250 mm (only left or right) and Maximum Thickness, t = 16 mm at 16% chord length from the root.
- Four pressure tapping points have been fabricated approximately 15%, 37.5%, 60% and 82.5% of chord length from the nose on each surface of the right wing.
- The tapping points have been fabricated at 25%, 50%, 75% and 90% from the root of right wing ie sixteen tapping holes have been made on each upper and lower surfaces of right wing.
- Another four (04) tapping points have been made near the stagnation point at the leading edge of right wing at 25%, 50%, 75% and 90% from the root to measure the point surface pressure near the stagnation point.
- All 36 point surface pressure points are connected with the 32-Way Pressure Display Unit through flexible plastic tubes.

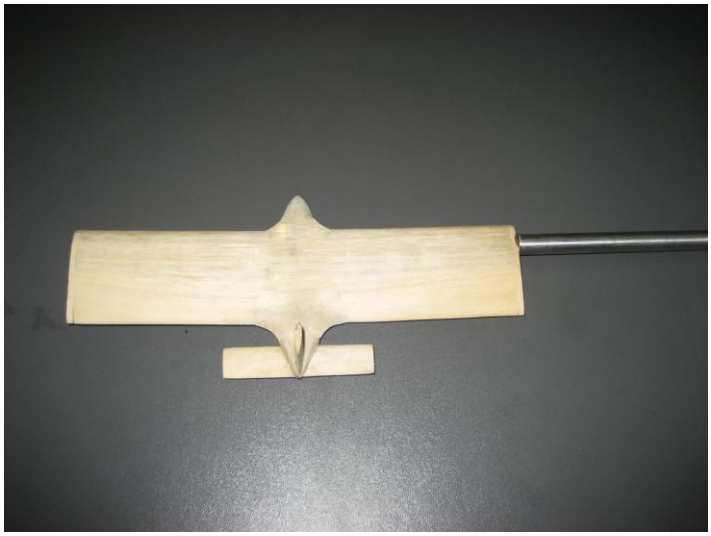

Figure 5.5: Conventional Cylindrical Shaped Fuselage UAV Model

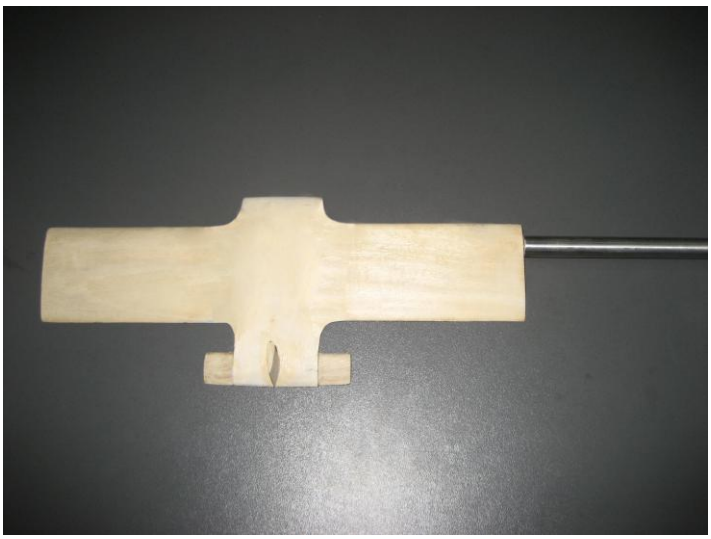

Figure 5.6: Aerofoil Shaped Fuselage UAV Model

Figure 5.7: Right Wing of Conventional Cylindrical Shaped Fuselage UAV Model

Figure 5.8: Right Wing of Aerofoil Shaped Fuselage UAV Model

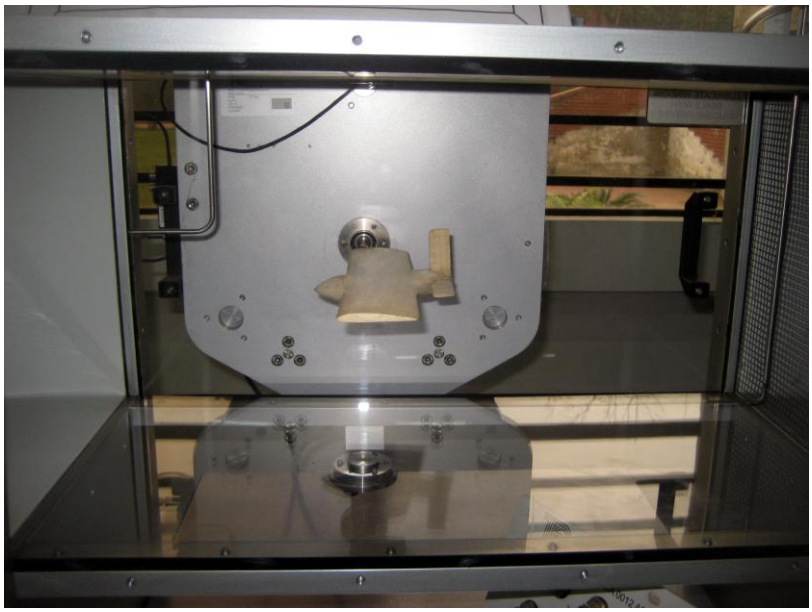

Figure 5.9: Conventional Cylindrical Shaped Fuselage UAV Model fitted with the Wind Tunnel

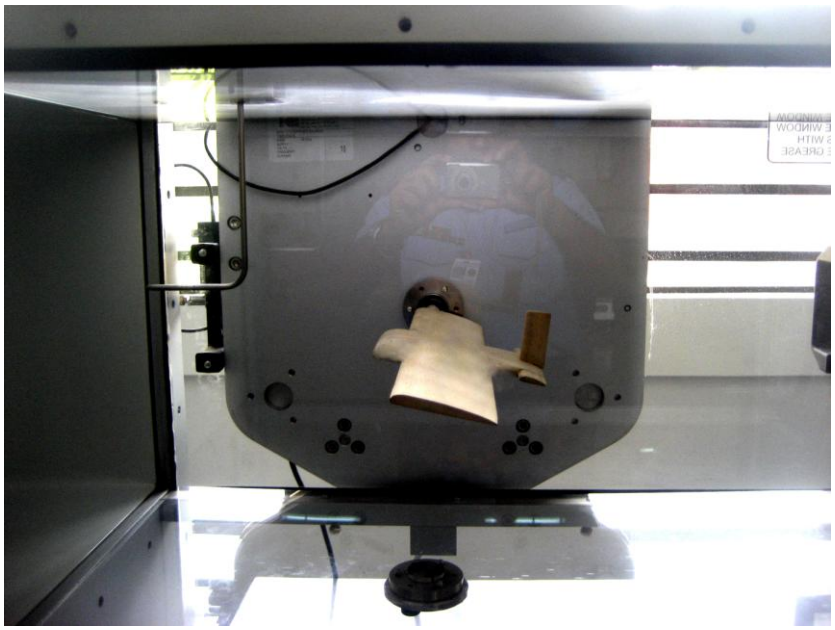

Figure 5.10: Aerofoil Shaped Fuselage UAV Model fitted with the Wind Tunnel

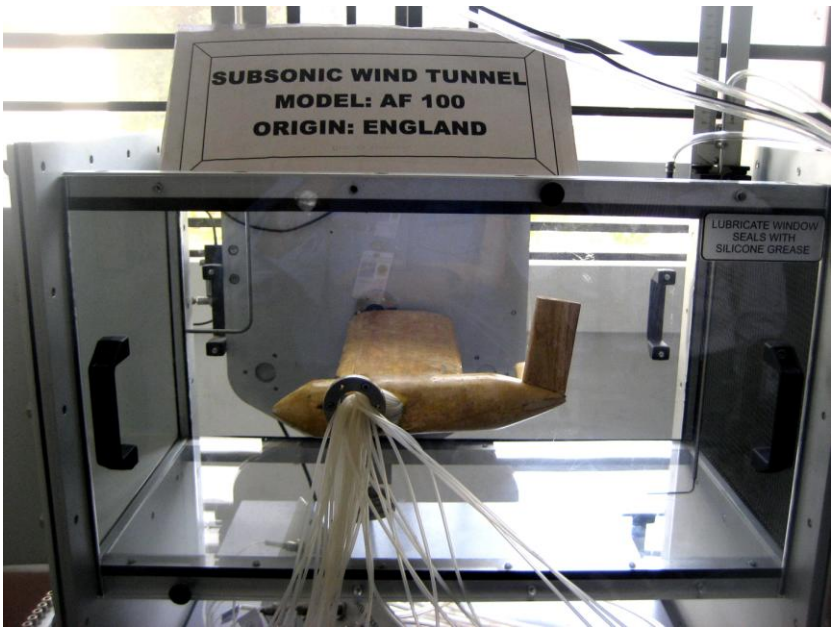

Figure 5.11: Right Wing of Conventional Cylindrical Shaped Fuselage UAV Model fitted with the Wind Tunnel

Figure 5.12: Right Wing of Aerofoil Shaped Fuselage UAV Model fitted with the Wind Tunnel

5.10 Test Section Upstream Velocity Profiles for 20 m/s and 40 m/s.

Air flows over the conventional cylindrical shaped fuselage and aerofoil shaped fuselage UAV models at 20 m/s and 40 m/s respectively at different angle of attacks from -3º to 18º angles of attack. A smoke generator unit has been fitted with the wind tunnel model AF 100 and operated to visualize the flow over the models. Smoke is created inside the unit by burning a special type of fuel with air. The generated smoke passes through a specialized nozzle fitted with the smoke generator. This nozzle is placed in front of the diffuser section of the wind tunnel, smoke is sucked and flowed through the fabricated models. Steam-line flow over both the models as well as understanding the test section upstream velocity profiles could be visualized from the breakage of streamline.

The wall effect on the streamlines of air flow over the surface of the test objects could also be visualized from the generated smoke. Free stream velocity has been

measured through pitot-static tube at 25mm, 50mm, 75mm, 100mm and 125mm distances from the test object at different velocities. Wall effect has only observed through separation of streamline and change of free stream velocity at only 100mm and 125mm distances from the test object but no wall velocity has been observed within 75mm distance from the test object. The air velocity over the surface of the test object at 3mm, 6mm, 9mm, 12mm and 15mm inside the test section has been measured from the pitot-static tube to know about the upstream velocity profiles at different speeds. The upstream velocities at 3mm, 6mm, 9mm, 12mm and 15mm distance from the test object inside the wind tunnel test section are found 20.4m/s, 20.8 m/s, 21.3 m/s, 21.8 m/s and 21.2 m/s respectively when air speed in front of the object has been kept at 20m/s. Further more, the upstream velocities at 3mm, 6mm, 9mm, 12mm and 15mm distances from the test object inside the wind tunnel test section are found 40.5m/s, 40.9 m/s, 41.3 m/s, 41.8 m/s and 41.1 m/s respectively when air speed in front of the object has been kept at 40m/s. Figure 5.13, 5.14, 5.15, 5.16 and 5.17 show upstream velocity profiles on the test object at different velocities.

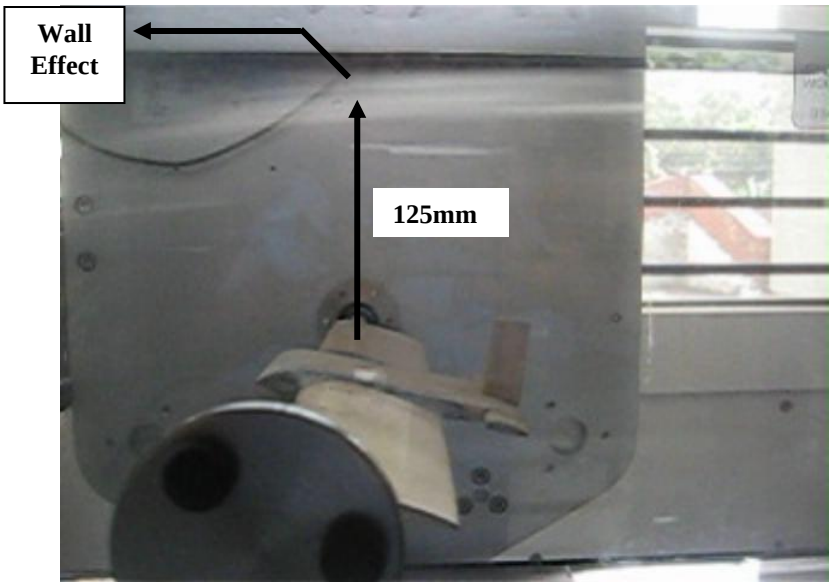

Figure 5.13: Generated smoke shows the upstream velocity profile and wall effect at 125mm distance from the test object

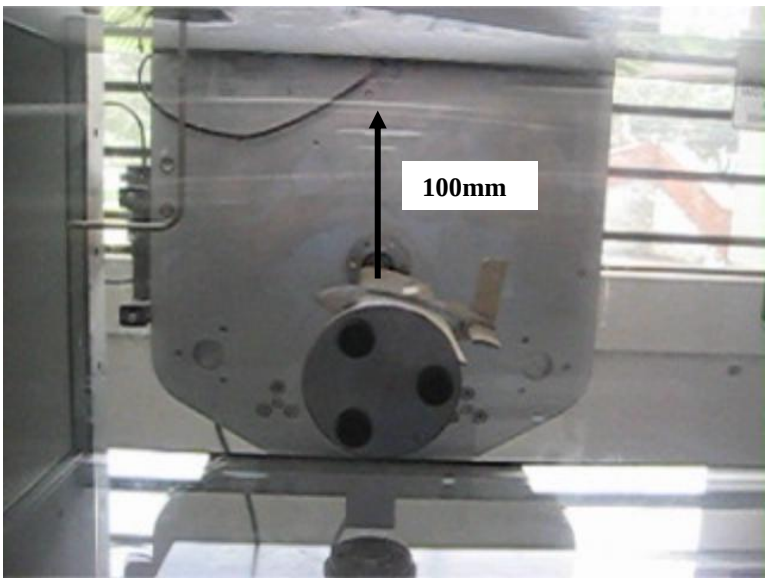

Figure 5.14: Generated smoke shows the upstream velocity profile and wall effect at 100mm distance from the test object

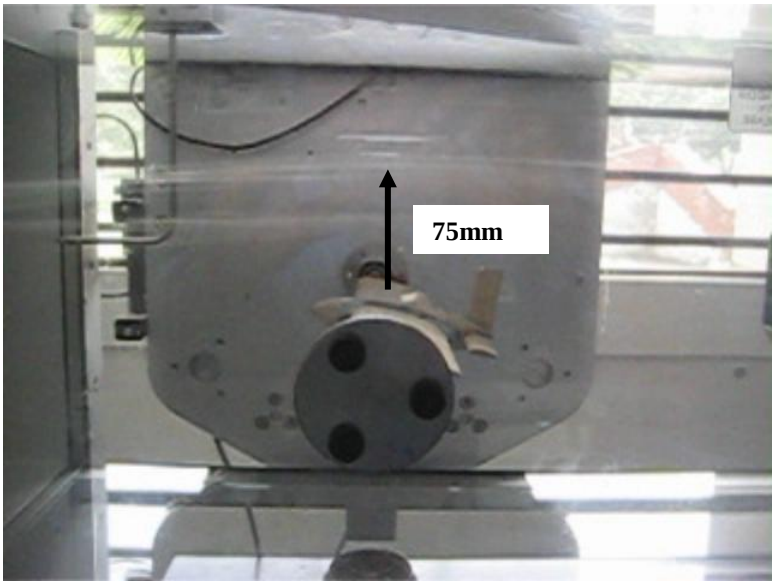

Figure 5.15: Generated smoke shows the upstream velocity profile at 75mm distance from the test object

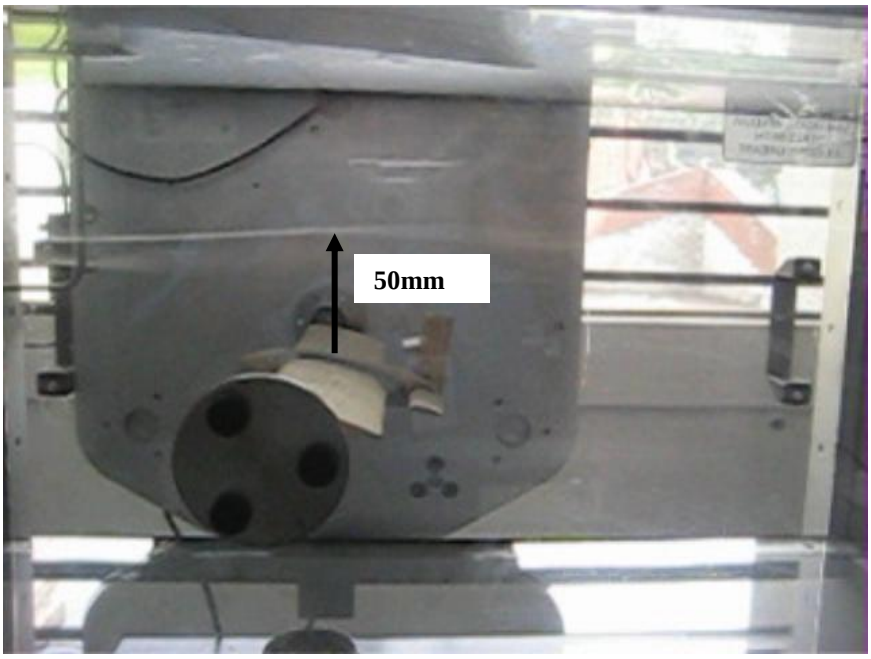

Figure 5.16: Generated smoke shows the upstream velocity profile at 50mm distance from the test object

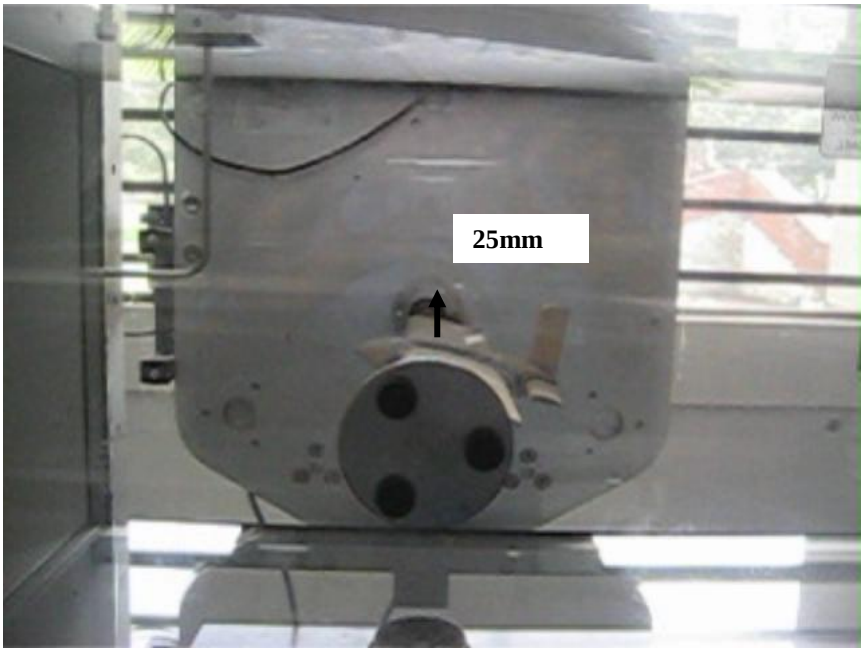

Figure 5.17: Generated smoke shows the upstream velocity profile at 25mm distance from the test object

EXPERIMENTAL RESULTS

6.1 Collection of Experimental Data

For investigation of the aerodynamic characteristics of both aerofoil shaped fuselage and conventional cylindrical shaped fuselage configurations, NACA 4416 cambered aerofoil has been used. Open circuit subsonic wind tunnel model AF 100 has been used to test both the UAV models. The flow is considered to be incompressible and subsonic flow. The free stream airflow has been kept as 20 m/s and 40 m/s respectively and the effect of temperature has been neglected. The experimental data have been obtained at different angles of attack from -3° to 18° angle of attack. All the four set up have been fitted with the wind tunnel one by one and lift force, drag force and their coefficients as well as point surface pressures have been measured experimentally.

6.2 Aerodynamic Characteristics of Conventional Cylindrical Shaped Fuselage at 20 m/s

The variation of lift coefficient with angle of attack at 20 m/s for conventional cylindrical shaped fuselage model at different angle of attack is shown in Figure 6.1. The zero lift angle has been found at -3º angle of attack. Then the lift coefficient increases almost linearly with the increase of angle of attack up to approximately 14°. In other wards, the lift coefficient increases linearly with the increase of angle of attack up to 14°. After wards, the lift coefficient decreases with the further increase of angle of attack. As such, the stalling angle of conventional model is found at about 14˚. It is also observed that the maximum lift coefficient, C_{Lmax} for this type of model is approximately 0.63.

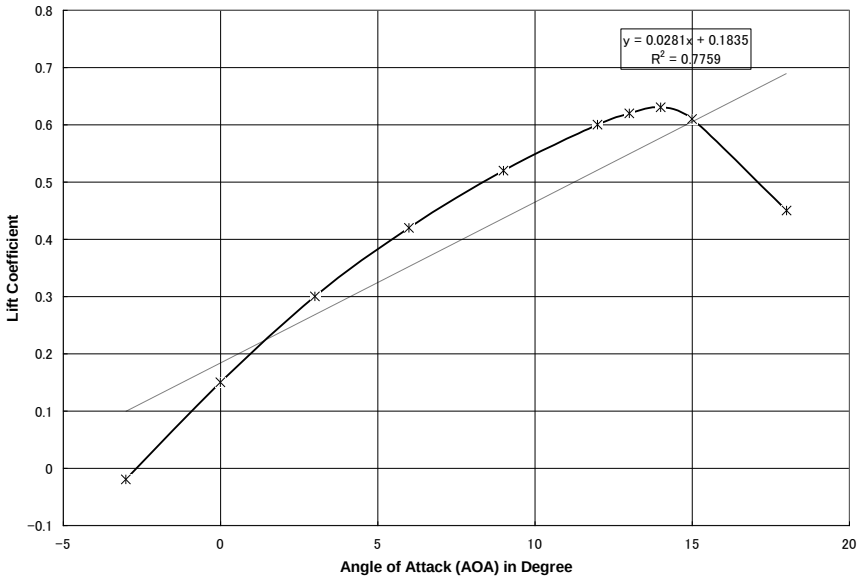

Figure 6.1: Variation of Lift Coefficient with Angle of Attack for Conventional Cylindrical Shaped Fuselage Model at 20 m/s.

The variation of drag coefficient with angle of attack at 20 m/s for conventional cylindrical shaped fuselage model at different angle of attack is shown in Figure 6.2. The shape of the drag coefficient vs angle of attack curve is found parabolic nature. As such, the drag coefficient increases with the increase of angle of attack. The value of drag coefficient for this conventional model at 14° angle of attack is found 0.075.

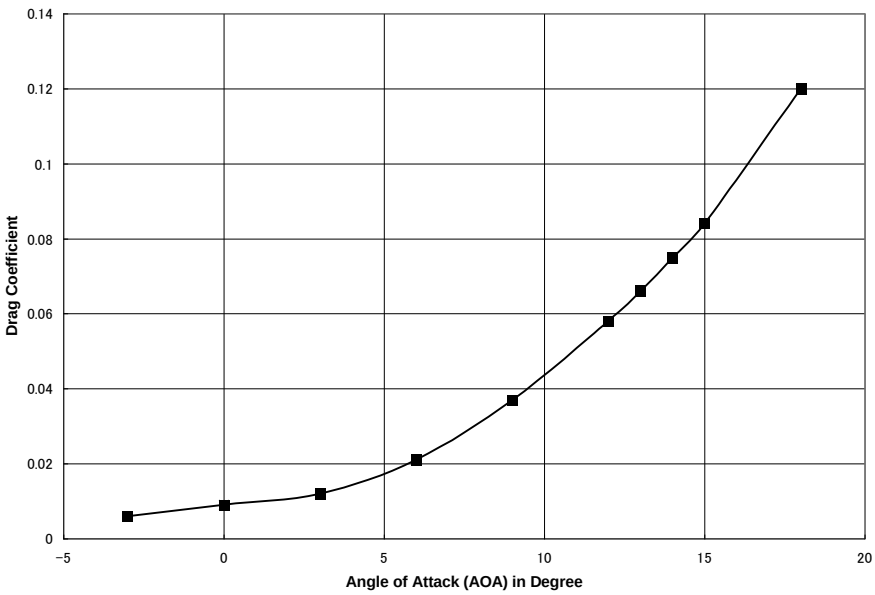

Figure 6.2: Variation of Drag Coefficient with Angle of Attack for Conventional Cylindrical Shaped Fuselage Model at 20 m/s.

6.3 Aerodynamic Characteristics of Aerofoil Shaped Fuselage at 20 m/s

The variation of lift coefficient with angle of attack at 20 m/s for aerofoil shaped fuselage model at different angle of attack is shown in Figure 6.3. The zero lift angle has been found at -3º angle of attack. Then the lift coefficient increases almost linearly with the increase of angle of attack up to approximately 14º. In other wards, the lift coefficient increases linearly with the increase of angle of attack up to 14º. After wards, the lift coefficient decreases with the further increase of angle of attack. As such, the stalling angle of aerofoil shaped fuselage UAV model is found at about 14˚. It is also observed that the maximum lift coefficient, C_{Lmax} for this type of model is approximately 0.78.

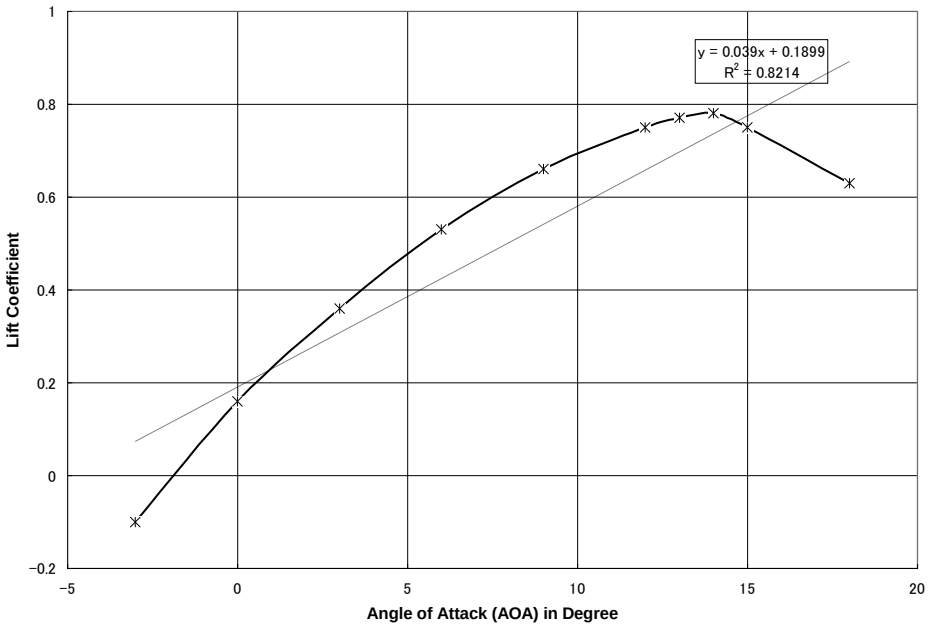

Figure 6.3: Variation of Lift Coefficient with Angle of Attack for Aerofoil Shaped Fuselage Model at 20 m/s.

The variation of drag coefficient with angle of attack at 20 m/s for aerofoil shaped fuselage UAV model at different angle of attack is shown in Figure 6.4. The shape of the drag coefficient vs angle of attack curve is found parabolic nature. As such, the drag coefficient increases with the increase of angle of attack. The value of drag coefficient for this aerofoil shaped fuselage UAV model at 14º angle of attack is found 0.089.

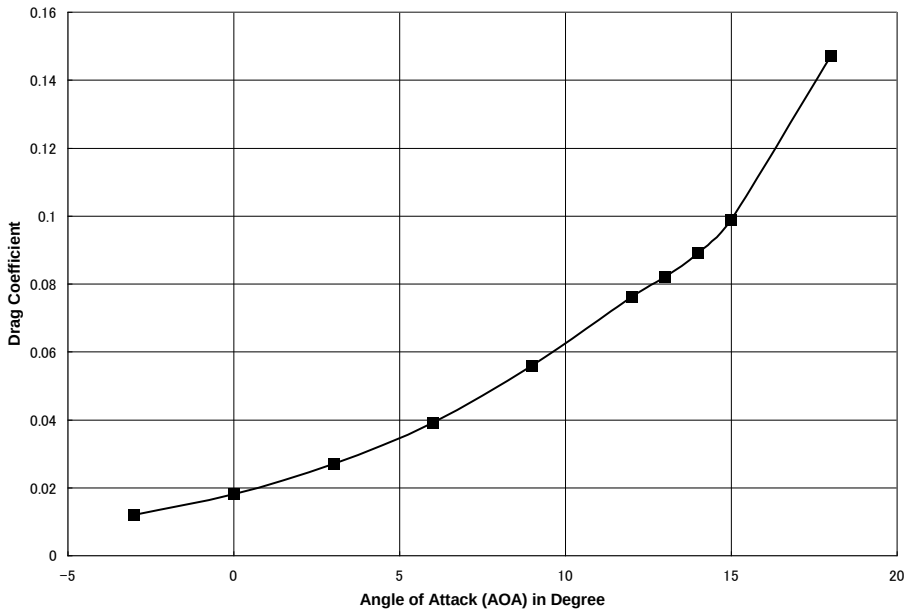

Figure 6.4: Variation of Drag Coefficient with Angle of Attack for Aerofoil Shaped Fuselage Model at 20 m/s.

6.4 Aerodynamic Characteristics of Conventional Cylindrical Shaped Fuselage at 40 m/s

The variation of lift coefficient with angle of attack at 40 m/s for conventional cylindrical shaped fuselage model at different angle of attack is shown in Figure 6.5. The zero lift angle has been found at -3º angle of attack. Then the lift coefficient increases almost linearly with the increase of angle of attack up to approximately 14°. In other wards, the lift coefficient increases linearly with the increase of angle of attack up to 14°. After wards, the lift coefficient decreases with the further increase of angle of attack. As such, the stalling angle of conventional model is found at about 14˚. It is also observed that the maximum lift coefficient, C_{Lmax} for this type of model is approximately 0.68.

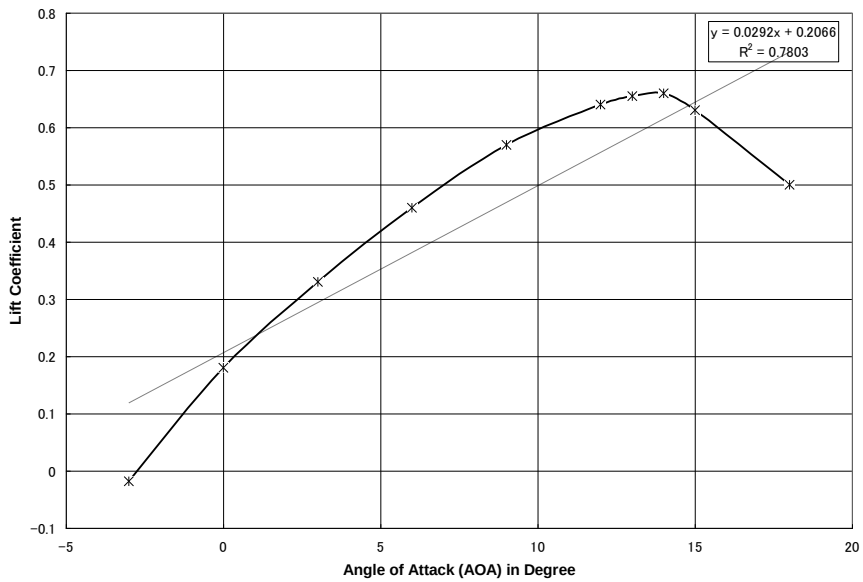

Figure 6.5: Variation of Lift Coefficient with Angle of Attack for Conventional Cylindrical Shaped Fuselage Model at 40 m/s.

The variation of drag coefficient with angle of attack at 40 m/s for conventional cylindrical shaped fuselage model at different angle of attack is shown in Figure 6.6. The shape of the drag coefficient vs angle of attack curve is found parabolic nature. As such, the drag coefficient increases with the increase of angle of attack. The value of drag coefficient for this conventional model at 14° angle of attack is found 0.08.

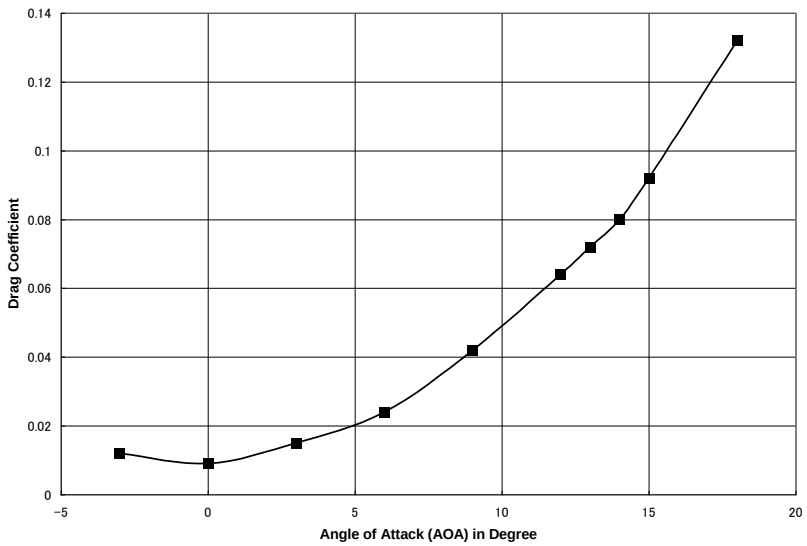

Figure 6.6: Variation of Drag Coefficient with Angle of Attack for Conventional Cylindrical Shaped Fuselage Model at 40 m/s.

6.5 Aerodynamic Characteristics of Aerofoil Shaped Fuselage at 40 m/s

The variation of lift coefficient with angle of attack at 40 m/s for aerofoil shaped fuselage model at different angle of attack is shown in Figure 6.7. The zero lift angle has been found at -3° angle of attack. Then the lift coefficient increases almost linearly with the increase of angle of attack up to approximately 14°. In other wards, the lift coefficient increases linearly with the increase of angle of attack up to 14°. After wards, the lift coefficient decreases with the further increase of angle of attack. As such, the stalling angle of aerofoil shaped fuselage UAV model is found at about 14˚. It is also observed that the maximum lift coefficient, C_{Lmax} for this type of model is approximately 0.81.

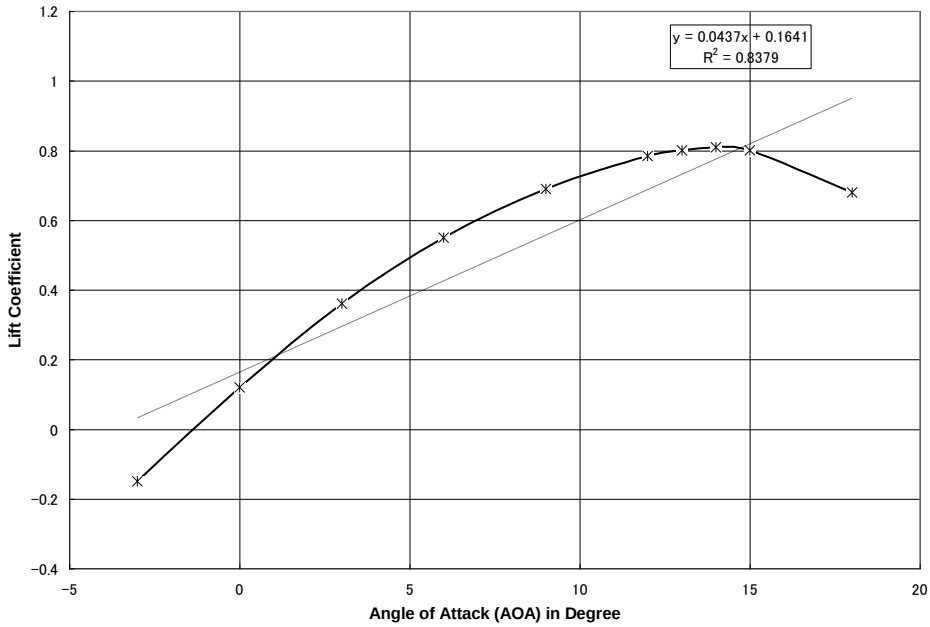

Figure 6.7: Variation of Lift Coefficient with Angle of Attack for Aerofoil Shaped Fuselage Model at 40 m/s.

The variation of drag coefficient with angle of attack at 40 m/s for aerofoil shaped fuselage model at different angle of attack is shown in Figure 6.8. The shape of the drag coefficient vs angle of attack curve is found parabolic nature. As such, the drag coefficient increases with the increase of angle of attack. The

value of drag coefficient for this aerofoil shaped fuselage UAV model at 14° angle of attack is found 0.086.

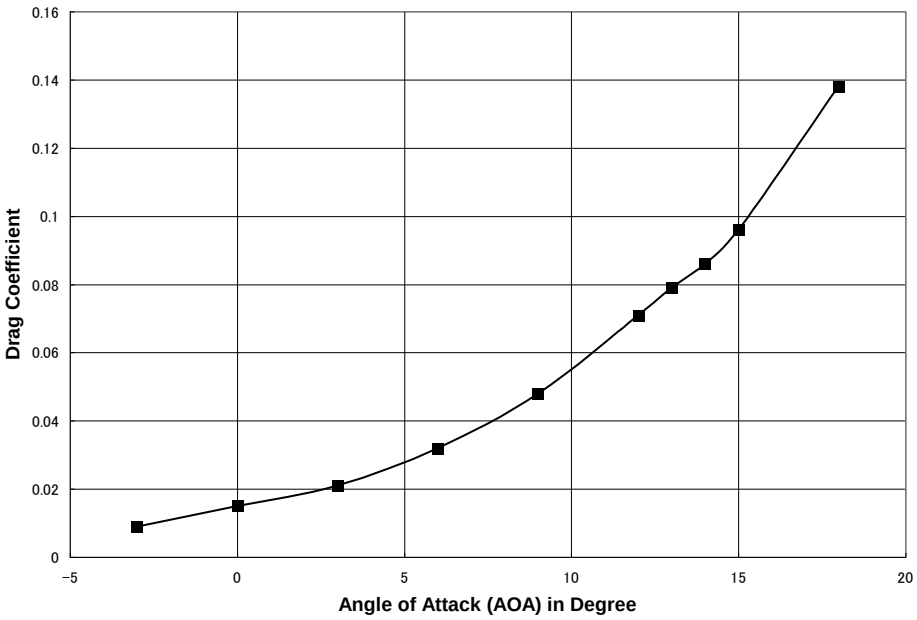

Figure 6.8: Variation of Drag Coefficient with Angle of Attack for Aerofoil Shaped Fuselage Model at 40 m/s.

6.6 Surface Pressure of Conventional Cylindrical Shaped Fuselage at 20 m/s

Four pressure tapping points have been made on the upper and lower surface of 3D Conventional Cylindrical Shaped Fuselage UAV model at 25%, 50%, 75% and 90% from the root of right wing. Another four tapping points have been made at the leading edge of same model at 25%, 50%, 75% and 90% from the root of right wing. Figure 6.9 and 6.10 show the tapping points made on both upper and lower surfaces of the right wing of Conventional Cylindrical Shaped Fuselage UAV model. The variation of Pressure with chord length for Conventional Cylindrical Shaped Fuselage UAV model at 3°, 9°, 14° (stall angle) and 18° angle of attack for 20 m/s is shown in **Appendix – 'G'** to Figure 6.11 (a, b, c and d), 6.12 (a, b, c and d), 6.13 (a, b, c and d) and 6.14 (a, b, c and d) respectively. The difference of pressure between the lower surface pressure (pressure side) and the upper surface pressure (suction side) determines the amount of lift and drag force produced by this type of aerofoil. The height of the upper surface suction peak increases with the

increase of angle of attack up to about 14°. Afterwards, separation starts due to sudden flattening of the upper surface pressure distribution (reduction of suction peak) with further increase of angle of attack. Furthermore increase of angle of attack will further reduce the lift.

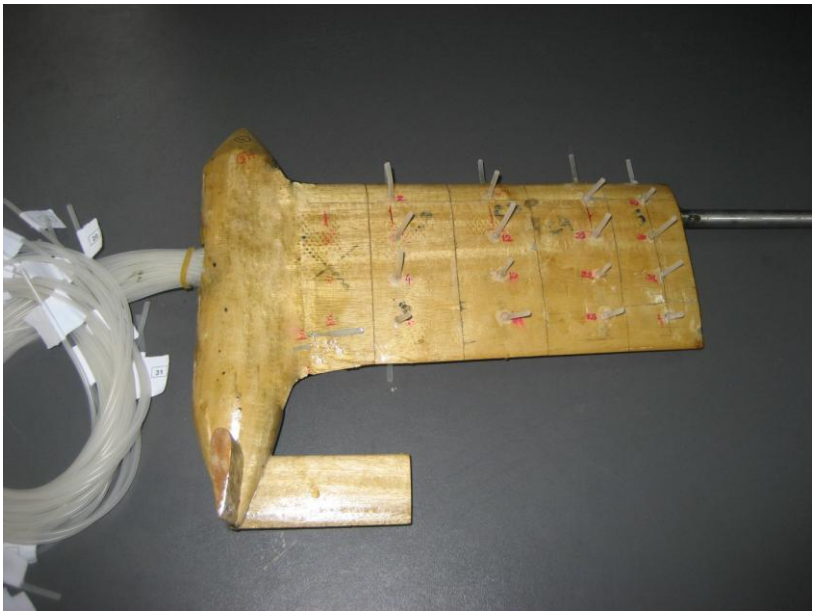

Figure 6.9: Photograph of Right Wing of Conventional Cylindrical Shaped Fuselage UAV Model showing the Location of Tapping Points

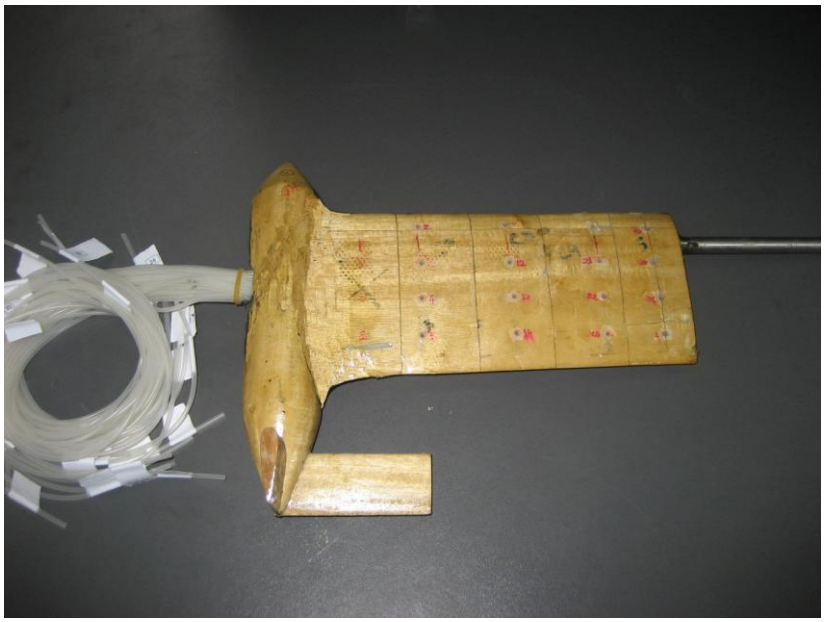

Figure 6.10: Final Photograph of Right Wing of Conventional Cylindrical Shaped Fuselage UAV Model having 36 Tapping Points

6.7 Surface Pressure of Aerofoil Shaped Fuselage at 20 m/s

Four pressure tapping points have been made on the upper and lower surface of 3D Aerofoil Shaped Fuselage UAV model at 25%, 50%, 75% and 90% from the root of right wing. Another four tapping points have been made at the leading edge of same model at 25%, 50%, 75% and 90% from the root of right wing. Figure 6.15 and 6.16 show the tapping points made on both upper and lower surfaces of the right wing of Aerofoil Shaped Fuselage UAV model. The variation of Pressure with chord length for Aerofoil Shaped Fuselage UAV model at 3°, 9°, 14° (stall angle) and 18° angle of attack for 20 m/s is shown in **Appendix – 'H'** to Figure 6.17 (a, b, c and d), 6.18 (a, b, c and d), 6.19 (a, b, c and d) and 6.20 (a, b, c and d) respectively. The difference of pressure between the lower surface pressure (pressure side) and the upper surface pressure (suction side) determines the amount of lift and drag force produced by this type of aerofoil. The height of the upper surface suction peak increases with the increase of angle of attack up to about 14°. Afterwards, separation starts due to sudden flattening of the upper surface pressure distribution (reduction of suction peak) with further increase of angle of attack. Furthermore increase of angle of attack will further reduce the lift.

Figure 6.15: Photograph of Right Wing of Aerofoil Shaped Fuselage UAV Model showing the Location of Tapping Points

Figure 6.16: Final Photograph of Right Wing of Aerofoil Shaped Fuselage UAV Model having 36 Tapping Points

6.8 Surface Pressure of Conventional Cylindrical Shaped Fuselage at 40 m/s

Four pressure tapping points have been made on the upper and lower surface of Conventional Cylindrical Shaped Fuselage UAV model at 25%, 50%, 75% and 90% from the root of right wing. Another four tapping points have been made at the leading edge of same model at 25%, 50%, 75% and 90% from the root of right wing. The variation of Pressure with chord length for Conventional Cylindrical Shaped Fuselage UAV model at 3°, 9°, 14° (stall angle) and 18° angle of attack for 40 m/s is shown in **Appendix – 'J'** to Figure 6.21 (a, b, c and d), 6.22 (a, b, c and d), 6.23 (a, b, c and d) and 6.24 (a, b, c and d) respectively. The difference of pressure between the lower surface pressure (pressure side) and the upper surface pressure (suction side) determines the amount of lift and drag force produced by this type of aerofoil. The height of the upper surface suction peak increases with the increase of angle of attack up to about 14°. Afterwards, separation starts due to sudden flattening of the upper surface pressure distribution (reduction of suction peak) with further increase of angle of attack. Furthermore increase of angle of attack will further reduce the lift.

6.9 Surface Pressure of Aerofoil Shaped Fuselage at 40 m/s

Four pressure tapping points have been made on the upper and lower surface of Aerofoil Shaped Fuselage UAV model at 25%, 50%, 75% and 90% from the root of left wing. Another four tapping points have been made at the leading edge of same model at 25%, 50%, 75% and 90% from the root of right wing. The variation of Pressure with chord length for Aerofoil Shaped Fuselage UAV model at 3°, 9°, 14° (stall angle) and 18° angle of attack for 40 m/s is shown in **Appendix – 'K'** to Figure 6.25 (a, b, c and d), 6.26 (a, b, c and d), 6.27 (a, b, c and d) and 6.28 (a, b, c and d) respectively. The difference of pressure between the lower surface pressure (pressure side) and the upper surface pressure (suction side) determines the amount of lift and drag force produced by this type of aerofoil. The height of the upper surface suction peak increases with the increase of angle of attack up to about 14°. Afterwards, separation starts due to sudden flattening of the upper surface pressure distribution (reduction of suction peak) with further increase of angle of attack. Furthermore increase of angle of attack will further reduce the lift.

VALIDATION AND ERROR ANALYSIS

7.1 Validation

The result of the present work has been compared with some journal papers and books related to aerodynamics. The research result has been validated with the standard results of journal papers and books. The comparison of both the result with similar scale is discussed below:

a. **Journal Paper-1 (Aerodynamics of a Circular Planform Aircraft).** Research has been carried out with a circular planform non-spinning body (Geobat model) with an airfoil section which offers advantages over a conventional wing aircraft type Cessna 172 model [Bryan, 2008]. The researcher has been used NACA 23012 aerofoil profile for designing Geobat model and Clark Y profile for Cessna 172 model. Figure 7.1 and 7.2 show the photograph of both the models. The comparison of lift curve, drag curve and drag polar are shown in Figure 7.3 to 7.5 respectively.

Figure 7.1: Photograph of the Geobat model

Figure 7.2: Photograph of the Cessna 172 model.

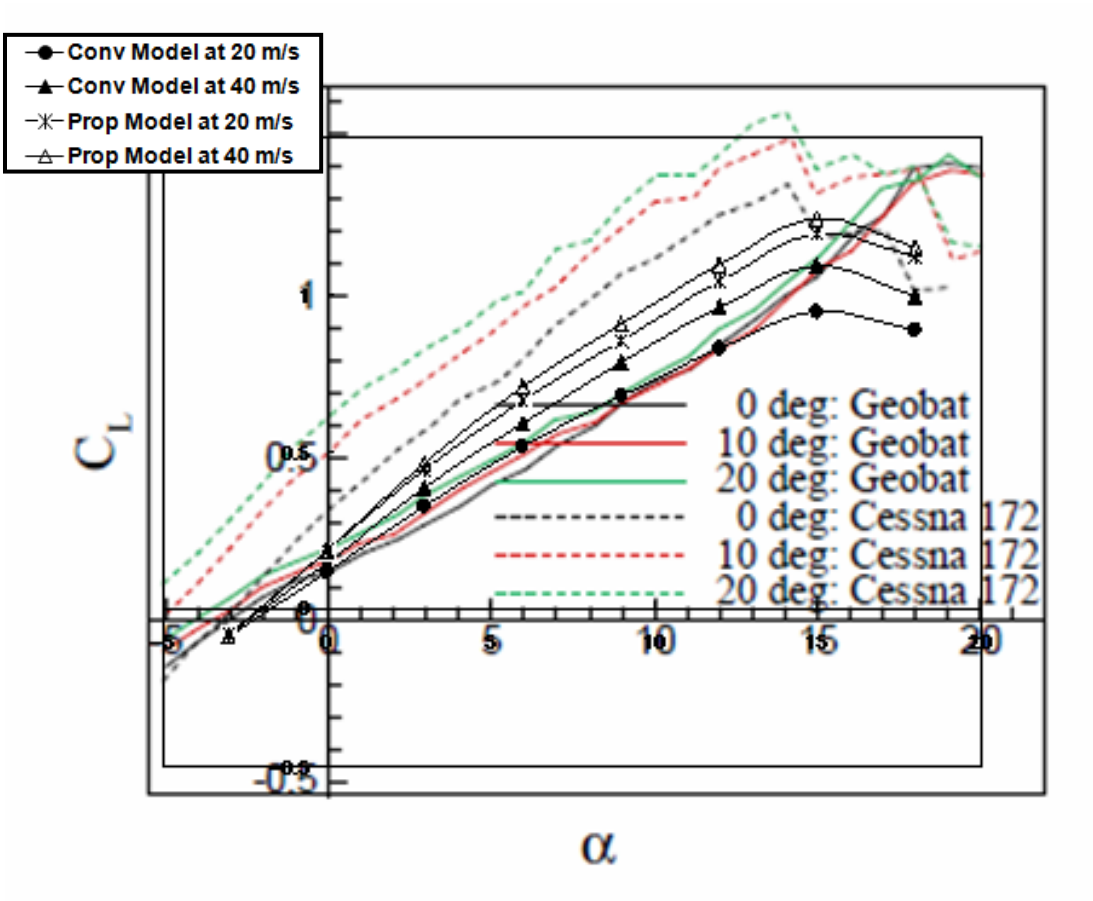

Figure 7.3: Comparison of Lift Curve.

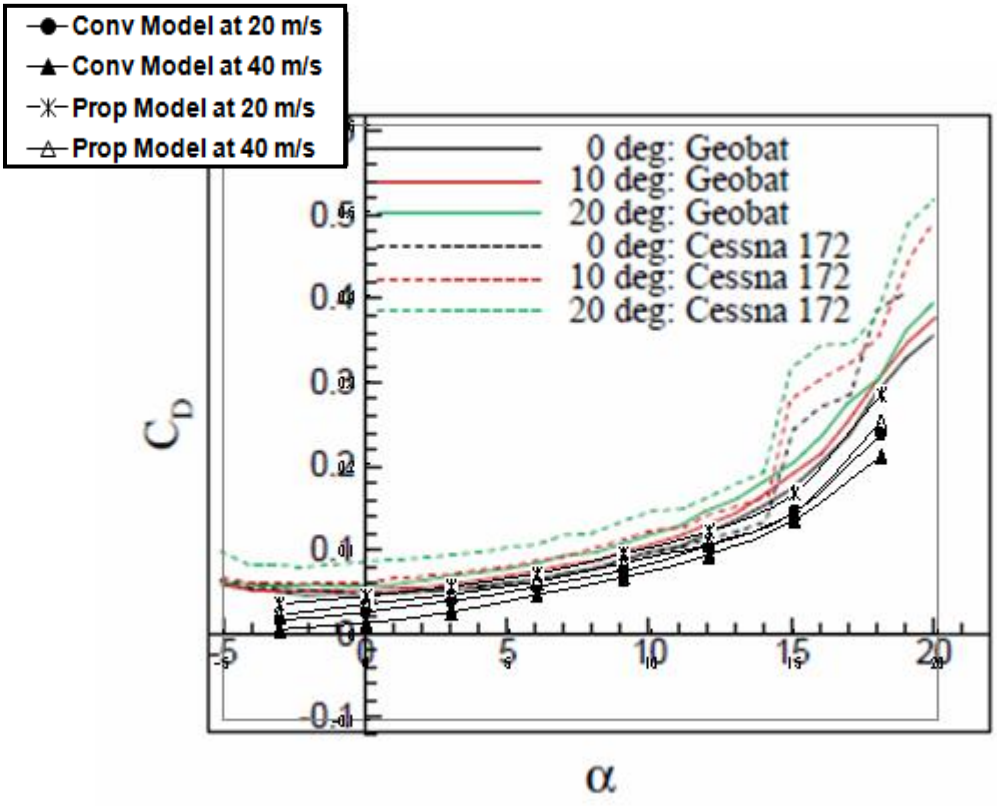

Figure 7.4: Comparison of Drag Curve.

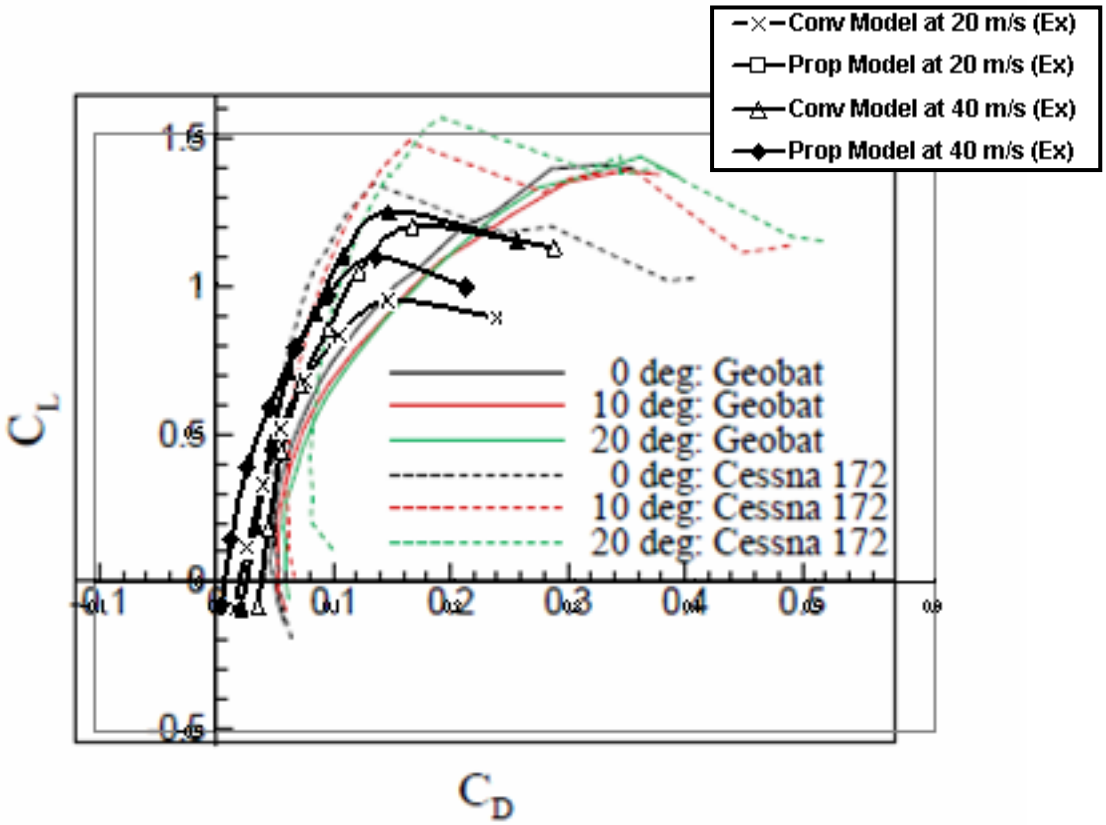

Figure 7.5: Comparison of Drag Polar

Analysis. From Figure 7.3 to 7.5, it is found that stall angle for the present research models (conventional and cylindrical shaped fuselage models), Cessna 172 and Geobat models are 15°, 14° and 18° respectively. C_{Lmax} for Cessna and Geobat model are almost same but C_{Lmax} for the presently research models is slightly lesser in amount. It is because Cessna 172 and Geobat models have use flap and elevator in deflected condition during taking reading. The maximum Lift to Drag (L/D_{max}) for the present research models, Cessna 172 and Geobat models are approximately 8.4, 11.0 and 7.5 respectively.

b. **Journal Paper-2 (Miniature Aerial Vehicle – Airframe Characteristics).** Research has been carried out with a 0.6m fixed wing aerial vehicle [Shivkumar et al., 2008]. The researcher has been used NACA 4412 aerofoil profile for designing the miniature aerial vehicle models. Figure 7.6 show the photograph of the miniature aerial vehicle models. The comparison of lift curve, and drag polar are shown in Figure 7.7.

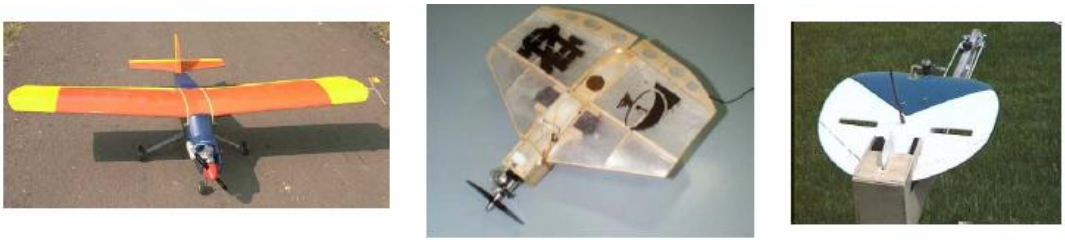

Figure 7.6: Photograph of the Miniature Aerial Vehicle Models

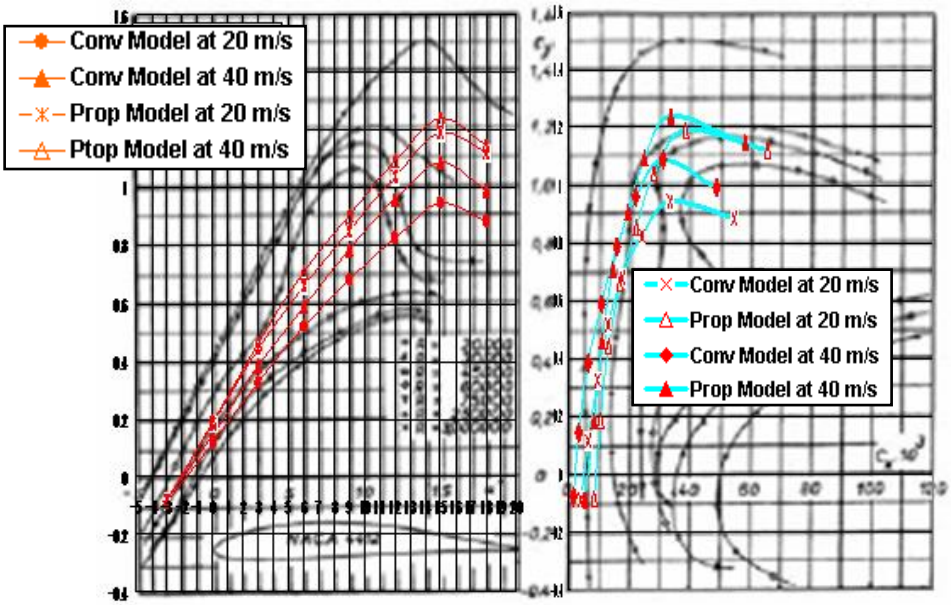

Figure 7.7: Comparison of Lift Curve and Drag Polar

Analysis. From Figure 7.6 and 7.7, it is found that the stall angle for the present research models (conventional and cylindrical shaped fuselage models) are 15° but miniature aerial vehicle models are 11 to 15°. C_{Lmax} for miniature aerial vehicle models and presently research models are found little different and slightly lesser in amount. It is because the size of the miniature aerial vehicle models is very small and their may be scale effect of the wing tunnel. More so, they have been tested from high to low speed ranges (10 to 15 m/s) and at different Reynolds' Number (60,000 – 150,000). The present research models have been carried out at 20 m/s and 40 m/s respectively and Reynolds' Number are 137,000 (for 20 m/s) and 274,000 (for 40 m/s) respectively.

c. **Book-1 (A catalog of Low Reynolds Number airfoil data for Wind Turbine applications).** Research has been carried out with small wind energy conversion systems (SWECS) for design and performance analysis. The researcher has been used NACA 4415 aerofoil profile for designing the SWECS [Miley, 1982]. Figure 7.8 show the comparison of lift curve.

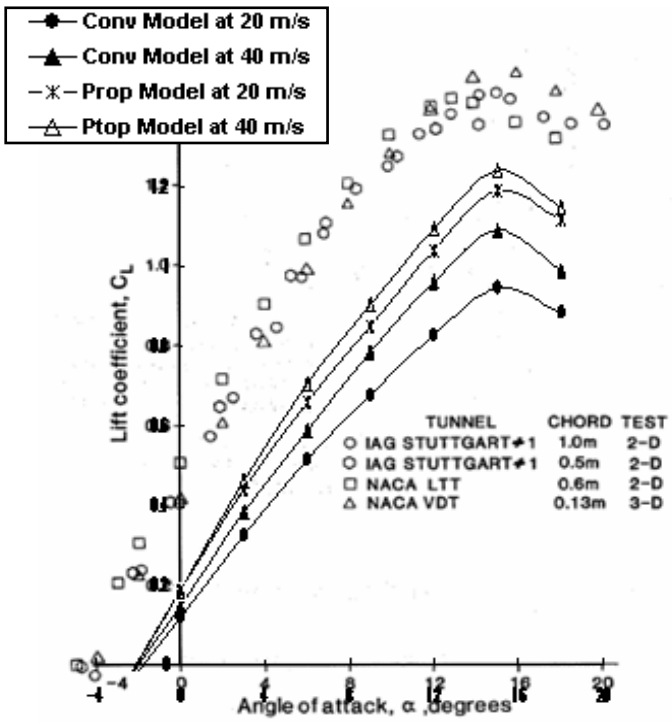

Figure 7.8: Comparison of Lift Curve

Analysis. From Figure 7.8, it is found that the stall angle for both the present research models (conventional and cylindrical shaped fuselage models) and for the small wind energy conversion systems (SWECS) is of 15°. But the C_{Lmax} for SWECS and presently research models are found little different and slightly lesser in amount. It is because the SWECS has been operated at 80 m/s and Reynolds' Number are 15,00,000 where as the present research models have been operated at 20 m/s and 40 m/s respectively and the Reynolds' Number are 137,000 (for 20 m/s) and 274,000 (for 40 m/s) respectively.

c. **Book-2 (Theory of Wing Sections).** Research has been carried out with different summary of airfoil data. However, only the data and graph of NACA 4415 aerofoil profile has been chosen [Abbott and Doenhoff, 1959]. Figure 7.9 show the comparison of lift curve.

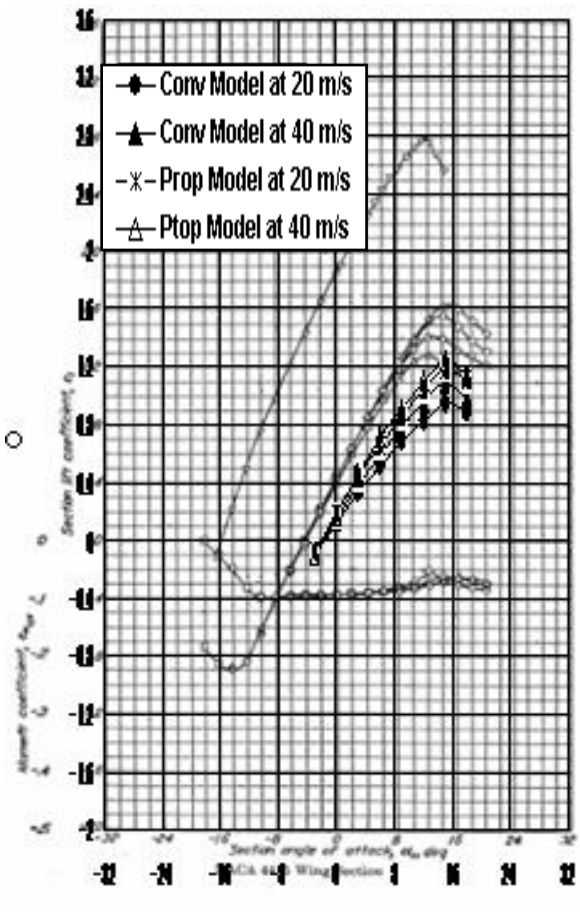

Figure 7.9: Comparison of Lift Curve

Analysis. From Figure 7.9, it is found that the stall angle for the present research models (conventional and cylindrical shaped fuselage models) and NACA 4415 profile is of 15°. C_{Lmax} for the presently research models is slightly lesser in amount. It is because the research on NACA 4415 profile has been carried out with split flap in deflected condition.

7.2 Error Analysis

Error is a scientific measurement means the inevitable uncertainty that attends all measurements. Error analysis is a tool used to study and evaluation of uncertainty in measurements. Measurements can be inaccurate for many reasons. The tool doing the measuring can be different than other tools of the same model, environmental factors could change the measurements and human error can affect the measurements. In order to recognize and allow for inaccuracies in measurements, error analysis is being used [Taylor, 1982].

By using the error analysis, the deviate of results from the accurate value could be ascertained. For doing the error analysis, subtract the computational value from the experimental value after measuring the item. Divide that number by the computational value to have the error analysis in decimal form. Multiply the error analysis in decimal form by 100 to get the percentage of error analysis. **Appendix 'L' to Table 3** shows the numerical and fabricated ordinate of NACA 4416 Profile used for the present research. The standard equation of Percent Error is shown below:

$$Percent\ Error = \frac{(Computational\ Value\ \sim\ Actual\ Value)}{Computational\ Value} \times 100$$

The calculation of percent error for stall angle, lift/drag (L/D) curve for both the cylindrical shaped and aerofoil shaped fuselages is shown below:

$$Percent\ Error = \left(\frac{15 - 14}{15}\right) \times 100$$

(for Stall Angle)

$$= 6.67\%$$

$$Percent\ Error = \left(\frac{8.50 - 8.28}{8.28}\right) \times 100$$

(for Cylindrical Shaped Fuselage)

$$= 2.66\%$$

$$Percent\ Error = \left(\frac{9.42 - 8.42}{8.42}\right) \times 100$$

(for Aerofoil Shaped Fuselage)

$$= 11.88\%$$

Analysis. The percent error for stall angle, lift-drag (L/D) curve for both cylindrical and aerofoil shaped fuselages are found within 2.66% to 11.88%. More so, validation with different journal papers as well as aerofoil related books have been also compared, consulted and the present research result is found acceptable. Further to mention that it is quite difficult to maintain the exact scale factor / ratio between the numerical and fabricated ordinate data of NACA 4416 profile. However, all possible steps have been taken to maintain the same scale factor / ratio during fabrication of the wing, fuselage, horizontal and vertical stabilizer of the both UAV model manually like the numerical data – even though there might be some chance of error, which might lead to increase the percentage error [Ordinate data, Appendix 'L' to Table 3]. Use of Computerized Numerical Control (CNC) lathe or milling machine for fabrication of UAV models might reduce the percentage error.

RESULTS AND DISCUSSION OF COMPUTATIONAL DESIGN

8.1 Lift Drag Curve of 2D NACA 4416 Aerofoil Profile at 20 m/s

The lift drag curve of 2D NACA 4416 Aerofoil Profile at 20 m/s is shown in Figure 8.1. For 2D NACA 4416 Aerofoil Profile, induced drag is not happened, only profile drag is considered to be happened. At low and moderate lift coefficients, there is no appreciable flow separation and the drag is caused due to mainly by skin friction. As the lift coefficient increases, drag coefficient also increases exponentially due to form and skin friction drag. A sharp increase of drag coefficient occurs at the stall angle i.e. 15° angle of attack due to flow separation after reaching the maximum lift coefficient value. The lift drag ratio at the stall angle for this profile is found 10.35.

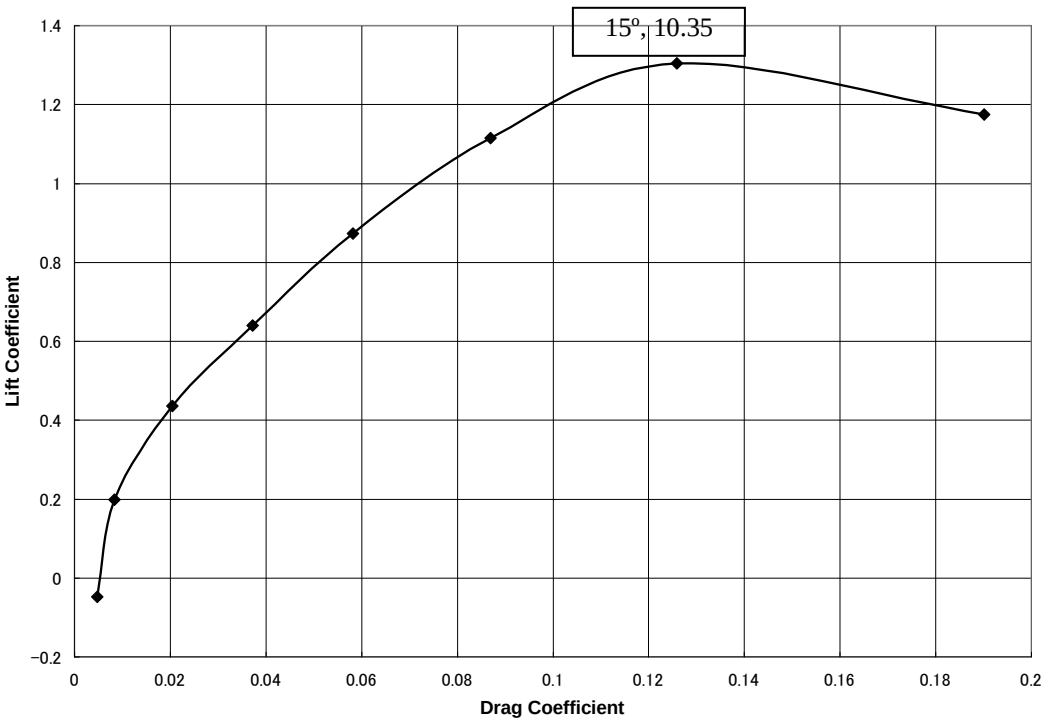

Figure 8.1: Lift Drag Curve of 2D NACA 4416 Aerofoil Profile at 20 m/s

8.2 Lift Drag Curve of Conventional Cylindrical Shaped Fuselage UAV Model at 20 m/s

The lift drag curve of conventional cylindrical shaped fuselage UAV model at 20 m/s is shown in Figure 8.2. The wing tip experienced mostly induced drag due to wing tip vortices. A significant amount of drag is also produced due to shape and skin friction effects of the cylindrical shaped fuselage model which are termed as profile drag. So, both induced and profile drags have been experienced by this type of model. From Figure 8.2, it is found that at low and moderate lift coefficients, there is no appreciable flow separation. As the lift coefficient increases, drag coefficient also increases up to stall angle of attack i.e. 15º angle of attack. Afterwards, a sharp increase of drag coefficient with reduction of lift coefficient occurs for this type of model at the stall angle due to flow separation. The lift drag ratio at the stall angle for this model is found 6.57.

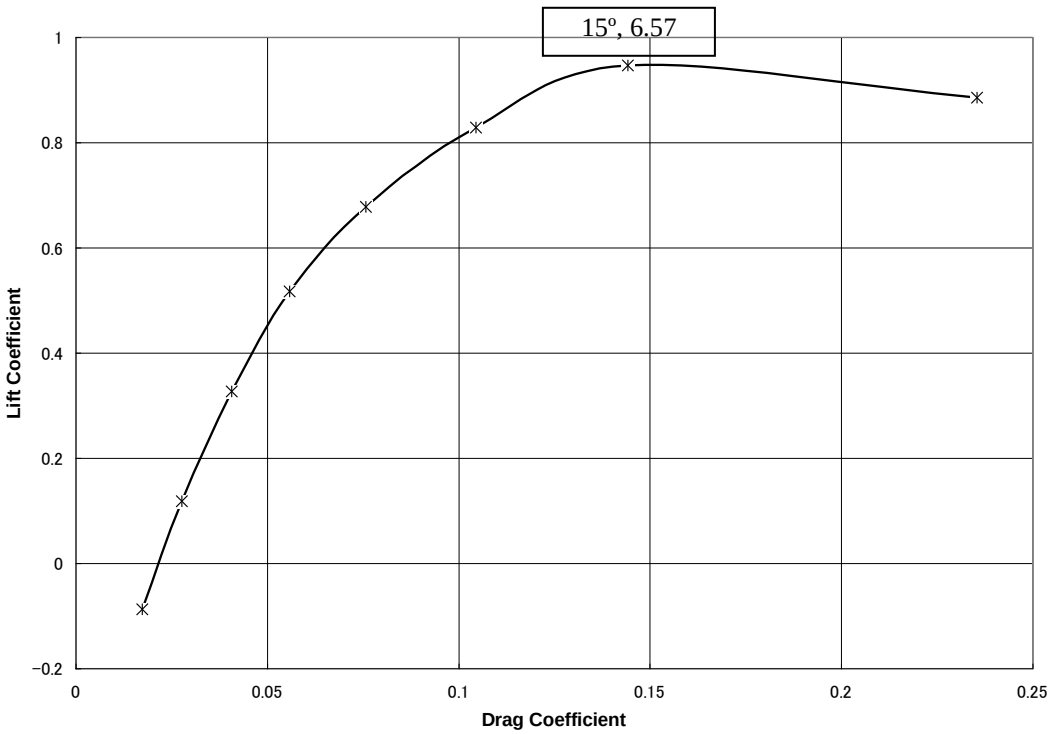

Figure 8.2: Lift Drag Curve of Conventional Cylindrical Shaped Fuselage UAV model at 20 m/s.

8.3 Lift Drag Curve of Aerofoil Shaped Fuselage UAV Model at 20 m/s

The lift drag curve of aerofoil shaped fuselage UAV model at 20 m/s is shown in Figure 8.3. The wing and fuselage tip experienced mostly induced drag due to tip vortices. A significant amount of drag is also produced due to shape and skin friction effects of the aerofoil shaped fuselage model which are termed as profile drag. So, both induced and profile drags have been experienced by this type of model. Profile drag of both cylindrical and aerofoil shaped models is same as both the models has the same volume. The lift to drag coefficient is found less for aerofoil shaped fuselage UAV model due to increase of induced drag for trailing edge vortices of this model. But said model also increases a significant amount of extra lift from it's fuselage due to aerofoil shape. From Figure 8.3, it is found that at low and moderate lift coefficients, there is no appreciable flow separation. As the lift coefficient increases, drag coefficient also increases up to stall angle of attack i.e. 15º angle of attack. Afterwards, a sharp increase of drag coefficient with reduction of lift coefficient occurs for this type of model at the stall angle due to flow separation. The lift drag ratio at the stall angle for this model is found 7.23.

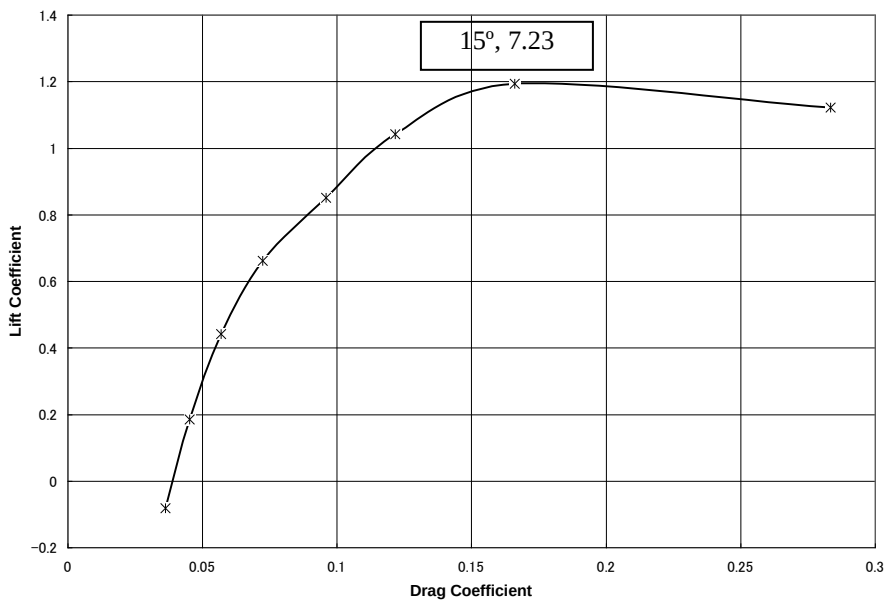

Figure 8.3: Lift Drag Curve of Aerofoil Shaped Fuselage UAV model at 20 m/s.

8.4 Lift Drag Curve of 2D NACA 4416 Aerofoil Profile at 40 m/s

The lift drag curve of 2D NACA 4416 Aerofoil Profile at 40 m/s is shown in Figure 8.4. For 2D NACA 4416 Aerofoil Profile, induced drag is not happened, only profile drag is considered to be happened. At low and moderate lift coefficients, there is no appreciable flow separation and the drag is caused due to mainly by skin friction. As the lift coefficient increases, drag coefficient also increases exponentially due to form and skin friction drag. A sharp increase of drag coefficient occurs at the stall angle due to flow separation after reaching the maximum lift coefficient value. The lift drag ratio at the stall angle for this profile is found 12.90.

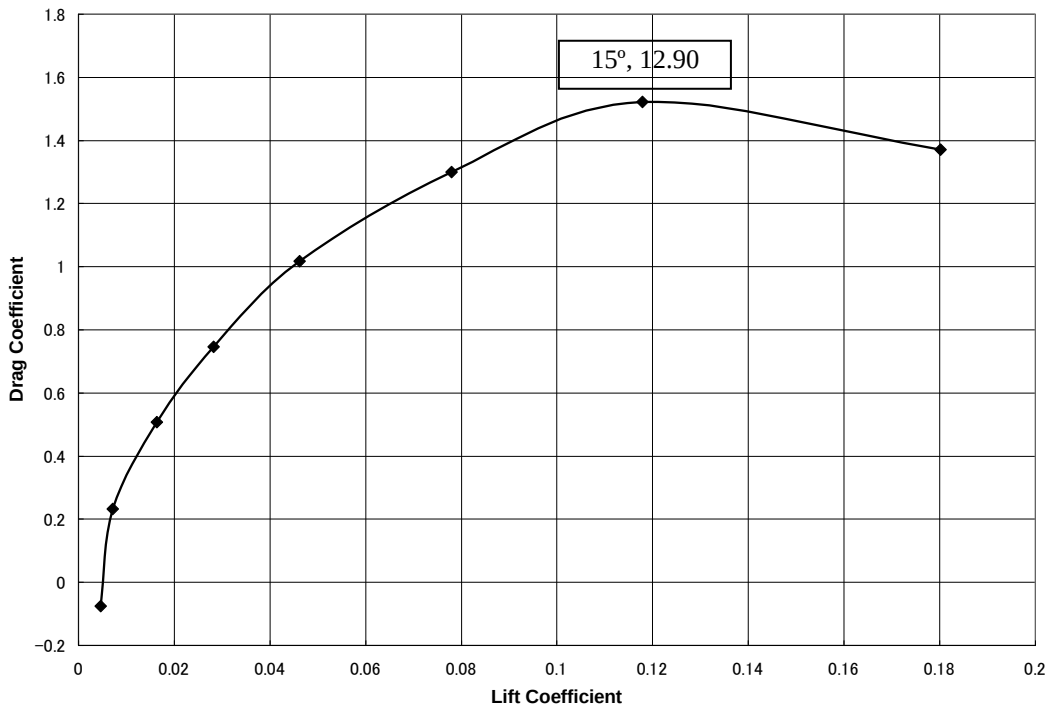

Figure 8.4: Lift Drag Curve of 2D NACA 4416 Aerofoil Profile at 40 m/s

8.5 Lift Drag Curve of Conventional Cylindrical Shaped Fuselage UAV Model at 40 m/s

The lift drag curve of conventional cylindrical shaped fuselage UAV model at 40 m/s is shown in Figure 8.5. The wing tip experienced mostly induced drag due to wing tip vortices. A significant amount of drag is also produced due to shape and skin friction effects of the cylindrical shaped fuselage model which are termed as profile drag. So, both induced and profile drags have been experienced by this type of model. From Figure 8.5, it is found that at low and moderate lift coefficients, there is no appreciable flow separation. As the lift coefficient increases, drag coefficient also increases up to stall angle of attack i.e. 15° angle of attack. Afterwards, a sharp increase of drag coefficient with reduction of lift coefficient occurs for this type of model at the stall angle due to flow separation. The lift drag ratio at the stall angle for this model is found 8.28.

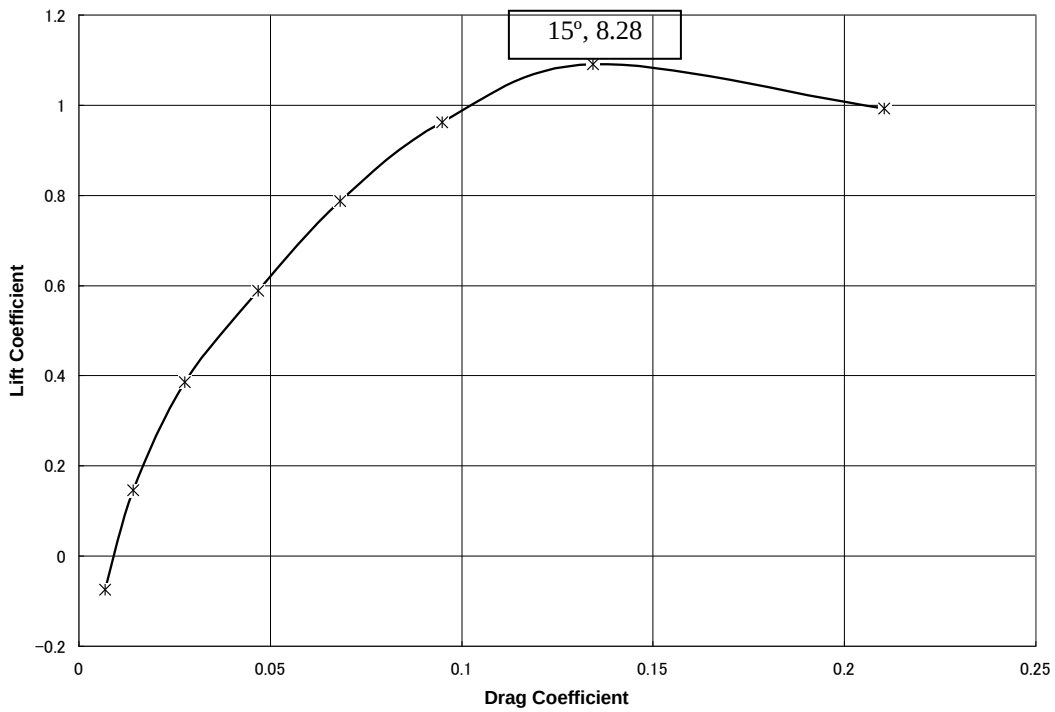

Figure 8.5: Lift Drag Curve of Conventional Cylindrical Shaped Fuselage UAV model at 40 m/s.

8.6 Lift Drag Curve of Aerofoil Shaped Fuselage UAV Model at 40 m/s

The lift drag curve of aerofoil shaped fuselage UAV model at 40 m/s is shown in Figure 8.6. The wing and fuselage tip experienced mostly induced drag due to tip and trailing edge vortices. A significant amount of drag is also produced due to shape and skin friction effects of the aerofoil shaped fuselage model which are termed as profile drag. So, both induced and profile drags have been experienced by this type of model. Profile drag of both cylindrical and aerofoil shaped UAV models is same as both the models has the same volume. The lift to drag coefficient is found less for aerofoil shaped fuselage model due to increase of induced drag from tip and trailing edge vortices. But said model also increases a significant amount of extra lift from it's fuselage due to aerofoil shape. From Figure 8.6, it is found that at low and moderate lift coefficients, there is no appreciable flow separation. As the lift coefficient increases, drag coefficient also increases up to stall angle of attack i.e. 15º angle of attack. Afterwards, a sharp increase of drag coefficient with reduction of lift coefficient occurs for this type of model at the stall angle due to flow separation. The lift drag ratio at the stall angle for this model is found 8.42. Table-1 shows the lift to drag ratio of all the configurations at the stalling angle and two different velocities.

Figure 8.6: Lift Drag Curve of Aerofoil Shaped Fuselage UAV model at 40 m/s.

Table-1: Lift to Drag Ratio of Six Configurations at Stalling Angle and two Different Velocities.

Configurations	Stall Angle	C_{Lmax}	C_{Dmax}	L/D Ratio
NACA 4416 Aerofoil Profile at 20 m/s	15.0°	1.304	0.126	10.35
Aerofoil Shaped Fuselage Model at 20 m/s	15.0°	1.20	0.166	7.23
Conventional Model at 20 m/s	15.0°	0.946	0.144	6.57
NACA 4416 Aerofoil Profile at 40 m/s	15.0°	1.521	0.118	12.90
Aerofoil Shaped Fuselage Model at 40 m/s	15.0°	1.221	0.145	8.42
Conventional Model at 40 m/s	15.0°	1.109	0.134	8.28

8.7 Comparison of Lift and Drag Coefficient with 2D NACA 4416 Aerofoil Profile.

The variation of lift and drag coefficient with angle of attack between 2D NACA 4416 profile with conventional cylindrical and aerofoil shaped fuselage UAV models is shown in Figure - 8.7 to 8.10. It is seen that “2D NACA 4416 Aerofoil Profile at 40 m/s” provides more lift and drag coefficients than other two UAV models. Among the six configurations, “2D NACA 4416 Aerofoil Profile at 40 m/s” provides maximum lift than other five types of configuration at about 15° angle of attack. Next lift providing configuration is “Aerofoil shaped fuselage configuration at 40 m/s”; next is “Aerofoil shaped fuselage configuration at

20 m/s" and next to next is "Conventional cylindrical shaped fuselage at velocity 40 m/s". "Conventional cylindrical shaped fuselage at velocity 20 m/s" provides minimum lift coefficient than other five configurations. During drag analysis, it is seen that among the six different types of configurations, "Aerofoil shaped fuselage configuration at 20 m/s" provides maximum drag than other five configurations. Next drag producing configuration is "Aerofoil shaped fuselage configuration at 40 m/s", next is "Conventional cylindrical shaped fuselage at velocity 20 m/s" and next to next is "Conventional cylindrical shaped fuselage at velocity 40 m/s". "Conventional cylindrical shaped fuselage at velocity 40 m/s" provides minimum drag coefficient than other five configurations.

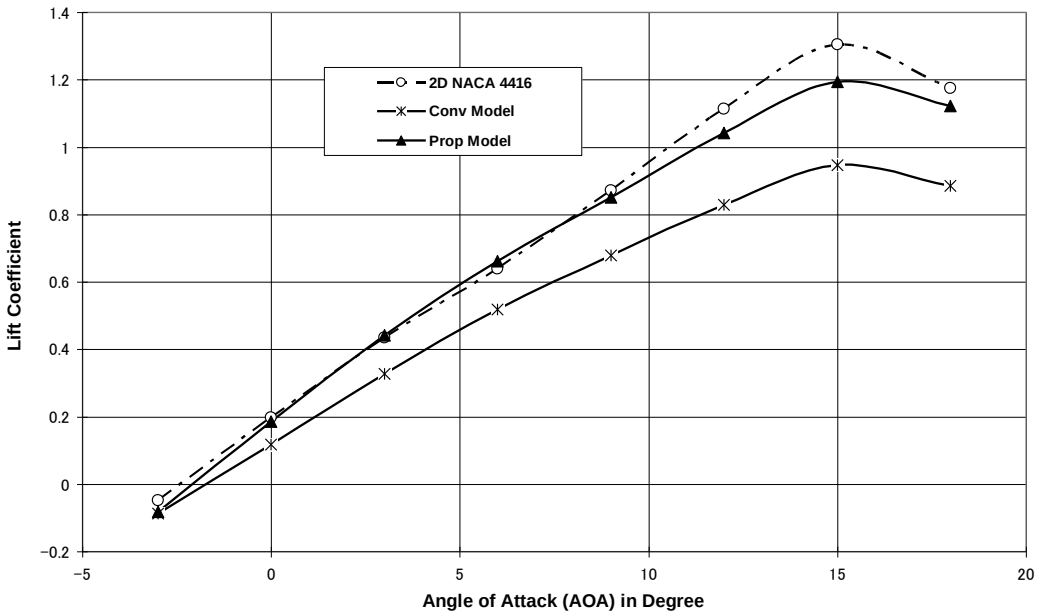

Figure 8.7: Comparison of Lift Coefficient VS AOA of Different Models of UAV with 2D NACA 4416 Aerofoil Profile at 20 m/s.

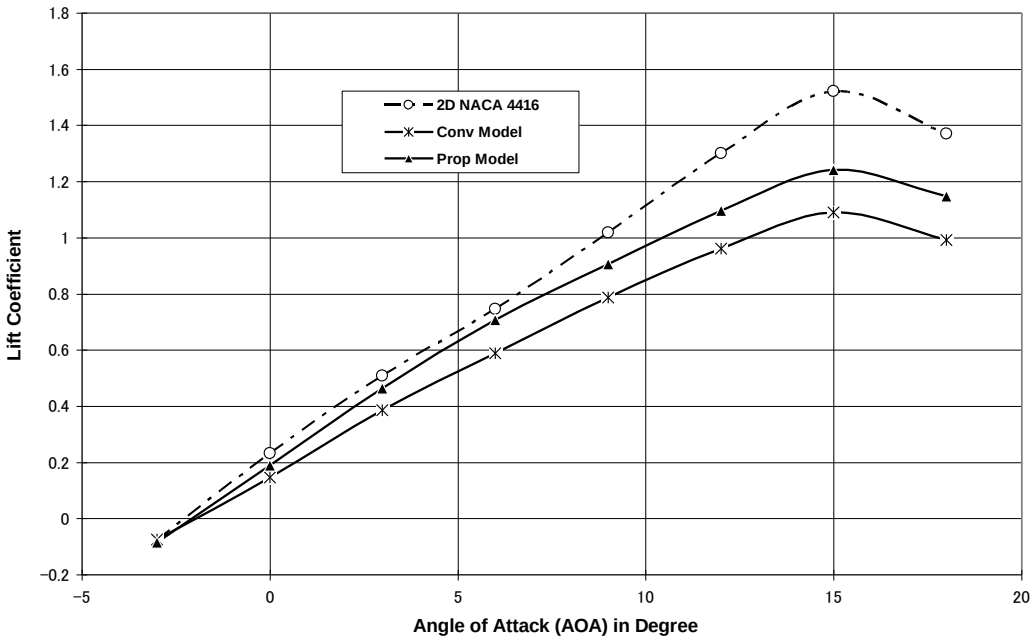

Figure 8.8: Comparison of Lift Coefficient VS AOA of Different Models of UAV with 2D NACA 4416 Aerofoil Profile at 40 m/s.

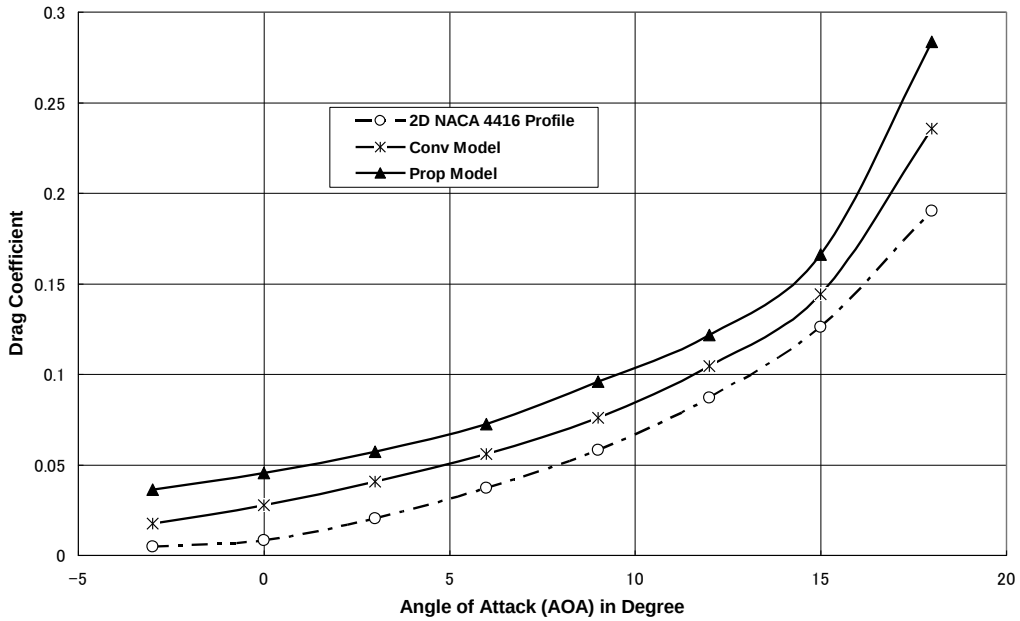

Figure 8.9: Comparison of Drag Coefficient VS AOA of Different Models of UAV with 2D NACA 4416 Aerofoil Profile at 20 m/s.

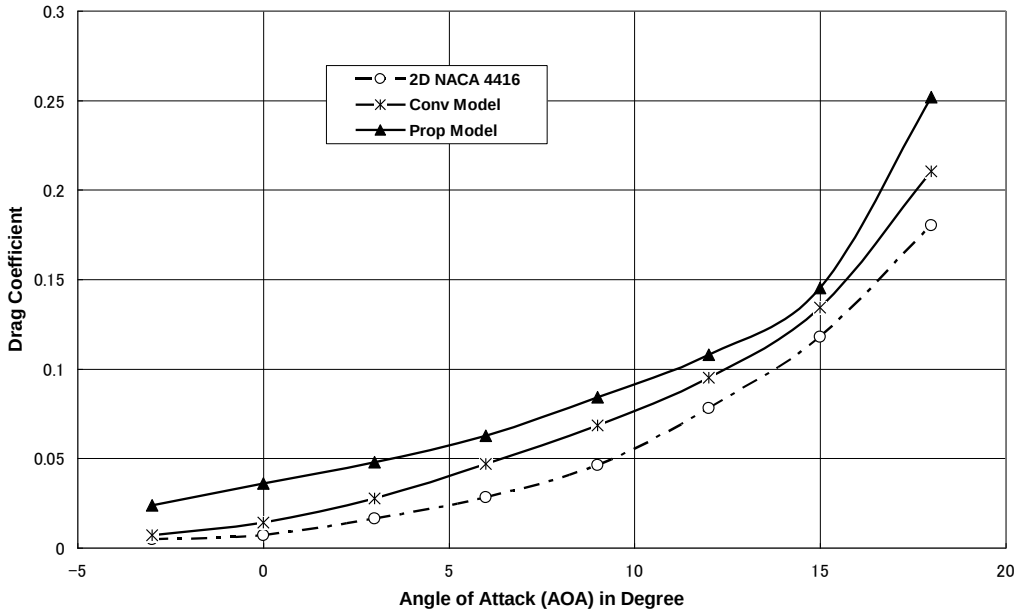

Figure 8.10: Comparison of Drag Coefficient VS AOA of Different Models of UAV with 2D NACA 4416 Aerofoil Profile at 40 m/s.

8.8 Comparison of Lift and Drag Coefficient VS AOA of Different Profiles

The comparison of lift coefficient VS angle of attack (AOA) of two different configurations of conventional cylindrical and aerofoil shaped fuselage UAV models at two different velocities is shown in Figure 8.11. The zero lift angle has been found approximately at -3º angle of attack. Then the lift coefficient increases almost linearly with the increase of angle of attack up to 15º. Among the two configurations, the aerofoil shaped fuselage has produced more lift coefficient than that of the conventional cylindrical shaped fuselage. The aerofoil shaped fuselage UAV model produced a significant amount of extra lift from it's fuselage due to it's aerofoil shape. Among the four studies, maximum lift coefficient is produced by the aerofoil shaped fuselage UAV model at velocity 40 m/s. Next increment of

lift coefficient is provided by the aerofoil shaped fuselage UAV model at 20 m/s and next to next is provided by the conventional cylindrical shaped fuselage UAV model at 40 m/s. The conventional cylindrical shaped fuselage at 20 m/s provides minimum lift coefficient among the four types of studies.

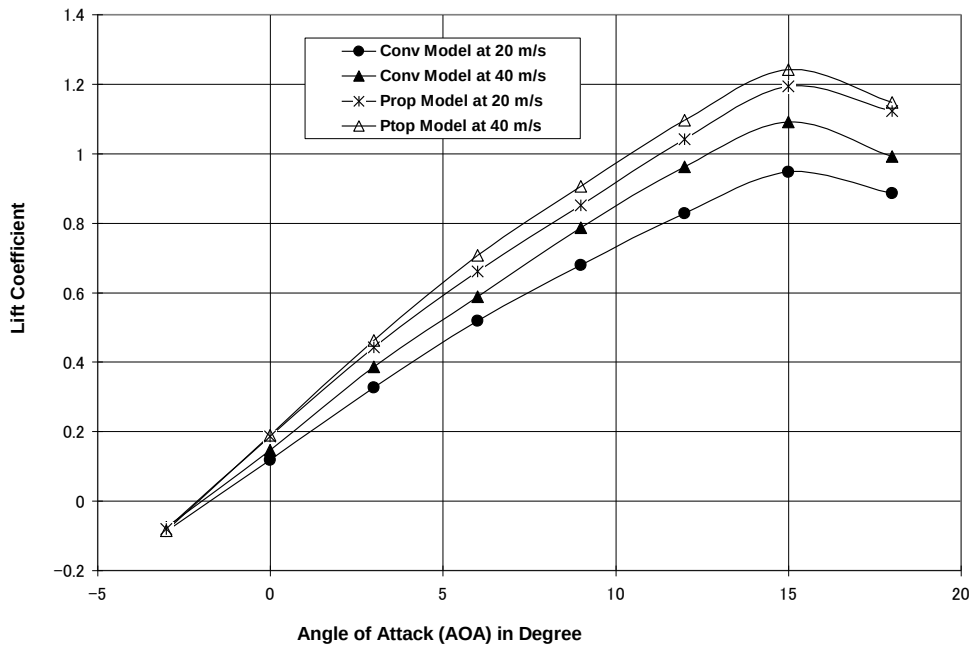

Figure 8.11: Variation of Lift Coefficient VS AOA of Two Different Models of UAV at Different Velocities

The comparison of drag coefficient VS angle of attack (AOA) of two different configurations of conventional cylindrical and aerofoil shaped fuselage at two different velocities is shown in Figure - 8.12. The shape of the drag coefficient VS angle of attack curve is found parabolic nature. As such, the drag coefficient increases with the increase of angle of attack. Among the two models, the aerofoil shaped fuselage has produced more drag coefficient than that of the conventional cylindrical shaped fuselage. Drag coefficient for aerofoil shaped fuselage is found more due to increase of induced drag from tip and trailing edge vortices. A significant amount of the total drag is also produced due to shape and skin friction effects of both the models which are termed as profile drag. Profile drag of both the models is same as both the models has the same volume. Among the four studies, maximum drag coefficient is produced by the

aerofoil shaped fuselage UAV model at velocity 20 m/s. It is because flow separation starts earlier for aerofoil shaped fuselage model at 20 m/s. Out of four studies, next drag coefficient is found more for the aerofoil shaped fuselage model at 40 m/s and next to next is found for conventional cylindrical shaped fuselage at 20 m/s. Conventional cylindrical shaped fuselage at 40 m/s provides minimum drag coefficient among the four types of studies.

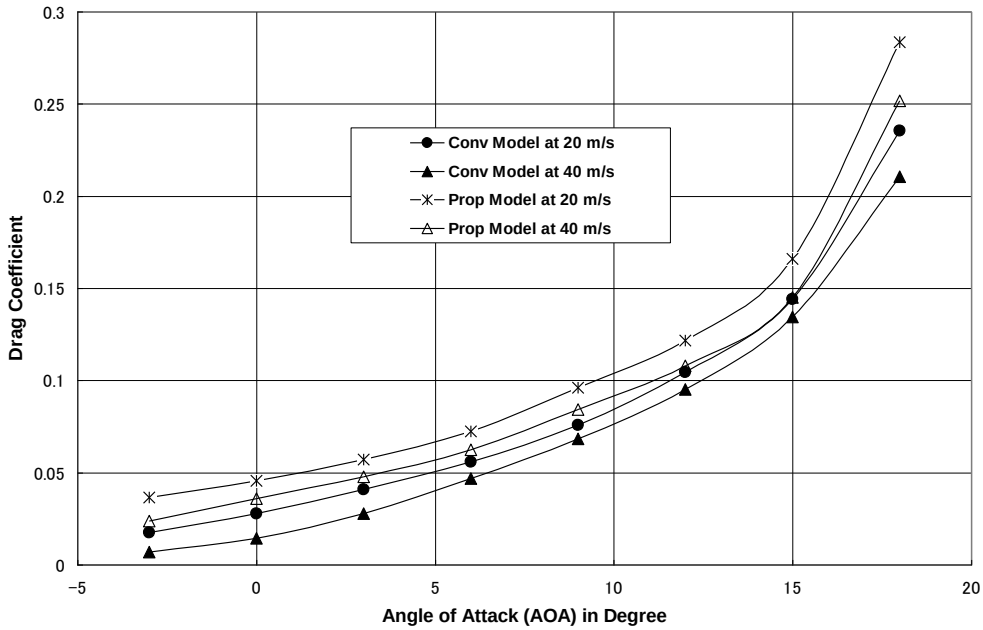

Figure 8.12: Variation of Drag Coefficient VS AOA of Two Different Models of UAV at Different Velocities

8.9 Increment of Lift and Drag Coefficient by Aerofoil Shaped Fuselage UAV Model at 20 m/s than Conventional Cylindrical Shaped Fuselage UAV Model

Percentage increase of lift and drag coefficient of aerofoil shaped (AS) fuselage model at 20 m/s than that of conventional cylindrical shaped (CS) fuselage model at different angle of attack are shown in Figure 8.13 and 8.14 respectively. The aerofoil shaped fuselage configuration provides more lift as well as drag coefficient than that

of the conventional cylindrical shaped fuselage configuration. The formula for percentage increment of lift / drag coefficient of aerofoil shaped fuselage configuration is as follows:

$$\text{\% Increase of Lift/Drag Force at Specific Angle of Attack} = \left[\frac{\text{(Lift/Drag Force Produced by AS Fuselage - Lift/Drag Force Produced by CS Fuselage)}}{\text{Lift/Drag Force Produced by AS Fuselage}} \right] \times 100$$

From Figure 8.13, it is observed that out of two different studies, the percentage increment of lift coefficient is more for “aerofoil shaped fuselage configuration at 20 m/s” than that of the “conventional cylindrical shaped fuselage” at velocity 20 m/s and 40 m/s respectively. Again from Figure 8.14, it is also observed that the percentage increment of drag coefficient is found more for “aerofoil shaped fuselage configuration at 20 m/s” than that of the “conventional cylindrical shaped fuselage” at velocity 20 m/s and 40 m/s respectively. It is also seen from Figure 8.13 that “aerofoil shaped fuselage configuration at 20 m/s” provides approximately 20.73% and 8.62% more lift force coefficient at 15° angle of attack (stall angle) than that of the conventional cylindrical shaped fuselage configuration at velocity 20 m/s and 40 m/s respectively. It is also found from Figure 8.14 that the “aerofoil shaped fuselage configuration at 20 m/s” provides approximately 13.12% and 19.11% more drag coefficient at 15° angle of attack (stall angle) than that of the conventional cylindrical shaped fuselage configuration at velocity 20 m/s and 40 m/s respectively.

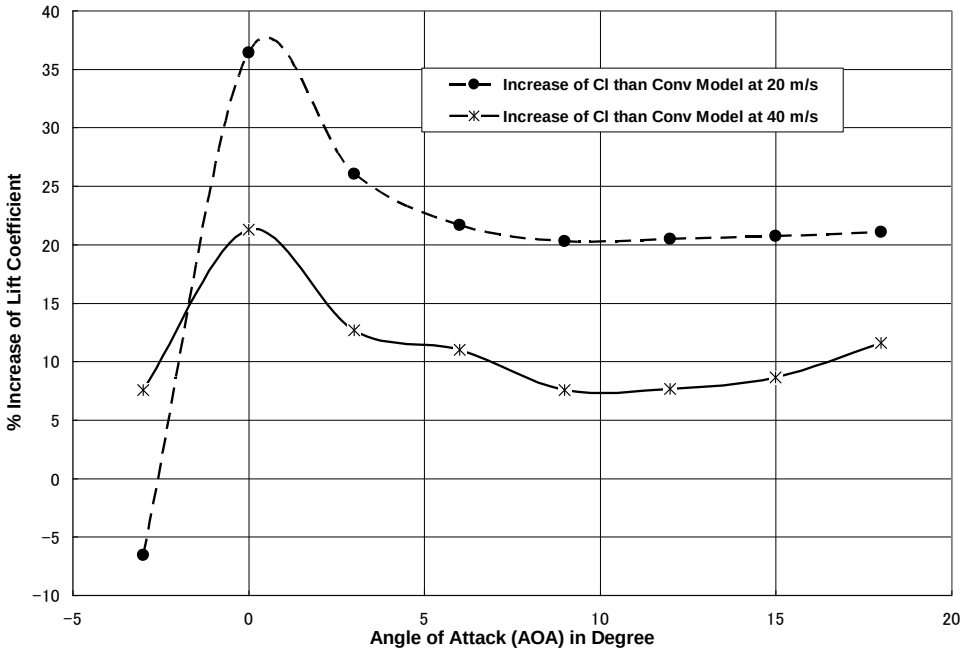

Figure 8.13: Percentage Increase of Lift Coefficient of "Aerofoil shaped fuselage configuration at 20 m/s" than that of "Conventional cylindrical shaped fuselage configuration at 20 m/s and 40 m/s" and different AOA.

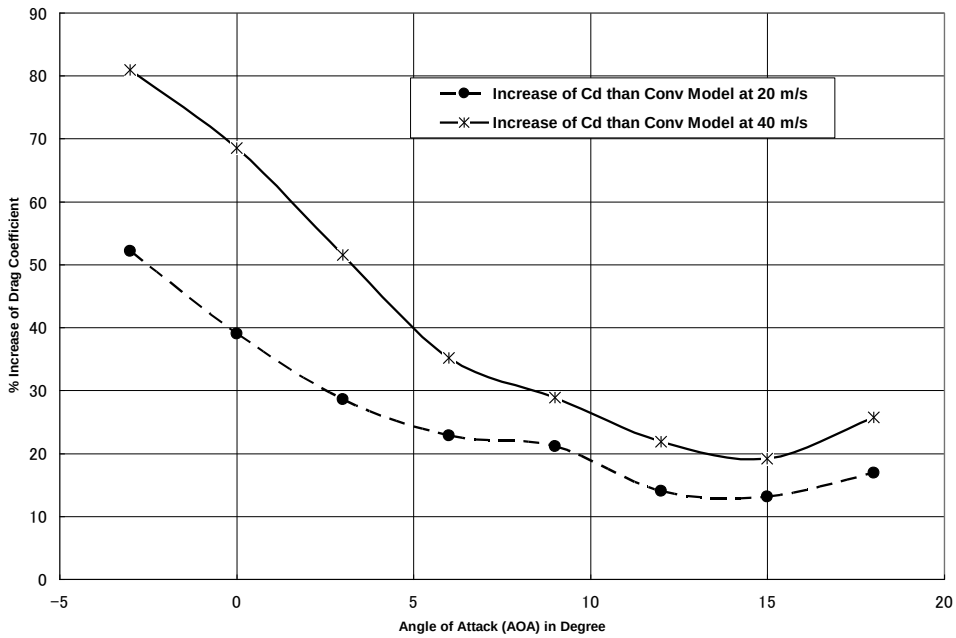

Figure 8.14: Percentage Increase of Drag Coefficient of "Aerofoil shaped fuselage configuration at 20 m/s" than that of "Conventional cylindrical shaped fuselage configuration at 20 m/s and 40 m/s" and different AOA.

8.10 Increment of Lift and Drag Coefficient by Aerofoil Shaped Fuselage UAV Model at 40 m/s than Conventional Cylindrical Shaped Fuselage UAV Model

Percentage increase of lift and drag coefficient of aerofoil shaped fuselage model at 40 m/s than that of conventional cylindrical shaped fuselage model at different angle of attack are shown in Figure 8.15 and 8.16 respectively. The aerofoil shaped fuselage configuration provides more lift as well as drag coefficient than that of the conventional cylindrical shaped fuselage configuration.

From Figure 8.15, it is observed that out of two different studies, the percentage increment of lift coefficient is found more for "aerofoil shaped fuselage configuration at 40 m/s" than that of "conventional cylindrical shaped fuselage" at velocity 20 m/s and 40 m/s respectively. Again from Figure 8.16, it is also observed that the percentage increment of drag coefficient is more for "aerofoil shaped fuselage configuration at 40 m/s" than that of "conventional cylindrical shaped fuselage" at velocity 20 m/s and 40 m/s respectively. It is seen from Figure 8.15 that the "aerofoil shaped fuselage configuration at 40 m/s" provides approximately 23.79% and 12.15% more lift coefficient at 15° angle of attack (stall angle) than that of the conventional cylindrical shaped fuselage configuration at velocity 20 m/s and 40 m/s respectively. It is also found from Figure 8.16 that the "proposed aerofoil shaped fuselage configuration at 40 m/s" provides approximately 0.58% and 7.42% more drag coefficient at 15° angle of attack (stall angle) than that of the conventional cylindrical shaped fuselage configuration at velocity 20 m/s and 40 m/s respectively.

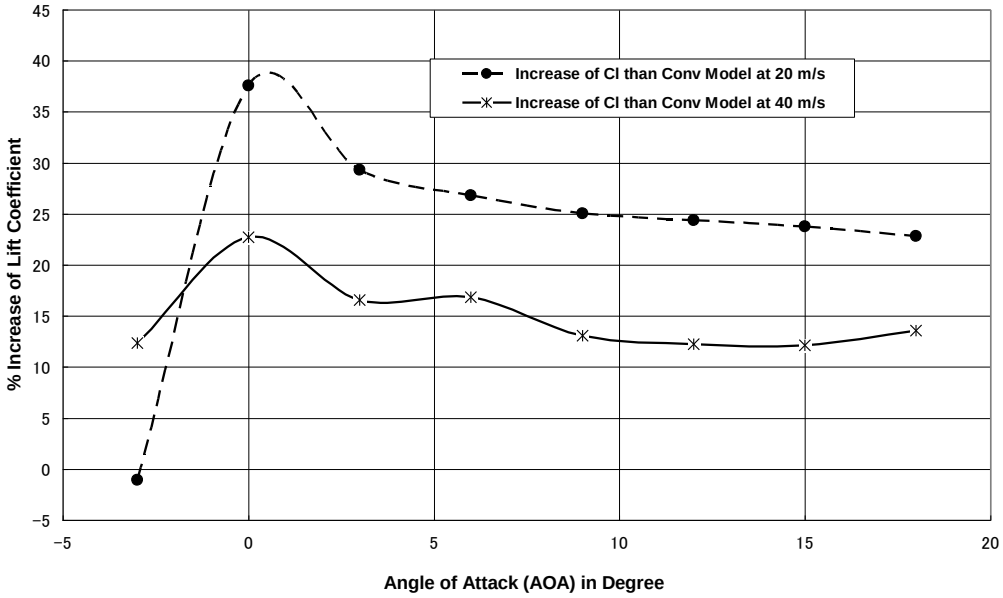

Figure 8.15: Percentage Increase of Lift Coefficient of "Aerofoil shaped fuselage configuration at 40 m/s" than that of "Conventional cylindrical shaped fuselage configuration at 20 m/s and 40 m/s" and different AOA.

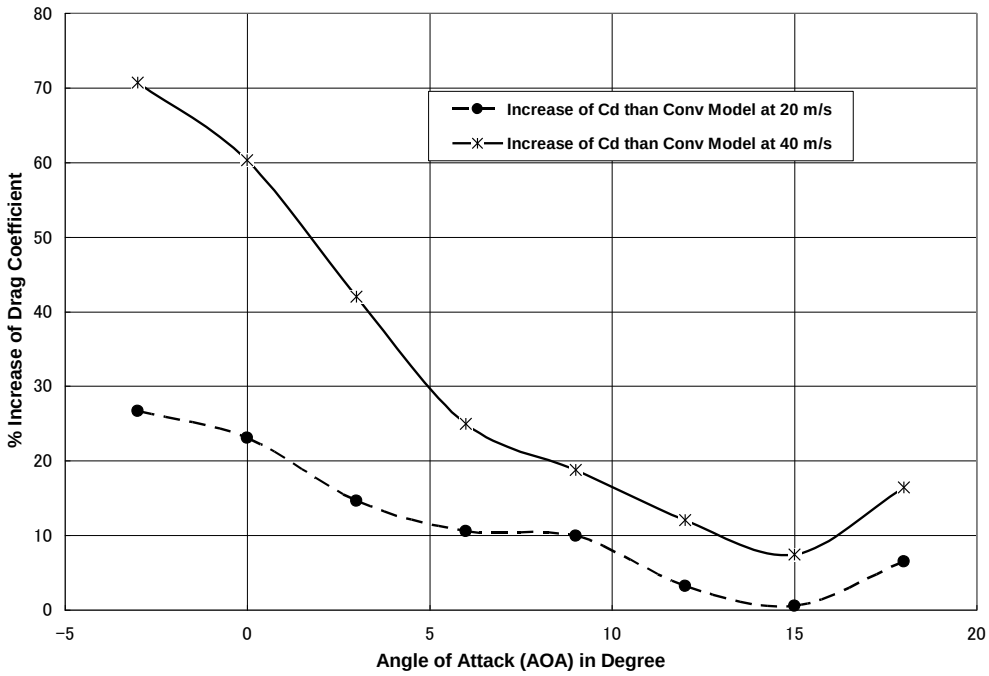

Figure 8.16: Percentage Increase of Drag Coefficient of "Aerofoil shaped fuselage configuration at 40 m/s" than that of "Conventional cylindrical shaped fuselage configuration at 20 m/s and 40 m/s" and different AOA.

8.11 Comparison of Pressure at Different Percentage from the Root of Conventional Cylindrical Shaped Fuselage UAV Model at 20 m/s

Surface Pressure of Conventional Cylindrical Shaped Fuselage UAV model at 25%, 50%, 75% and 90% from the root has been analyzed from -3° to 18° angle of attack at 20 m/s. The variation of Pressure with chord length of said model at 25%, 50%, 75% and 90% from the root at different angle of attack is shown in **Appendix – 'M'** to Figure 8.17 to 8.20. The difference in pressure produced by the lower surface and upper surface of the wings determines the amount of lift and drag force produced by this model. The suction pressure mainly determines the amount of lift force to be produced by this model. It is seen that the difference of pressure between the lower surface (pressure side) and the upper surface (suction side) of the wings is more at 25%, followed by 50% and next is 75% in all the cases. Pressure difference is found least at 90% from the root. Flow separation mostly starts after 90% from the root. The height of the upper surface suction peak of the wings is found maximum at 15 $^\circ$ angle of attack i.e. at the stall angle. Afterwards, separation starts due to sudden flattening of the upper surface pressure distribution (reduction of suction peak) with further increase of angle of attack. Furthermore increase of angle of attack will further reduce the lift.

8.12 Comparison of Pressure at Different Percentage from the Root of Aerofoil Shaped Fuselage UAV Model at 20 m/s

Surface Pressure of Aerofoil Shaped Fuselage UAV model at 25%, 50%, 75% and 90% from the root has been analyzed from -3° to 18° angle of attack at 20 m/s. The variation of Pressure with chord length of said model at 25%, 50%, 75% and 90% from the root at different angle of attack is shown in **Appendix – 'N'** to Figure- 8.21 to 8.24. The difference in pressure produced by the lower surface and upper surface of the wings and fuselages determines the amount of lift and drag force produced by this model. The suction pressure mainly determines the amount

of lift force to be produced by this model. It is seen that the difference in pressure between the lower surface (pressure side) and the upper surface (suction side) of the wings and fuselages is more at 25%, followed by 50% and next is 75% in all the cases. Pressure difference is found least at 90% from the root. Flow separation mostly starts after 90% from the root. The height of the upper surface suction peak of the wings is found maximum at 15° angle of attack i.e. at the stall angle. Afterwards, separation starts due to sudden flattening of the upper surface pressure distribution (reduction of suction peak) with further increase of angle of attack. Furthermore increase of angle of attack will further reduce the lift.

8.13 Comparison of Pressure at Different Percentage from the Root of Conventional Cylindrical Shaped Fuselage UAV Model at 40 m/s

Surface Pressure of Conventional Cylindrical Shaped Fuselage UAV model at 25%, 50%, 75% and 90% from the root has been analyzed from -3° to 18° angle of attack at 40 m/s. The variation of Pressure with chord length of said model at 25%, 50%, 75% and 90% from the root at different angle of attack is shown in **Appendix – 'P'** to Figure 8.25 to 8.28. The difference in pressure produced by the lower surface and upper surface of the wings determines the amount of lift and drag force produced by this model. The suction pressure mainly determines the amount of lift force to be produced by this model. It is seen that the difference of pressure between the lower surface (pressure side) and the upper surface (suction side) of the wings is more at 25%, followed by 50% and next is 75% in all the cases. Pressure difference is found least at 90% from the root. Flow separation mostly starts after 90% from the root. The height of the upper surface suction peak of the wings is found maximum at 15 $^{\circ}$ angle of attack i.e. at the stall angle. Afterwards, separation starts due to sudden flattening of the upper surface pressure distribution (reduction of suction peak) with further increase of angle of attack. Furthermore increase of angle of attack will further reduce the lift.

8.14 Comparison of Pressure at Different Percentage from the Root of Aerofoil Shaped Fuselage UAV Model at 40 m/s

Surface Pressure of Aerofoil Shaped Fuselage UAV model at 25%, 50%, 75% and 90% from the root has been analyzed from -3° to 18° angle of attack at 40 m/s. The variation of Pressure with chord length of said model at 25%, 50%, 75% and 90% from the root at different angle of attack is shown in **Appendix – 'Q'** to Figure 8.29 to 8.32. The difference in pressure produced by the lower surface and upper surface of the wings and fuselages determines the amount of lift and drag force produced by this model. The suction pressure mainly determines the amount of lift force to be produced by this model. It is seen that the difference of pressure between the lower surface (pressure side) and the upper surface (suction side) of the wings and fuselages is more at 25%, followed by 50% and next is 75% in all the cases. Pressure difference is found least at 90% from the root. Flow separation mostly starts after 90% from the root. The height of the upper surface suction peak of the wings is found maximum at 15°angle of attack i.e. at the stall angle. Afterwards, separation starts due to sudden flattening of the upper surface pressure distribution (reduction of suction peak) with further increase of angle of attack. Furthermore increase of angle of attack will further reduce the lift.

8.15 Effective Area of Force/Pressure Distribution on Wings and Fuselages

Table 4 shows the effective area of force/pressure distribution on wings and fuselages for Aerofoil Shaped and Conventional Cylindrical Shaped Fuselages. The total area throughout the NACA 4416 aerofoil for both cylindrical and aerofoil shaped fuselage UAV model concerned with force/pressure distribution has been divided into 20 equal segments. Average pressure force in each segment has been measured and compared with one another. Most effective area of pressure distribution for NACA 4416 airfoil is found between leading edge to 75% of chord

length. More so, percentage of force/pressure distribution is found more for aerofoil shaped fuselage in each segment.

Table-4: Effective Area of Force/Pressure Distribution on Wings and Fuselages for Aerofoil Shaped and Conventional Cylindrical Shaped Fuselages

% of Chord Length (X/C)	Pressure Distribution for Cylindrical Shaped Fuselage (%)	Pressure Distribution for Aerofoil Shaped Fuselage (%)
5	83.91	84.52
10	94.62	96.50
15	71.43	76.92
20	58.93	62.23
25	46.55	47.62
30	34.97	39.29
35	23.12	32.74
40	21.68	28.57
45	18.18	23.81
50	13.29	20.83
55	9.79	17.86
60	7.69	14.88
65	4.60	13.09
70	4.19	10.71
75	3.49	8.33
80	2.79	6.55
85	0.98	5.95
90	0.90	4.167
95	0.80	2.38

RESULTS AND DISCUSSION OF EXPERIMENTAL DESIGN

9.1 Lift Drag Curve of Conventional Cylindrical Shaped Fuselage UAV Model at 20 m/s

The lift drag curve of conventional cylindrical shaped fuselage UAV model at 20 m/s is shown in Figure 9.1. The wing tip experienced mostly induced drag due to wing tip and trailing edge vortices. A significant amount of drag is also produced due to shape and skin friction effects of the cylindrical shaped fuselage model which are termed as profile drag. So, both induced and profile drags have been experienced by this type of model. From Figure 9.1, it is found that at low and moderate lift coefficients, there is no appreciable flow separation. As the lift coefficient increases, drag coefficient also increases up to stall angle of attack i.e. 14º angle of attack. Afterwards, a sharp increase of drag coefficient with reduction of lift coefficient occurs for this type of model at the stall angle due to flow separation. The lift drag ratio at the stall angle for this model is found 8.40.

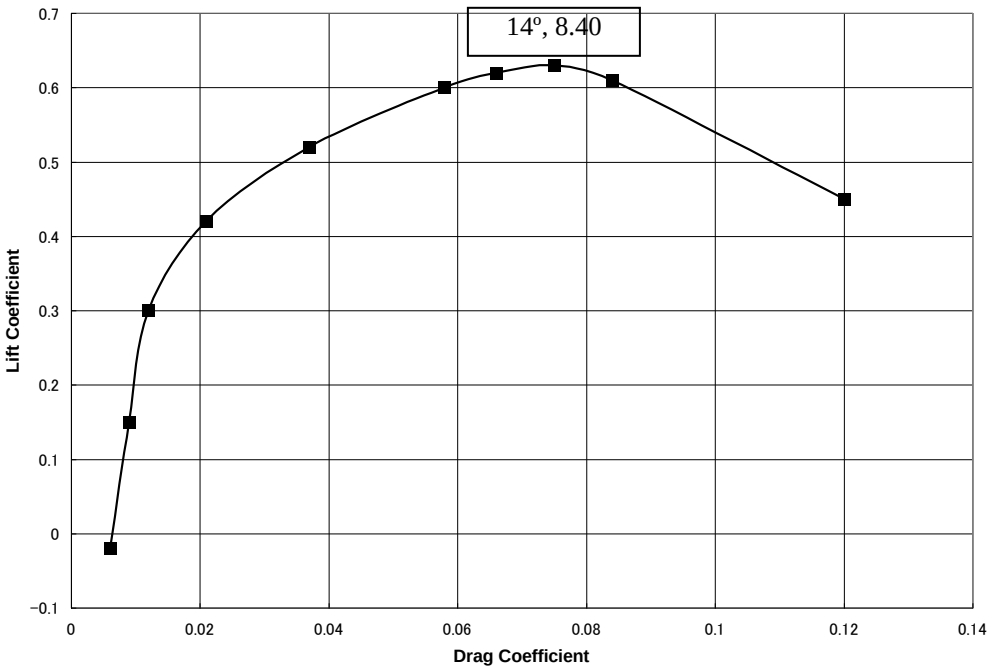

Figure 9.1: Lift Drag Curve of Conventional Cylindrical Shaped Fuselage UAV model at 20 m/s.

9.2 Lift Drag Curve of Aerofoil Shaped Fuselage UAV Model at 20 m/s

The lift drag curve of aerofoil shaped fuselage UAV model at 20 m/s is shown in Figure 9.2. The wing and fuselage tip experienced mostly induced drag due to tip and trailing edge vortices. A significant amount of drag is also produced due to shape and skin friction effects of the aerofoil shaped fuselage model which are termed as profile drag. So, both induced and profile drags have been experienced by this type of model. Profile drag of both cylindrical and aerofoil shaped models is same as both the models has the same volume. The lift to drag coefficient is found less for aerofoil shaped model due to increase of induced drag from the aerofoil shaped fuselage. But said model also increases a significant amount of extra lift from it's fuselage due to aerofoil shape. From Figure 9.2, it is found that at low and moderate lift coefficients, there is no appreciable flow separation. As the lift coefficient increases, drag coefficient also increases up to stall angle of attack i.e. 14º angle of attack. Afterwards, a sharp increase of drag coefficient with reduction of lift coefficient occurs for this type of model at the stall angle due to flow separation. The lift drag ratio at the stall angle for this model is found 8.76.

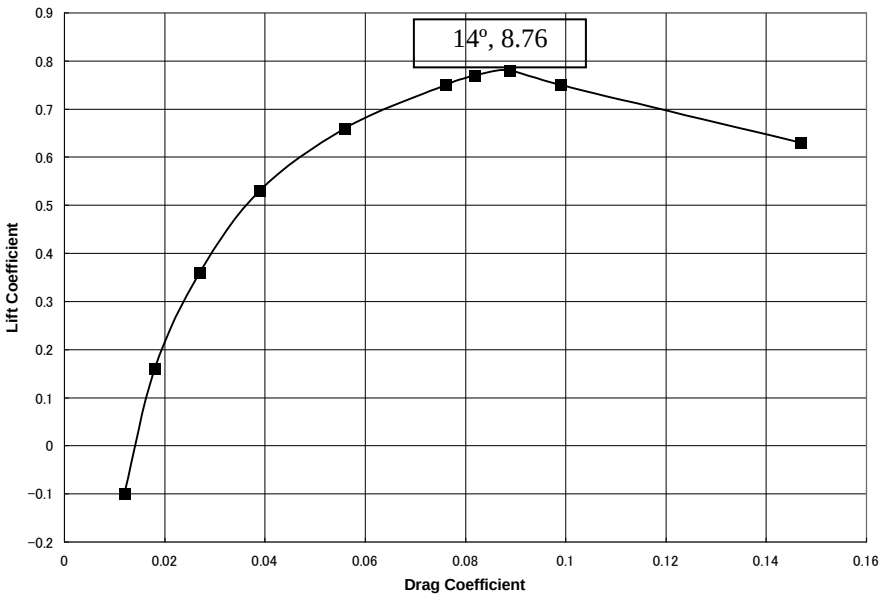

Figure 9.2: Lift Drag Curve of Aerofoil Shaped Fuselage UAV model at 20 m/s.

9.3 Lift Drag Curve of Conventional Cylindrical Shaped Fuselage UAV Model at 40 m/s

The lift drag curve of conventional cylindrical shaped fuselage UAV model at 40 m/s is shown in Figure 9.3. The wing tip experienced mostly induced drag due to wing tip vortices. A significant amount of drag is also produced due to shape and skin friction effects of the cylindrical shaped fuselage model which are termed as profile drag. So, both induced and profile drags have been experienced by this type of model. From Figure 9.3, it is found that at low and moderate lift coefficients, there is no appreciable flow separation. As the lift coefficient increases, drag coefficient also increases up to stall angle of attack i.e. 14º angle of attack. Afterwards, a sharp increase of drag coefficient with reduction of lift coefficient occurs for this type of model at the stall angle due to flow separation. The lift drag ratio at the stall angle for this model is found 8.50.

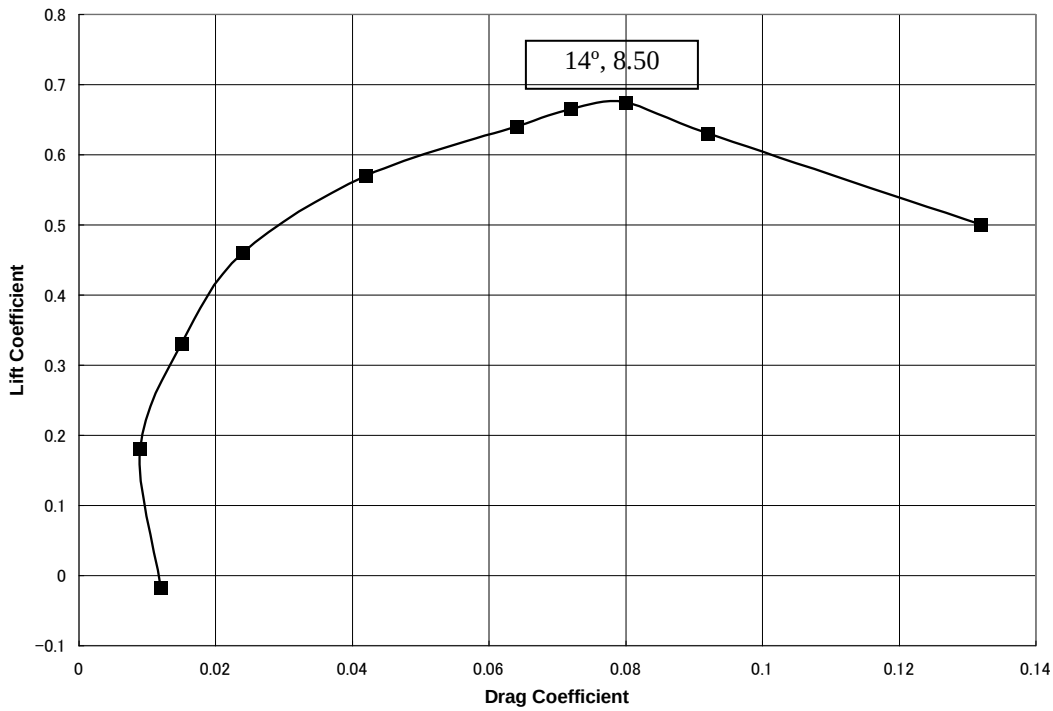

Figure 9.3: Lift Drag Curve of Conventional Cylindrical Shaped Fuselage UAV model at 40 m/s.

9.4 Lift Drag Curve of Aerofoil Shaped Fuselage UAV Model at 40 m/s

The lift drag curve of aerofoil shaped fuselage UAV model at 40 m/s is shown in Figure 9.4. The wing and fuselage tip experienced mostly induced drag due to tip and trailing edge vortices. A significant amount of drag is also produced due to shape and skin friction effects of the aerofoil shaped fuselage model which are termed as profile drag. So, both induced and profile drags have been experienced by this type of model. Profile drag of both cylindrical and aerofoil shaped models is same as both the models has the same volume. The lift to drag coefficient is found less for aerofoil shaped model due to increase of induced drag from the aerofoil shaped fuselage. But said model also increases a significant amount of extra lift from it's fuselage due to aerofoil shape. From Figure 9.4, it is found that at low and moderate lift coefficients, there is no appreciable flow separation. As the lift coefficient increases, drag coefficient also increases up to stall angle of attack i.e. 14º angle of attack. Afterwards, a sharp increase of drag coefficient with reduction of lift coefficient occurs for this type of model at the stall angle due to flow separation. The lift drag ratio at the stall angle for this model is found 9.42. Table-2 shows the lift to drag ratio of all the configurations at the stalling angle and two different velocities.

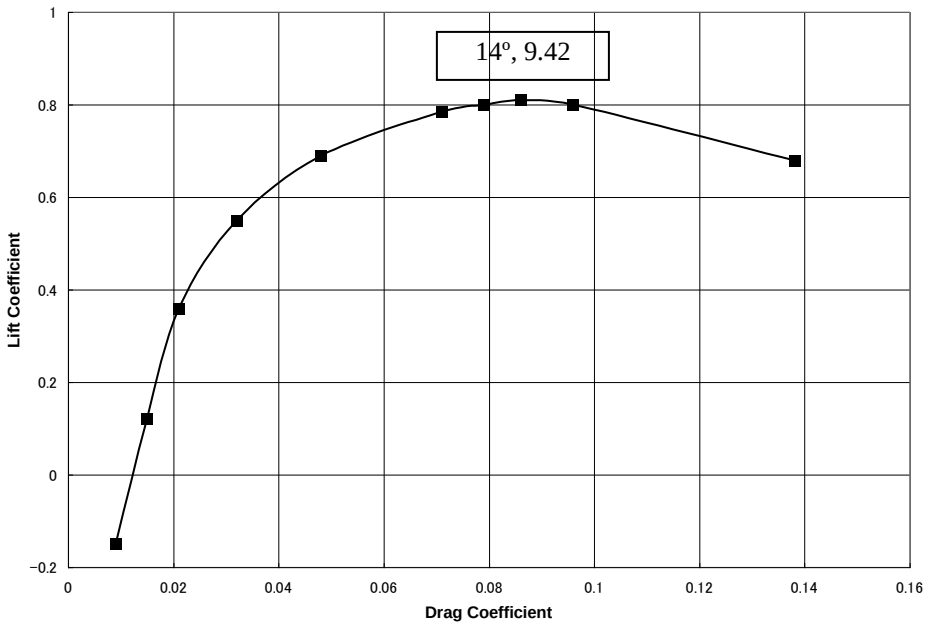

Figure 9.4: Lift Drag Curve of Aerofoil Shaped Fuselage UAV model at 40 m/s.

Table 2: Lift to Drag Curve of Four Configurations at Stalling Angle and two Different Velocities.

Configurations	Stall Angle	C_{Lmax}	C_{Dmax}	L/D Ratio
Aerofoil Shaped Fuselage Model at 20 m/s	14.0°	0.78	0.089	8.76
Conventional Model at 20 m/s	14.0°	0.63	0.075	8.40
Aerofoil Shaped Fuselage Model at 40 m/s	14.0°	0.81	0.086	9.42
Conventional Model at 40 m/s	14.0°	0.68	0.08	8.50

9.5 Comparison of Lift and Drag Coefficient VS AOA of Different Profiles

The comparison of lift coefficient VS angle of attack (AOA) of two different configurations of conventional cylindrical and aerofoil shaped fuselage at two different velocities is shown in Figure 9.5. The zero lift angle has been found approximately at -2º angle of attack. Then the lift coefficient increases almost linearly with the increase of angle of attack up to 14º. Among the two configurations, the aerofoil shaped fuselage has produced more lift coefficient than that of the conventional cylindrical shaped fuselage. The aerofoil shaped fuselage UAV model produced a significant amount of extra lift from it's fuselage due to it's aerofoil shape. Among the four studies, maximum lift coefficient is produced by the aerofoil shaped fuselage model at velocity 40 m/s. Next increment of lift coefficient is provided by the aerofoil shaped

fuselage model at 20 m/s and next to next is provided by the conventional cylindrical shaped fuselage at 40 m/s. The conventional cylindrical shaped fuselage at 20 m/s provides minimum lift coefficient among the four types of studies.

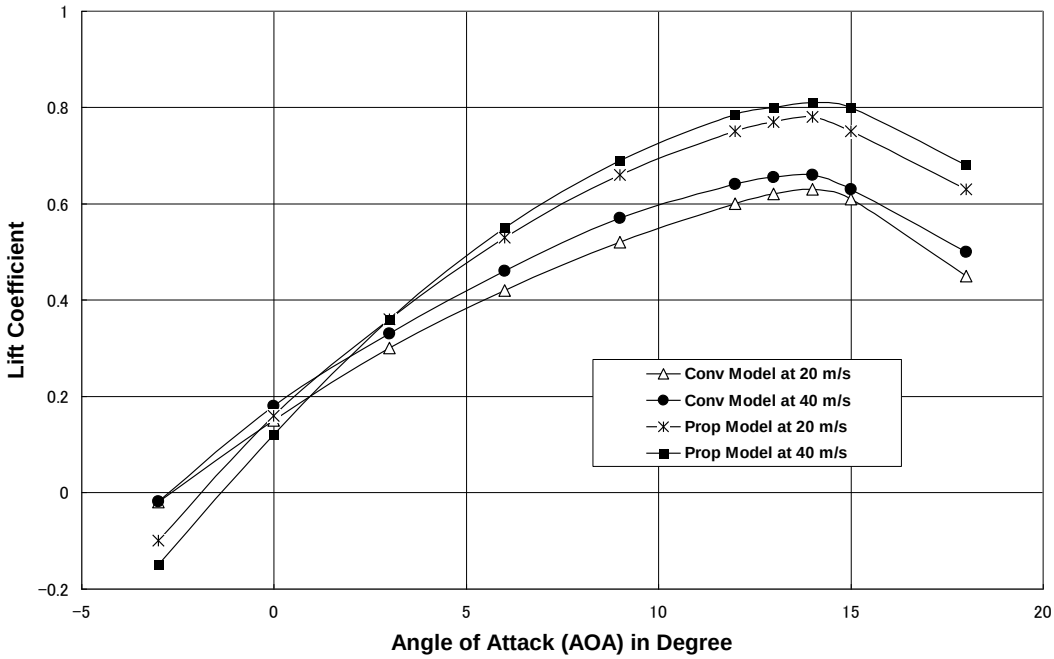

Figure 9.5: Variation of Lift Coefficient VS AOA of Two Different UAV Models at Different Velocities

The comparison of drag coefficient VS angle of attack (AOA) of two different configurations of conventional cylindrical and aerofoil shaped fuselage at two different velocities is shown in Figure 9.6. The shape of the drag coefficient VS angle of attack curve is found parabolic nature. As such, the drag coefficient increases with the increase of angle of attack. Among the two models, the aerofoil shaped fuselage has produced more drag coefficient than that of the conventional cylindrical shaped fuselage. Drag coefficient for aerofoil shaped fuselage is found more due to increase of induced drag for tip and trailing edge vortices of aerofoil shaped wing and fuselage of said UAV model. A significant amount of the total drag is also produced due to shape and skin friction effects of both the models which are termed as profile drag. Profile drag of both the models is same as both the models has the same volume. Among the four

studies, maximum drag coefficient is produced by the aerofoil shaped fuselage model at velocity 20 m/s. It is because flow separation starts earlier for aerofoil shaped fuselage model at 20 m/s. Out of four studies, next drag coefficient is found more for the aerofoil shaped fuselage UAV model at 40 m/s and next to next is found for conventional cylindrical shaped fuselage UAV model at 40 m/s. Conventional cylindrical shaped fuselage at 20 m/s provides minimum drag coefficient among the four types of studies.

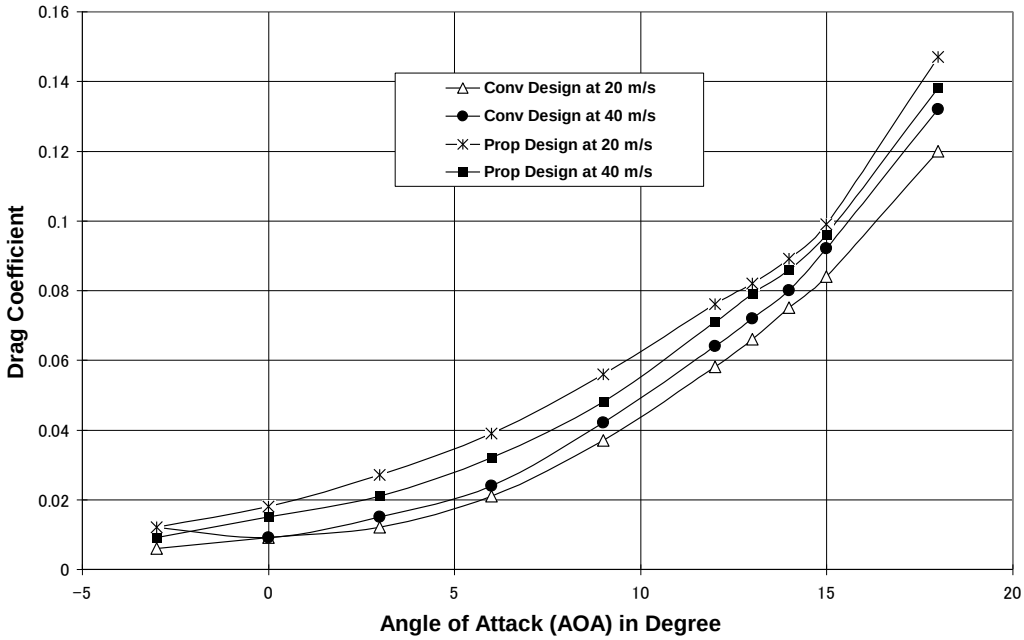

Figure 9.6: Variation of Drag Coefficient VS AOA of Two Different UAV Models at Different Velocities

9.6 Increment of Lift and Drag Coefficient by Aerofoil Shaped Fuselage Model at 20 m/s than Conventional Cylindrical Shaped Fuselage Model

Percentage increase of lift and drag coefficient of aerofoil shaped (AS) fuselage model at 20 m/s than that of conventional cylindrical shaped (CS) fuselage model at different angle of attack are shown in Figure 9.7 and 9.8 respectively. The aerofoil shaped fuselage configuration provides more lift as well as drag coefficient than that of the conventional cylindrical shaped fuselage UAV configuration. The formula for percentage increment of lift / drag coefficient of aerofoil shaped fuselage configuration is as follows:

$$\text{\% Increase of Lift/Drag Force at Specific Angle of Attack} = \left[\frac{\text{(Lift/Drag Force Produced by AS Fuselage - Lift/Drag Force Produced by CS Fuselage)}}{\text{Lift/Drag Force Produced by AS Fuselage}} \right] \times 100$$

From Figure 9.7, it is observed that out of two different studies, the percentage increment of lift coefficient is more for “aerofoil shaped fuselage configuration at 20 m/s” than that of the “conventional cylindrical shaped fuselage” at velocity 20 m/s and 40 m/s respectively. Again from Figure 9.8, it is also observed that the percentage increment of drag coefficient is found more for “aerofoil shaped fuselage configuration at 20 m/s” than that of the “conventional cylindrical shaped fuselage” at velocity 20 m/s and 40 m/s respectively. It is also seen from Figure 9.7 that “proposed aerofoil shaped fuselage configuration at 20 m/s” provides approximately 19.23% and 13.46% more lift force coefficient at 14° angle of attack (stall angle) than that of the conventional cylindrical shaped fuselage UAV configuration at velocity 20 m/s and 40 m/s respectively. It is also found from Figure 9.8 that the “proposed aerofoil shaped fuselage configuration at 20 m/s” provides approximately 15.73% and 10.11% more drag coefficient at 14° angle of attack (stall angle) than

that of the conventional cylindrical shaped fuselage configuration at velocity 20 m/s and 40 m/s respectively.

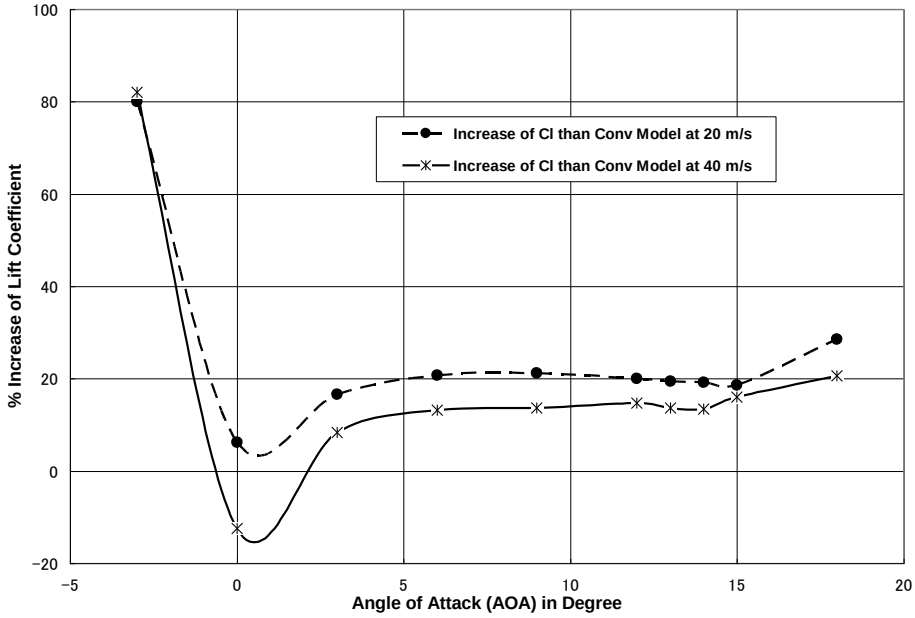

Figure 9.7: Percentage Increase of Lift Coefficient of "Aerofoil shaped fuselage configuration at 20 m/s" than that of "Conventional cylindrical shaped fuselage configuration at 20 m/s and 40 m/s" and different AOA.

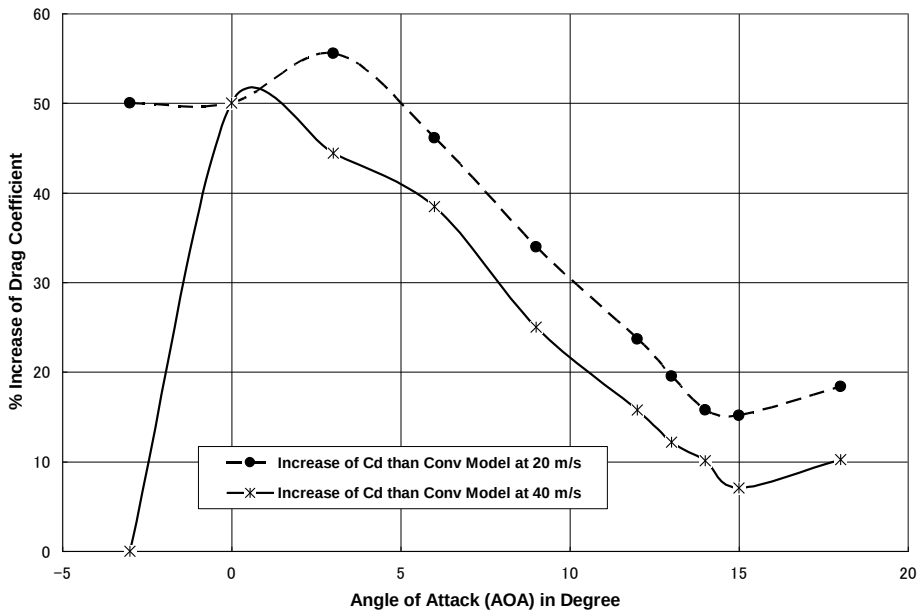

Figure 9.8: Percentage Increase of Drag Coefficient of "Aerofoil shaped fuselage configuration at 20 m/s" than that of "Conventional cylindrical shaped fuselage configuration at 20 m/s and 40 m/s" and different AOA.

9.7 Increment of Lift and Drag Coefficient by Aerofoil Shaped Fuselage Model at 40 m/s than Conventional Cylindrical Shaped Fuselage Model

Percentage increase of lift and drag coefficient of aerofoil shaped fuselage UAV model at 40 m/s than that of conventional cylindrical shaped fuselage UAV model at different angle of attack are shown in Figure 9.9 and 9.10 respectively. The aerofoil shaped fuselage configuration provides more lift as well as drag coefficient than that of the conventional cylindrical shaped fuselage configuration.

From Figure 9.9, it is observed that out of two different studies, the percentage increment of lift coefficient is found more for "aerofoil shaped fuselage configuration at 40 m/s" than that of "conventional cylindrical shaped fuselage" at velocity 20 m/s and 40 m/s respectively. Again from Figure 9.10, it is also observed that the percentage increment of drag coefficient is more for "aerofoil shaped fuselage configuration at 40 m/s" than that of "conventional cylindrical shaped fuselage" at velocity 20 m/s and 40 m/s respectively. It is seen from Figure 9.9 that the "aerofoil shaped fuselage configuration at 40 m/s" provides approximately 22.22% and 16.67% more lift coefficient at 14° angle of attack (stall angle) than that of the conventional cylindrical shaped fuselage configuration at velocity 20 m/s and 40 m/s respectively. It is also found from Figure 9.10 that the "proposed aerofoil shaped fuselage configuration at 40 m/s" provides approximately 12.79% and 6.98% more drag coefficient at 14° angle of attack (stall angle) than that of the conventional cylindrical shaped fuselage configuration at velocity 20 m/s and 40 m/s respectively.

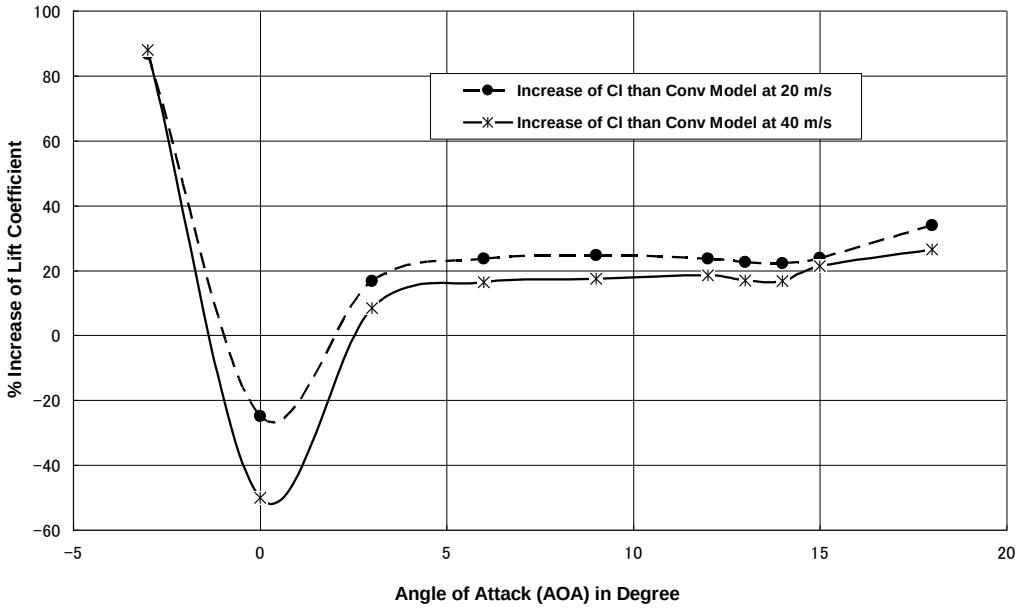

Figure 9.9: Percentage Increase of Lift Coefficient of "Aerofoil shaped fuselage configuration at 40 m/s" than that of "Conventional cylindrical shaped fuselage configuration at 20 m/s and 40 m/s" and different AOA.

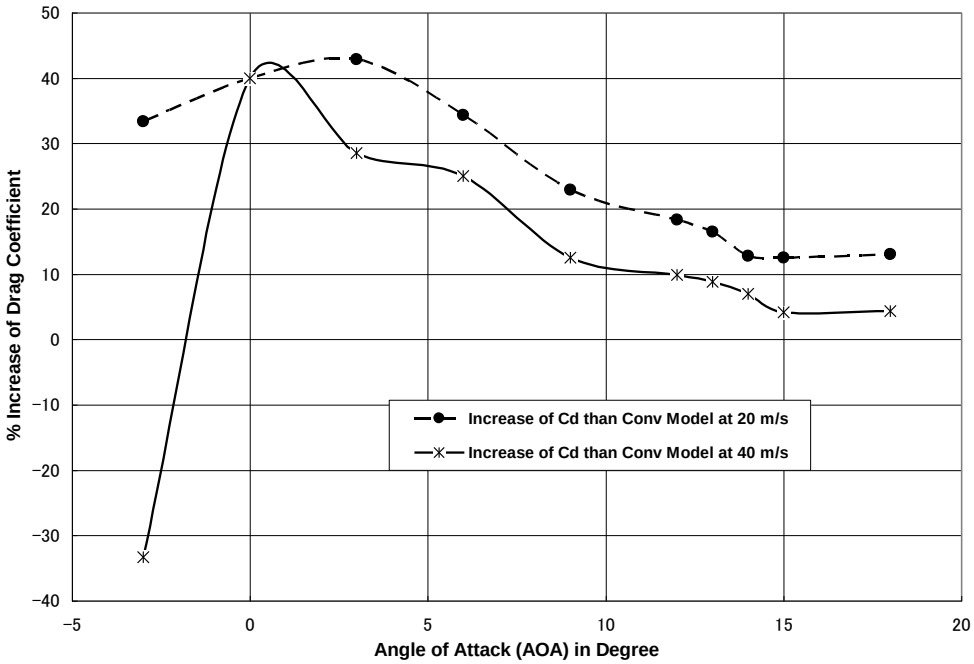

Figure 9.10: Percentage Increase of Drag Coefficient of "Aerofoil shaped fuselage configuration at 40 m/s" than that of "Conventional cylindrical shaped fuselage configuration at 20 m/s and 40 m/s" and different AOA.

9.8 Comparison of Computational and Experimental Lift and Drag Coefficient between two Models.

The variation of lift and drag coefficient with angle of attack between computational and experimental data of conventional cylindrical and aerofoil shaped fuselage UAV models is shown in Figure 9.11 to 9.18. It is seen that “Aerofoil shaped fuselage configuration at 40 m/s” provides more lift and drag coefficients than other three configurations for both computational and experimental design. It is also seen that the lift and drag force coefficients obtained from computational result is more than the experimental result for all configurations. Among the four configurations (from Figure 9.11 to 9.14), “Aerofoil shaped fuselage configuration at 40 m/s” provides maximum lift than other three types of configuration at about 14° angle of attack. Next lift providing configuration is “Aerofoil shaped fuselage configuration at 20 m/s” and next to next is “Conventional cylindrical shaped fuselage at velocity 40 m/s”. “Conventional cylindrical shaped fuselage at velocity 20 m/s” provides minimum lift coefficient than other three configurations. During drag analysis, it is seen from Figure 9.15 to 9.18 that among the four different types of configurations, “Aerofoil shaped fuselage configuration at 20 m/s” provides maximum drag than other three configurations. Next drag producing configuration is “Aerofoil shaped fuselage configuration at 40 m/s” and next to next is “Conventional cylindrical shaped fuselage at velocity 20 m/s”. “Conventional cylindrical shaped fuselage at velocity 40 m/s” provides minimum drag coefficient than other three configurations.

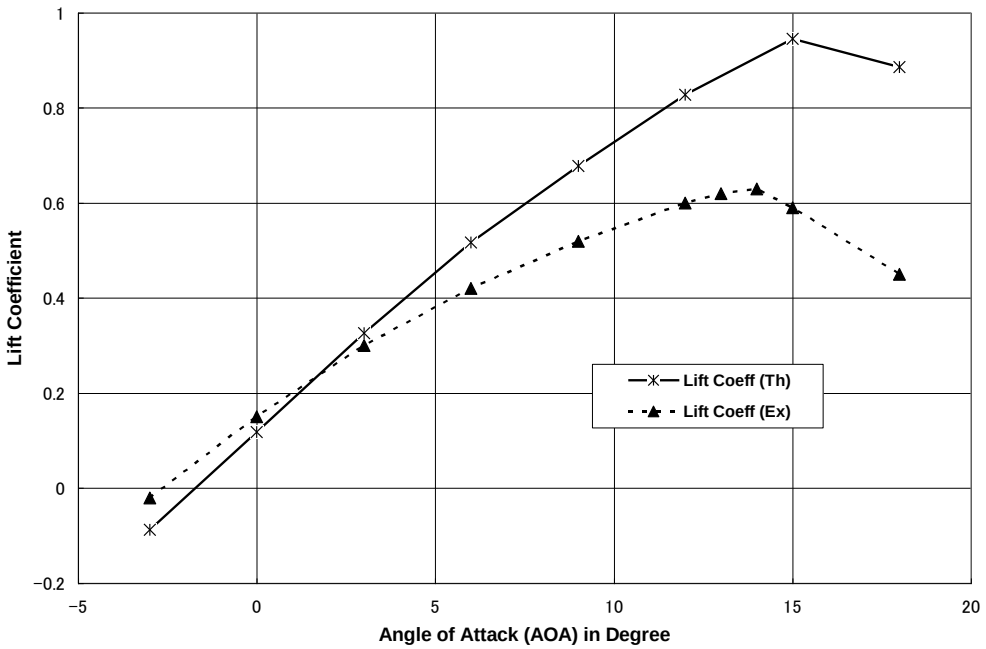

Figure 9.11: Comparison of Lift Coefficient VS AOA between Computational and Experimental Data of Conventional Cylindrical Shaped Fuselage UAV Model at 20 m/s.

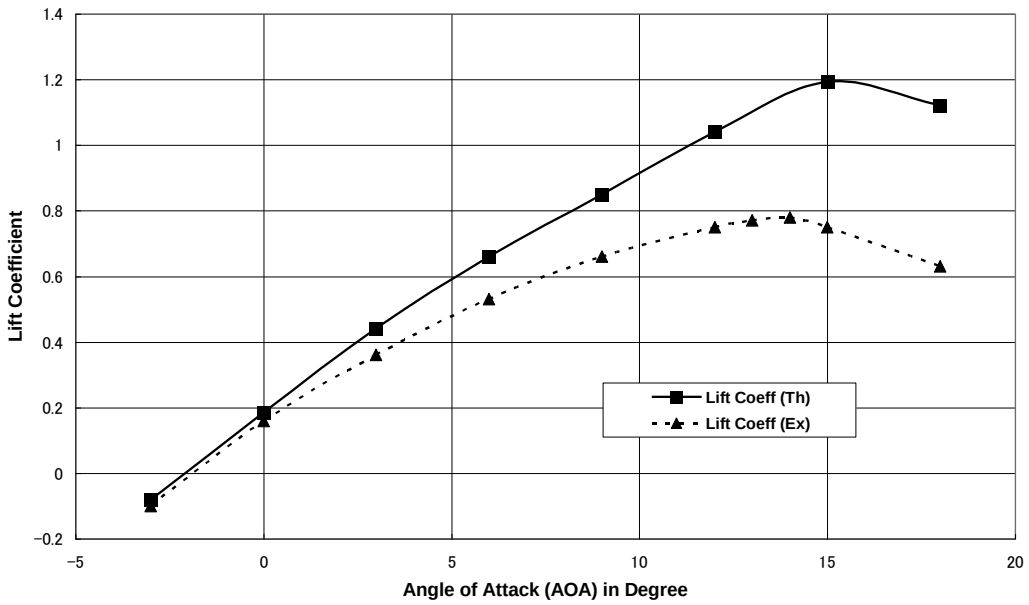

Figure 9.12: Comparison of Lift Coefficient VS AOA between Computational and Experimental Data of Aerofoil Shaped Fuselage UAV Model at 20 m/s.

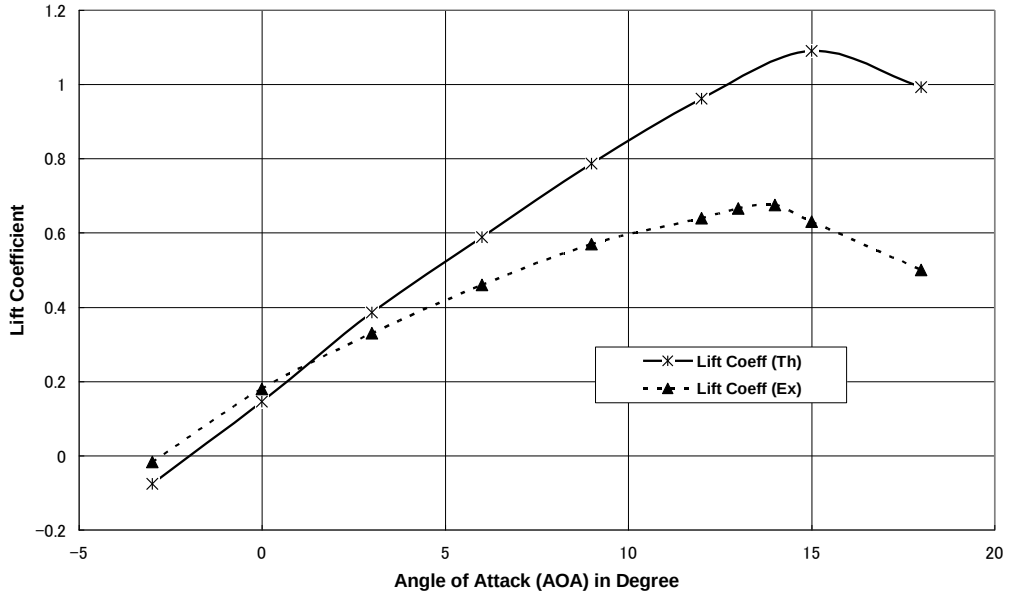

Figure 9.13: Comparison of Lift Coefficient VS AOA between Computational and Experimental Data of Conventional Cylindrical Shaped Fuselage UAV Model at 40 m/s.

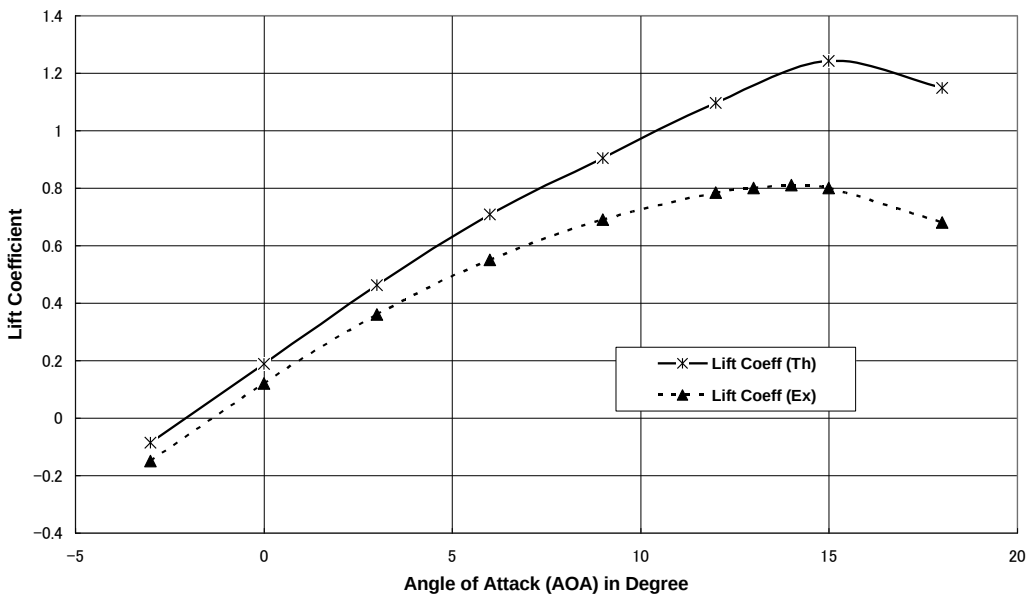

Figure 9.14: Comparison of Lift Coefficient VS AOA between Computational and Experimental Data of Aerofoil Shaped Fuselage UAV Model at 40 m/s.

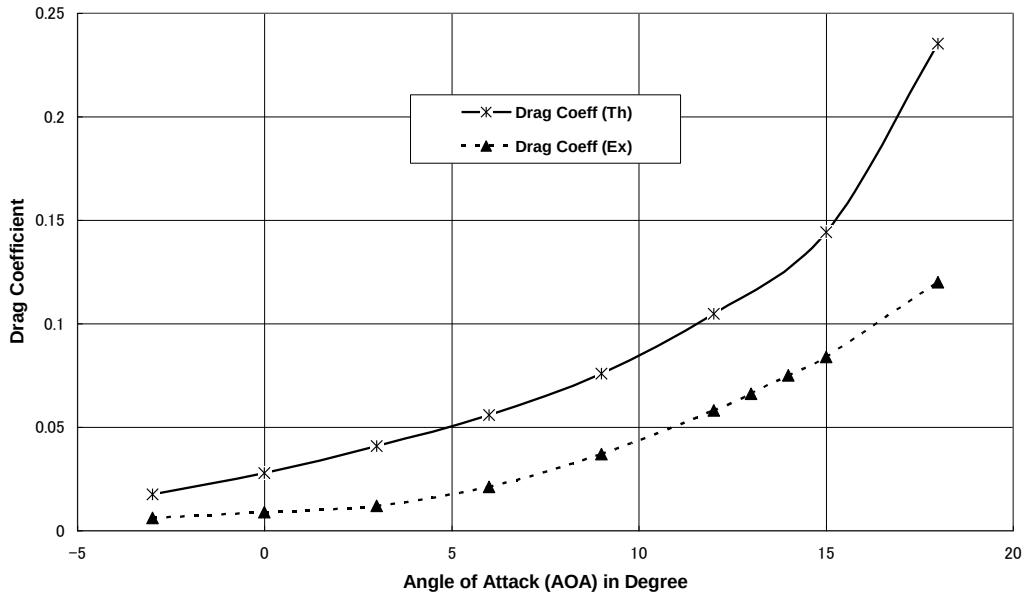

Figure 9.15: Comparison of Drag Coefficient VS AOA between Computational and Experimental Data of Conventional Cylindrical Shaped Fuselage UAV Model at 20 m/s.

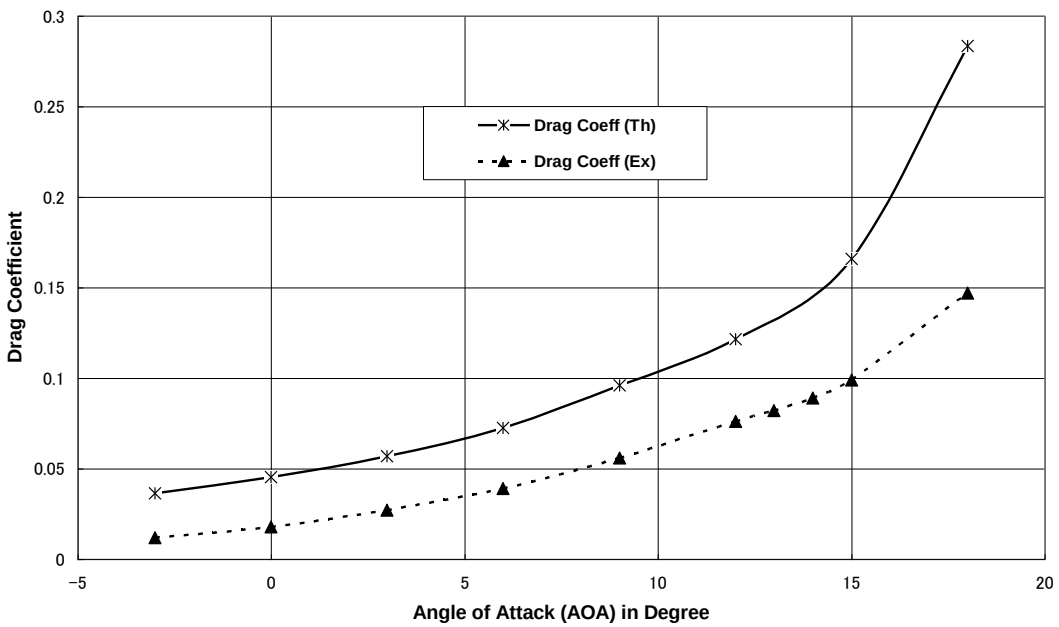

Figure 9.16: Comparison of Drag Coefficient VS AOA between Computational and Experimental Data of Aerofoil Shaped Fuselage UAV Model at 20 m/s.

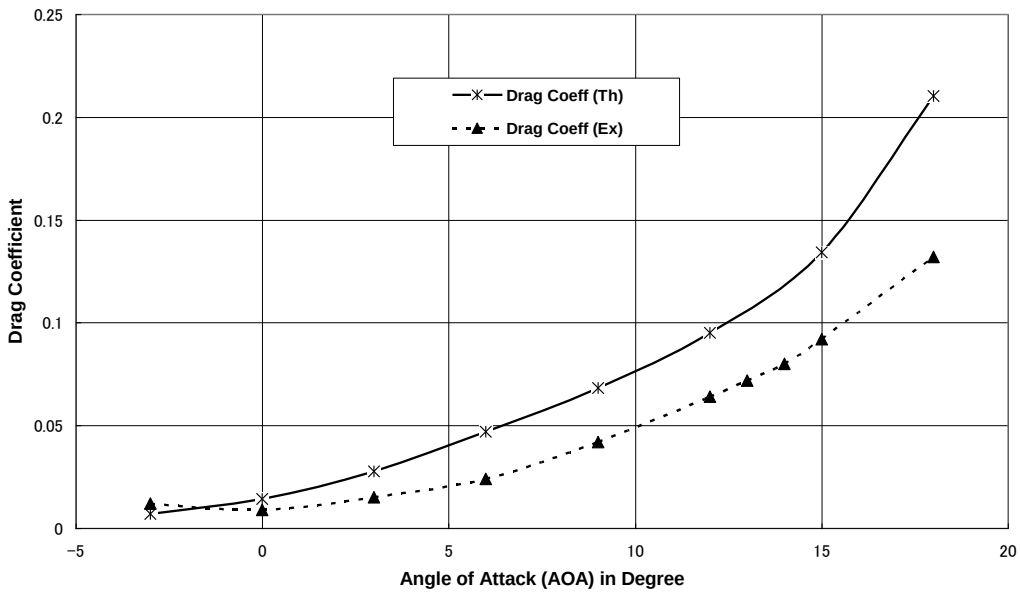

Figure 9.17: Comparison of Drag Coefficient VS AOA between Computational and Experimental Data of Conventional Cylindrical Shaped Fuselage UAV Model at 40 m/s.

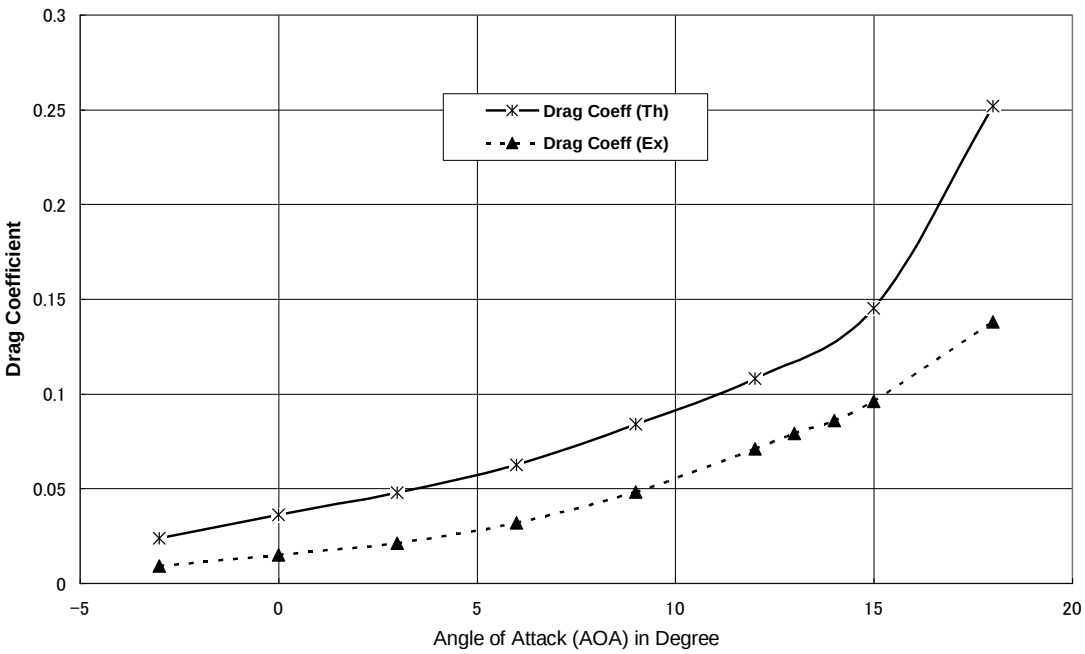

Figure 9.18: Comparison of Drag Coefficient VS AOA between Computational and Experimental Data of Aerofoil Shaped Fuselage UAV Model at 40 m/s.

9.9 Comparison of Pressure at Different Percentage from the Root of Conventional Cylindrical Shaped Fuselage UAV Model at 20 m/s

Surface Pressure of Conventional Cylindrical Shaped Fuselage UAV model at 25%, 50%, 75% and 90% from the root has been analyzed from -3° to 18° angle of attack at 20 m/s. The variation of Pressure with chord length of said model at 25%, 50%, 75% and 90% from the root at different angle of attack is shown in **Appendix 'R'** to Figure 9.19 to 9.22. The difference in pressure produced by the lower surface and upper surface of the wings determines the amount of lift and drag force produced by this model. The suction pressure mainly determines the amount of lift force to be produced by this model. It is seen that the difference of pressure between the lower surface (pressure side) and the upper surface (suction side) of the wings is more at 25%, followed by 50% and next is 75% in all the cases. Pressure difference is found least at 90% from the root. Flow separation mostly starts after 90% from the root. The height of the upper surface suction peak of the wings is found maximum at 14 $^\circ$ angle of attack i.e. at the stall angle. Afterwards, separation starts due to sudden flattening of the upper surface pressure distribution (reduction of suction peak) with further increase of angle of attack. Furthermore increase of angle of attack will further reduce the lift.

9.10 Comparison of Pressure at Different Percentage from the Root of Aerofoil Shaped Fuselage UAV Model at 20 m/s

Surface Pressure of Aerofoil Shaped Fuselage UAV model at 25%, 50%, 75% and 90% from the root has been analyzed from -3° to 18° angle of attack at 20 m/s. The variation of Pressure with chord length of said model at 25%, 50%, 75% and 90% from the root at different angle of attack is shown in **Appendix 'S'** to Figure 9.23 to 9.26. The difference in pressure produced by the lower surface and upper surface of the wings and fuselages determines the amount of lift and drag force produced by this model. The suction pressure mainly determines the amount of lift

force to be produced by this model. It is seen that the difference of pressure between the lower surface (pressure side) and the upper surface (suction side) of the wings and fuselages is more at 25%, followed by 50% and next is 75% in all the cases. Pressure difference is found least at 90% from the root. Flow separation mostly starts after 90% from the root. The height of the upper surface suction peak of the wings is found maximum at 14° angle of attack i.e. at the stall angle. Afterwards, separation starts due to sudden flattening of the upper surface pressure distribution (reduction of suction peak) with further increase of angle of attack. Furthermore increase of angle of attack will further reduce the lift.

9.11 Comparison of Pressure at Different Percentage from the Root of Conventional Cylindrical Shaped Fuselage UAV Model at 40 m/s

Surface Pressure of Conventional Cylindrical Shaped Fuselage UAV model at 25%, 50%, 75% and 90% from the root has been analyzed from -3° to 18° angle of attack at 40 m/s. The variation of Pressure with chord length of said model at 25%, 50%, 75% and 90% from the root at different angle of attack is shown in **Appendix 'T'** to Figure 9.27 to 9.30. The difference in pressure produced by the lower surface and upper surface of the wings determines the amount of lift and drag force produced by this model. The suction pressure mainly determines the amount of lift force to be produced by this model. It is seen that the difference of pressure between the lower surface (pressure side) and the upper surface (suction side) of the wings is more at 25%, followed by 50% and next is 75% in all the cases. Pressure difference is found least at 90% from the root. Flow separation mostly starts after 90% from the root. The height of the upper surface suction peak of the wings is found maximum at 14 $^{\circ}$ angle of attack i.e. at the stall angle. Afterwards, separation starts due to sudden flattening of the upper surface pressure distribution (reduction of suction peak) with further increase of angle of attack. Furthermore increase of angle of attack will further reduce the lift.

9.12 Comparison of Pressure at Different Percentage from the Root of Aerofoil Shaped Fuselage UAV Model at 40 m/s

Surface Pressure of Aerofoil Shaped Fuselage UAV model at 25%, 50%, 75% and 90% from the root has been analyzed from -3° to 18° angle of attack at 40 m/s. The variation of Pressure with chord length of said model at 25%, 50%, 75% and 90% from the root at different angle of attack is shown in **Appendix 'U'** to Figure 9.31 to 9.34. The difference in pressure produced by the lower surface and upper surface of the wings and fuselages determines the amount of lift and drag force produced by this model. The suction pressure mainly determines the amount of lift force to be produced by this model. It is seen that the difference of pressure between the lower surface (pressure side) and the upper surface (suction side) of the wings and fuselages is more at 25%, followed by 50% and next is 75% in all the cases. Pressure difference is found least at 90% from the root. Flow separation mostly starts after 90% from the root. The height of the upper surface suction peak of the wings is found maximum at 14° angle of attack i.e. at the stall angle. Afterwards, separation starts due to sudden flattening of the upper surface pressure distribution (reduction of suction peak) with further increase of angle of attack. Furthermore increase of angle of attack will further reduce the lift.

9.13 Requirements for Aerofoil Shaped Fuselage Design for Test Flight

The present work of aerofoil shaped fuselage has been designed using NACA 4416 aerofoil profile and based on the seven crack points of conceptual design. Salient features on those points are as follows:

Requirements and Mission Profile: The designed UAV will be used for aerial photography; surveillance and reconnaissance, defence as well as many national

purposes. The Aerofoil Shaped Fuselage UAV mission profile is shown in Figure 7.59.

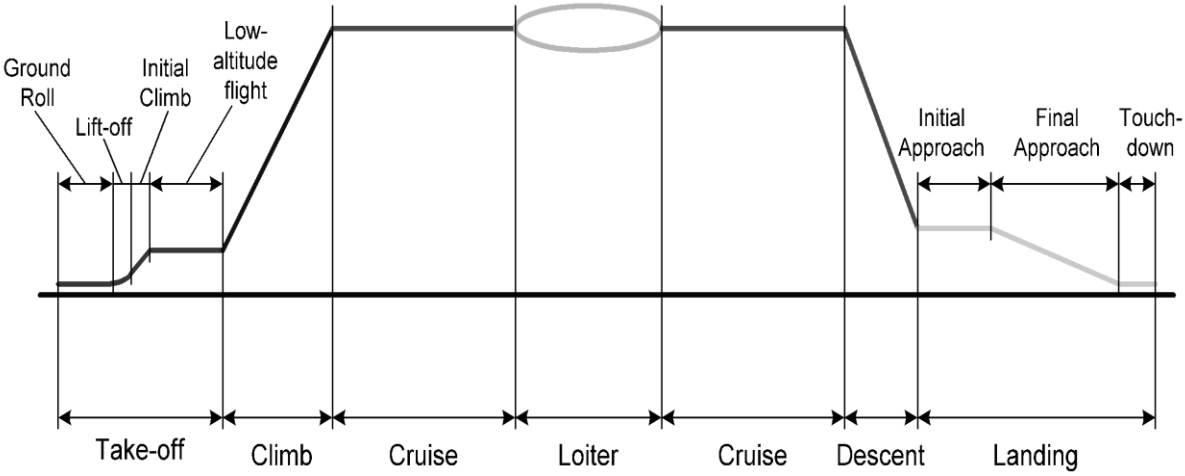

Figure 9.35: Aerofoil Shaped Fuselage UAV Mission Profile

Weight: Net gross weight of the proposed UAV will be approximately 10 kg (including weight of fuel will be 1000 ml and other associated weight is 3 kg).

Critical Performance Parameters:

(1). Maximum lift coefficient, (C_{Lmax}) – Approximately 0.8 to 1.3. To be determined from CFD.

(2). Engine Thrust- Approximately 4.47 HP.

(3). Engine r.p.m : Approximately 8,000.

(4). Wing and Fuse ledge : Aerofoil shaped fuselage by using NACA 4416 profile.

(5). Landing gear : Tri-cycle type, non-retractable.

Performance Analysis:

(1). Payload : Approximately 6 kg.

(2). Endurance : Approx 30 min.

(3). Range : Approx 10 km.

(4). Ceiling Height : Approx (1,500 - 1,800) m.

(5). Speed : Approximately 20 m/s to 40 m/s.

(6). Maximum take off weight : Approx 18 kg.

(7). Take off distance : Approx (5 - 6) ft.

(8). Landing distance : Approx 750 – 850 m.

(9). Stability : Stable and less maneuverable.

Engine Horse Power Calculation:

- UAV Empty **w**eight : 06 kg.
- Fuel weight : 1000 ml (01 kg).
- Other weight : 03 kg.
- Range : 10 km.
- Maximum velocity : 40 m/s.
- Acceleration : 3.0 m/s^2.
- Endurance : 30 min.
- Design load factor : 5.
- Factor of Safety : 2.

So, Thrust (T) = Mass x Acceleration = $M\,a$ = 10 x 3.0 = 30 Newton

Work Done (W) = Force x Distance = T d = 30 x (2 x 10,000)

= 6,00,000 N-m/s or J/s.

Now,

$$\text{Calculated required power} = \frac{\text{Thrust x Distance}}{\text{Time}}$$

$$= \frac{\text{Work Done}}{\text{Time}}$$

$$= \frac{\mathbf{6,00,000}}{\mathbf{30 \times 60}}$$

= 333.33 N-m / s.

Actual Power (considering all aspects) = (333.33 x Design Load Factor x Factor of Safety)

= 333.333 x 5 x 2

= 3333.33 N-m / s.

$$= \frac{3333.33}{746}$$

= 4.47 HP.

<u>Comment</u>: The performance of development of all lifting vehicle technology like aerofoil shaped fuselage has been investigated thoroughly during carry out research on small sized UAV. The fuselage of UAV might be a good source of lifting force. The designed aerofoil shaped fuselage UAV would fly under autonomous control of both an Intelligent Controller (IC) running on an onboard computer operating from the ground if suitable engine, landing gear and electronic circuits/device related to control would be incorporated with the system. For a basic weight approximately 10 kg, endurance 30 minute, range 10 km having fixed tri-cycle type landing gear – a motor operated engine with approximately 4.47 HP would be required to manufacture an UAV having aerofoil shaped fuselage.

CONCLUSION AND RECOMMENDATION

10.1 Conclusion:

Operation of UAV proved to be easy and adaptable for versatile tasks including military as well as many civil applications in the recent years. But UAV requires higher lifting force with a smaller size. In order to maximize the efficiency of an UAV - the concept of development of all lifting vehicle technology might bring good result for research on future UAV. For this, the aerofoil shaped fuselage of an UAV is likely to be a good source of lifting force. As such, after thorough research, the following conclusions may be brought from this investigation about the effect of "NACA 4416 Aerofoil Shaped Fuselage" on the performance of an UAV:

1. The lift coefficient starts from -2º degree angle of attack and increases almost linearly with the increase of angle of attack up to 14° - 15º.

2. Lift coefficient decreases with the increase of angle of attack above 14° to 15º.

3. Stall angle for theoretical design is 15º and experimental design is 14° for both the models.

4. The shape of 'Drag Coefficient VS Angle of Attack' is exponential.

5. Drag coefficient increases with the increase of angle of attack.

6. Difference in pressure by the lower surface aerofoil and upper surface aerofoil determines the amount of lift and drag force produced by each model.

7. 2D NACA 4416 profile provides maximum lift coefficient and minimum drag coefficient among all other configurations.

8. **"**Aerofoil shaped fuselage configuration at 20 m/s" provides approximately **20.73% and 8.62%** more lift coefficient at 15° AOA (stall angle) than that of the conventional cylindrical shaped fuselage configuration at velocity 20 m/s and 40 m/s respectively for theoretical design.

9. "Aerofoil shaped fuselage configuration at 20 m/s" provides approximately **13.12% and 19.11%** more drag coefficient at 15° AOA (stall angle) than that of the conventional cylindrical shaped fuselage configuration at velocity 20 m/s and 40 m/s respectively for theoretical design.

10. "Aerofoil shaped fuselage configuration at 40 m/s" provides approximately **23.79% and 12.15%** more lift coefficient at 15° AOA (stall angle) than that of the conventional cylindrical shaped fuselage configuration at velocity 20 m/s and 40 m/s respectively for theoretical design.

11. "Aerofoil shaped fuselage configuration at 40 m/s" provides approximately **0.58% and 7.42%** more drag coefficient at 15° AOA (stall angle) than that of the conventional cylindrical shaped fuselage configuration at velocity 20 m/s and 40 m/s respectively for theoretical design.

12. **"**Aerofoil shaped fuselage configuration at 20 m/s" provides approximately **19.23% and 13.46%** more lift coefficient at 14° AOA (stall angle) than that of the conventional cylindrical shaped fuselage configuration at velocity 20 m/s and 40 m/s respectively for experimental design.

13. "Aerofoil shaped fuselage configuration at 20 m/s" provides approximately **15.73% and 10.11%** more drag coefficient at 14° AOA (stall angle) than

that of the conventional cylindrical shaped fuselage configuration at velocity 20 m/s and 40 m/s respectively for experimental design.

14. "Aerofoil shaped fuselage configuration at 40 m/s" provides approximately **22.22% and 16.67%** more lift coefficient at 14° AOA (stall angle) than that of the conventional cylindrical shaped fuselage configuration at velocity 20 m/s and 40 m/s respectively for experimental design.

15. "Aerofoil shaped fuselage configuration at 40 m/s" provides approximately **12.79% and 6.98%** more drag coefficient at 14° AOA (stall angle) than that of the conventional cylindrical shaped fuselage configuration at velocity 20 m/s and 40 m/s respectively for experimental design.

16. The L/D Ratio of "2D NACA 4416 Profile" at 15° AOA at 20 and 40 m/s are **10.35 and 12.90** respectively for theoretical design.

17. The L/D Ratio of "Cylindrical shaped fuselage configuration" at 15° AOA at 20 and 40 m/s are **6.57 and 8.28** respectively for theoretical design.

18. The L/D Ratio of "Aerofoil shaped fuselage configuration" at 15° AOA at 20 and 40 m/s are **7.23 and 8.42** respectively for theoretical design.

19. The L/D Ratio of "Cylindrical shaped fuselage configuration" at 14° AOA at 20 and 40 m/s are **8.40 and 8.50** respectively for experimental design.

20. The L/D Ratio of "Aerofoil shaped fuselage configuration" at 14° AOA at 20 and 40 m/s are **8.76 and 9.42** respectively for experimental design.

21. The lift and drag force coefficient obtained from theoretical result is found more than that of the experimental result for all types of configurations.

22. Aerofoil shaped fuselage has produced more lift coefficient than that of conventional cylindrical shaped fuselage.

23. Significant amount of extra lift has been produced by aerofoil shaped fuselage due to it's shape.

24. Aerofoil shaped fuselage has produced extra drag due to it's increased fuselage frontal area, fuselage-wing interference effect and trailing edge vortex.

25. Difference in suction and positive pressure of aerofoil shaped fuselage is found more in comparison with the cylindrical shaped fuselage. The difference has been increased for aerofoil shaped fuselage at 40 m/s than that at 20 m/s.

26. Out of four parameters (25%, 50%, 75% and 90% from the root of the wing), the maximum difference in suction and positive pressure is found at 25% from the root of the wing for both the designs.

27. The difference in suction and positive pressure has been reduced from root towards tip of each wing for both the designs.

28. The maximum difference in suction and positive pressure is found at 25% from the root of the wing of "Aerofoil shaped fuselage at 40 m/s" than other three configurations for both the design.

29. The difference in suction and positive pressure is found maximum within 12 to 15% of chord length for all type of configurations for both the designs.

30. The aerofoil shaped fuselage might be a good option for designing the future UAV.

10.2 Recommendation:

The author would like to make the following recommendations for future work in this field:

1. Ways for reduction of drag from the aerofoil shaped fuselage may be investigated for future research.

2. A 3D computational UAV model having aerofoil shaped fuselage with winglet at the end of the fuselage may be designed for investigation of the aerodynamic characteristics.

3. A 3D UAV model having aerofoil shaped fuselage with winglet at the end of fuselage may be fabricated and tested at the wind tunnel for investigation of the aerodynamic characteristics experienced by this model and compared both the computational and experimental result.

4. Point surface Pressure on the surfaces of aerofoil shaped fuselage UAV model (with or without winglet) may be investigated and analyzed.

5. Coefficient of moment of aerofoil shaped fuselage (with or without winglet) may be analyzed and compared with that of the conventional cylindrical shaped UAV model.

6. Aerofoil section other than NACA 4416 may be used for the design of aerofoil shaped fuselage UAV models.

7. UAV models having aerofoil shaped fuselage may be fabricated/manufactured and test trial may be given for flying.

REFERENCES

Abbott I. H. and Doenhoff A. E. V., 1959, "Theory of Wing Sections including a Summary of Aerofoil Data", Dover Publications, Inc, New York.

Abbott, Ira H., Von Doenhoff, Albert E., and Stivers, Louis S., 1945, "Summary of Aerofoil Data", NACA Report No. 824.

Allen, H. Julian, 1939, "A Simplified Method for the Calculation of Aerofoil Pressure Distribution", NACA TN No. 708.

Allen, H. Julian, 1938, "Calculation of the Chordwise Load Distribution over Aerofoil Sections with Plain, Split or Serially-hinged Trailing Edge Flaps", NACA Report No. 634.

Allen, H. Julian, 1943, "General Theory of Aerofoil Sections having Arbitrary Shape or Pressure Distribution", NACA ACR No. 3G29.

Anderson J. D., 1995, "Computational Fluid Dynamics – The Basics with Applications", McGraw – Hill International Edition.

Anderson J.D., 1991, "Fundamentals of Aerodynamics", McGraw-Hill Companies, 2nd edition.

Anderson John.D., 1999, "Aircraft Performance and Design", McGraw-Hill Companies; International edition.

Bruce T. Clough, 2005, "Unmanned Aerial Vehicles: Autonomous Control Challenges, a Researcher's Perspective", Journal of Aerospace Computing, Information and Communication, Vol. 2.

Bryan Recktenwald, 2008, "Aerodynamics of a Circular Planform Aircraft", American Institute of Aeronautics and Astronautics 022308, pp 1-7.

Chennakeshu S. and Ganapathi K.K., 1993, "Aircraft Production technology and management" Interline Publishing.

Clancy L. J., 1975, "Aerodynamics", John Wiley, New York.

Corke Thomas C., 2005, "Design of Aircraft", PEARSON Education, Inc..

Daniel P. Raymer, 1999, "Aircraft Design: A conceptual Approach", American Institute of Aeronautics and Astronautics, pp. 1-10.

Glauert, H., 1926, "The Elements of Aerofoil and Airscrew Theory", Cambridge University Press, London.

Greg T. Busch and Michael B. Bragg, 2009, "Experimental study of Full-Scale Iced-Airfoil Aerodynamic Performance using Sub-scale Simulations", AIAA 2009-4264,

Ilan Kroo, 2001, “Drag due to Lift: Concepts for Prediction and Reduction”, Annual Review, Fluid Mechanics vol-33, pp 587-617.

Ira H. Abbott and Albert E. Von Doenhoff, 1959, “Theory of Wing Sections – including a summary of airfoil data’’, Dover Publications, Inc, pp 488-493.

Jacobs, Eastman N., and Pinkerton, Robert M., 1930, “Pressure Distribution over a Symmetrical Aerofoil Section with Trailing Edge Flap”, NACA Report No. 360.

Jay P. Boris, 1989, “New Directions in Computational Fluid Dynamics” Annual Reviews, pp 345-351.

Jodi A. Miller, Paul D. Minear, Albert F. Niessner, Jr, Anthony M. DeLullo, Brian R. Geiger, Lyle N. Long and Joseph F. Horn, 2007, “Intelligent Unmanned Air Vehicle Flight Systems”, Journal of Aerospace Computing, Information and Communication, pp. 816-823.

Kermode A. C., 1989, “Flight without Formula”, Pitman, 8th edition.

Korbacher G.K., 1974, “Aerodynamics of Powered High-Lift Systems”, Annual Review Fluid Mechanics, page 319 – 358.

Labrujere Th. E. and Slooff J.W., 1993, “Computational Methods for the Aerodynamic Design of Aircraft Components”, Annual Review Fluid Mechanics, page 183-214.

Lissaman P. B. S., 1983, “Low-Reynolds-Number Airfoils” Annual Review Fluid Mechanics, page 223-239.

Loftin, Laurence K., Jr., and Cohen, Kenneth S., 1947, “Aerodynamic Characteristics of a Number of Modified NACA Four-digit-series Aerofoil Sections”, NACA RM No. L7122.

Miley S.J., 1982, “A catalog of low Reynolds Number Airfoil Data for Wind Turbine applications”, Department of Aerospace Engineering, Texas A&M University, Texas, RFP-3387 UC-60, pp 1-44.

Munk, Max M., 1945, “Calculation of Span Lift Distribution (Part 2) Aero Digest”, Vol. 48, No.3, page 84.

Munk, Max M., 1924, “Elements of the Wing Section Theory” , NACA Report No. 191.

Ramesh Agarwal, 1999, “Computational Fluid Dynamics of Whole-Body Aircraft” Annual Reviews, Fluid Mechanics, pp. 125-136.

Randal Beard, Derek Kingston, Morgan Quigley, Deryl Snyder, Reed Christiansen, Walt Johnson, Timothy McLain and Michael A. Goodrich, 2005, “Autonomous Vehicle Technologies for Small Fixed-Wing UAVs”, Journal of Aerospace Computing, Information and Communication, pp. 92-94.

Recklenwald Bryan, 2008, “Aerodynamics of a Circular Planform Aircraft”, Journal of American Institute of Aeronautics and Astronautics.

Rolald D. Joslin, 1998, “Aircraft Laminar Flow control”, Annual Review Fluid Mechanics, page 1-29.

Schouwenaars T., Valenti M., Feron E. and How J., 2006, “Linear Programming and Language Processing for Human / Unmanned – Aerial – Vehicle Team Missions”, Journal of Guidance, Control and Dynamics, Vol-29, No. 2.

Secanell, A. Suleman and P. Gamboa, 2005, “Design of a Morphing Airfoil for a Light Unmanned Aerial Vehicle using High-Fidelity Aerodynamic Shape Optimization” Journal of American Institute of Aeronautics and Astronautics (AIAA 2005-1891), pp. 1-20.

Shermam, Albert, 1939, “A Simple Method of Obtaining Span Load Distribution”, NACA TN No. 732.

Shivhumar R., Hemendra Arya and K. Sudhakar, 2002, “Miniature Aerial Vehicle – Airframe Characterization”, Department of Aerospace Engineering, Indian Institute of Technology, Bombay.

Shlomo Tsach, Akiva Peled, David Penn and David Hillel Touitou, 2004, “Civil Applications and Economical Effectivity of Potential UAV Configurations”, AIAA 3rd Unmanned Unlimited Technical Conference, Workshop and Exhibit.

Stanley G.Rubin, 1992, “Parabolized/Reduced Navier-Stokes Computational Techniques”, Annual Review Fluid Mechanics, page 117 – 144.

Taylor, J. R, 1982, “An Introduction to Error Analysis; The Study of Uncertainties in Physical Measurements”, 2nd Edition, University Science Books.

Theuniseen E. and Goossens A.A.H.E., 2005, “UAV Mission management Functions to Support Integration in a Strategic and Tactical ATC and C^2 Environment”, AIAA Modeling and Simulation Technologies Conference and Exhibit, AIAA 2005-6310.

Timothy X brown, Brian Argrow, Cory Dixon, Sheetalkumar Doshi, Roshan-George Thekkekunel and Daniel Henkel, 2004, “Ad Hoc UAV Ground Network (AUGNET)”, AIAA 3rd Unmanned Unlimited Technical Conference, Workshop and Exhibit, September 2004.

Thomas J. Muller and James D. Delaurier, 2003, “Aerodynamics of Small Vehicles”, Annual Reviews, Fluid Mechanics, pp. 89 – 111.

Thomas Bowden, Thomas Carroll, Ben Havrilesku, Mathew Heller, Tyler Lamb, C. Kyser Miree and Willium O. Runge, 2009, “Rocket Based Deployment of a Reconnaissance UAV”, American Institute of Aeronautics and Astronautics.

U.S. Department of Transportation, Federal Aviation Administration, 1998, “Airframe and Power plant Mechanics – Airframe Handbook”.

Wang C.Y., 1991, "Exact Solutions of the steady-State Navier-Stokes Equations", Annual Review Fluid Mechanics, page 159-177.

Wood R. M., 2003, "The Contributions of Vincent Justus Burnelli" AIAA 2003-0292.

The thesis titled **"Investigation of the Effect of NACA 4416 Aerofoil Shaped Fuselage on the Performance of an Unmanned Air Vehicle"** submitted by G.M. Jahangir Alam, Roll No : P10071002P, Session : October 2007 has been accepted as satisfactory in partial fulfillment of the requirements for the degree of Doctor of Philosophy (Ph.D) on 17 December 2013.

1.	---------- Dr. Mohammad Mamun Professor Department of Mechanical Engineering, BUET.	Chairman
2.	---------- Dr. Md. Abu Taher Ali Professor (Retired) Department of Mechanical Engineering, BUET.	Member
3.	---------- Dr. Mohammad Ehsan Professor & Head Department of Mechanical Engineering, BUET.	Member (Ex-Officio)
4.	---------- Dr. Md. Quamrul Islam Professor Department of Mechanical Engineering, BUET.	Member
5.	---------- Dr. Md Mustafa Kamal Chowdhury Professor Department of Mathematics, BUET.	Member
6.	---------- Dr. A. K. M. Sadrul Islam Professor Department of Mechanical & Chemical Engineering, IUT, Gazipur.	Member
7.	---------- Dr. Alamgir Hossain Associate Professor Mechanical Engineering Department, MIST.	Member (External)

CANDIDATE'S DECLARATION

It is hereby declared that this thesis or any part of it has not been submitted elsewhere for the award of any degree or diploma.

Signature of the Candidate:

G.M. Jahangir Alam

ACKNOWLEDGEMENT

The author expressed his deep gratitude to Almighty ALLAH for showing him the right path and giving him courage and strength to accomplish the work successfully. This research work was conducted under close supervision and thorough guidance of Dr. Mohammad Mamun, Professor, Department of Mechanical Engineering, Bangladesh University of Engineering and Technology (BUET). The author is highly grateful to his supervisor for providing continuous support, untiring help and encouragement during entire tenure of his research work.

The author expresses his profound gratitude to the doctoral committee (Professor Dr. M. A. Taher Ali, Professor Dr. Md. Quamrul Islam, Professor Dr. Md Mustafa Kamal Chowdhury, Professor Dr. A. K. M. Sadrul Islam and Professor Dr. Md. Ehsan) for their dedicated supervision, ceaseless inspiration, deliberate encouragement and untiring support throughout this research work and for their continuous pursuit of the developments at different stages of this research work. The author feels highly grateful to Group Captain Md Abdus Salam, Head of Aeronautical Engineering (AE) Department, Military Institute of Science and Technology (MIST) for providing necessary assistance, support and cooperation to use wind tunnel Model AF 100 to obtain data at different stages of this thesis work. The author remembers the assistance and cooperation from Mr Dibakar Tarafder, SWO Md Shahdat Hossain, Md Nazmul Hossain and Mr Abinash Chandra Barman of MIST for fabricating, assembling and data collection during various stages of his work. He also thanks to Md Abdur Razzak of Fluid Machinery Laboratory, Department of Mechanical Engineering, BUET for his cooperation in manufacturing of the experimental set up.

Finally, the author would like to express his sincere thanks to all other teachers of the Mechanical Engineering Department, BUET and MIST and his friends who encouraged him during the research work and helps for the successful completion of the work.

ABSTRACT

The piloted aircraft were predominantly used for surveillance and reconnaissance missions but the vast technological improvements in anti-aircraft weapons, interceptor aircraft coupled with the high cost of state of the art aircraft and crew training led to the development of UAVs. Operation of UAV proved to be easy and adaptable for a variety of tasks. Recent advancement in technology made it possible to use low cost fixed wing UAVs for many applications like surveillance and reconnaissance for law enforcement and homeland security, scientific data gathering, forest fire monitoring, geological survey etc. As such, a lot of researches on the performance of UAVs are presently on going in many laboratories of the world but not that much as yet carried out in Bangladesh.

UAVs mostly fly under low speed conditions. The aerodynamic characteristics of the UAVs have many similarities than that of the monoplane configuration. Research on UAV configurations has been carried out mostly in the developed countries but sufficient research data on enhancement of performance is not readily available to extend further research in this area. Due to the UAV's potential for carrying out so many tasks without direct risk to the crew or humans, they are ideal for testing new concepts which have been put forward as means to further increase the vehicle's capability and performance.

The present work will contain the design and fabrication of two different UAV models – one is having aerofoil shaped fuselage and another one is conventional cylindrical shaped fuselage. The volume of both the models has been kept same. The air flow over the aerofoils is incompressible and subsonic. NACA 4416 aerofoil profile and CFD software have been used extensively for those design. 2D NACA 4416 profile has also been designed by CFD software and investigated to compare the result with different configurations. This thesis briefly explains the detail design procedure of both the models. The fabricated models has been tested in AF 100 wind tunnel. This thesis investigates the aerodynamic characteristics of both the models at two different velocities (20 m/s and 40 m/s respectively) and at different

angle of attack from -3° to 18°. The stalling angle for both the designs is found at about 15° theoretically and 14° experimentally. The lift and drag forces obtained from computational result is found more than that of the experimental result. UAV requires higher lifting force with a smaller size. The fuselage of UAV might be a good source of lifting force. As such, the performance of development of all lifting vehicle technology like aerofoil shaped fuselage has been investigated thoroughly during carry out research on small sized UAV. This thesis will also analyze the flow pattern for both the models.

Static pressure distribution on upper and lower surfaces of the wings for both the design has been investigated and analyzed. The difference in suction and positive pressure of aerofoil shaped fuselage is found more in comparison with the cylindrical shaped fuselage model. The difference in pressure has been increased for aerofoil shaped fuselage at 40 m/s than that has been obtained at 20 m/s. Out of four parameters (25%, 50%, 75% and 90% from the root of the wing), the maximum difference in suction and positive pressure is found at 25% from the root of the wing for both the designs. The difference in suction and positive pressure has been reduced from root towards tip of each wing. The maximum difference in suction and positive pressure is found at 25% from the root of the wing of *"Aerofoil shaped fuselage at 40 m/s"* than other three configurations. The difference in suction and positive pressure is found maximum within 12 to 15% of chord length for all type of configurations.

The *'aerofoil shaped fuselage configuration'* at both 20 and 40 m/s provides extra lift from it's fuselage due to it's aerofoil shape than that of the *'conventional cylindrical shaped fuselage'* configuration. But this model has produced some extra drag due to it's increased fuselage frontal area, fuselage-wing interference effect and trailing edge vortex. The effect of fuselage frontal area is found minimum due to smaller size of UAV. The fuselage-wing interference effect has been reduced here by selecting the up wing blended type model. After thorough investigation, finally it is revealed that the aerofoil shaped fuselage would be a good option for designing the future UAV.

CONTENTS

LIST OF FIGURES

LIST OF TABLES

NOMENCLATURE

CAD	Computer Aided Design
CFD	Computational Fluid Dynamics
NACA	National Advisory Committee for Aeronautics
UAV	Unmanned Air Vehicle
VDAS	Versatile Data Acquisition System
C_D	Coefficient of drag
C_L	Coefficient of lift
C_{Dmax}	Maximum drag coefficient
C_{Lmax}	Maximum lift coefficient
D or D_1 or D_f	Drag force
L or L_1 or L_f	Lift force
Re	Reynold's Number
S	Wing area
V	Velocity of air
b	Wing span
c	Wing chord or Chord Length
$\overline{c}$	Mean geometric chord
d	Maximum camber
g	Gravitational acceleration
t	Maximum aerofoil thickness
xx	Chord Line
yy	Mean Camber Line
^{o}	Degree
α	Angle of attack
ρ or ρ_a	Density of air
μ_a	Absolute viscosity of air
γ_a	Kinematic viscosity of air
L/D	Lift-to-drag ratio
W/S	Wing loading
T/W	Thrust-to-weight ratio

INTRODUCTION

1.1 Preamble

An air vehicle having no onboard pilot and capable of pre-programmed operation as well as reception of intermittent commands either independently or from a human operator at a distance from the ground is called Unmanned Air Vehicle (UAV). The UAVs fly under autonomous control of both an Intelligent Controller (IC) running on an onboard computer and an autopilot [Thomas and James, 2003]. The IC provides the mission control while the autopilot controls the vehicle navigation and flight control [Bruce, 2005]. The UAVs may operate independently or in cooperation with one another to carry out a specified mission [Thomas et al., 2009]. UAVs have been used to perform “dull, dirty and dangerous” missions successfully [Jodi et al., 2007].

The piloted aircraft were predominantly used for surveillance and reconnaissance missions but the vast technological improvements in anti aircraft weapons, interceptor aircraft coupled with the high cost of state of the art aircraft and crew training led to the development of UAVs. Operation of UAV proved to be easy and adaptable for a variety of tasks over a hostile territory [Schouwenaars et al., 2006]. Military UAVs such as Predator and Global Hawk etc demonstrated reconnaissance and surveillance capabilities in Iraq, Bosnia, Kosovo and Afghanistan war. UAVs can be used effectively in nuclear contaminated environment. Recent advancement in communications, solid-state devices and battery technology have made small, low cost fixed wing UAVs which can provide important information for low-altitude and high resolution applications [Theuniseen and Goossens, 2005 and Timothy et al., 2004]. UAVs can be used scientific data gathering, surveillance for law enforcement and homeland security, precision agriculture, forest fire monitoring, geological survey and many more scientific and commercial applications [Beard et al., 2005]. As such, a lot of researches on the performance of UAVs are presently on going in many laboratories of the world but not that much as yet carried out in Bangladesh.

UAVs mostly fly under low speed conditions. The aerodynamic characteristics of the UAVs have many similarities than that of the monoplane configuration. Research on UAV configurations has been carried out mostly in developed countries but sufficient research data on enhancement of performance is not readily available to extend further research in this area. More so, work with the Computational Fluid Dynamics (CFD) analysis is not available that much till today. In the recent years, the use of small UAVs for aerial surveillance in various civil applications has been increased manifold due to greater deploy ability of UAV in comparison with the conventional manned aircraft [Shlomo et al., 2004]. Due to the UAV's potential for carrying out so many tasks without direct risk to the crew or humans in general as well as smaller in size, they are ideal for testing new concepts which have been put forward as means to further increase the vehicle's capability [Secanell et al., 2005]. The basic aim for design of an aircraft is to increase it's lift along with reduction of drag. The aerofoil section of wings used in conventional airplane basically produced the lift but it's fuselage has little or no contribution in it [Greg and Michael, 2009]. The shape of an aircraft could not be changed to aerofoil shaped due to requirement of space for man, materials and equipments but such research could easily be carried out for an UAV with incorporation of aerofoil shaped fuselage as UAV requires higher lifting force and does not require much space [Rolald, 1998].

With this view, the concept of development of all lifting vehicle technology might bring good result for research on UAV. In conventional design, the fuselages are generally cylindrical and the wings are aerofoil shaped. It is assumed that the fuselage of an UAV might be a good source of lifting force [Korbacher, 1974]. Although the cylindrical shaped fuselage has less drag but it produces almost no lift. On the other hand, if an aerofoil shaped fuselage is incorporated instead of cylindrical shaped fuselage in an UAV, then it will produce some extra lift. Ultimately, it might increase the overall performance of an UAV. As such, the performance of development of all lifting vehicle technology for an UAV by incorporation of aerofoil shaped fuselage has been investigated thoroughly during carry out said research.

1.2 Background of the Work on Aerofoil Shaped Fuselage

A famous aircraft designer Mr Vincent Justus Burnelli [Wood, 2003] developed the concept of all body lifting aircraft in early 20th century, where he used fuselages of aerofoil cross-section. But such fuselages should have sufficient thickness, so that man could ride inside it. At that time, the scientists raised a number of technical concerns due to large shaped fuselage and it's effect on aerodynamics [Lissaman, 1983]. As such, said research was not carried out further for a manned aircraft due to negative aerodynamic drag effects contributed to the lifting body fuselage for it's increased fuselage frontal area and for the fuselage wing interference effect. During that time, the scientists manufacture the models of aerodynamic objects and go for wind tunnel testing or go for direct flying. Software based modeling of objects was not possible at that time. Now-a-days, it is possible to carry out such aerodynamic research by using CFD software which might lead to have new/modified concepts on the aeronautical field.

Development of UAV has been employed in early eighties by the developed countries. Operation of UAV proved to be easy and adaptable for a variety of tasks. However, the fuselage of the existing UAV are still found mostly cylindrical shaped and it's wings are of aerofoil shaped [Wang, 1991]. The wings of a conventional UAV are producing the lift and it's fuselage has very little or no contribution on producing lift. But in order to maximize the efficiency of an UAV, it is assumed that the basic design of an UAV could be changed and it should be such that all components of an UAV should contribute to the total lift. In such case, the aerofoil shaped fuselage might be a good option for carrying out research in terms of producing some extra lift from it's fuselage along with the wing.

UAVs use different sophisticated sensors for versatile requirements which are smaller in size. Sufficient thickness of aerofoil shaped fuselage like a manned aircraft may not be required for an UAV as it is smaller in size and it would not be used for human carrier. As such, UAV requires higher lifting force with a smaller size. Though aerofoil shaped fuselage would produce some extra drag than that of the conventional shaped fuselage but in comparison of producing total amount of

lift as well as lift drag ratio, it is assumed that such type of fuselage would be more efficient and might create a good research field in future. More so, this concept includes not only new configurations and systems but also the concept of all body lifting structure might show the ways of changing the future UAV shape/design as well as future aircraft. As UAV's are used for reconnaissance or similar purpose and they usually operate between 15 m/s to 50 m/s, hence the present investigation and analysis has been carried out within this speed range ie at 20 m/s and 40 m/s respectively.

1.3 Objectives

The specific aim of this study is to design two UAV models having conventional cylindrical as well as aerofoil shaped fuselage, fabrication of both the models and investigate the aerodynamic characteristics both numerically and experimentally. The present research work consists of the following main objectives:

(i) Design of two types of UAV by using **NACA 4416** cambered aerofoil.

(ii) Analysis of the point surface pressure distributions on the wing surfaces of UAV.

(iii) Analysis on the flow pattern and aerodynamic characteristics at different angle of attack.

(iv) Analysis on the aerodynamic characteristics of both UAVs at two different velocities (20 m/s and 40 m/s).

(v) Fabrication of both the UAV models to carry out test by using wind tunnel based on the numerical findings.

(vi) Comparison and analysis of the computational results with that of the experimental results.

LITERATURE REVIEW

2.1 Effect of Air Flow over an Aerofoil

The science which deals with the forces acting on the body in the flow of air is called aerodynamics. The study of flow of air is very important for aerospace application like aircraft or UAV. The visualization of streamlines is a useful aid in the study of aerodynamics [Anderson, 1991 and Glauert, 1926]. Let us consider a flow of air over an aerofoil. Both the air speed and direction over the aerofoil can vary from point to point. The path followed by the moving fluid element is called a streamline of the flow. It is seen that the streamlines are close together near the top and bottom of the cylinder [Clancy, 1975]. The motion of the air over the aerofoil can be easily visualized by drawing the streamlines of the flow field. An actual photograph of streamlines over an aerofoil model at 10˚ angle of attack in a low speed subsonic wind tunnel is shown in Figure 2.1.

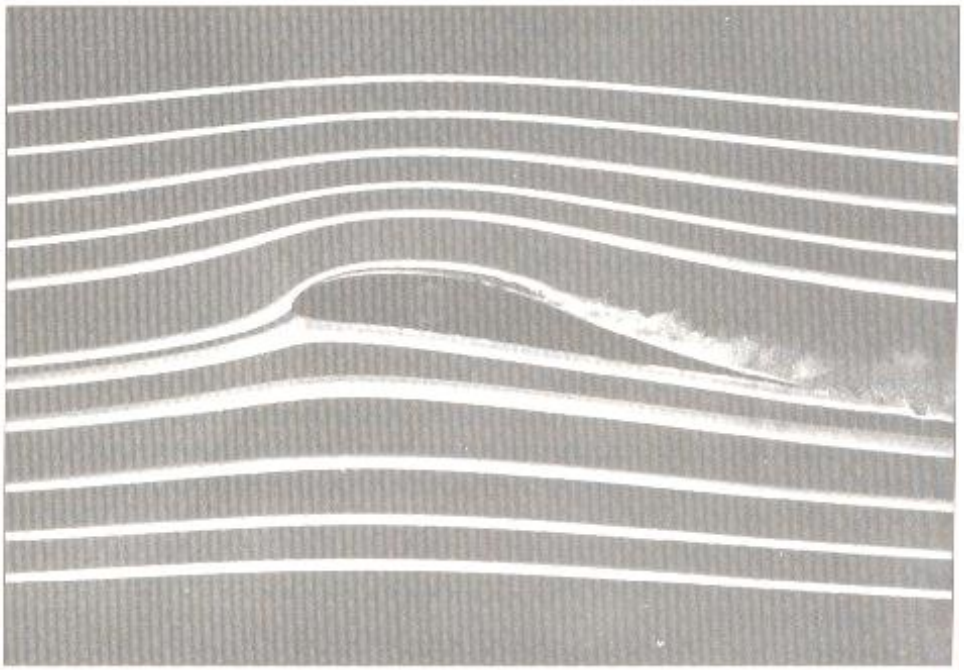

Figure 2.1: Photograph of Streamlines Over an Aerofoil Model in a Low Speed Subsonic Wind Tunnel

2.2 Familiarity with Aerofoil Section

The cross-sectional shape obtained by the intersection of an aircraft wing with the perpendicular plane is called an aerofoil [Anderson, 1991 and Glauert, 1926]. The major design feature of an aerofoil is the mean camber line, which is the locus of points halfway between the upper and lower surfaces. The most forward and rearward points of the mean camber line are the leading and trailing edges respectively. The straight line connecting the leading and trailing edges is the chord line of the aerofoil and the distance from the leading to the trailing edge measured along the chord line is called the chord of the aerofoil. The camber is the maximum distance between the mean camber line and chord line, measured perpendicular to the chord line [Clancy, 1975]. Here the research has been carried out by using NACA 4416 aerofoil profile. The angle between the relative wind and the chord line is the angle of attack of the airfoil. A typical aerofoil nomenclature is shown in Figure 2.2.

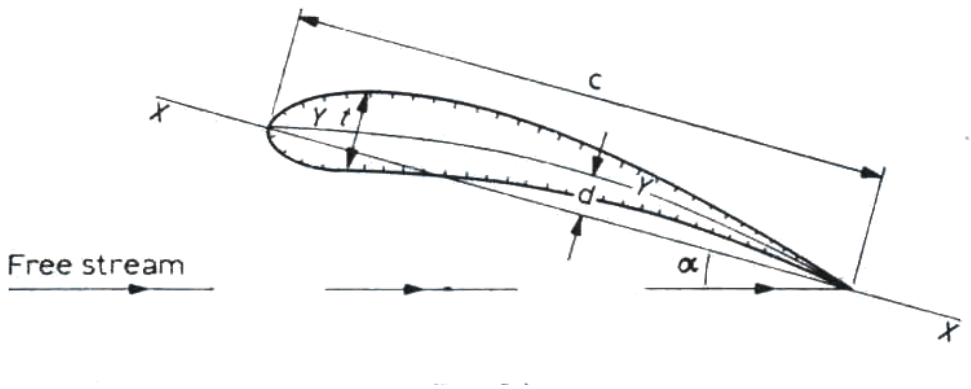

Figure 2.2: Typical Aerofoil Nomenclature

In the Figure 2.2, 'XX' is the Chord Line, 'c' is the Chord Length, 't' is the maximum thickness, 'YY' is the Mean Camber Line, 'α' is the Angle of Attack, 'd' is the maximum camber. There are various types of aerofoil like 4-digit, 5-digit, modified 4-/5-digit, 6-digit etc aerofoils. There are many similarities between those aerofoils but mainly two primary variables affect the shapes of an aerofoil which are the slope of the airfoil mean camber line and the thickness distribution above and below this line. These variations lead a series of equations to generate an entire

family of related NACA airfoil shapes. 4-digit NACA 4416 aerofoil profile has been chosen in this research work. The explanation of the 4-digit NACA 4416 aerofoil is as follows:

a. The first digit specifies the maximum camber in percentage of the chord [Abbott et al., 1945 and 1959],

b. The second digit indicates the position of the maximum camber in tenths of chord [Abbott et al., 1945 and 1959] and

c. The last two digits provide the maximum thickness of the airfoil in percentage of chord [Abbott et al., 1945 and 1959].

The thickness distribution above (+) and below (-) the mean line can be calculated by the following equation for each of the x-coordinates of 4-digit NACA aerofoil [Abbott and Doenhoff, 1959]:

$$\pm Y_t = \frac{t}{0.2}\left(0.2969\sqrt{x} - 0.1260x - 0.3516x^2 + 0.2843x^3 - 0.1015x^4\right)$$

2.3 Aerodynamic Forces Experienced by an UAV

An aircraft or UAV placed in the uniform flow of an air stream will experience aerodynamic forces which are created by virtue of the relative motion. The resultant of this force can be resolved into two force components – one parallel and another one perpendicular to the main flow direction. The component acting parallel to the flow is known as the drag force and the component perpendicular to the flow direction is the lift force. Pressure is one of the most fundamental and important variables in aerodynamics. The lift force is caused due to the pressure difference that exists between the lower and upper surfaces [Anderson, 1999 and Clancy, 1975]. Figure 2.3 shows the lift and drag forces produced by an UAV when it’s wing is placed in moving air.

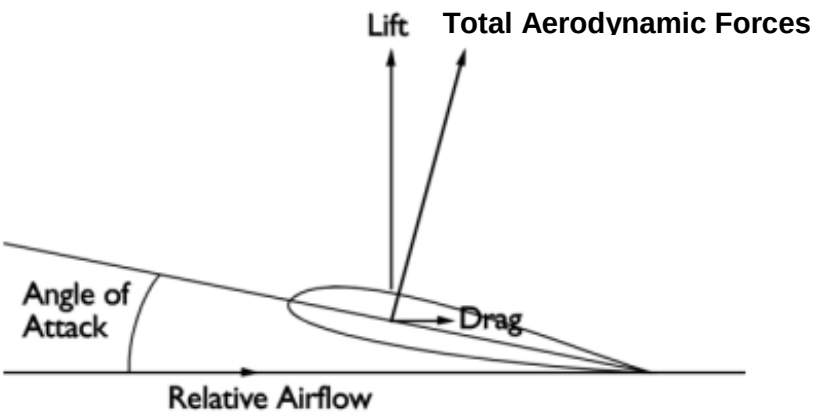

Figure 2.3: Aerodynamic Forces on a Typical UAV

Lift and drag force data are usually expressed in dimensionless terms by using **lift coefficient** and **drag coefficient**. The lift coefficient is defined as:

$$C_L = \frac{2L}{\rho V^2 A}$$

where L is the lift force, ρ is the fluid density, V is the free stream velocity far upstream of the wing and A is the area of the wing when seen from a top view perpendicular to the chord length C. The drag coefficient is defined as:

$$C_D = \frac{2D}{\rho V^2 A}$$

where D is the drag force.

2.4 Effect of Lift and Drag Force Coefficient with Change of Angle of Attack

The lift and drag force coefficient experienced by an aircraft will vary with change of angle of attack. For a cambered aerofoil, the zero-lift angle is negative. For example, an aerofoil with 2% camber will have zero lift angle -2˚ [Anderson 1999 and Glauert 1926]. As the angle of attack increases from the zero-lift value, the curve is linear over a considerable range. The slope of the curve begins to fall off when the effects of separation begin to be felt. As such, the lift coefficient reaches to a maximum value and then begins to decrease. The angle at which it does so is called the stalling angle and the value of the lift coefficient is denoted as C_{Lmax}. The stalling angle for a typical aircraft would be about 14˚ - 16° for a conventional low speed aerofoil [Clancy, 1975]. Variation of C_L with angle of attack is shown in Figure 2.4.

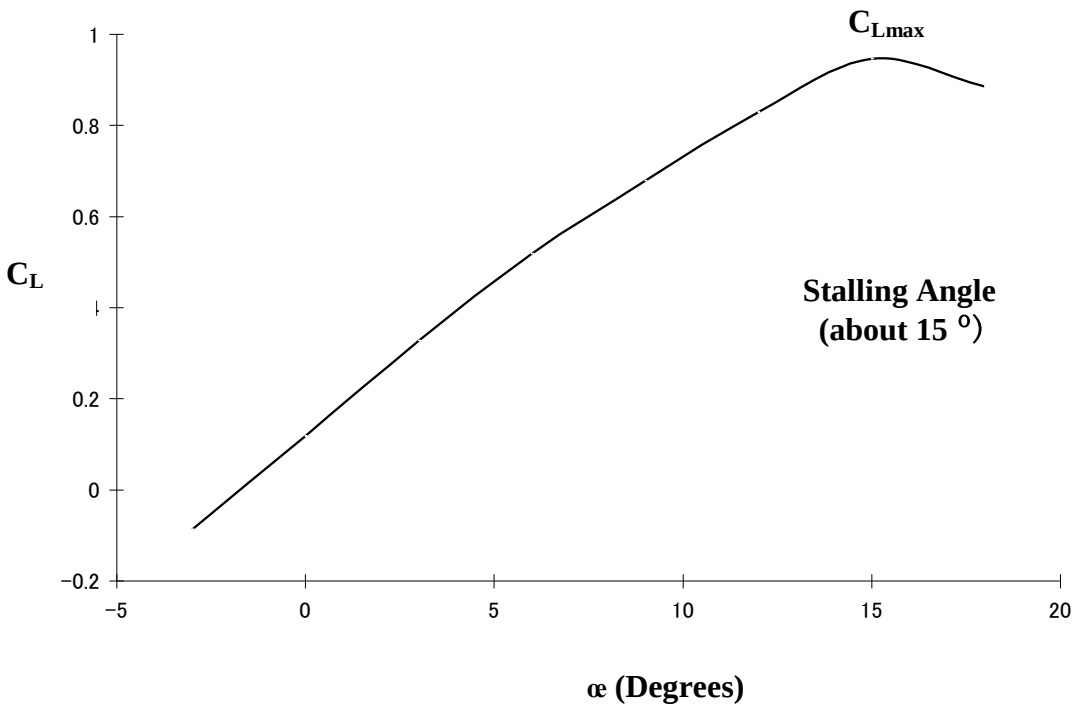

Figure 2.4: Variation of C_L with Angle of Attack, œ (in degree) for a Typical Cambered Aerofoil

There are mainly two types of drag forces experienced by a low speed UAV, which are parasite drag (zero lift drag) and induced drag (lift dependent drag). Parasite drag is the sum of form drag (depends on shape) and skin friction drag (depends on surface) [Kermode, 1989 and Ilan, 2001]. For a well-designed aerofoil at small angle of attack, the wake is thin and the form drag is very much smaller than the skin friction drag. As the angle of attack approaches to the stalling value, the separation point moves forward, causing the wake to thicken [Munk, 1924 and Clancy, 1975]. When a wing is producing lift - the pressure on the upper surface is generally found less than that on the lower surface. The upper and lower surface pressures must tend to the same value at the tips. It is also seen that the pressure is increasing from root to tip on upper surface and decreasing from root to tip on lower surface. For this reason, there is a change in magnitude and direction of pressure from root to tip and the wing tips sustain a downwash. This downwash causes the induced drag. The downwash varies in the stream wise direction [Clancy, 1975]. The shape of the drag force coefficient vs angle of attack is parabolic [Abbott and Doenhoff, 1959]. It is desirable for a wing to have the smallest possible drag. Variation of C_D with angle of attack is shown in Figure 2.5.

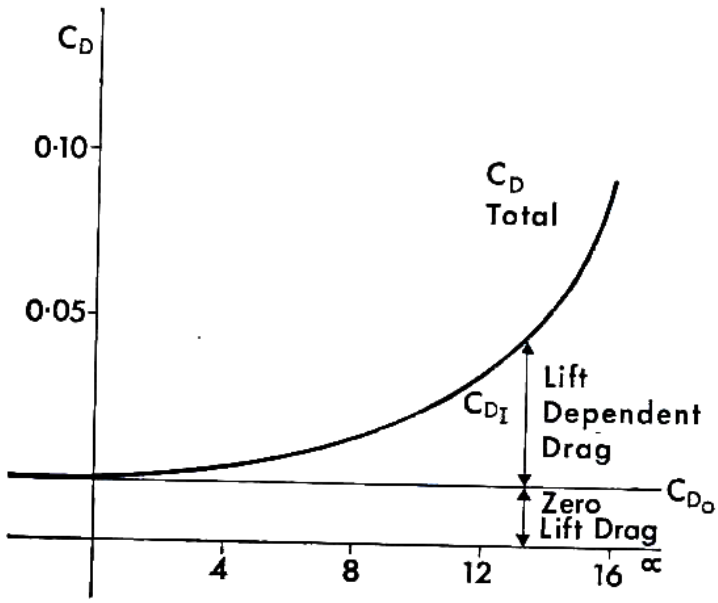

Figure 2.5: Variation of C_D with Angle of Attack for a Typical Cambered Aerofoil

2.5 Variation of Surface Static Pressure with Change of Chord Length

When a stream of air flows through an aerofoil, local changes in velocity round the aerofoil occur and changes in point surface (local) static pressure also occurs. This distribution of the pressure determines the amount of lift and drag force experienced by an aerofoil [Jacobs, 1930; Shermam, 1939 and Loftin, 1947]. To determine the lift force, it is useful to plot the pressure distributions (i.e. pressure coefficient) round the aerofoil against the chord length graphically. A positive pressure implies a pressure greater than the free stream value and a negative pressure implies a pressure less than the free stream value and will be referred as 'suction' [Allen, 1938, 1939, 1943; Munk, 1945 and Clancy, 1975]. The distribution of pressure round a two-dimensional aerofoil also varies with the change of angle of attack. A typical distribution of pressure round an aerofoil at a particular angle of attack is shown in Figure 2.6.

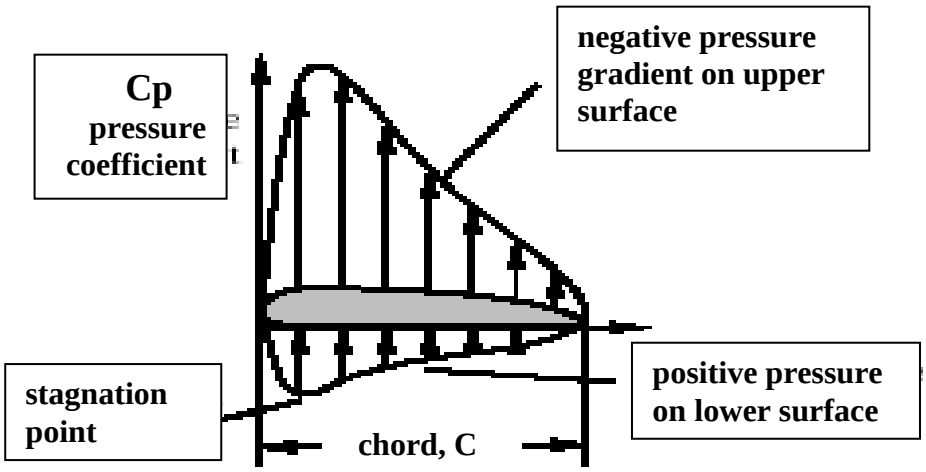

Figure 2.6: Variation of Static Pressure with Chord Length of a Typical Aerofoil at a Particular Angle of Attack

From the Figure 2.4 (Lift Coefficient vs Angle of Attack), it is seen that lift increases with angle of attack up to a certain angle usually about 14˚ to 16˚ for a conventional low speed aerofoil. A large value of lift is mainly contributed by the upper surface suction pressure than the lower surface pressure from a typical aerofoil. As the angle of attack increases, the height of the upper surface suction

peak increases and it moves further forward. The sudden flattening of the upper surface pressure distribution at high angle of attack is due to separation. The effect of this separation will cause a loss of lift at high angle of attack and further increase of angle of attack will reduce the lift still further. This phenomenon is called stall [Allen, 1943 and Clancy, 1975].

2.6 Wing Configurations of an UAV

Wings are made in different shapes and sizes depending on the desired flight characteristics, balance or stability during flight. The wing tip may be square, rounded or even pointed. Features of the wing will cause other variations in its design. Both the leading edge and trailing edge of the wing may be straight or curved depending on the design [U.S. Department of Transportation, Federal Aviation Administration, 1998]. Six common wing forms are low wing, high wing, gull wing, dihedral wing, mid wing and inverted gull wing. Common wing forms are shown in Figure 2.7. For research purpose, high wing blended with fuselage has been selected here.

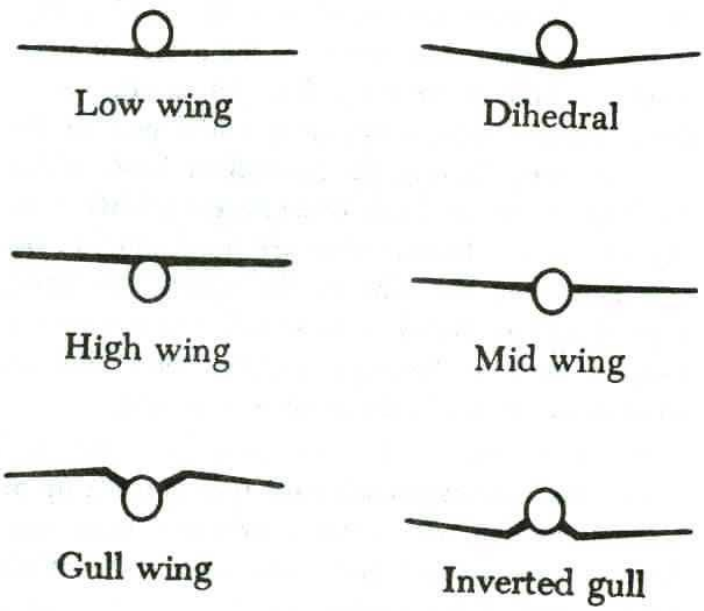

Figure 2.7: Common Wing Forms

2.7 Design of Aeronautical Equipments

Design of aeronautical equipments like aircraft or UAV is mainly associated with analytical disciplines of aerodynamics, structures, controls and propulsions. But many other key players also participate in the design process of an aeronautical item. As such, aeronautical design is not just the actual layout but also the analytical processes used to determine what should be designed and how the design should be modified to fulfill the requirements in a better way [Corke, 2005 and Daniel, 1995].

2.8 Phases of Design

Any design of aeronautical objects has mainly three phases – conceptual design, preliminary design and detail design. In the conceptual design, the requirements of design are to be determined and accordingly, the evaluation of the overall UAV configurations is to be chosen. Conceptual design may take as little a week to several years. However, one researcher should plan to study the requirements of an object and finalize the configuration layout according to a best concept within six months to finalize a conceptual design [Anderson 1999, Corke, 2005 and Daniel, 1995]. The product of the conceptual design phase is a layout (on paper or on a computer screen) of the UAV configuration. A Computer Aided Design (CAD) software may be used for the conceptual design. The conceptual design phase determines such fundamental aspects like the shape of the wings, location of wings relative to fuselage, shape and location of horizontal and vertical stabilizer etc [Anderson 1999]. Seven crack points of a conceptual design are shown in Figure 2.8.

Preliminary design will start when the requirements of an object have been finalized. During preliminary design, maturation of the selected design takes place. Structures and control systems of an UAV are required to design and analysis is to be carried out on those parts at this stage. More so, substantial wind tunnel testing, major computational fluid dynamics (CFD) calculations of the complete flow field over the

UAV are to be initiated in areas of aerodynamics, structures and controls in this phase. A mockup may also be constructed by using suitable software at this phase. The wind tunnel tests and / or CFD calculation will uncover some undesirable aerodynamic interference or some unexpected stability problems. The ultimate objective of the preliminary design is to ready for detail design stage [Anderson 1999 and Daniel, 1995].

During detail design phase, the fabrication of the actual pieces is to be decided. This is the large and most expensive phase of design. This phase is also called the production design. As such, the detail design ends with the fabrication of the first UAV [Anderson, 1999 and Daniel, 1995]. The typical design process flow chart of an aeronautical object is shown in Figure 2.9.

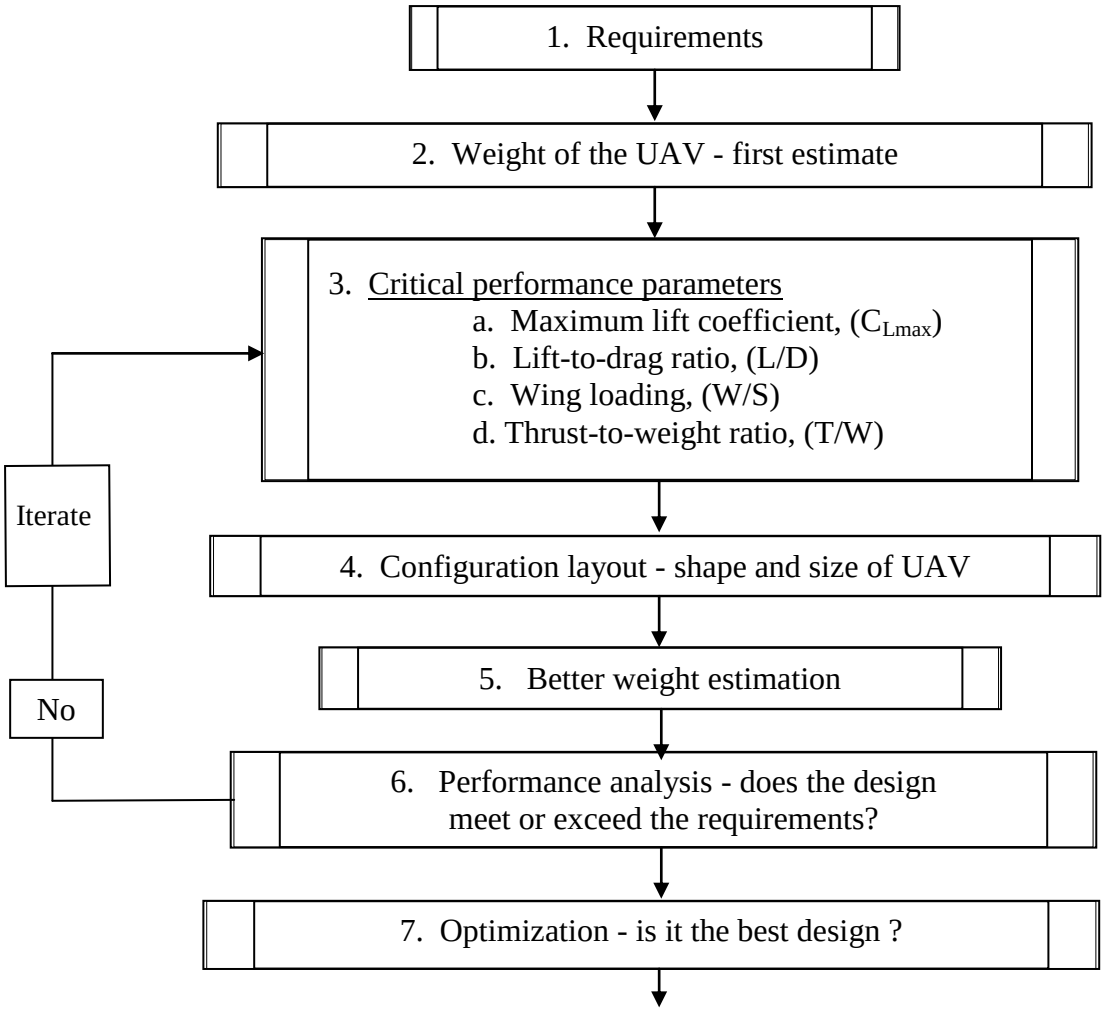

Figure 2.8: Seven Crack Points of Conceptual Design [Anderson, 1999].

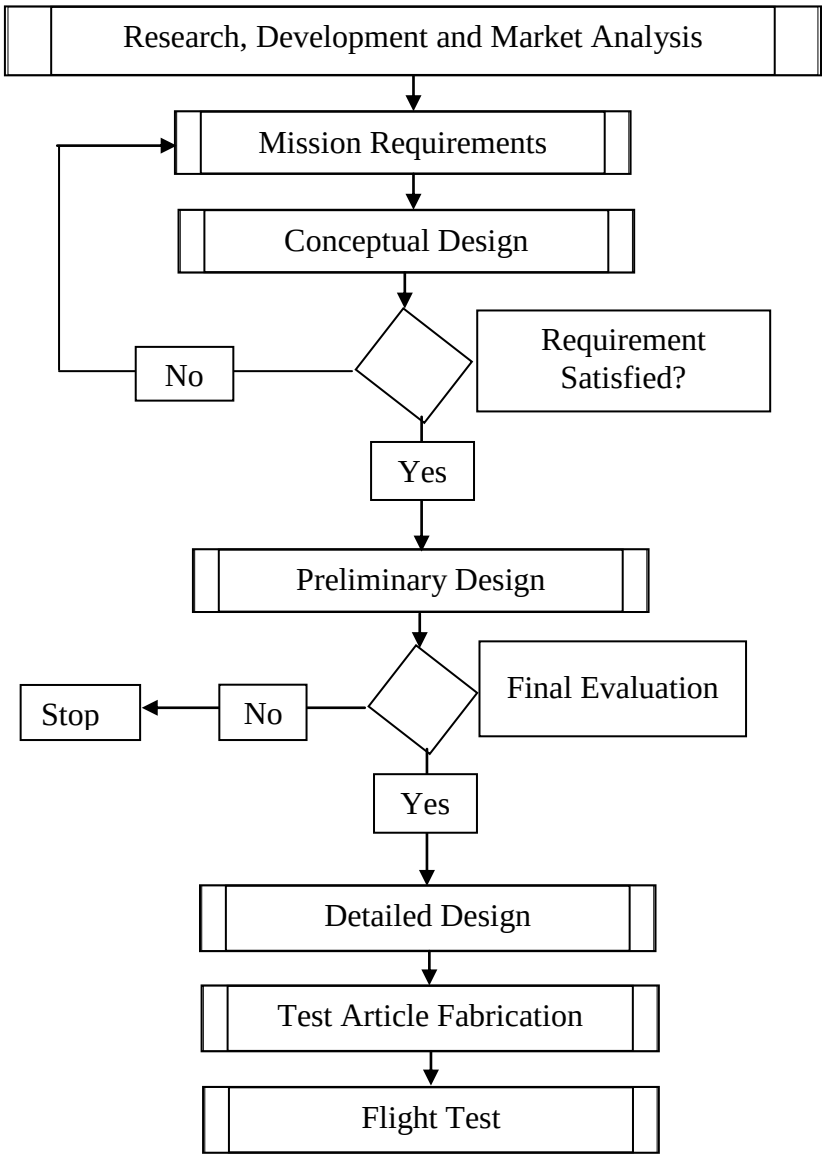

Figure 2.9: Typical Design Process Flow Chart [Corke, 2005].

2.9 Phases of Computational Design by CFD

Computational Fluid Dynamics (CFD) deals with the solution of fluid-dynamic equations on computers and the related use of computers in fluid-dynamics research [Anderson, 1995 and Jay, 1989]. There are three steps for designing an object successfully by using CFD software which are Pre-processing, Processing and Post-

processing phases [Labrujere and Slooff, 1993]. The pre-processing phase consists of creation of geometry, meshing geometry, specify boundary type, set up the problem and solve. After analyzing the result, the designed geometry may require further re-fining or re-meshing. As such, many trial and error involve during pre-processing phase before finalize a design.

Processing phase starts with import and scale the mesh file designed at GAMBIT. Here, physical models have been selected and checked the grid for accuracy. Afterwards, the solver formulation and equations are to be imposed about type of flow (like laminar/turbulent, heat transfer, multiple species etc) at this phase. Then operation conditions (material properties), boundary conditions followed by specification of numerical properties (under-relaxation factors etc) are to be imposed on the design. During processing phase, the variables are to be initialized by setting solver controls. Afterwards, set up the solution parameters for convergent monitors and observe. At the end, go for feedback into the solver as well as for engineering analysis and observe the result [Ramesh, 1999]. The typical solution procedure overview of CFD during processing phase is shown in Figure 2.10.

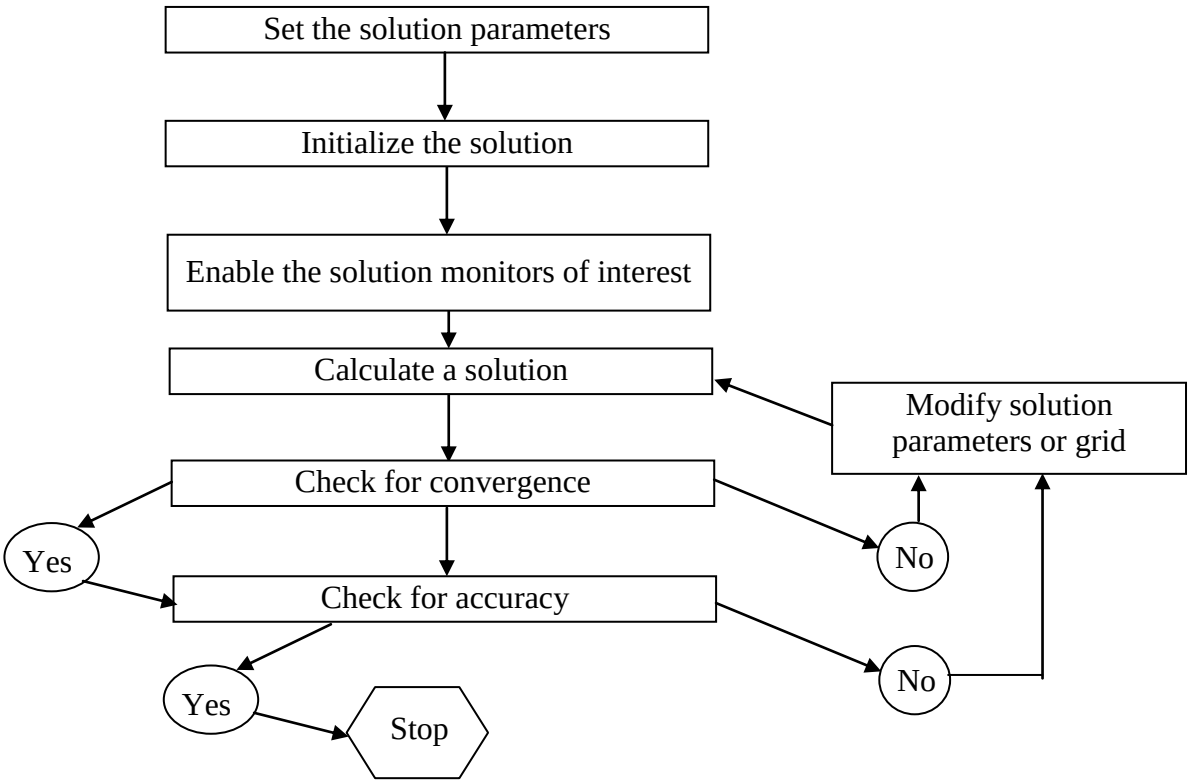

Figure 2.10: Typical Solution Procedure Overview of CFD.

Convergence result will occur when the convergence criterion for each variable has been reached. The default criterion for CFD software is that each residual will be reduced to a value of less than 10^{-3}, except the energy residual, for which the default criterion is 10^{-6} [Stanley, 1992]. Sometimes the residuals may not fall below the convergence criterion set in the case setup. However, monitoring the representative low variables through iterations may also indicate that the residuals have stagnated and do not change with further iterations. This could also be considered as convergence. Such convergent criteria is seen for lift and drag coefficients [Ramesh, 1999]. Typical Lift and Drag Coefficient plots indicating convergent criteria are shown in Figures 2.11 and 2.12 respectively.

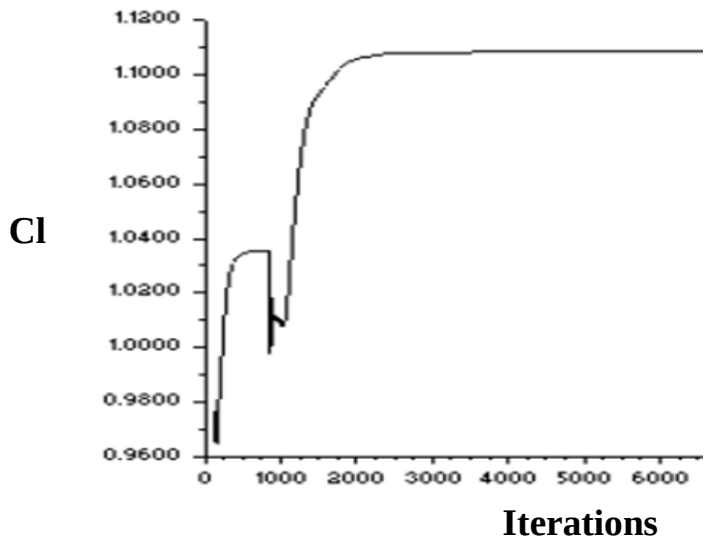

Figure 2.11: Typical Lift Coefficient Plot of CFD

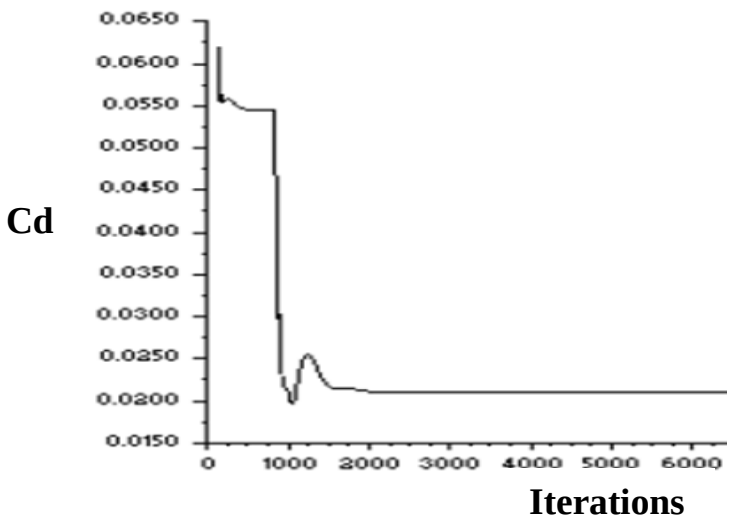

Figure 2.12: Typical Drag Coefficient Plot of CFD

At the post-processing stage, different engineering analyses have been carried out based on results, charts, graphs etc. If the numerical results are found acceptable, then those data will be used for experimental design, analysis of the objects and detail investigation about an object. Afterwards, the design, development and production of the new concept of UAV design based on aerofoil shaped fuselage are to be undertaken by an aeronautical firm / industry considering the role of the object, requirement of the object and market analysis [Chennakeshu and Ganapathi, 1993].

METHODOLOGY

3.1 Computational Design

The present work will contain the design and fabrication of two different UAV models – one is having conventional cylindrical shaped fuselage and another one is aerofoil shaped fuselage. The volume of both the models has been kept same, which is 534.102 cm^3 during computational design. The air flow over the aerofoils has been considered incompressible and subsonic. NACA 4416 aerofoil profile and CFD software have been used extensively for those designs [Labrujere and Slooff, 1993]. The free stream airflow has been kept as 20 m/s and 40 m/s respectively and the effect of temperature has been neglected. The density of air has been considered as $\rho_o = 1.225$ kg/m^3, operating pressure as 1.01 bar or 14.7 psi and absolute viscosity as $\mu = 1.789 \times 10^{-5}$ kg/m-s. The Reynold's Number has been considered as 1.37×10^5 (for 20 m/s) and 2.74×10^5 (for 40 m/s) respectively. The data have been obtained at different angles of attack from -3° to 18°. The static pressure distribution will also be determined at different percentage of chord length on the upper and lower surfaces of the both UAV configurations and the aerodynamic characteristics will be investigated. Finally, the data obtained from the computational design, has been used for fabrication of the models to test at the wind tunnel model AF 100.

3.2 Experimental Design

This thesis briefly explains the detail design procedure and fabrication of both the conventional cylindrical shaped fuselage and aerofoil shaped fuselage models based on the numerical findings – some of which were also validated with the experimental results. Four experimental set up have been fabricated by using NACA 4416 profile and utilizing the local resources. Among which, two set up of models have been fabricated to measure only the lift and drag forces and their coefficients. Another two set up of models have been used for measuring point surface pressures

of upper and lower surfaces of the models. The fabricated models have been tested in AF 100 wind tunnel. This thesis will analyze the flow pattern and investigates the aerodynamic characteristics at two different velocities (20 m/s and 40 m/s respectively) and different angle of attack. This thesis will also analysis the point surface pressure sustained by both upper and lower surfaces of the wings of both the models.

The flow of air through the aerofoils is considered to be incompressible and subsonic. The chord length of the aerofoil of the wing during experimental design to measure lift and drag coefficients has been kept 5.5 cm. Volume of both the models have been kept same, which is approximately 166.38 cm^3 during experimental design. The free stream airflow has been kept as 20 m/s and 40 m/s respectively and the effect of temperature has been neglected. The density of air has been considered as $\rho_o = 1.225$ kg/m^3, operating pressure as 1.01 bar or 14.7 psi and absolute viscosity as $\mu_a = 1.789 \times 10^{-5}$ kg/m-s. The Reynold's Number has been considered as 1.37×10^5 (for 20 m/s) and 2.74×10^5 (for 40 m/s) respectively. The data have been collected at different angles of attack from -3° to 18°. Total thirty six (36) tapping points have been made on the both surfaces of right wing of both the models to study the surface static pressure at each point. Finally, the results obtained from the experimental test for both the designs, would be investigated, analyzed and compared with the computational design.

The aerofoil shaped fuselage has produced some extra lift from the fuselages but it also generates some extra drag due to increased fuselage frontal area, fuselage-wing interference effect and trailing edge vortex. The effect of fuselage frontal area is not that much significant as the size of UAV is smaller. The fuselage-wing interference effect has been reduced by selecting the up wing type blended model. However, ways for reduction of the trailing edge vortex which leads to induced drag from the aerofoil shaped fuselage might be a good option for research in future.

Though aerofoil shaped fuselage would produce some extra drag than that of the conventional cylindrical shaped fuselage but in comparison of producing total

amount of lift from all of it's components (surfaces), such type of fuselage would be more efficient for use in future than that of the conventional cylindrical shaped fuselage. More so, the concept of all body lifting structure would also open a good research arena for designing the future UAV.

APPENDIX – 'G' TO FIGURE 6.11, 6.12, 6.13 and 6.14

on *"Surface Pressure of Conventional Cylindrical Shaped Fuselage at 20 m/s"*

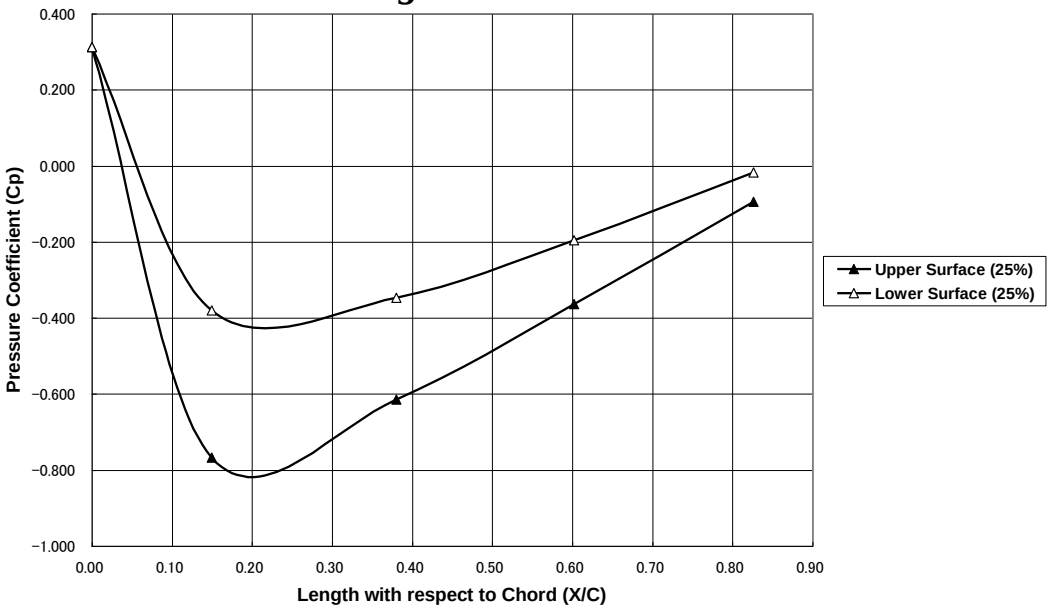

Figure 6.11a: Variation of Pressure with Chord Length for Conventional Cylindrical Shaped Fuselage UAV model at 25% from the root at 3° Angle of Attack.

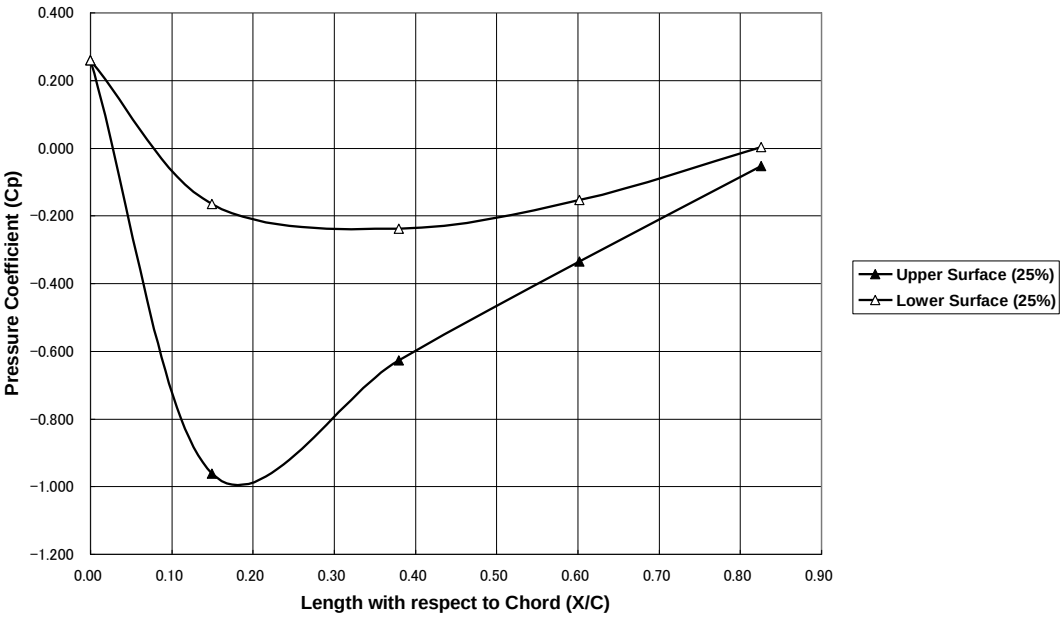

Figure 6.11b: Variation of Pressure with Chord Length for Conventional Cylindrical Shaped Fuselage UAV model at 25% from the root at 9° Angle of Attack.

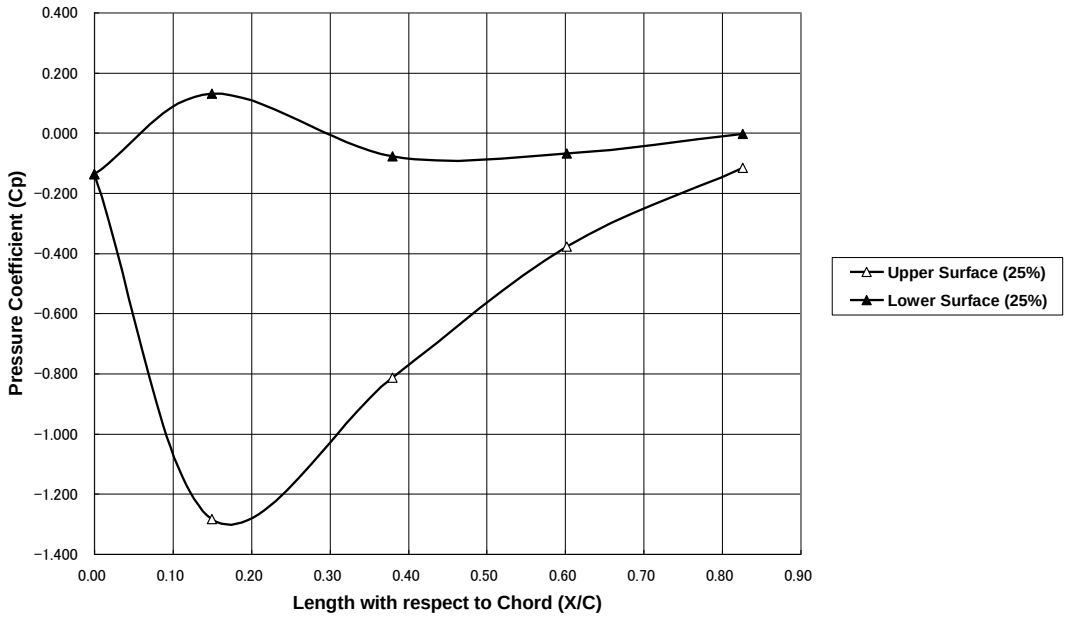

Figure 6.11c: Variation of Pressure with Chord Length for Conventional Cylindrical Shaped Fuselage UAV model at 25% from the root at 14° Angle of Attack.

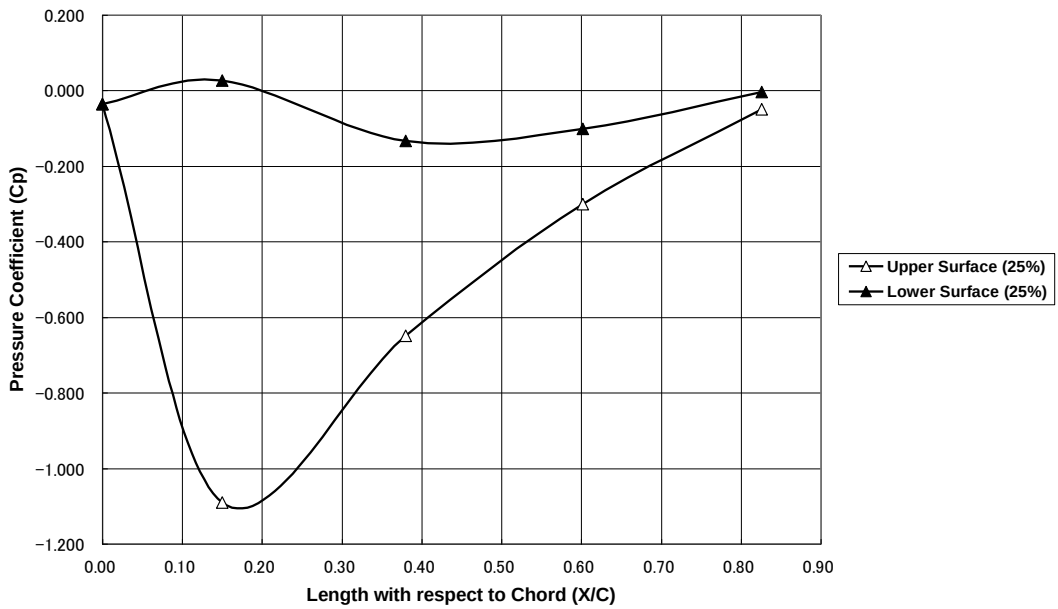

Figure 6.11d: Variation of Pressure with Chord Length for Conventional Cylindrical Shaped Fuselage UAV model at 25% from the root at 18° Angle of Attack.

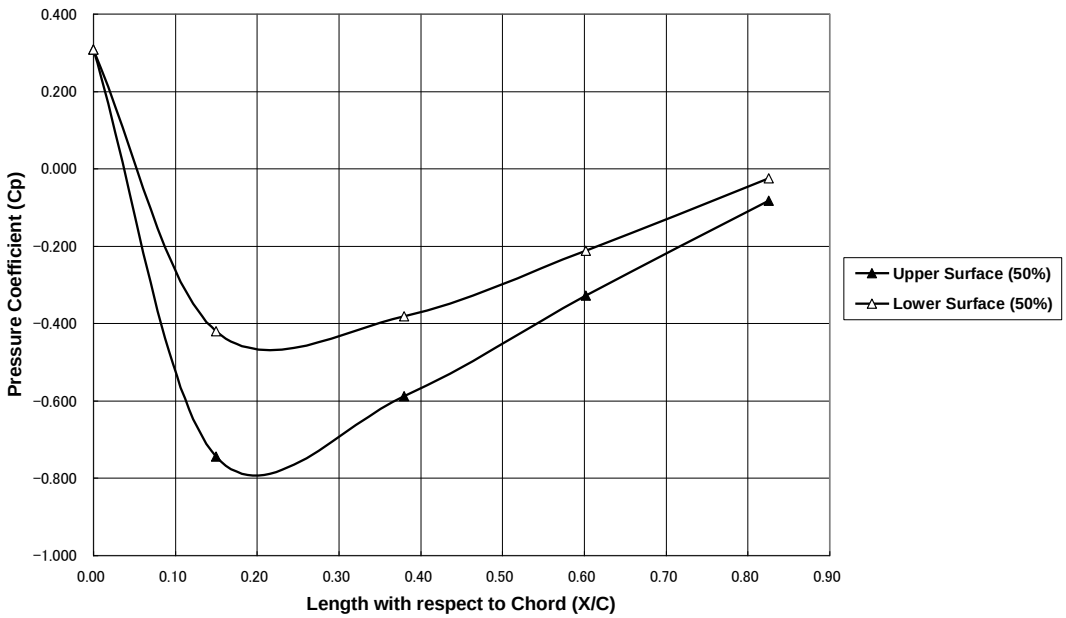

Figure 6.12a: Variation of Pressure with Chord Length for Conventional Cylindrical Shaped Fuselage UAV model at 50% from the root at 3° Angle of Attack.

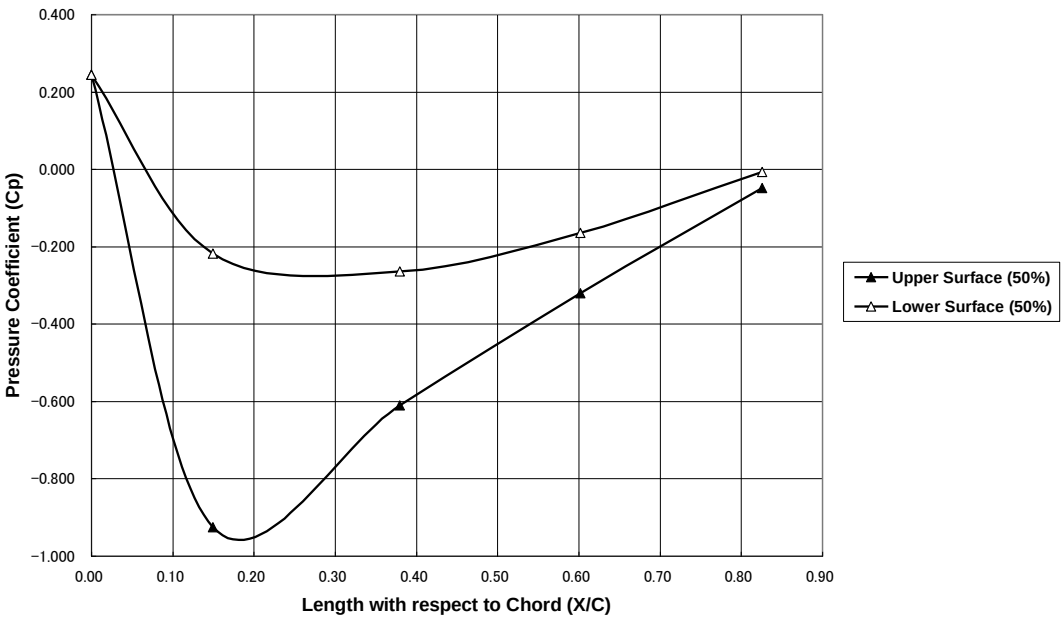

Figure 6.12b: Variation of Pressure with Chord Length for Conventional Cylindrical Shaped Fuselage UAV model at 50% from the root at 9° Angle of Attack.

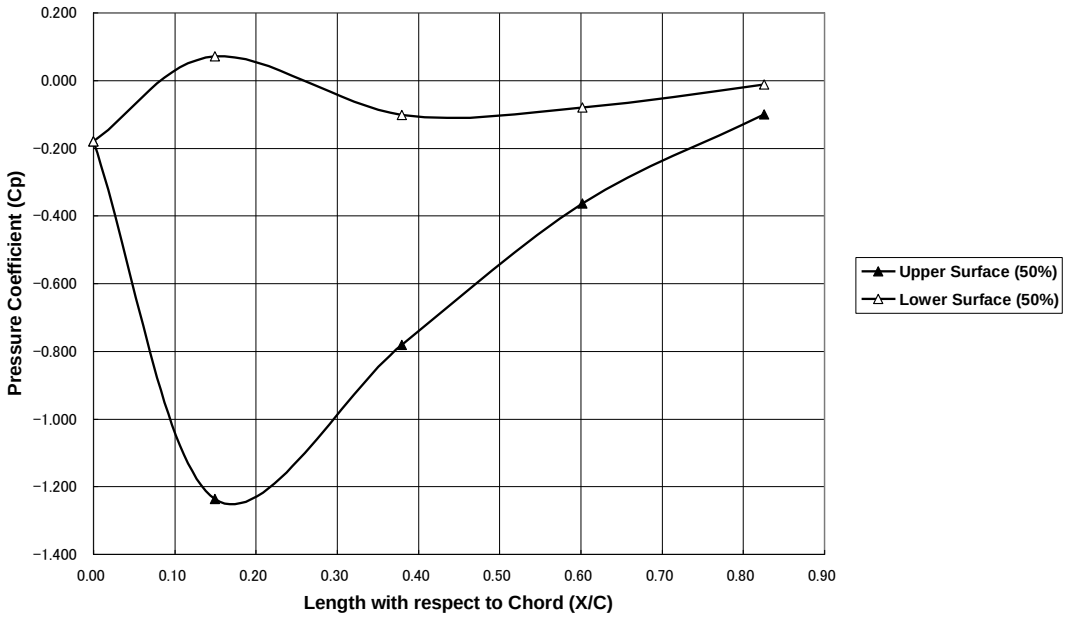

Figure 6.12c: Variation of Pressure with Chord Length for Conventional Cylindrical Shaped Fuselage UAV model at 50% from the root at 14° Angle of Attack.

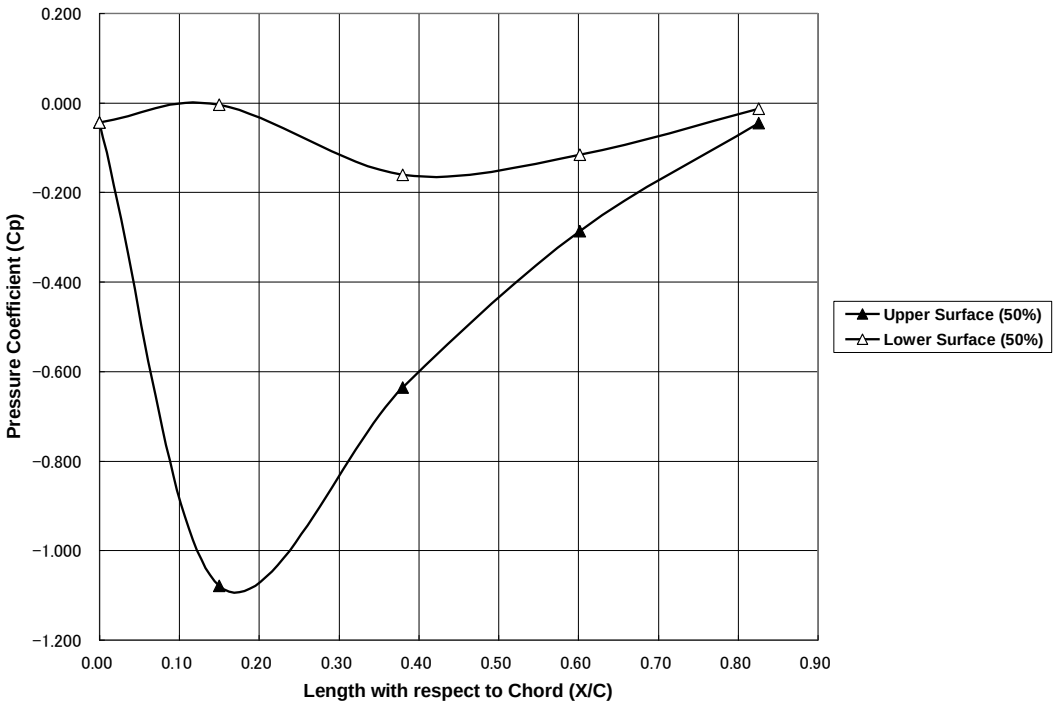

Figure 6.12d: Variation of Pressure with Chord Length for Conventional Cylindrical Shaped Fuselage UAV model at 50% from the root at 18° Angle of Attack.

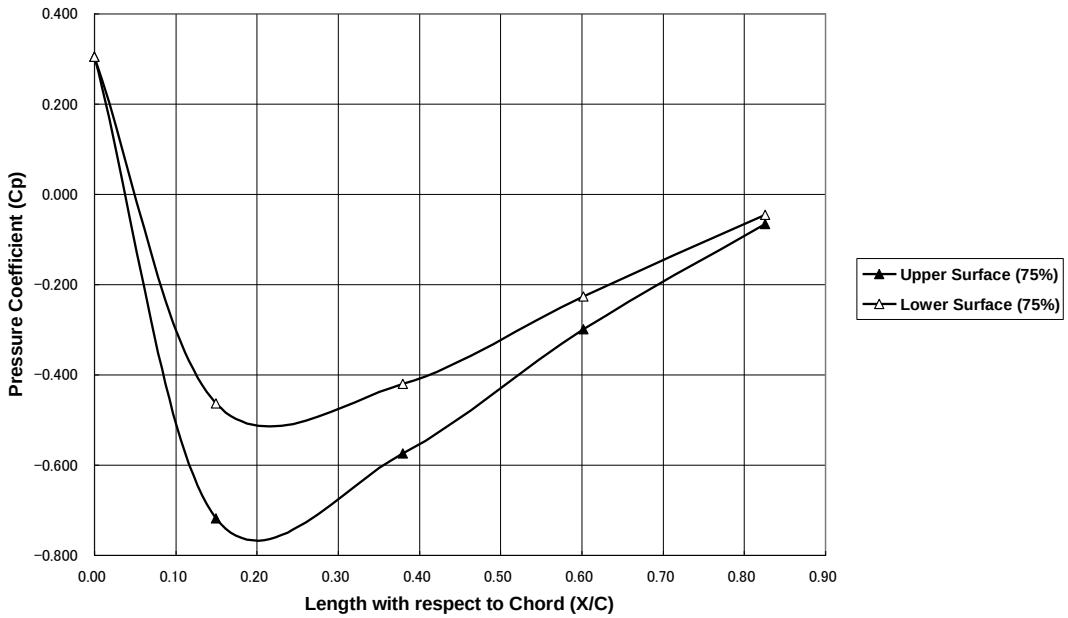

Figure 6.13a: Variation of Pressure with Chord Length for Conventional Cylindrical Shaped Fuselage UAV model at 75% from the root at 3° Angle of Attack.

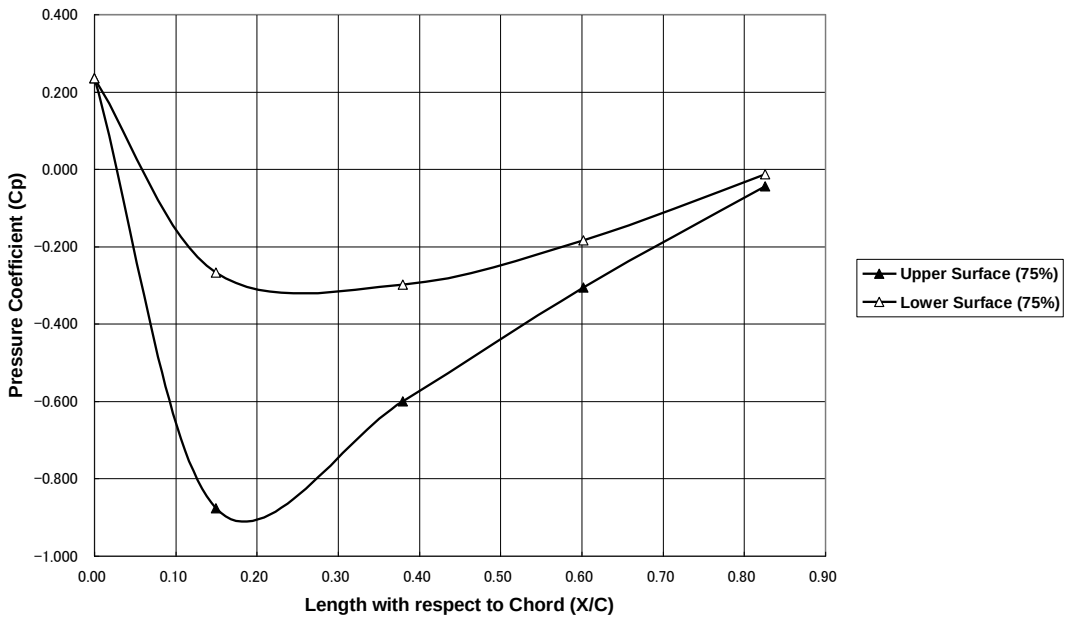

Figure 6.13b: Variation of Pressure with Chord Length for Conventional Cylindrical Shaped Fuselage UAV model at 75% from the root at 9° Angle of Attack.

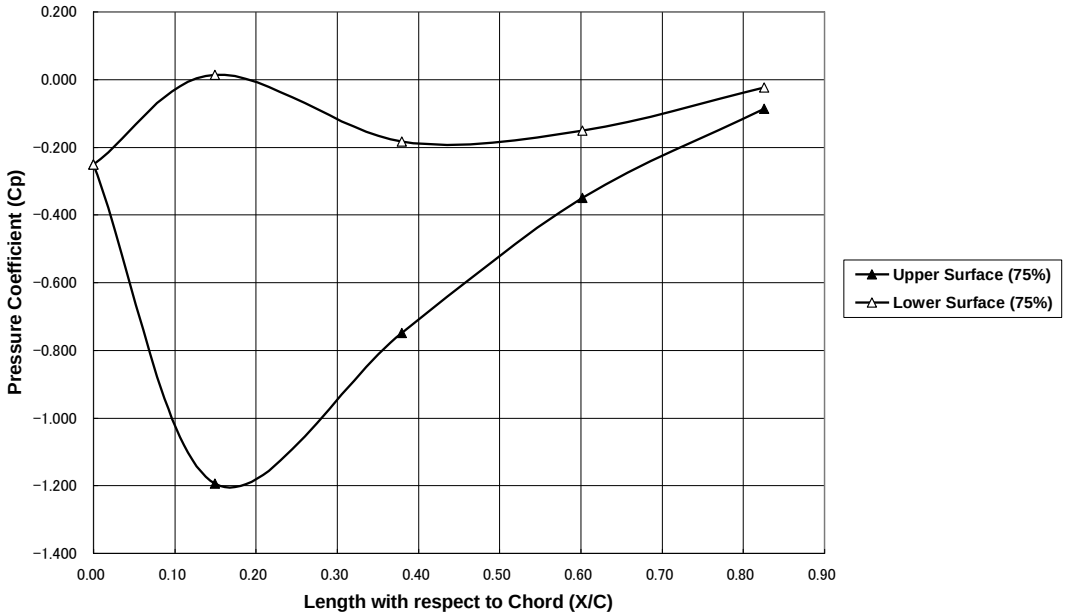

Figure 6.13c: Variation of Pressure with Chord Length for Conventional Cylindrical Shaped Fuselage UAV model at 75% from the root at 14° Angle of Attack.

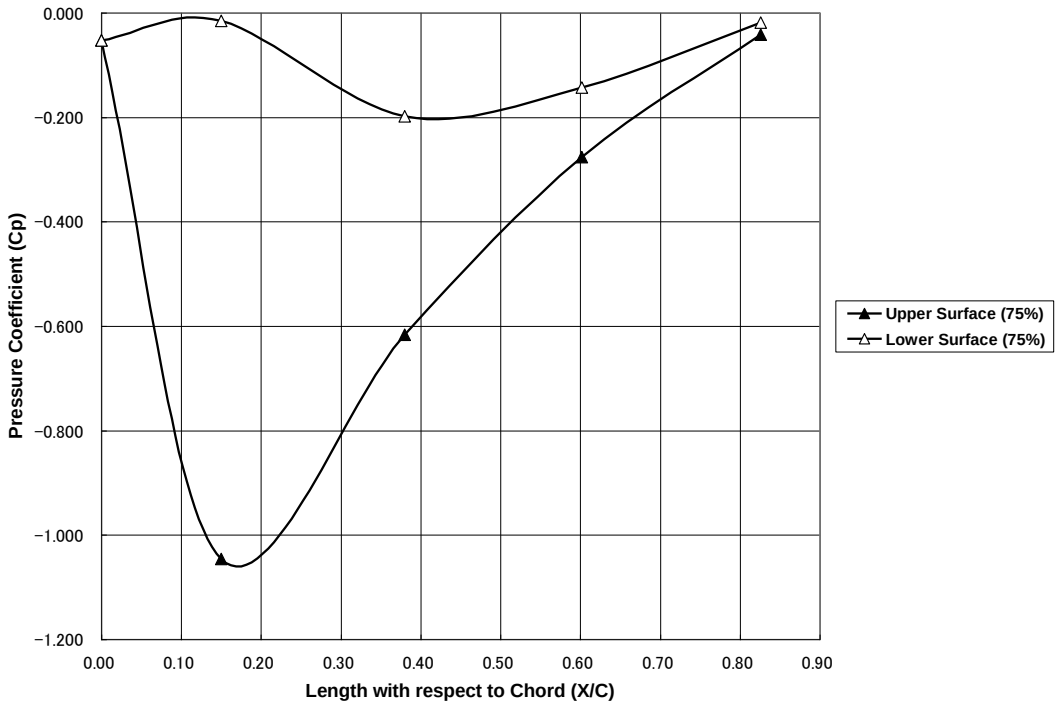

Figure 6.13d: Variation of Pressure with Chord Length for Conventional Cylindrical Shaped Fuselage UAV model at 75% from the root at 18° Angle of Attack.

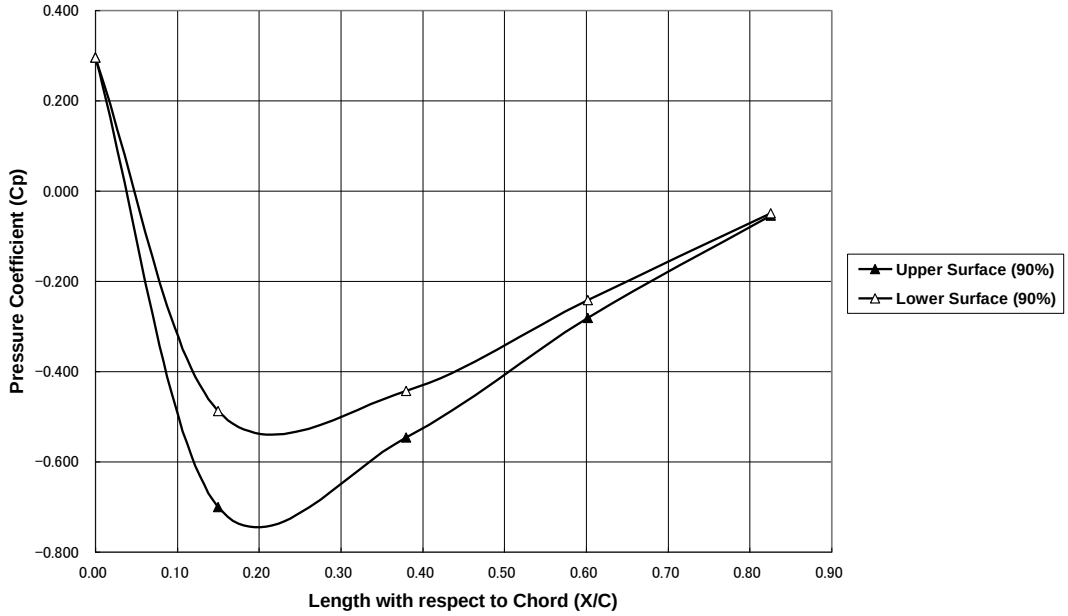

Figure 6.14a: Variation of Pressure with Chord Length for Conventional Cylindrical Shaped Fuselage UAV model at 90% from the root at 3° Angle of Attack.

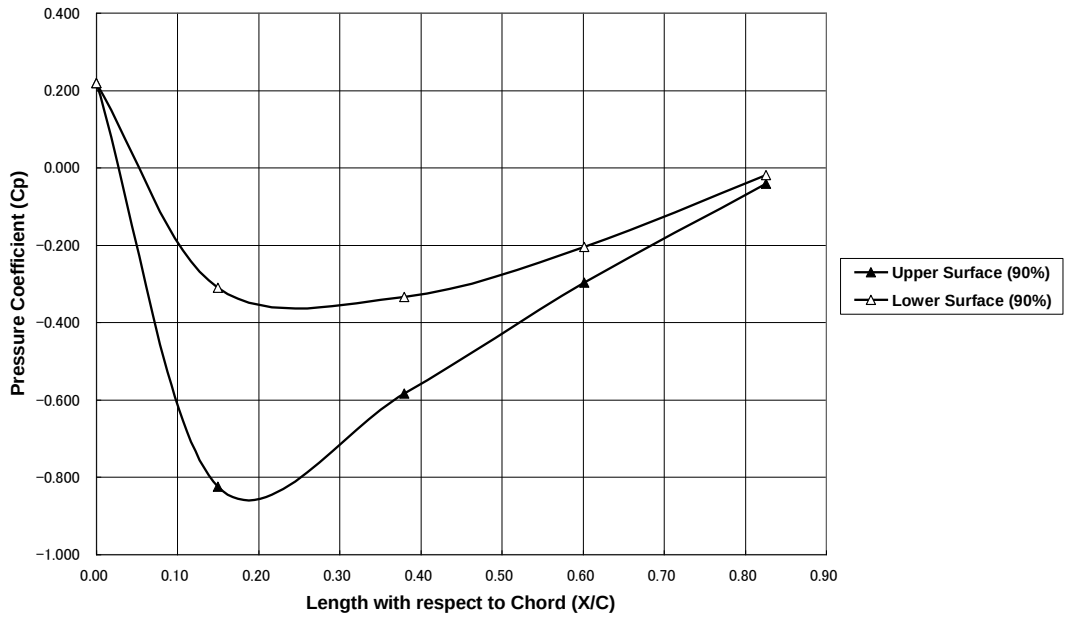

Figure 6.14b: Variation of Pressure with Chord Length for Conventional Cylindrical Shaped Fuselage UAV model at 90% from the root at 9° Angle of Attack.

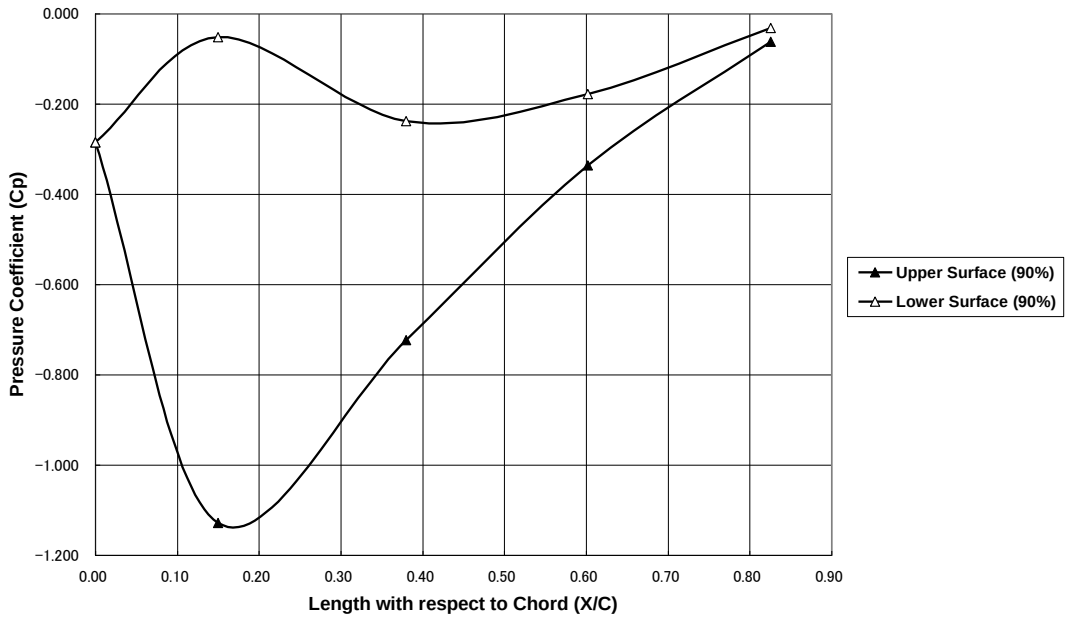

Figure 6.14c: Variation of Pressure with Chord Length for Conventional Cylindrical Shaped Fuselage UAV model at 90% from the root at 14° Angle of Attack.

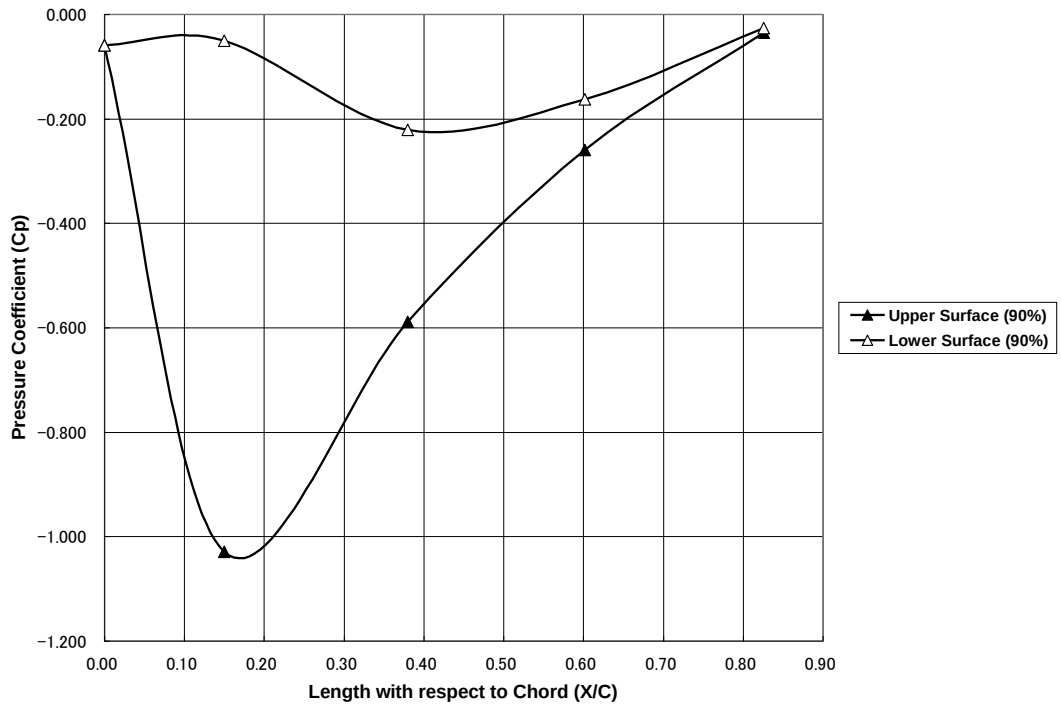

Figure 6.14d: Variation of Pressure with Chord Length for Conventional Cylindrical Shaped Fuselage UAV model at 90% from the root at 18° Angle of Attack.

APPENDIX – 'H' TO FIGURE 6.17, 6.18, 6.19 and 6.20

on *"Surface Pressure of Aerofoil Shaped Fuselage at 20 m/s"*

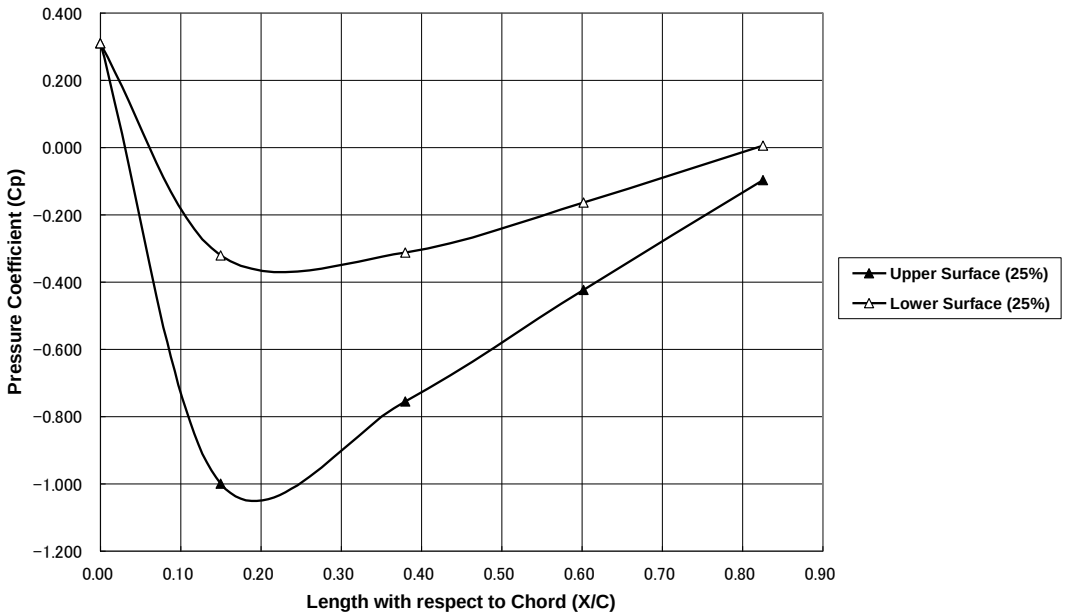

Figure 6.17a: Variation of Pressure with Chord Length for Aerofoil Shaped Fuselage UAV model at 25% from the root at 3° Angle of Attack.

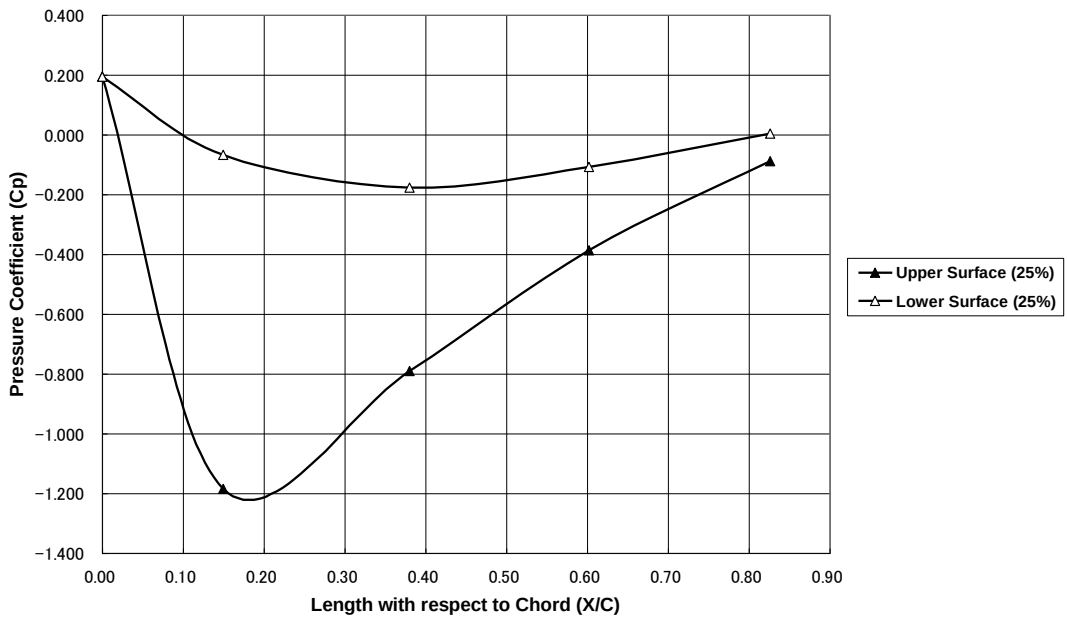

Figure 6.17b: Variation of Pressure with Chord Length for Aerofoil Shaped Fuselage UAV model at 25% from the root at 9° Angle of Attack.

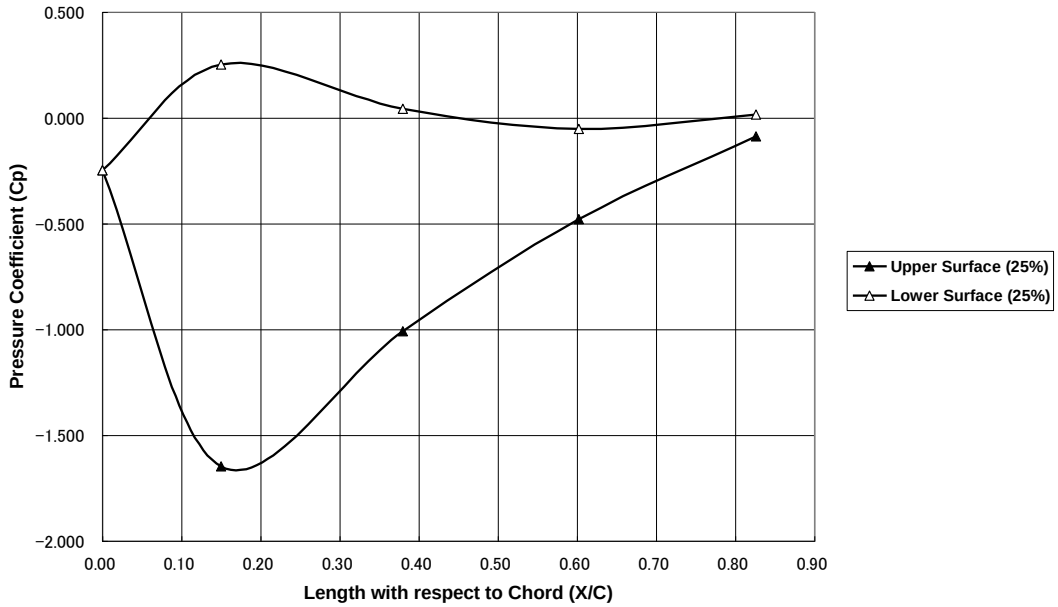

Figure 6.17c: Variation of Pressure with Chord Length for Aerofoil Shaped Fuselage UAV model at 25% from the root at 14° Angle of Attack.

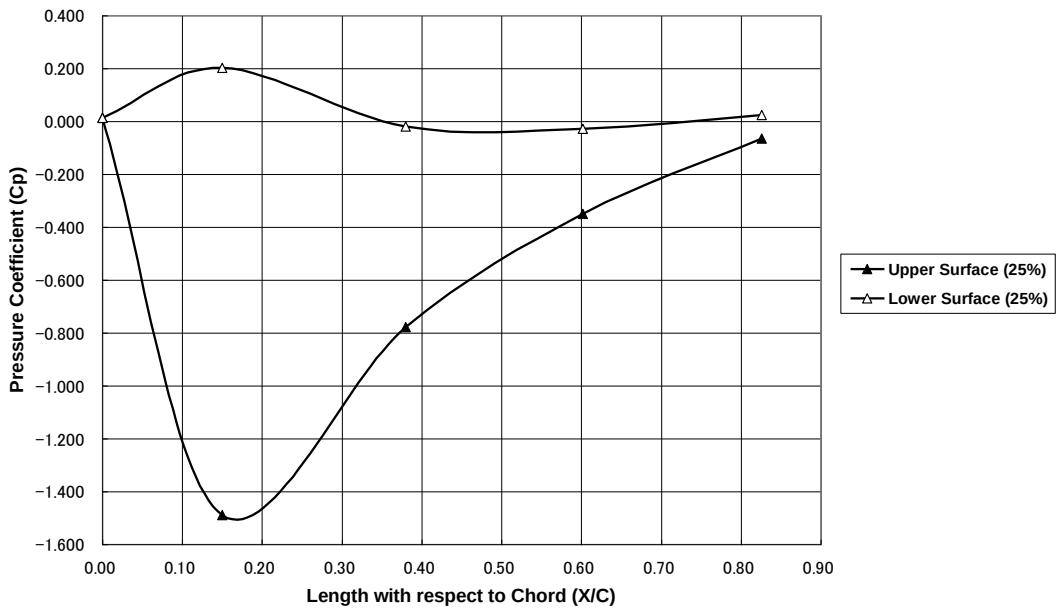

Figure 6.17d: Variation of Pressure with Chord Length for Aerofoil Shaped Fuselage UAV model at 25% from the root at 18° Angle of Attack.

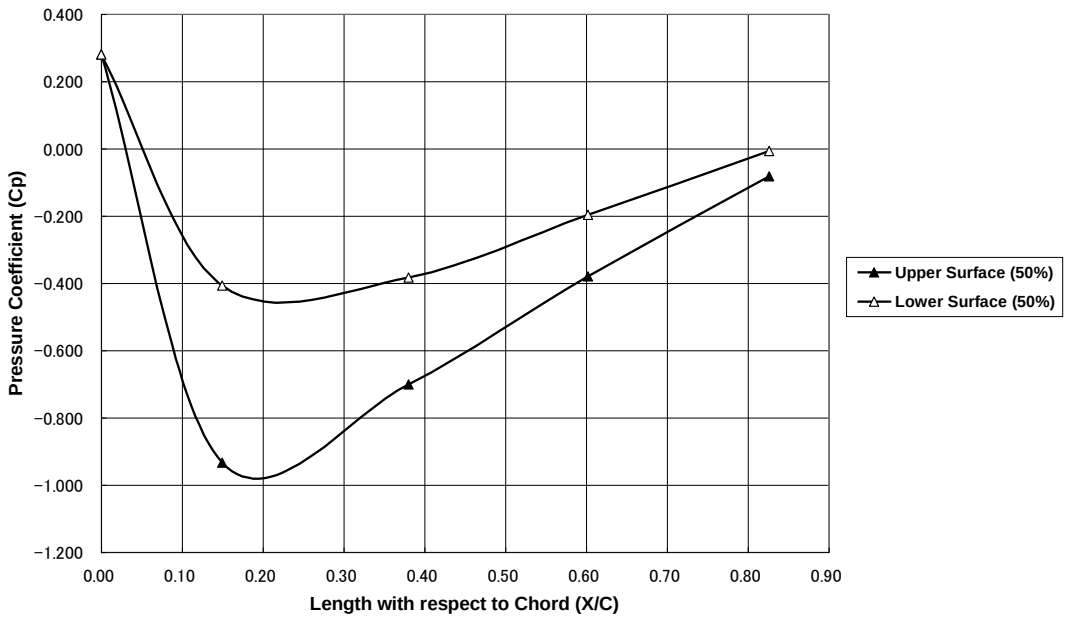

Figure 6.18a: Variation of Pressure with Chord Length for Aerofoil Shaped Fuselage UAV model at 50% from the root at 3° Angle of Attack.

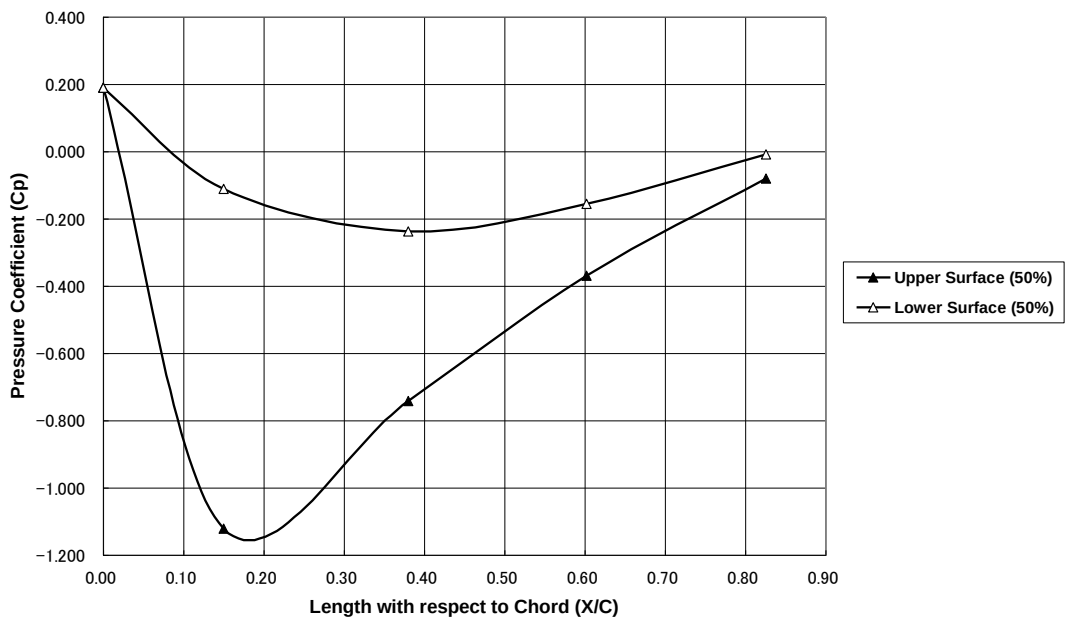

Figure 6.18b: Variation of Pressure with Chord Length for Aerofoil Shaped Fuselage UAV model at 50% from the root at 9° Angle of Attack.

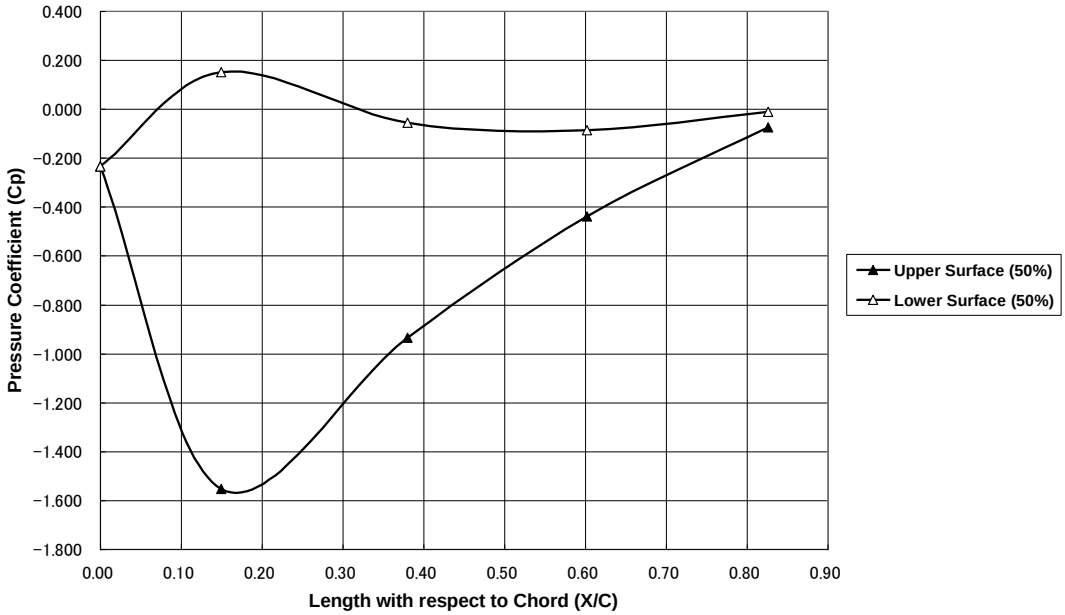

Figure 6.18c: Variation of Pressure with Chord Length for Aerofoil Shaped Fuselage UAV model at 50% from the root at 14° Angle of Attack.

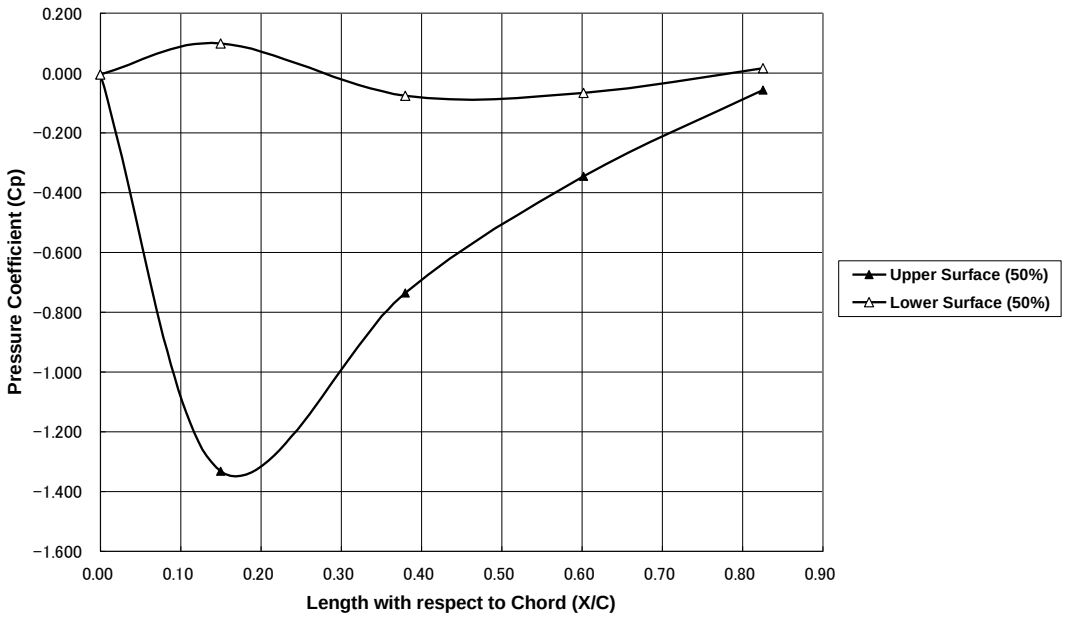

Figure 6.18d: Variation of Pressure with Chord Length for Aerofoil Shaped Fuselage UAV model at 50% from the root at 18° Angle of Attack.

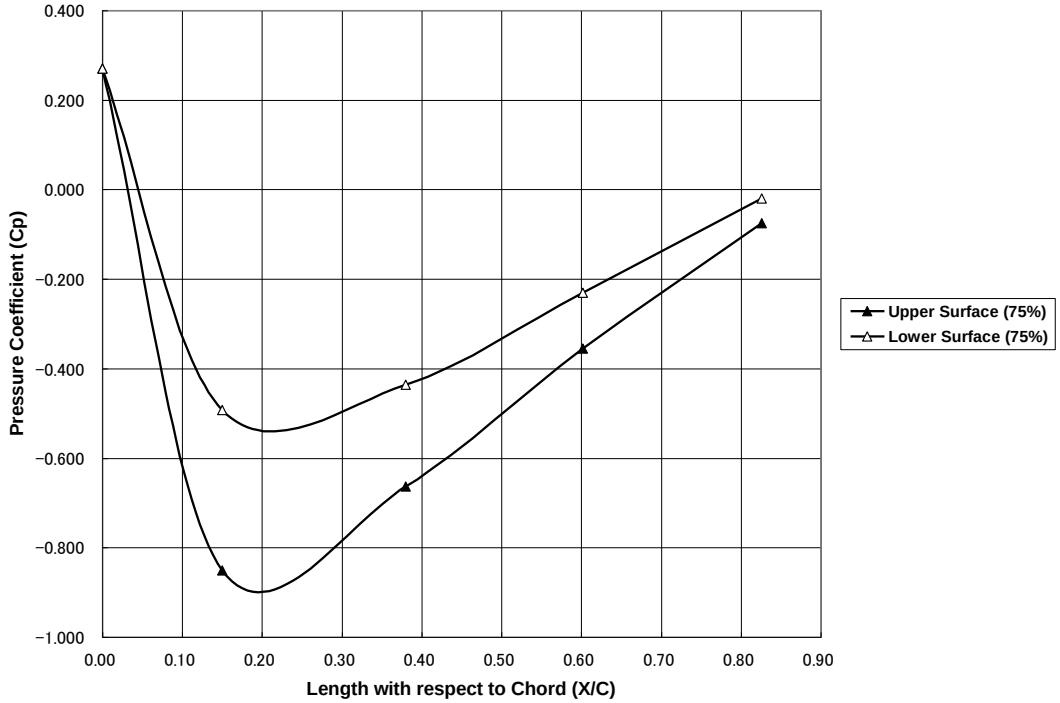

Figure 6.19a: Variation of Pressure with Chord Length for Aerofoil Shaped Fuselage UAV model at 75% from the root at 3° Angle of Attack.

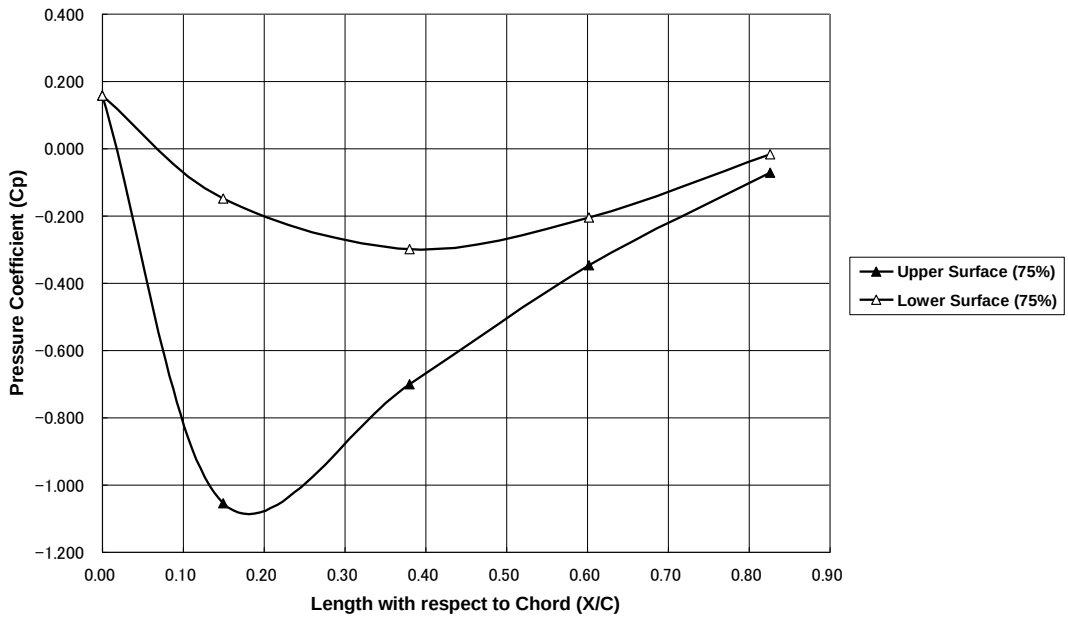

Figure 6.19b: Variation of Pressure with Chord Length for Aerofoil Shaped Fuselage UAV model at 75% from the root at 9° Angle of Attack.

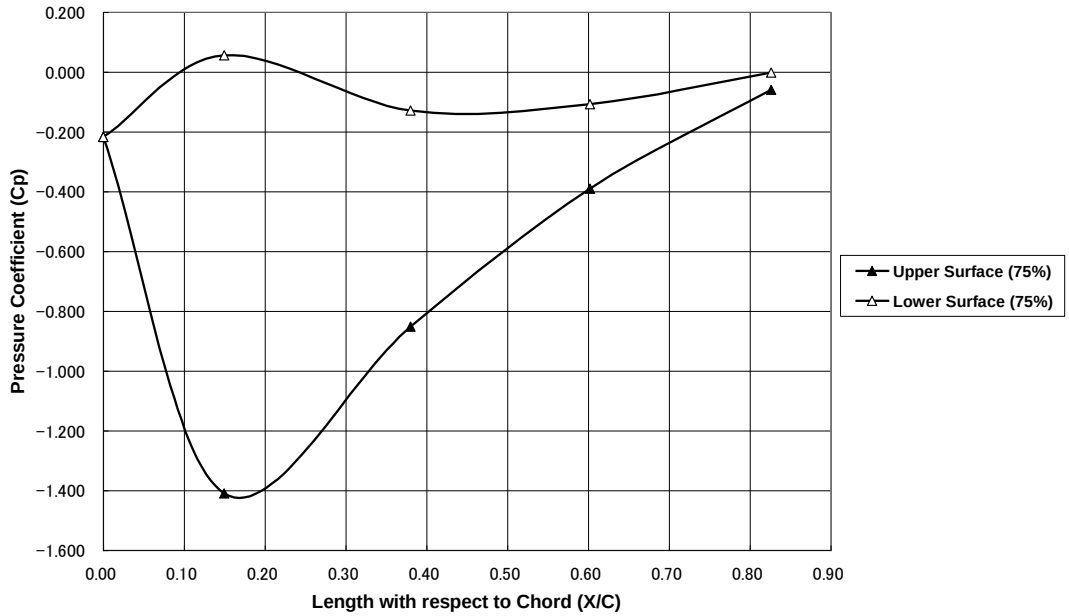

Figure 6.19c: Variation of Pressure with Chord Length for Aerofoil Shaped Fuselage UAV model at 75% from the root at 14° Angle of Attack.

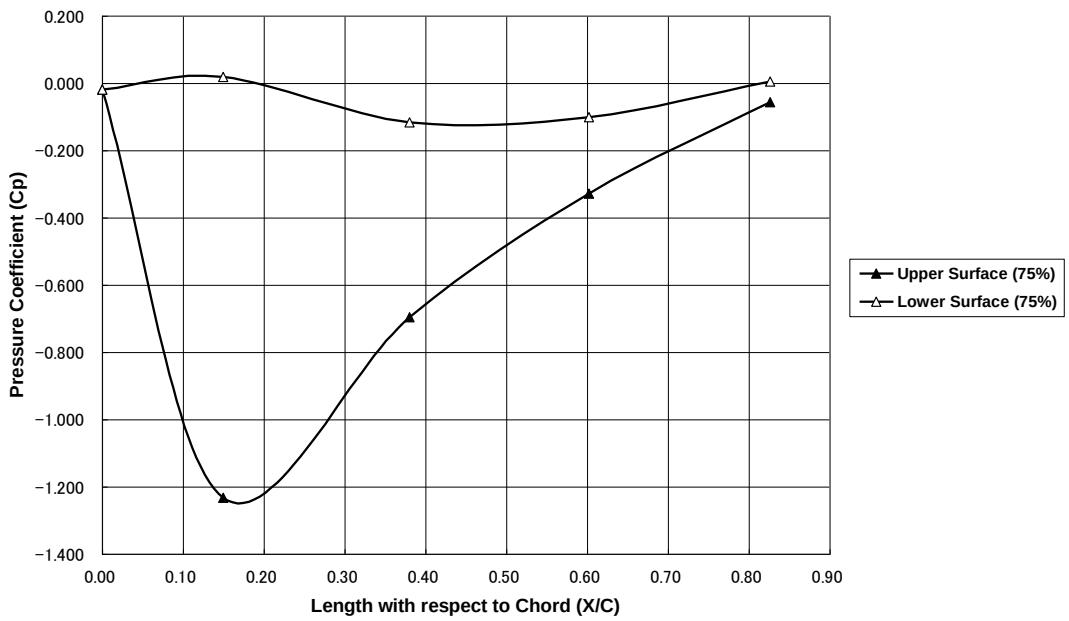

Figure 6.19d: Variation of Pressure with Chord Length for Aerofoil Shaped Fuselage UAV model at 75% from the root at 18° Angle of Attack.

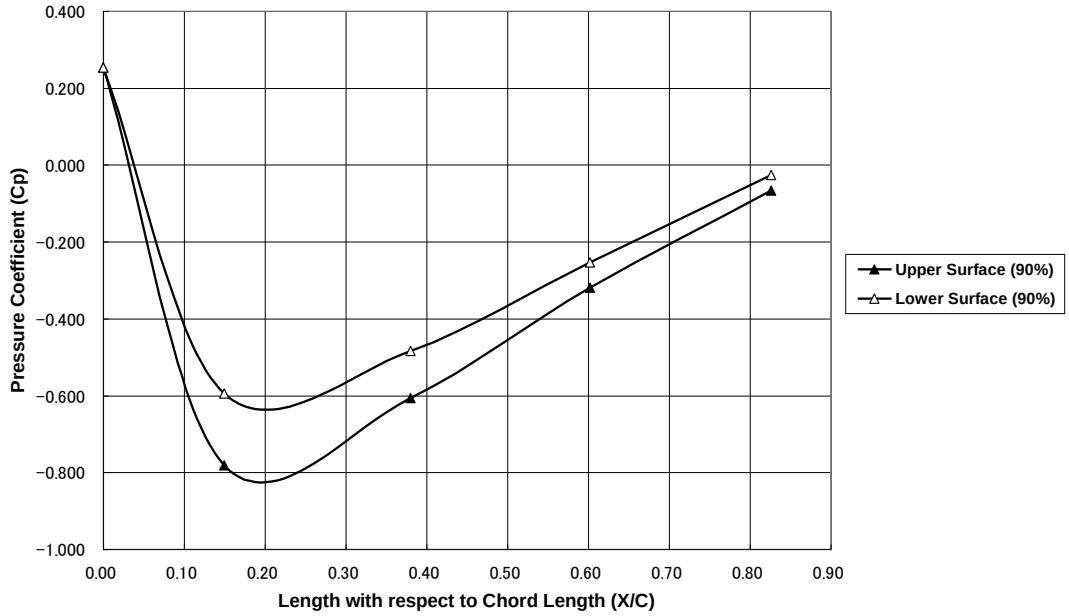

Figure 6.20a: Variation of Pressure with Chord Length for Aerofoil Shaped Fuselage UAV model at 90% from the root at 3° Angle of Attack.

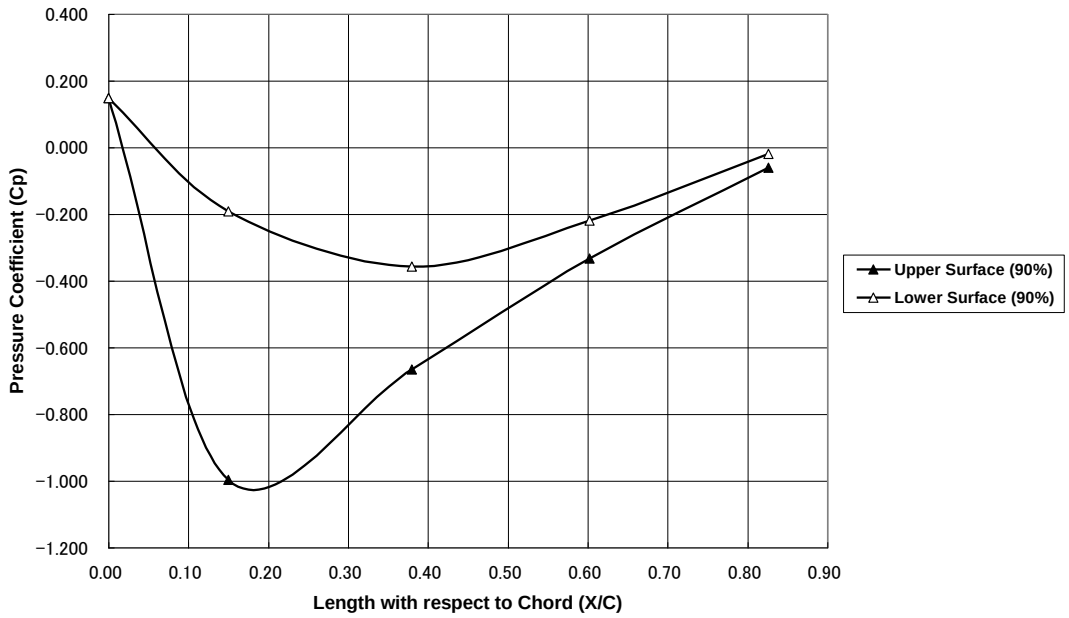

Figure 6.20b: Variation of Pressure with Chord Length for Aerofoil Shaped Fuselage UAV model at 90% from the root at 9° Angle of Attack.

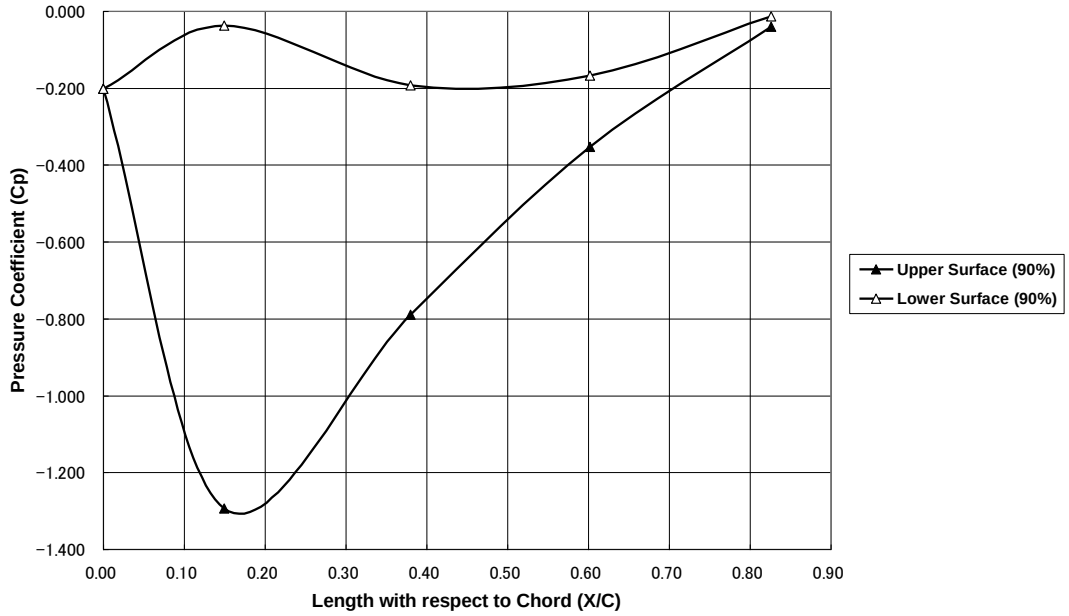

Figure 6.20c: Variation of Pressure with Chord Length for Aerofoil Shaped Fuselage UAV model at 90% from the root at 14° Angle of Attack.

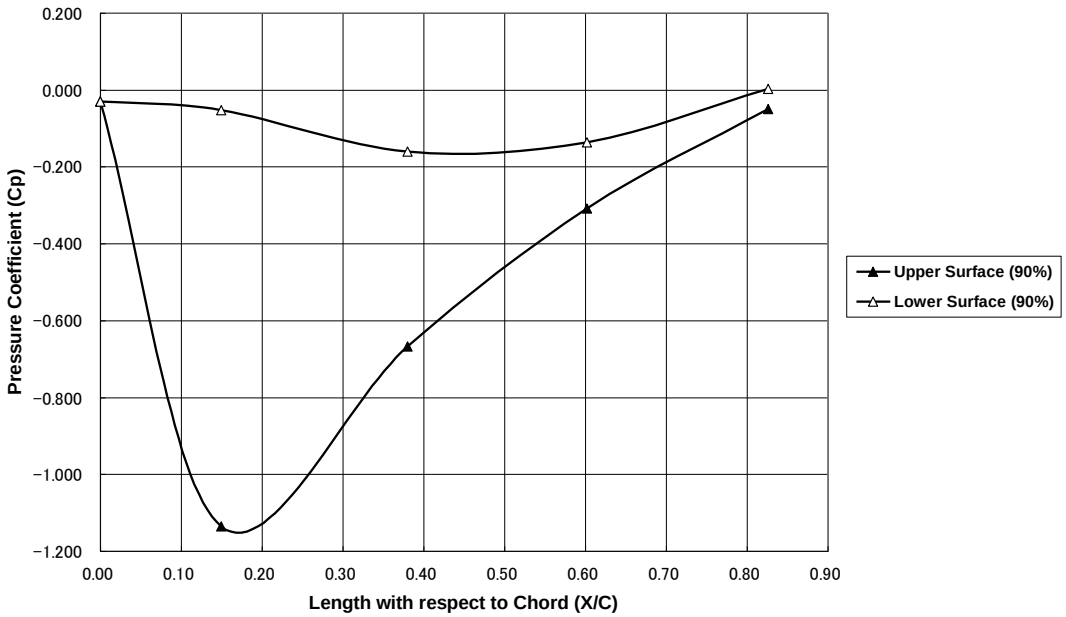

Figure 6.20d: Variation of Pressure with Chord Length for Aerofoil Shaped Fuselage UAV model at 90% from the root at 18° Angle of Attack.

APPENDIX – 'J' TO FIGURE 6.21, 6.22, 6.23 and 6.24

on *"Surface Pressure of Conventional Cylindrical Shaped Fuselage at 40 m/s"*

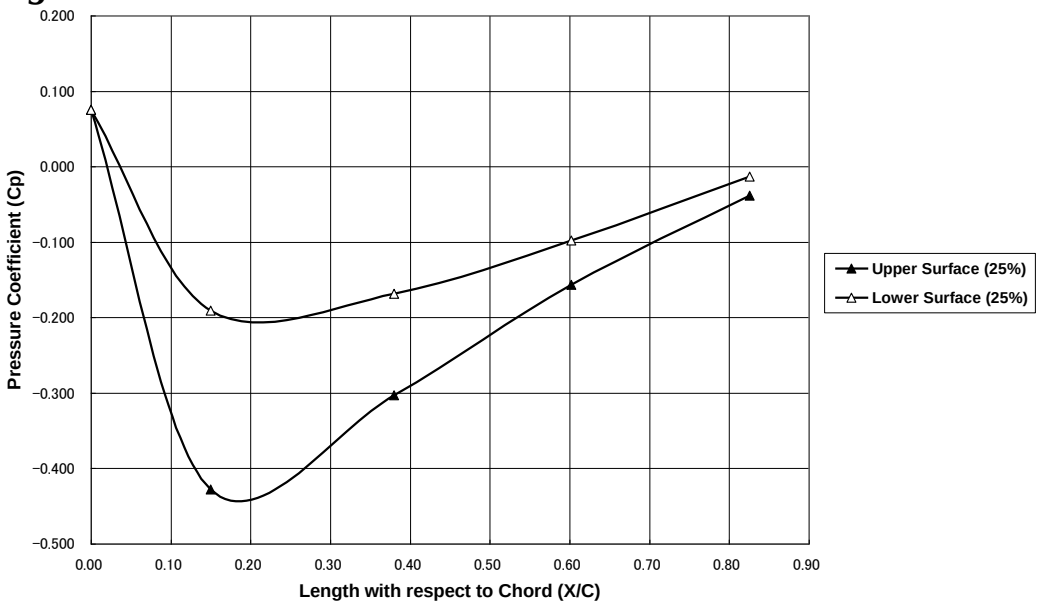

Figure 6.21a: Variation of Pressure with Chord Length for Conventional Cylindrical Shaped Fuselage UAV model at 25% from the root at 3° Angle of Attack.

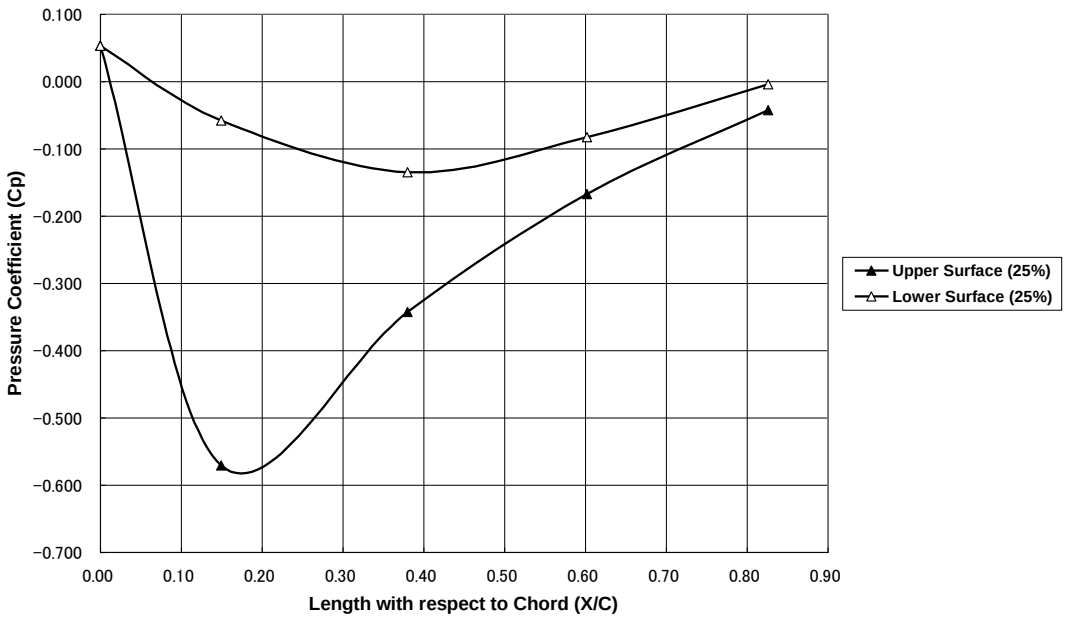

Figure 6.21b: Variation of Pressure with Chord Length for Conventional Cylindrical Shaped Fuselage UAV model at 25% from the root at 9° Angle of Attack.

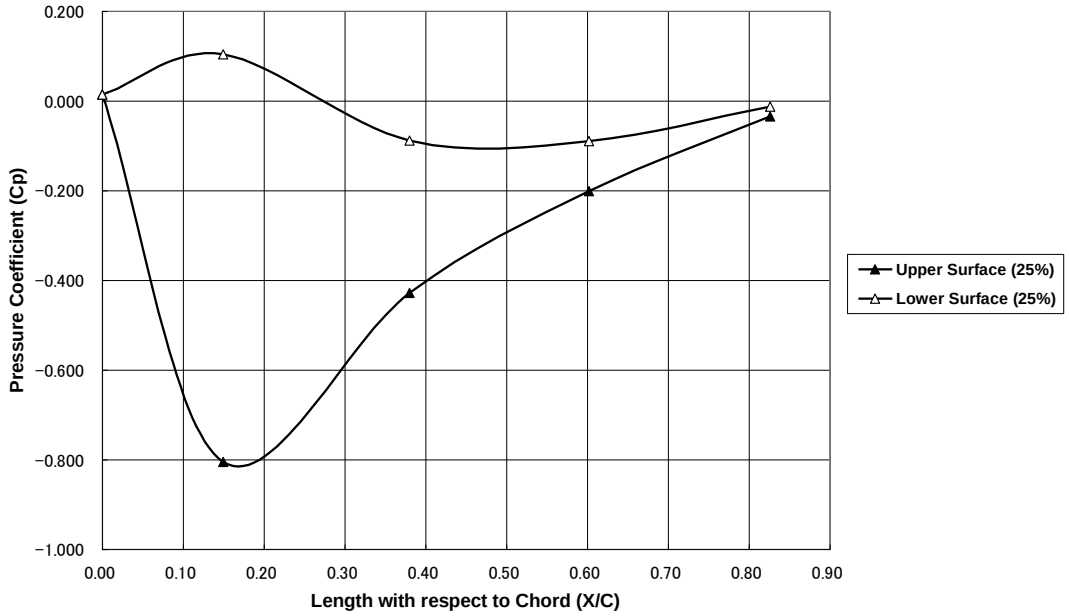

Figure 6.21c: Variation of Pressure with Chord Length for Conventional Cylindrical Shaped Fuselage UAV model at 25% from the root at 14° Angle of Attack.

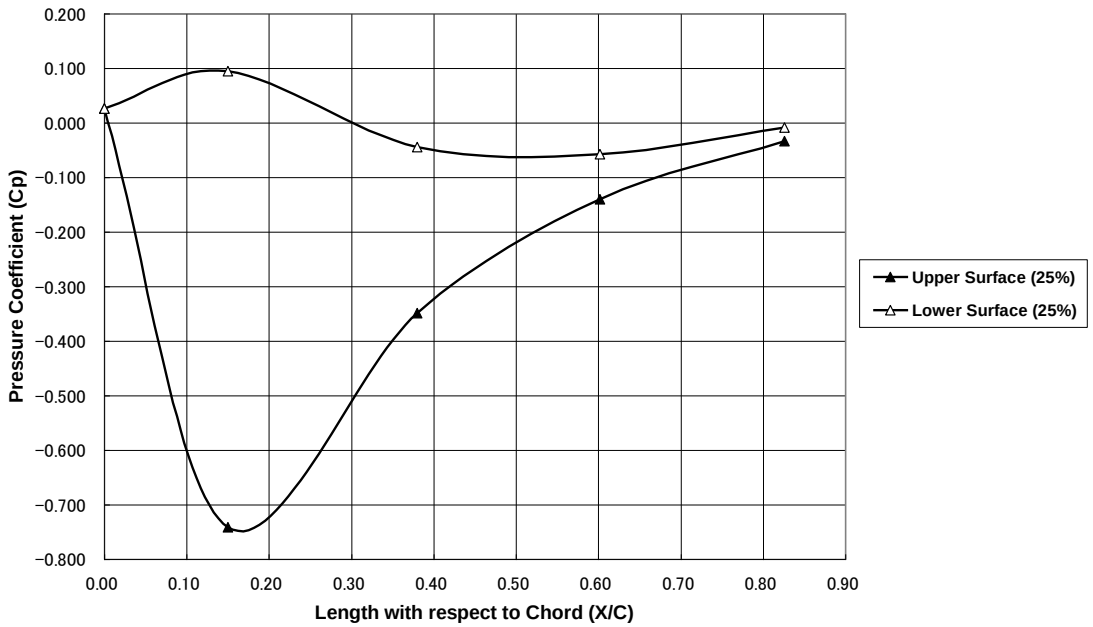

Figure 6.21d: Variation of Pressure with Chord Length for Conventional Cylindrical Shaped Fuselage UAV model at 25% from the root at 18° Angle of Attack.

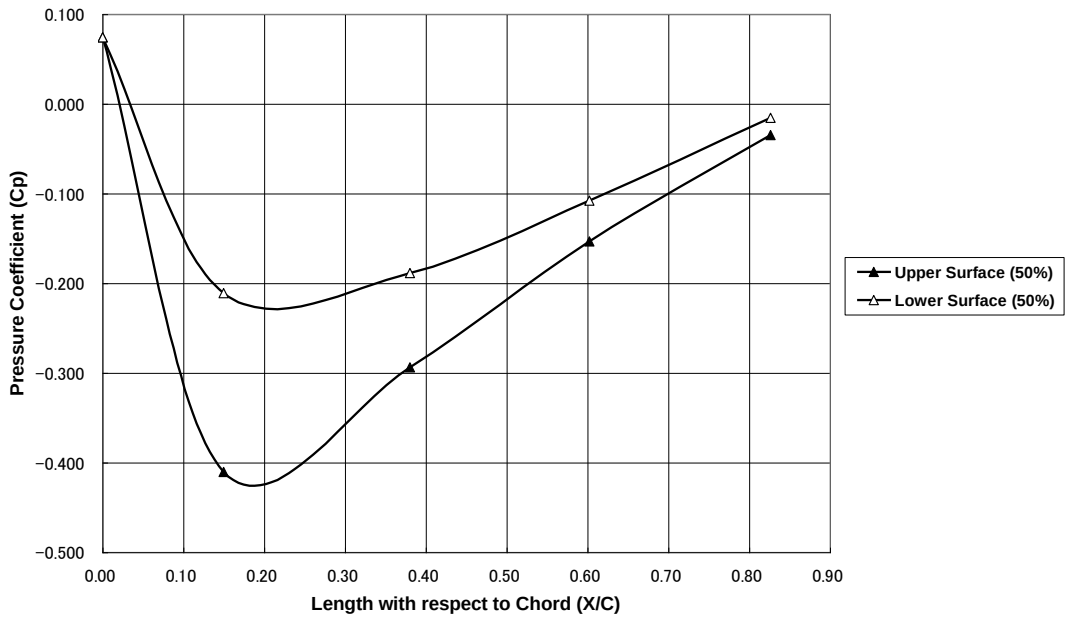

Figure 6.22a: Variation of Pressure with Chord Length for Conventional Cylindrical Shaped Fuselage UAV model at 50% from the root at 3° Angle of Attack.

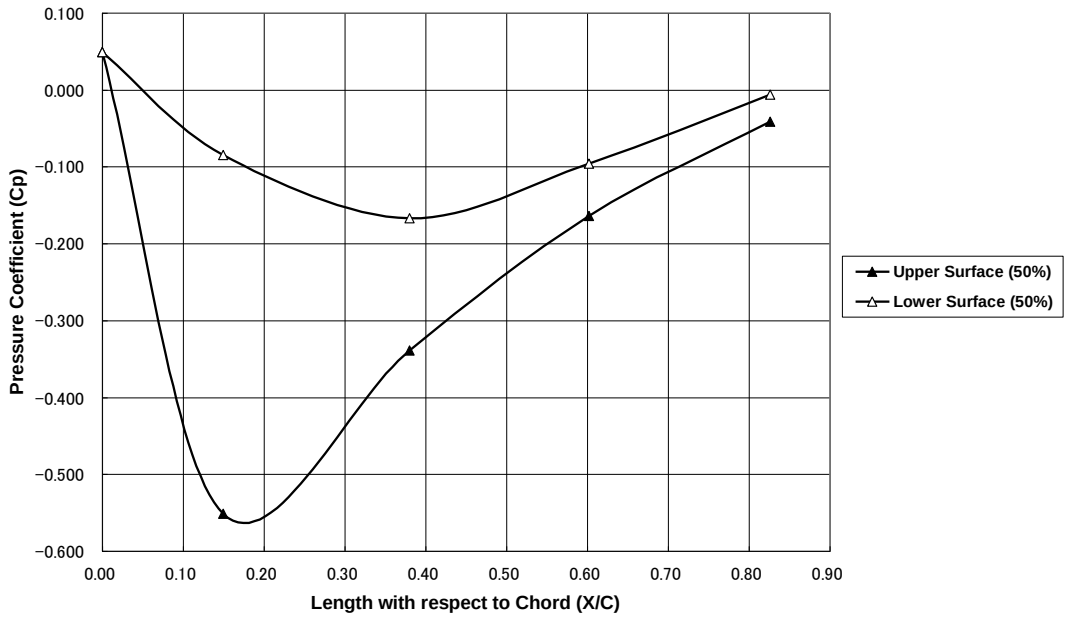

Figure 6.22b: Variation of Pressure with Chord Length for Conventional Cylindrical Shaped Fuselage UAV model at 50% from the root at 9° Angle of Attack.

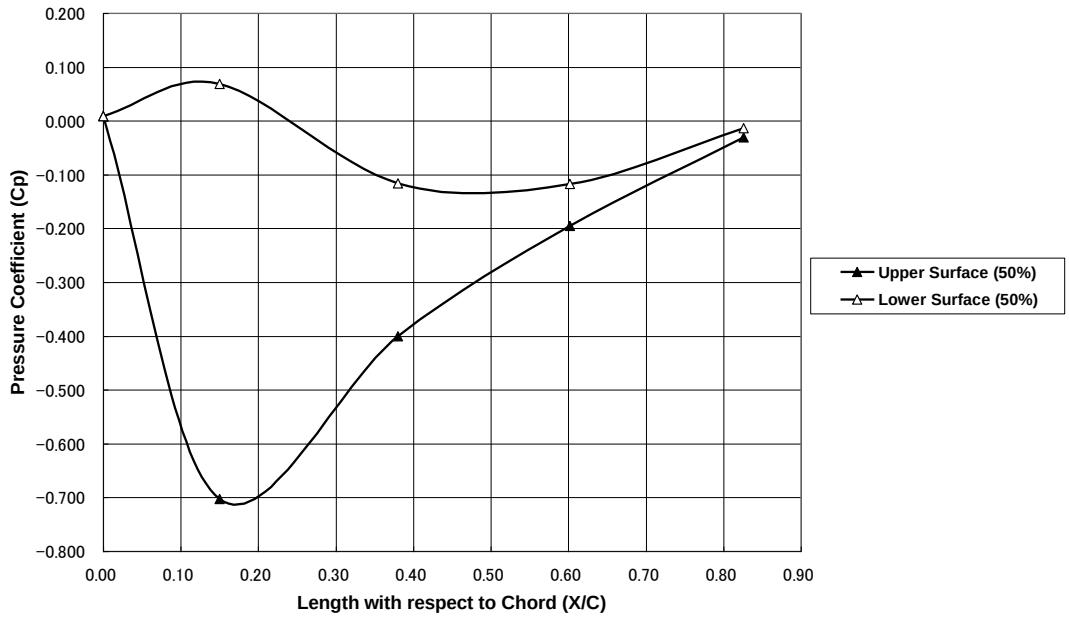

Figure 6.22c: Variation of Pressure with Chord Length for Conventional Cylindrical Shaped Fuselage UAV model at 50% from the root at 14° Angle of Attack.

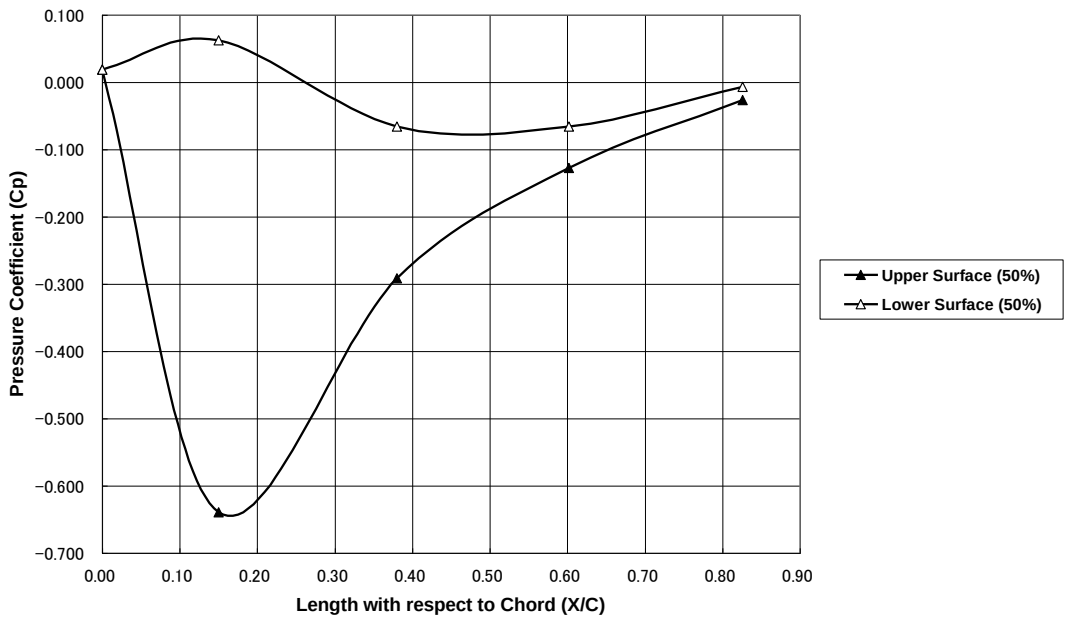

Figure 6.22d: Variation of Pressure with Chord Length for Conventional Cylindrical Shaped Fuselage UAV model at 50% from the root at 18° Angle of Attack.

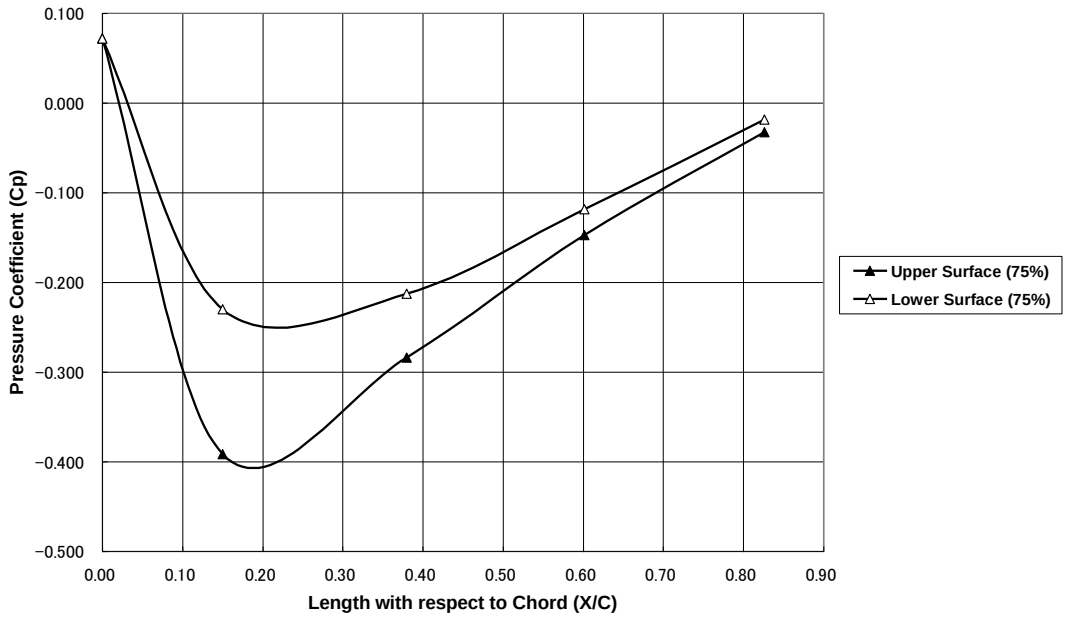

Figure 6.23a: Variation of Pressure with Chord Length for Conventional Cylindrical Shaped Fuselage UAV model at 75% from the root at 3° Angle of Attack.

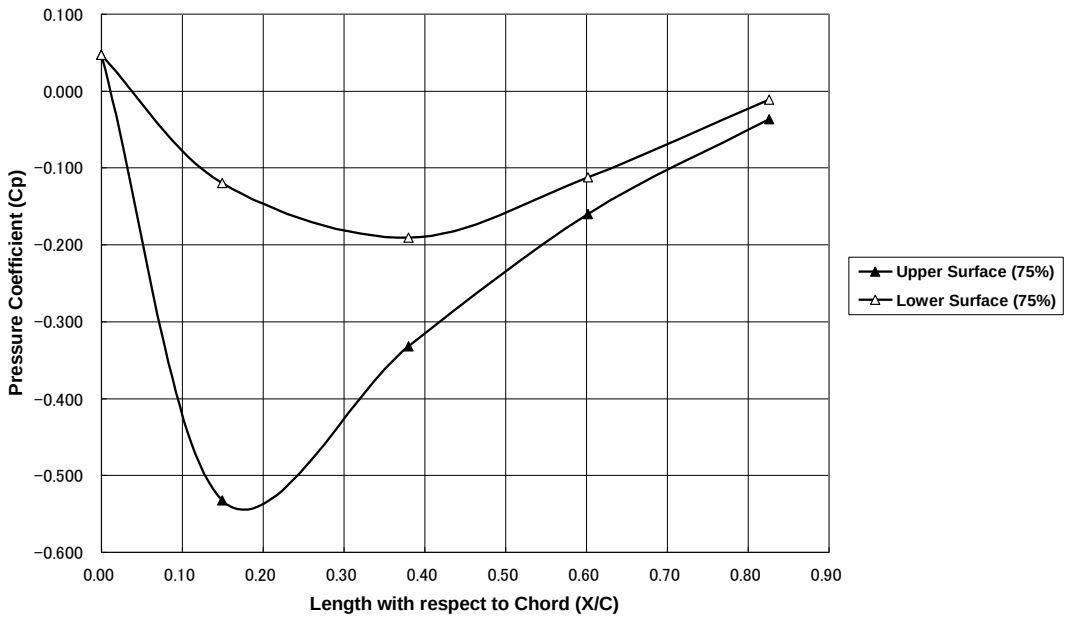

Figure 6.23b: Variation of Pressure with Chord Length for Conventional Cylindrical Shaped Fuselage UAV model at 75% from the root at 9° Angle of Attack.

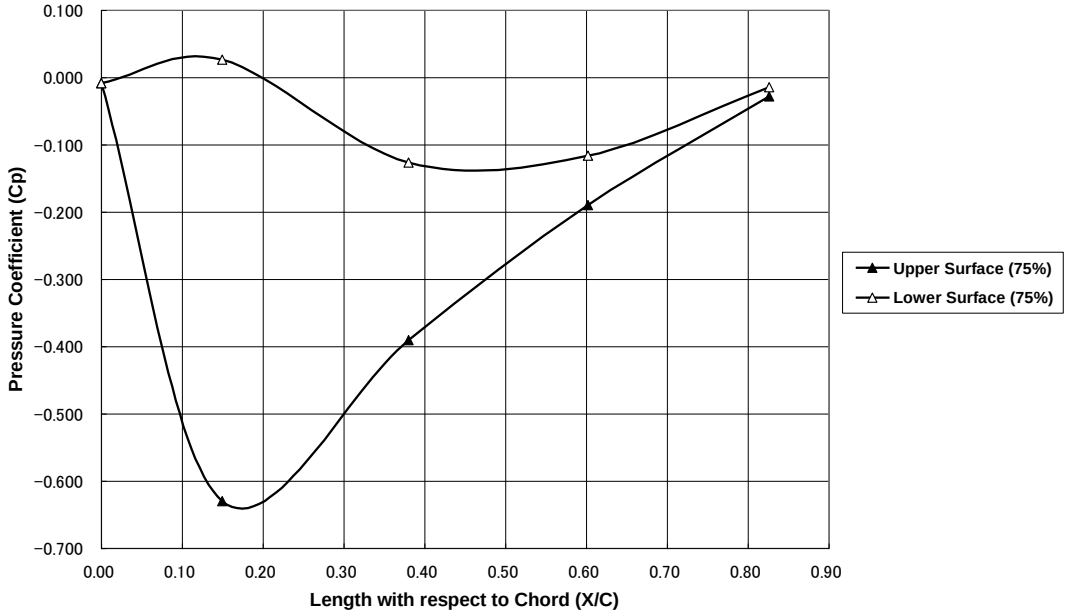

Figure 6.23c: Variation of Pressure with Chord Length for Conventional Cylindrical Shaped Fuselage UAV model at 75% from the root at 14° Angle of Attack.

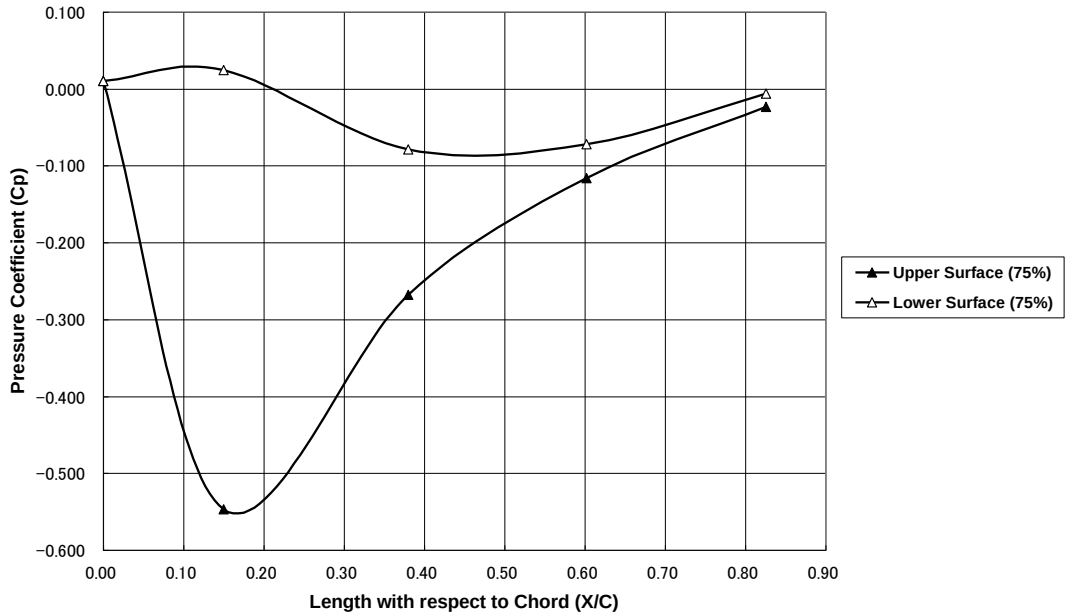

Figure 6.23d: Variation of Pressure with Chord Length for Conventional Cylindrical Shaped Fuselage UAV model at 75% from the root at 18° Angle of Attack.

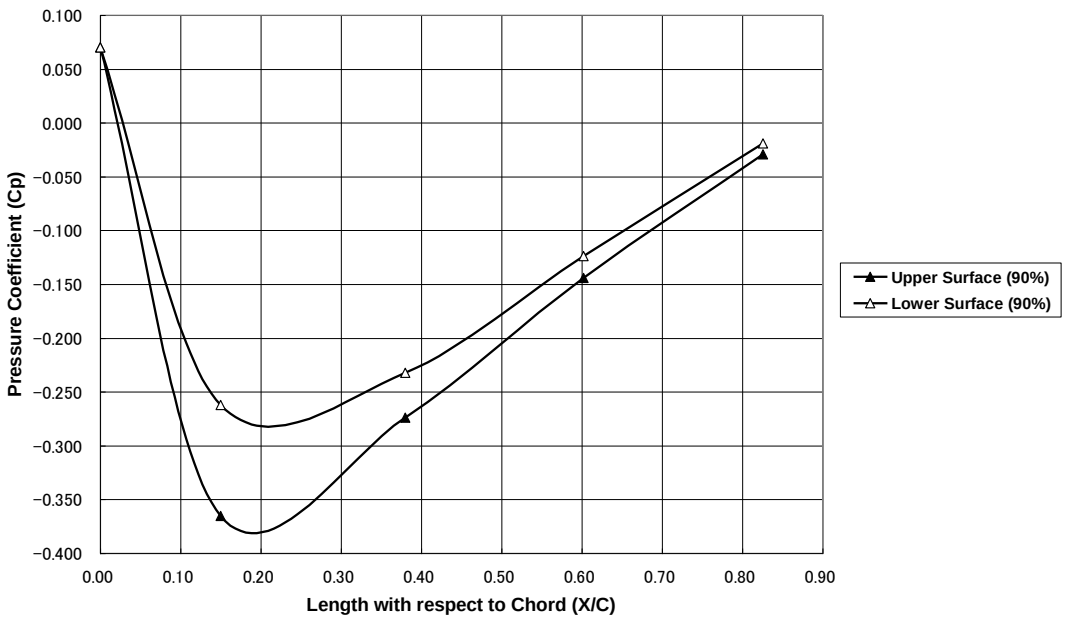

Figure 6.24a: Variation of Pressure with Chord Length for Conventional Cylindrical Shaped Fuselage UAV model at 90% from the root at 3° Angle of Attack.

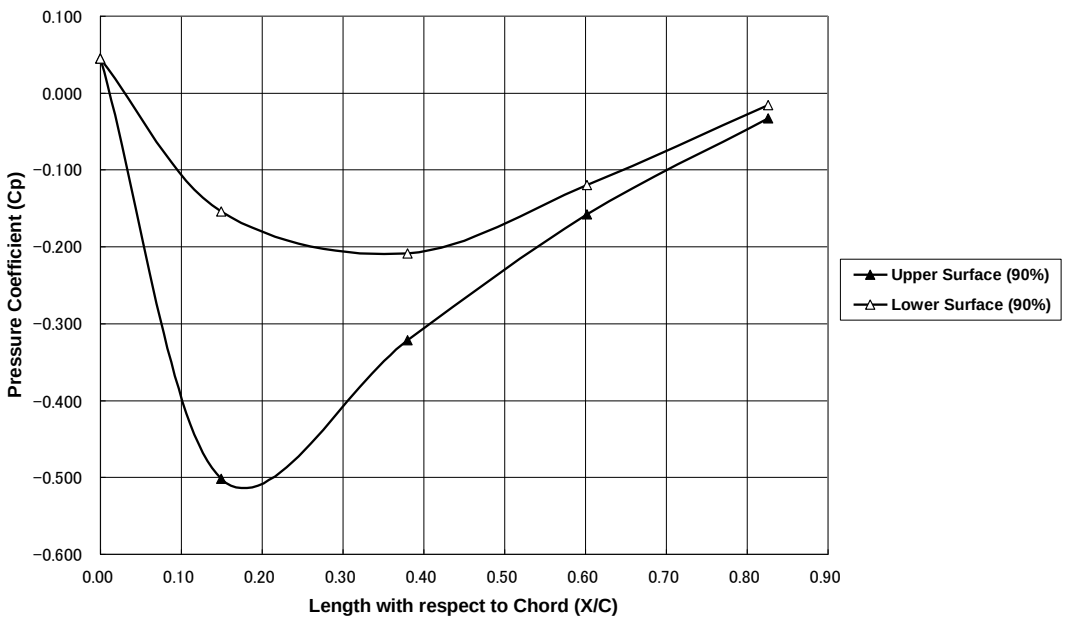

Figure 6.24b: Variation of Pressure with Chord Length for Conventional Cylindrical Shaped Fuselage UAV model at 90% from the root at 9° Angle of Attack.

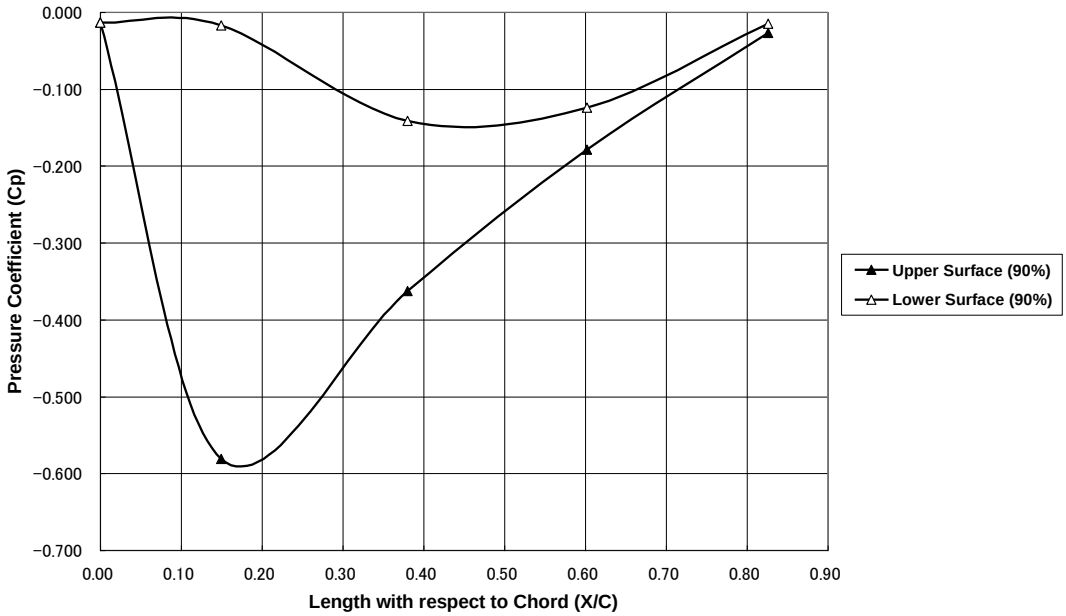

Figure 6.24c: Variation of Pressure with Chord Length for Conventional Cylindrical Shaped Fuselage UAV model at 90% from the root at 14° Angle of Attack.

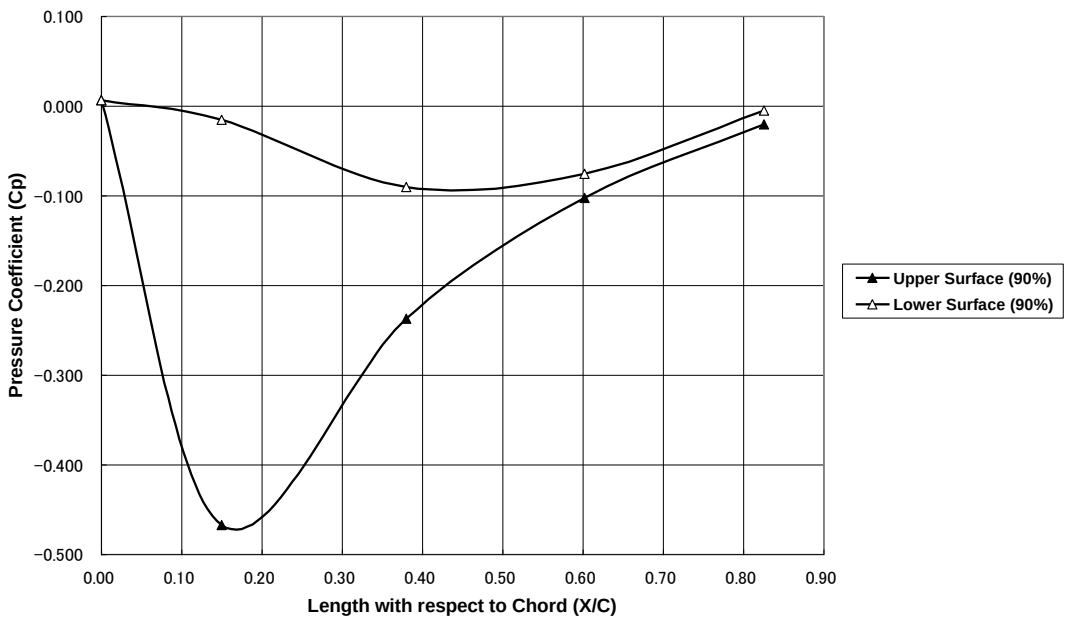

Figure 6.24d: Variation of Pressure with Chord Length for Conventional Cylindrical Shaped Fuselage UAV model at 90% from the root at 18° Angle of Attack.

APPENDIX – 'K' TO FIGURE 6.25, 6.26, 6.27 and 6.28

on *"Surface Pressure of Aerofoil Shaped Fuselage at 40 m/s"*

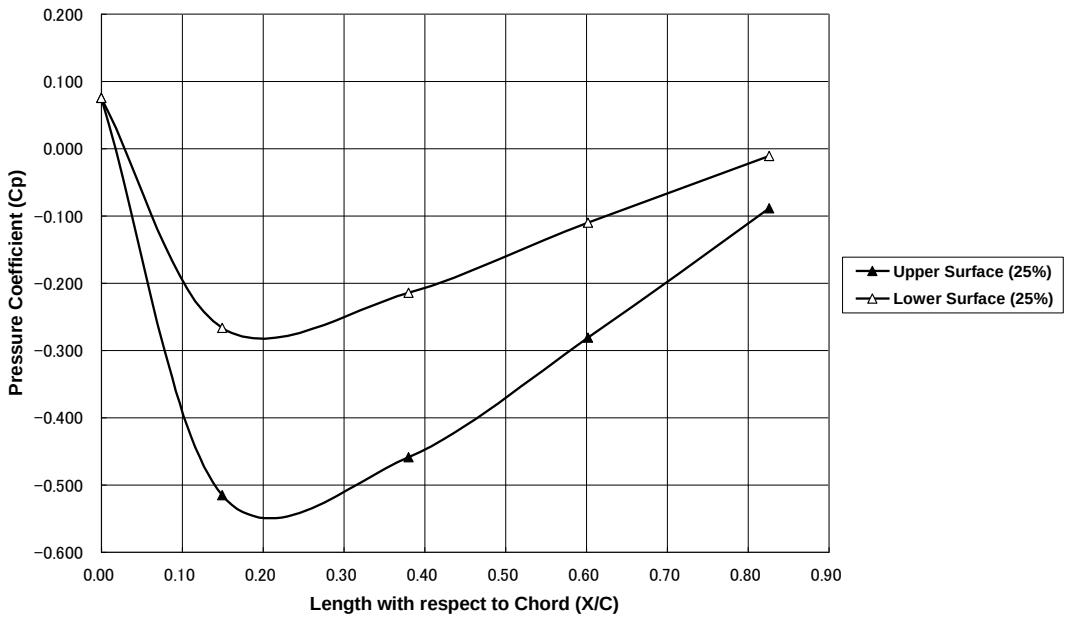

Figure 6.25a: Variation of Pressure with Chord Length for Aerofoil Shaped Fuselage UAV model at 25% from the root at 3° Angle of Attack.

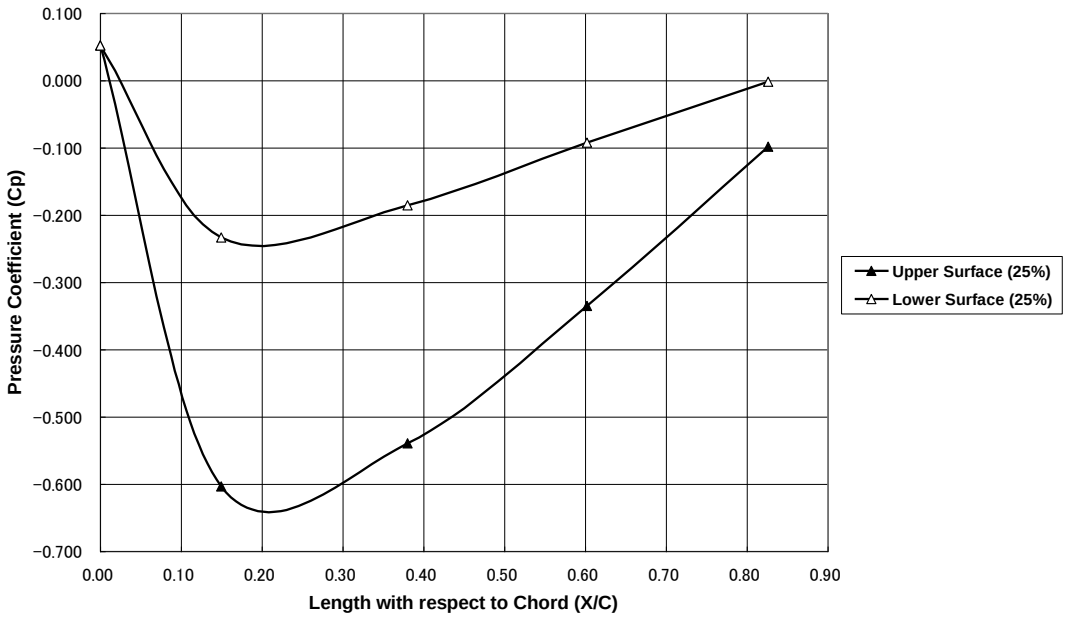

Figure 6.25b: Variation of Pressure with Chord Length for Aerofoil Shaped Fuselage UAV model at 25% from the root at 9° Angle of Attack.

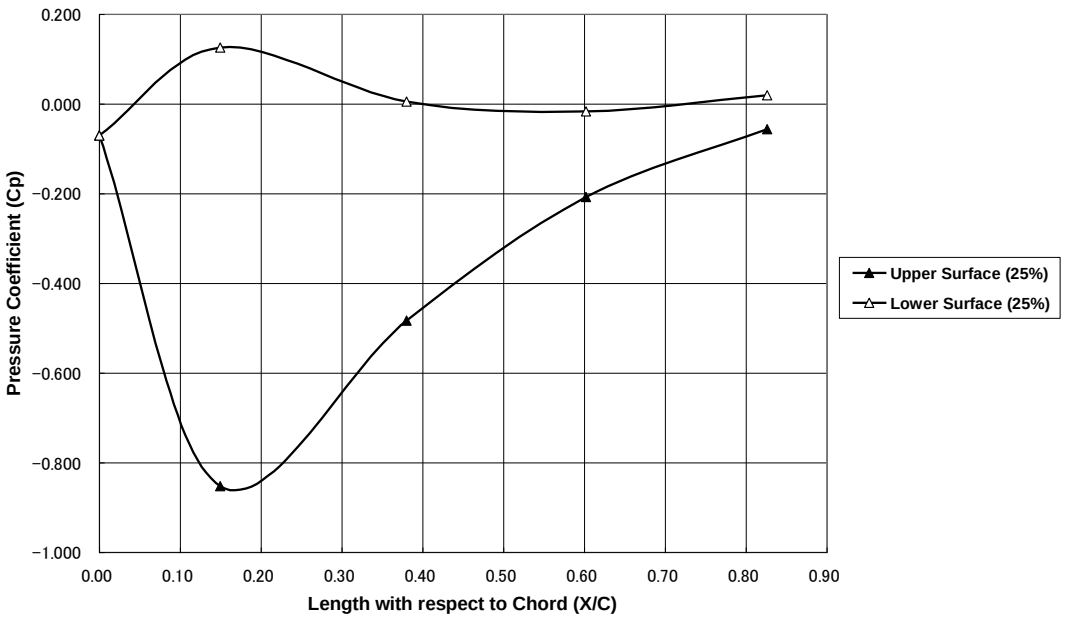

Figure 6.25c: Variation of Pressure with Chord Length for Aerofoil Shaped Fuselage UAV model at 25% from the root at 14° Angle of Attack.

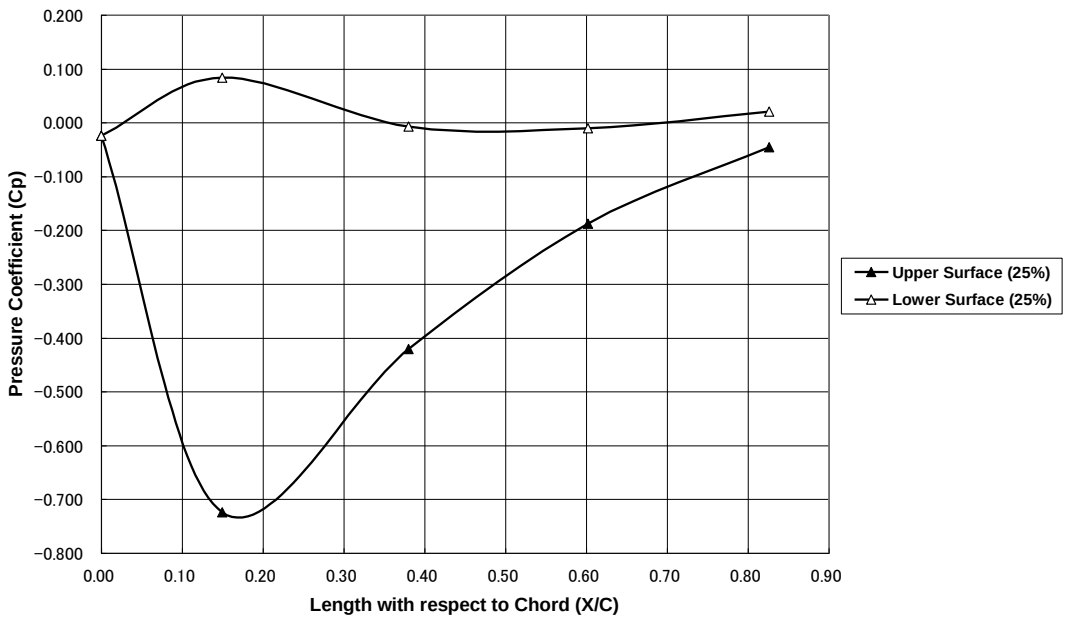

Figure 6.25d: Variation of Pressure with Chord Length for Aerofoil Shaped Fuselage UAV model at 25% from the root at 18° Angle of Attack.

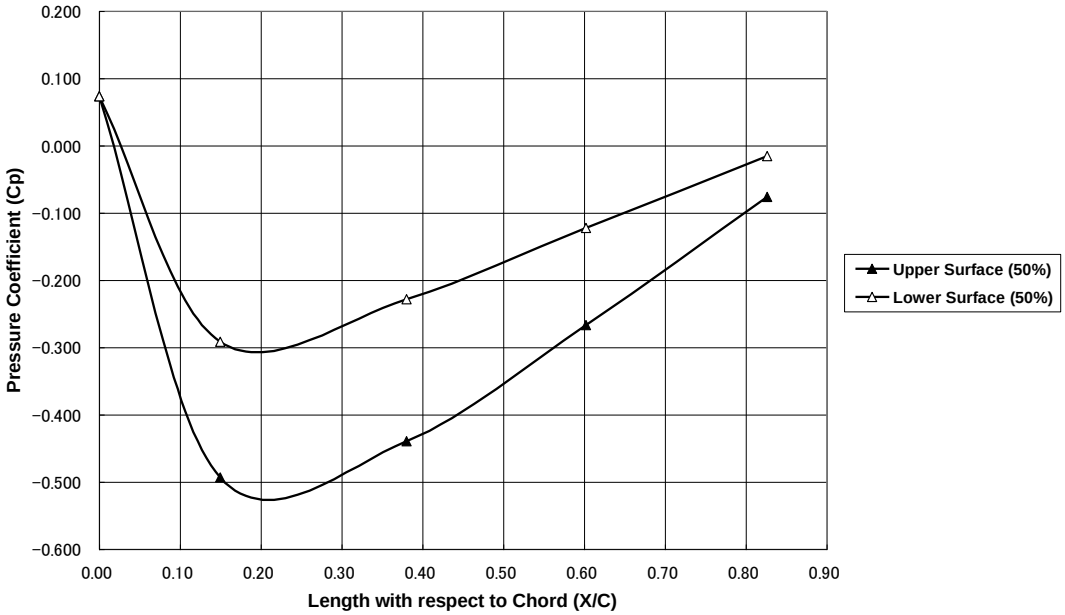

Figure 6.26a: Variation of Pressure with Chord Length for Aerofoil Shaped Fuselage UAV model at 50% from the root at 3° Angle of Attack.

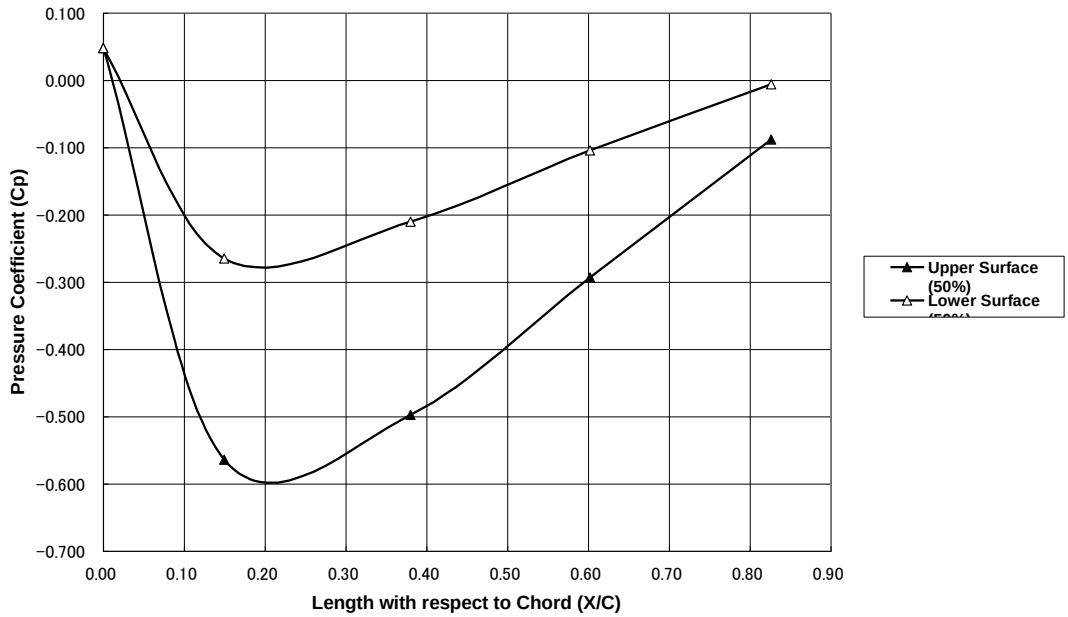

Figure 6.26b: Variation of Pressure with Chord Length for Aerofoil Shaped Fuselage UAV model at 50% from the root at 9° Angle of Attack.

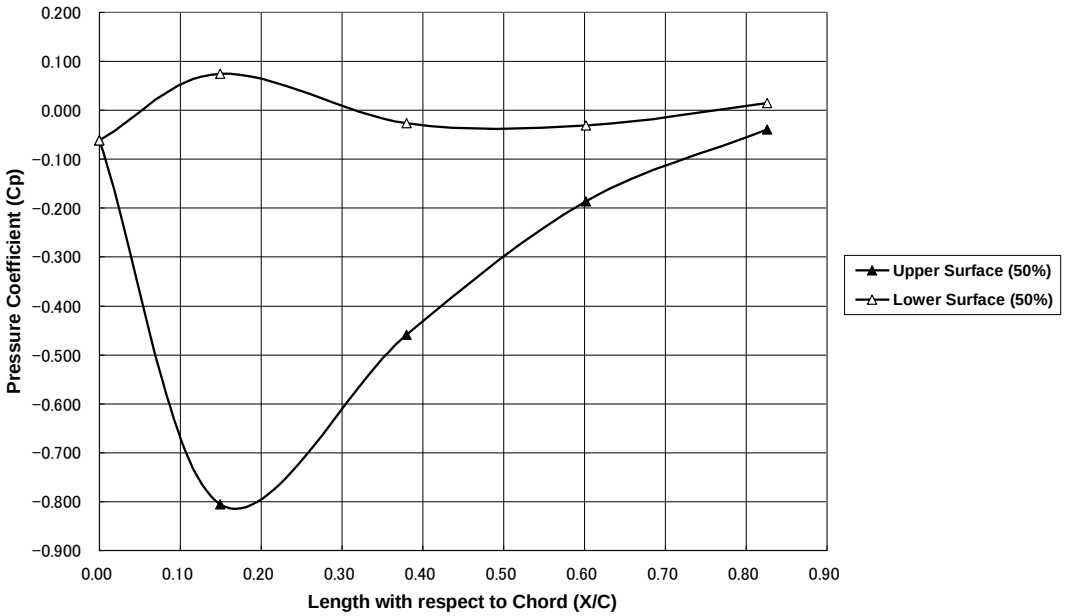

Figure 6.26c: Variation of Pressure with Chord Length for Aerofoil Shaped Fuselage UAV model at 50% from the root at 14° Angle of Attack.

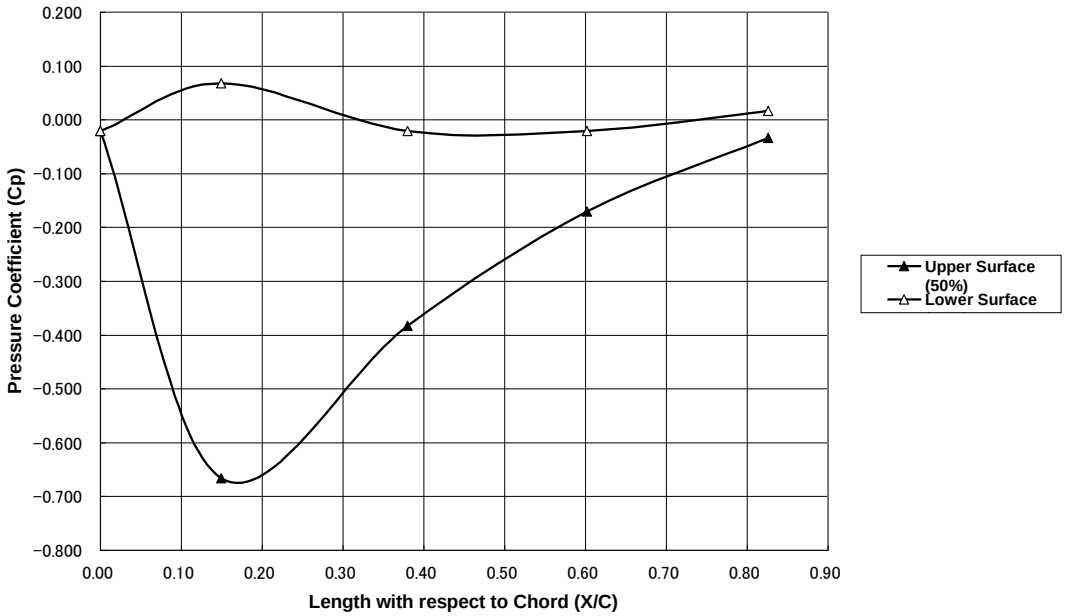

Figure 6.26d: Variation of Pressure with Chord Length for Aerofoil Shaped Fuselage UAV model at 50% from the root at 18° Angle of Attack.

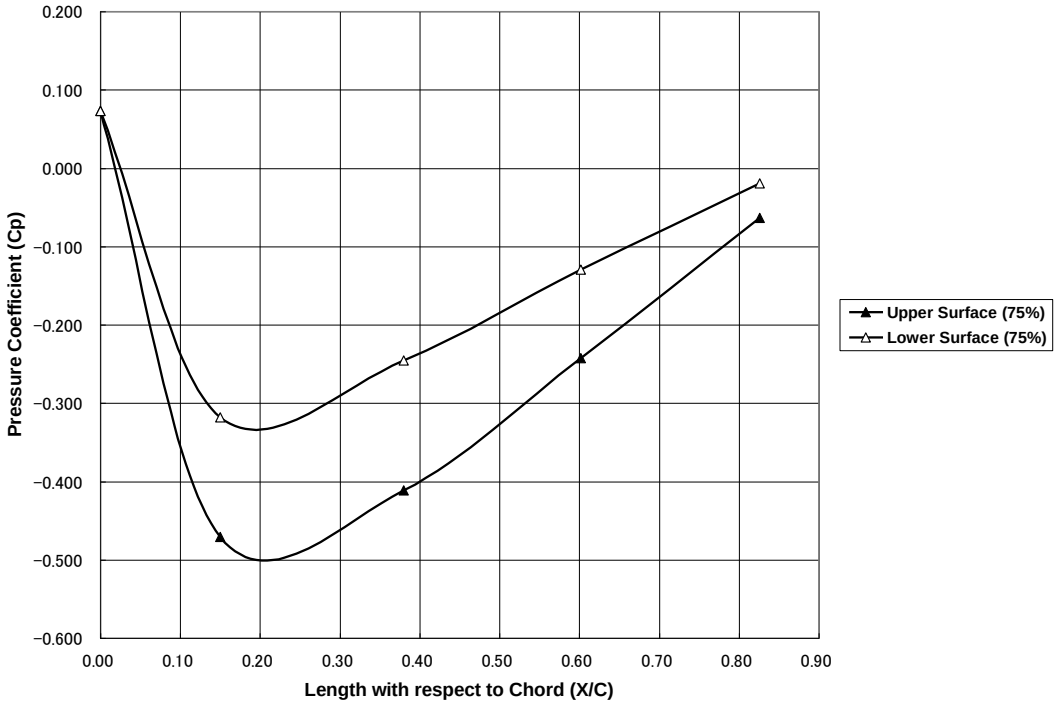

Figure 6.27a: Variation of Pressure with Chord Length for Aerofoil Shaped Fuselage UAV model at 75% from the root at 3° Angle of Attack.

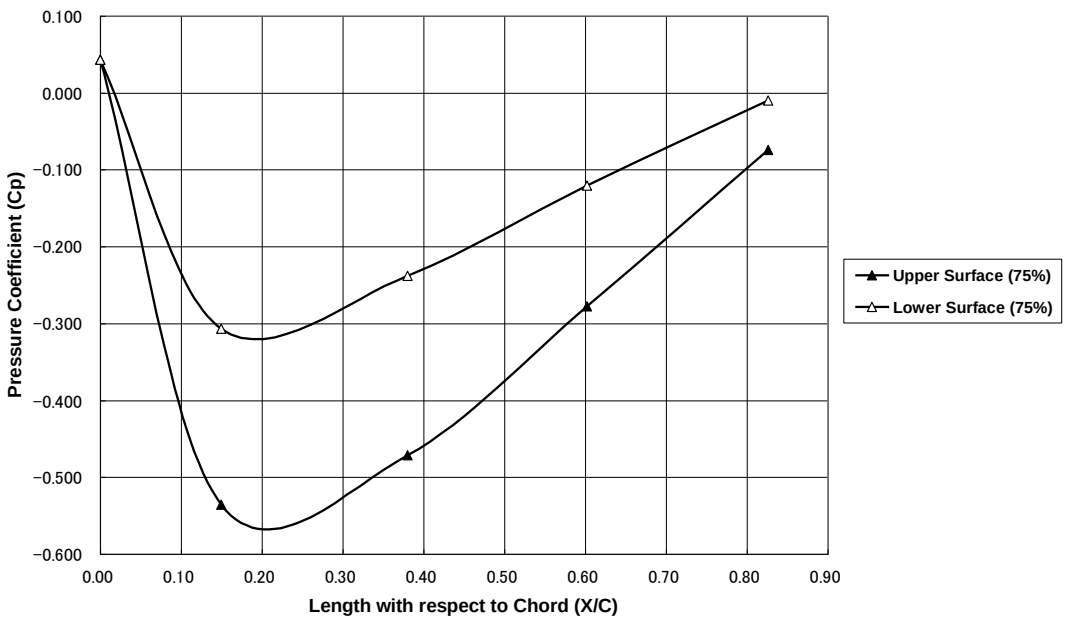

Figure 6.27b: Variation of Pressure with Chord Length for Aerofoil Shaped Fuselage UAV model at 75% from the root at 9° Angle of Attack.

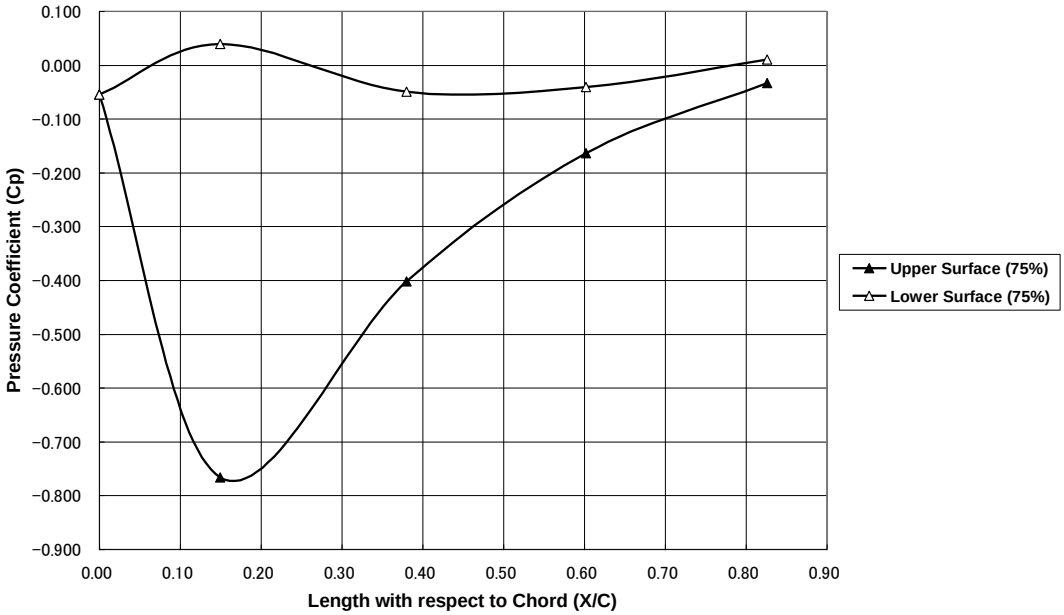

Figure 6.27c: Variation of Pressure with Chord Length for Aerofoil Shaped Fuselage UAV model at 75% from the root at 14° Angle of Attack.

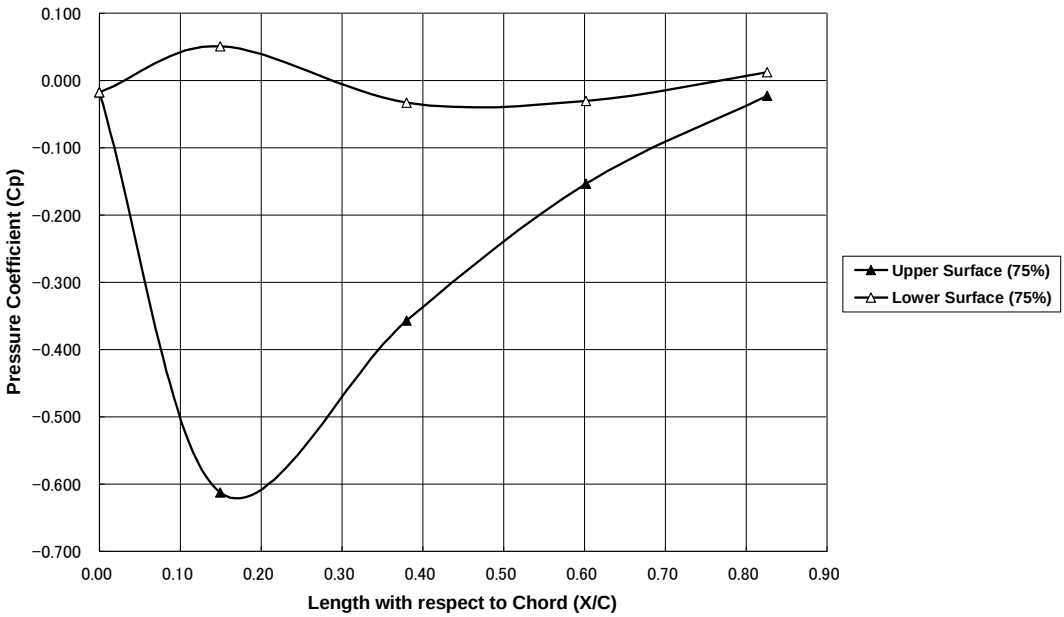

Figure 6.27d: Variation of Pressure with Chord Length for Aerofoil Shaped Fuselage UAV model at 75% from the root at 18° Angle of Attack.

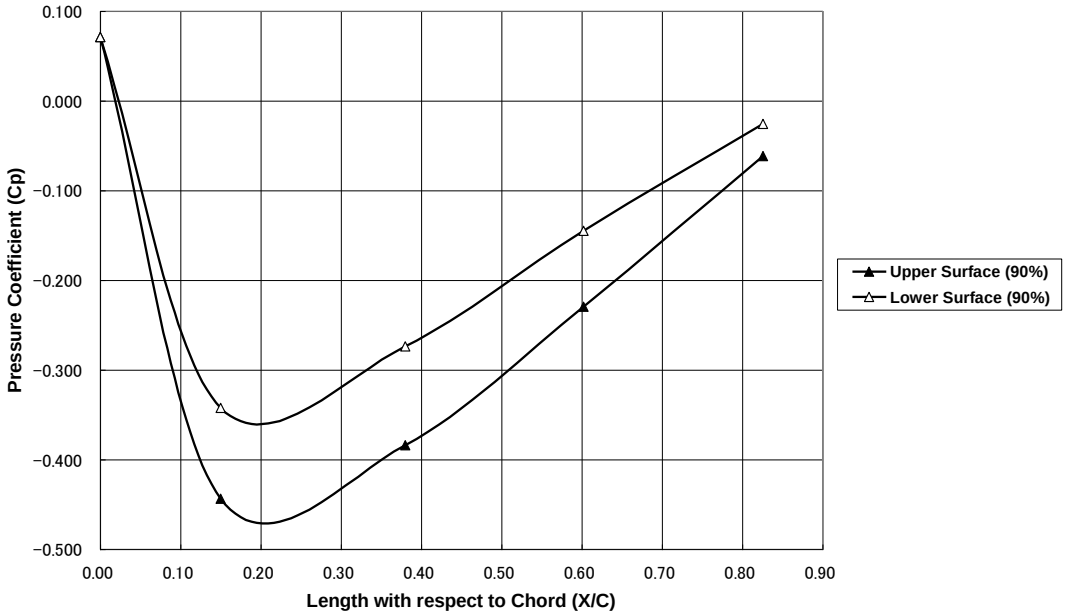

Figure 6.28a: Variation of Pressure with Chord Length for Aerofoil Shaped Fuselage UAV model at 90% from the root at 3° Angle of Attack.

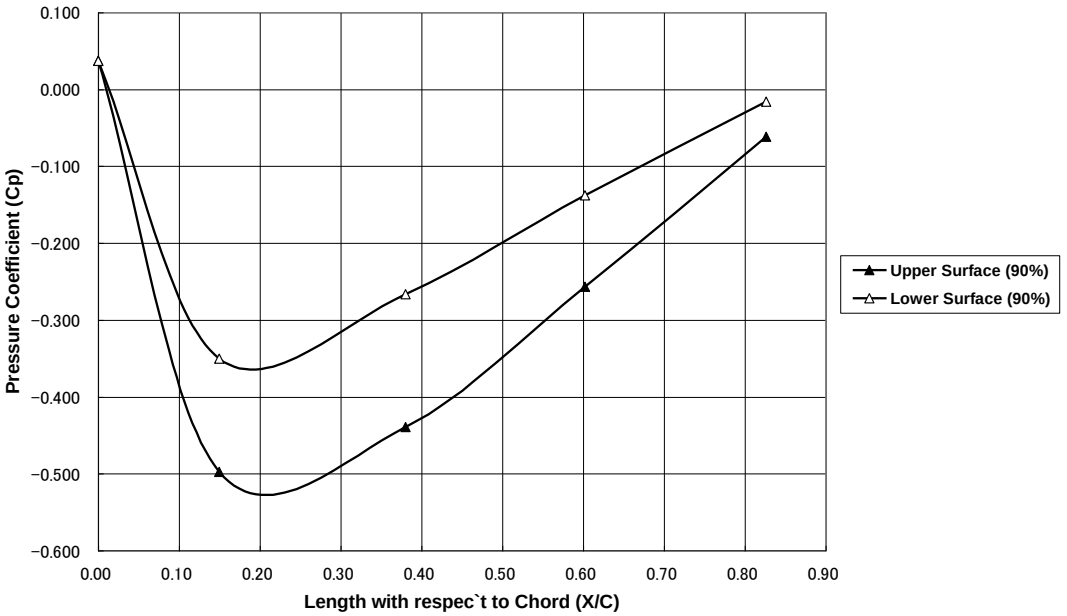

Figure 6.28b: Variation of Pressure with Chord Length for Aerofoil Shaped Fuselage UAV model at 90% from the root at 9° Angle of Attack.

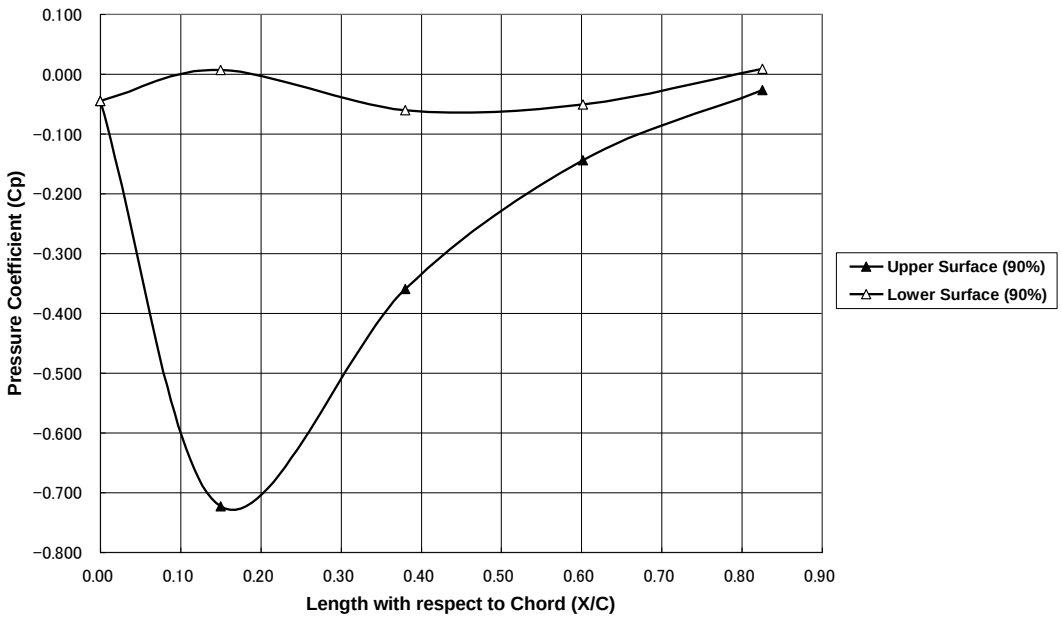

Figure 6.28c: Variation of Pressure with Chord Length for Aerofoil Shaped Fuselage UAV model at 90% from the root at 14° Angle of Attack.

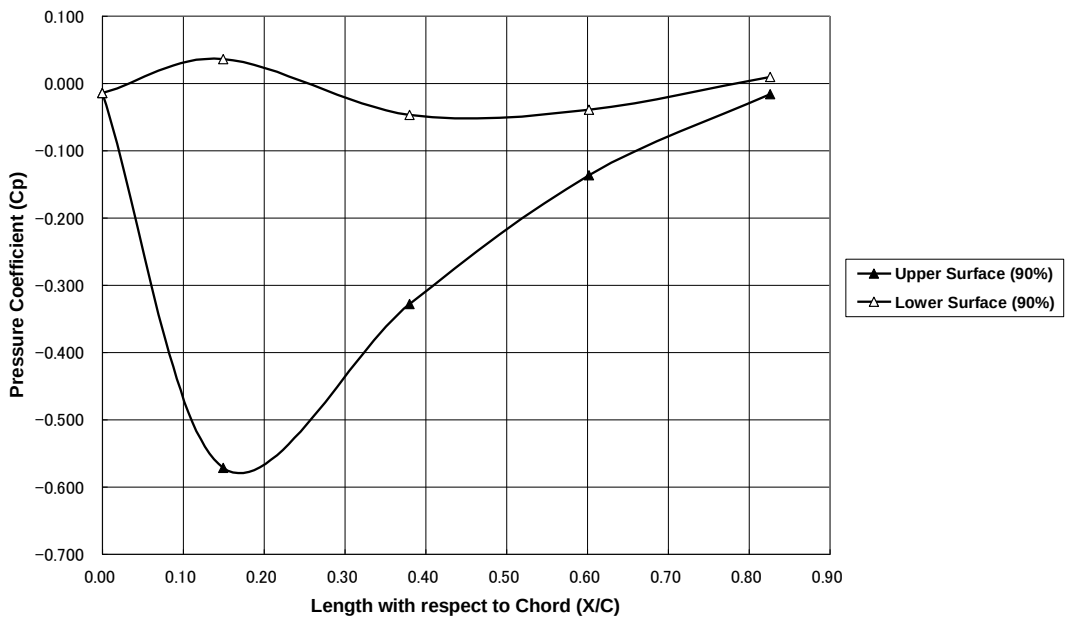

Figure 6.28d: Variation of Pressure with Chord Length for Aerofoil Shaped Fuselage UAV model at 90% from the root at 18° Angle of Attack.

TABLE 3: APPENDIX 'L' ON NUMERICAL AND FABRICATED ORDINATE OF NACA 4416 PROFILE

(Stations and Ordinates given in percent of airfoil chord)

NACA 4416 : Numerical Data of Wing Dimensions – (Scale Ratio - 1 : 1)

Upper Surface		Lower Surface	
Station (X – axis) in cm	**Ordinate (Y – axis) in cm**	**Station (X – axis) in cm**	**Ordinate (Y – axis) in cm**
0	---------	0	0
0.127842	0.313978	0.127842	-0.18307
0.255682	0.426478	0.255682	-0.25364
0.511364	0.587045	0.511364	-0.33444
0.767045	0.706705	0.767045	-0.37944
1.022727	0.801818	1.022727	-0.40705
1.534091	0.948069	1.534091	-0.42751
2.045455	1.048296	2.045455	-0.42444
2.556818	1.116818	2.556818	-0.40705
3.068182	1.150569	3.068182	-0.38353
4.090909	1.150569	4.090909	-0.33238
5.113636	1.076933	5.113636	-0.27818
6.136364	0.951136	6.136364	-0.21887
7.159091	0.780342	7.159091	-0.15853
8.181818	0.567615	8.181818	-0.10535
9.204545	0.315	9.204545	-0.05829
9.715909	0.170796	9.715909	-0.03682
10.0000	0.016364	10.0000	-0.01636
L.E. radius : 0.254545 Slope of radius through L.E. : 0.020455			

TABLE 3 (Continue): Fabricated Wing Dimensions of NACA 4416 Profile - (Scale Ratio - 1 : 0.55)

Upper Surface		Lower Surface	
Station (X – axis) in cm	**Ordinate (Y – axis) in cm**	**Station (X – axis) in cm**	**Ordinate (Y – axis) in cm**
0	---------	0	0
0.07	0.17	0.07	-0.10
0.14	0.24	0.14	-0.14
0.28	0.32	0.28	-0.18
0.42	0.39	0.42	-0.21
0.56	0.44	0.56	-0.22
0.84	0.52	0.84	-0.24
1.13	0.58	1.13	-0.23
1.41	0.61	1.41	-0.22
1.69	0.63	1.69	-0.21
2.25	0.63	2.25	-0.18
2.81	0.59	2.81	-0.15
3.38	0.52	3.38	-0.12
3.94	0.43	3.93	-0.09
4.50	0.31	4.50	-0.06
5.06	0.17	5.06	-0.03
5.34	0.094	5.34	-0.02
5.63	0.01	5.63	-0.01
L.E. radius : 0.14 Slope of radius through L.E. : 0.011			

TABLE 3 (Continue): Fabricated Aerofoil Shaped Fuselage Dimensions of NACA 4416 Profile – (Scale Ratio - 1 : 1.1)

Upper Surface		Lower Surface	
Station (X – axis) in cm	**Ordinate (Y – axis) in cm**	**Station (X – axis) in cm**	**Ordinate (Y – axis) in cm**
0	---------	0	0
0.14	0.35	0.14	-0.20
0.28	0.47	0.28	-0.28
0.56	0.65	0.56	-0.37
0.84	0.78	0.84	-0.42
1.13	0.88	1.13	-0.45
1.69	1.04	1.69	-0.47
2.25	1.15	2.25	-0.47
2.81	1.23	2.81	-0.45
3.38	1.27	3.38	-0.42
4.50	1.27	4.50	-0.37
5.63	1.18	5.63	-0.31
6.75	1.05	6.75	-0.24
7.88	0.86	7.88	-0.17
9.00	0.62	9.00	-0.12
10.13	0.35	10.13	-0.06
10.69	0.19	10.69	-0.04
11.25	0.02	11.25	-0.02
L.E. radius : 0.28 Slope of radius through L.E. : 0.023			

TABLE 3 (Continue): Fabricated Horizontal Stabilizer Dimensions of NACA 4416 Profile – (Scale Ratio - 1 : 0.165)

Upper Surface		Lower Surface	
Station (X – axis) in cm	**Ordinate (Y – axis) in cm**	**Station (X – axis) in cm**	**Ordinate (Y – axis) in cm**
0	-------	0	0
0.02	0.05	0.02	-0.03
0.04	0.07	0.04	-0.04
0.08	0.097	0.08	-0.06
0.13	0.12	0.13	-0.06
0.17	0.13	0.17	-0.07
0.25	0.16	0.25	-0.07
0.34	0.17	0.34	-0.07
0.42	0.18	0.42	-0.07
0.51	0.19	0.51	-0.06
0.68	0.19	0.68	-0.05
0.84	0.18	0.84	-0.05
1.01	0.16	1.01	-0.04
1.18	0.13	1.18	-0.03
1.35	0.09	1.35	-0.02
1.52	0.05	1.52	-0.01
1.60	0.03	1.60	-0.006
1.69	0.003	1.69	-0.003
L.E. radius : 0.04 Slope of radius through L.E. : 0.00034			

TABLE 3 (Continue): Fabricated Vertical Stabilizer Dimensions of NACA 4416 Profile – (Scale Ratio - 1 : 0.165)

Upper Surface		Lower Surface	
Station (X – axis) in cm	**Ordinate (Y – axis) in cm**	**Station (X – axis) in cm**	**Ordinate (Y – axis) in cm**
0	--------	0	-------
0.02	0.05	0.02	-0.05
0.04	0.07	0.04	-0.07
0.08	0.097	0.08	-0.097
0.13	0.12	0.13	-0.12
0.17	0.13	0.17	-0.13
0.25	0.16	0.25	-0.16
0.34	0.17	0.34	-0.17
0.42	0.18	0.42	-0.18
0.51	0.19	0.51	-0.19
0.68	0.190	0.68	-0.190
0.84	0.18	0.84	-0.18
1.01	0.16	1.01	-0.16
1.18	0.129	1.18	-0.13
1.35	0.094	1.35	-0.094
1.52	0.052	1.52	-0.052
1.60	0.03	1.60	-0.03
1.69	0.003	1.69	-0.003
L.E. radius : 0.04 Slope of radius through L.E. : 0.00034			

APPENDIX – 'M' TO FIGURE – 8.17 to 8.20

on *"Comparison of Pressure at Different Percentage from the Root of Conventional Cylindrical Shaped Fuselage UAV Model at 20 m/s"*

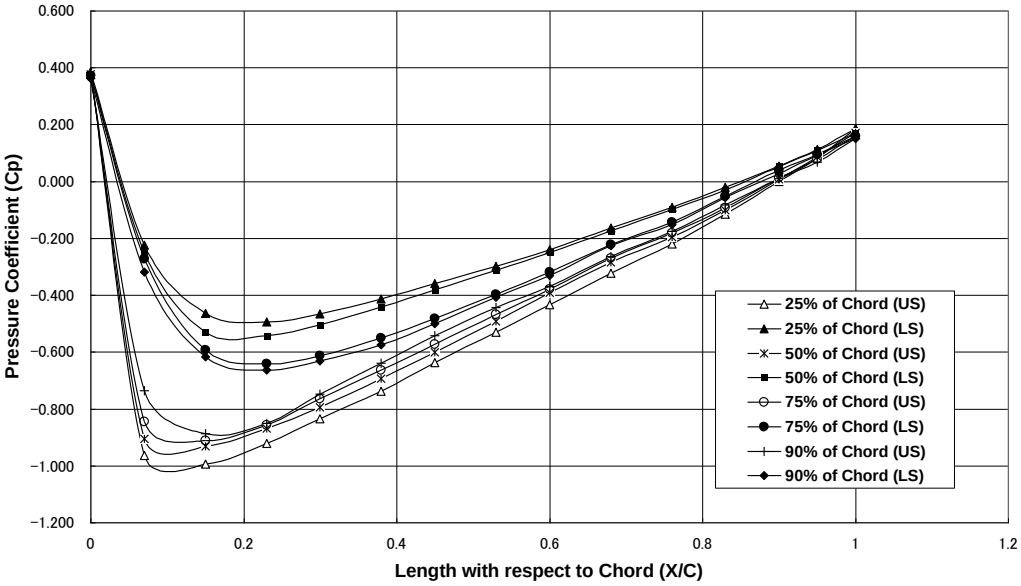

Figure 8.17: Surface Pressure at Different Percentage of Chord Length of Cylindrical Shaped Fuselage Model at 3° AOA and 20 m/s.

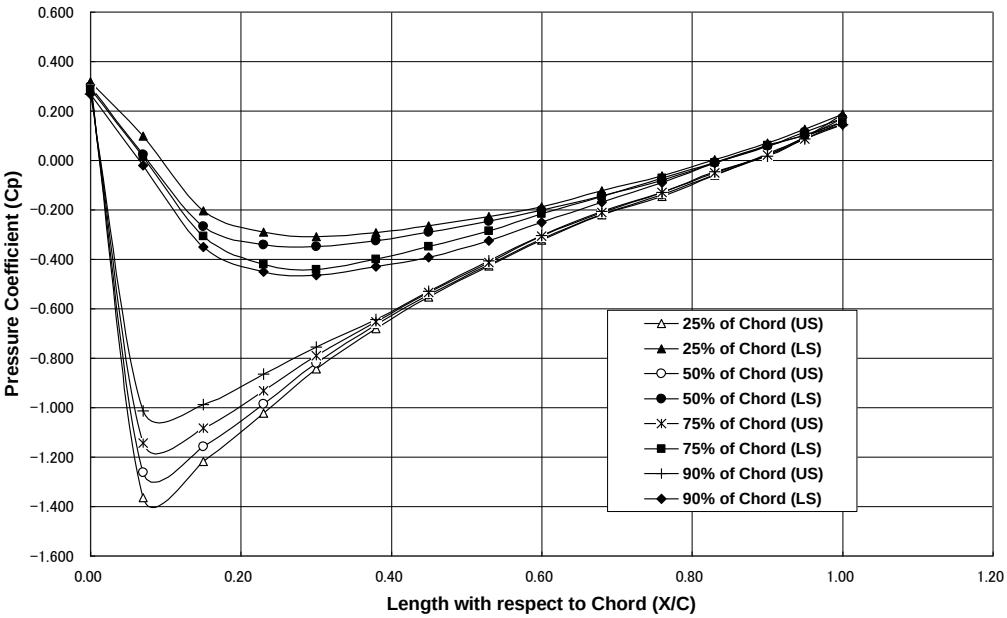

Figure 8.18: Surface Pressure at Different Percentage of Chord Length of Cylindrical Shaped Fuselage Model at 9° AOA and 20 m/s.

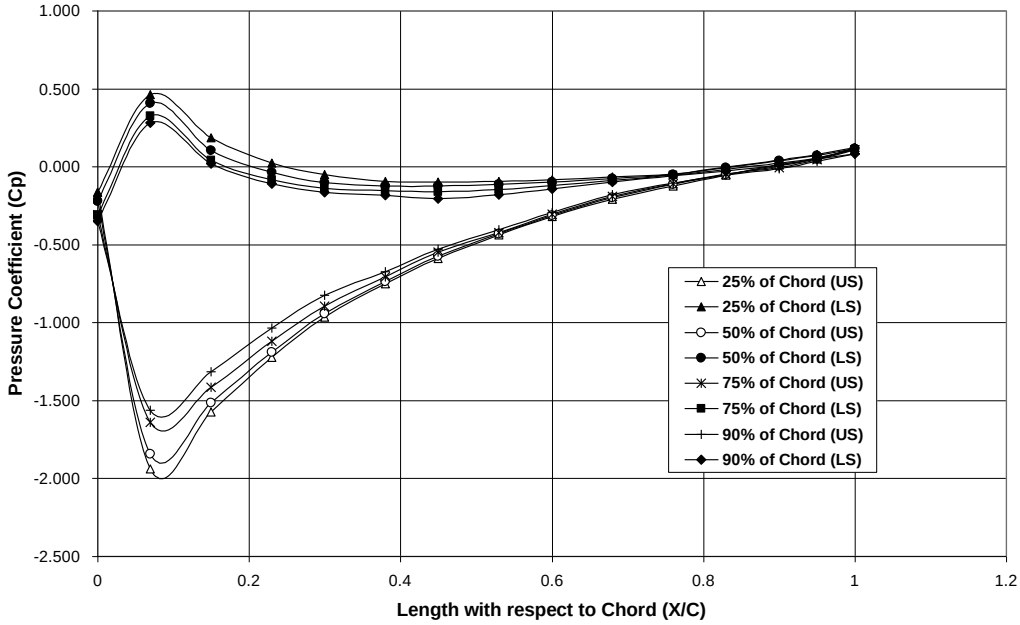

Figure 8.19: Surface Pressure at Different Percentage of Chord Length of Cylindrical Shaped Fuselage Model at 15° AOA and 20 m/s.

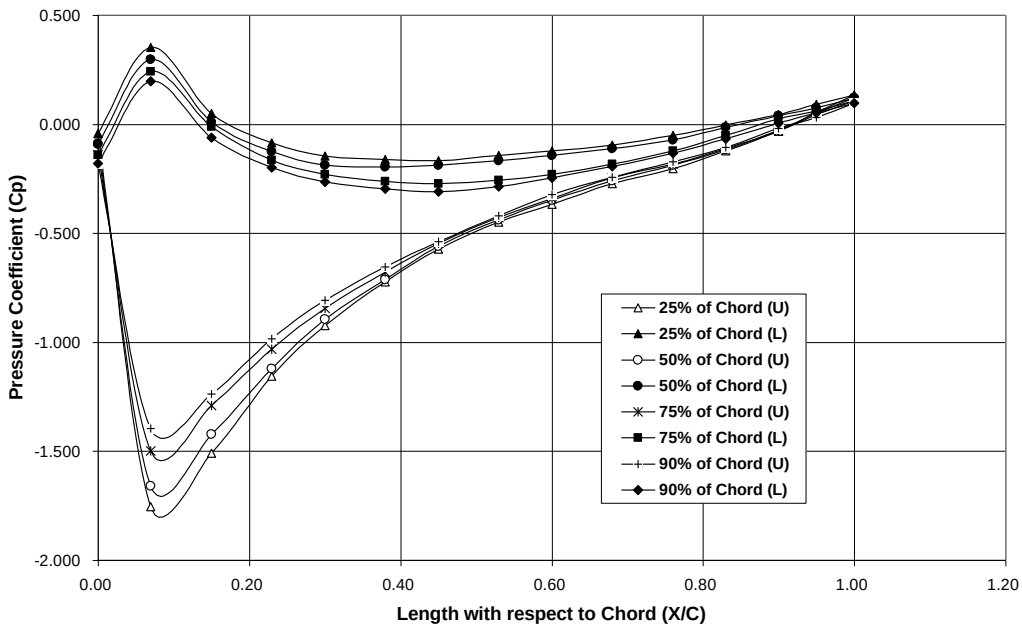

Figure 8.20: Surface Pressure at Different Percentage of Chord Length of Cylindrical Shaped Fuselage Model at 18°AOA and 20 m/s.

APPENDIX – 'N' TO FIGURE – 8.21 to 8.24

on *"Comparison of Pressure at Different Percentage from the Root of Aerofoil Shaped Fuselage UAV Model at 20 m/s"*

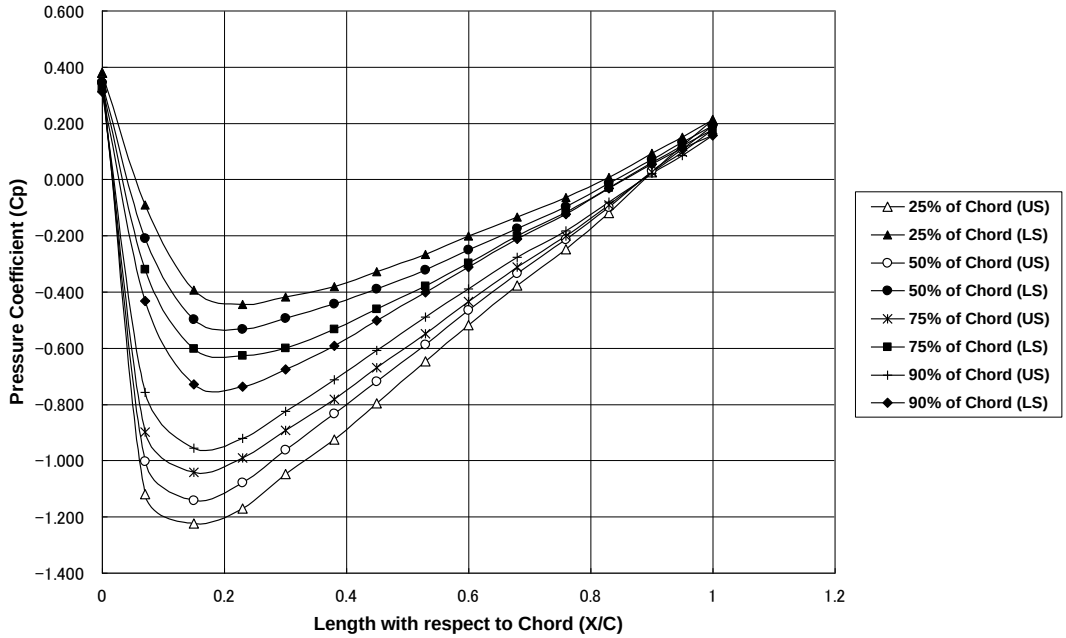

Figure 8.21: Surface Pressure at Different Percentage of Chord Length of Aerofoil Shaped Fuselage Model at 3° AOA and 20 m/s.

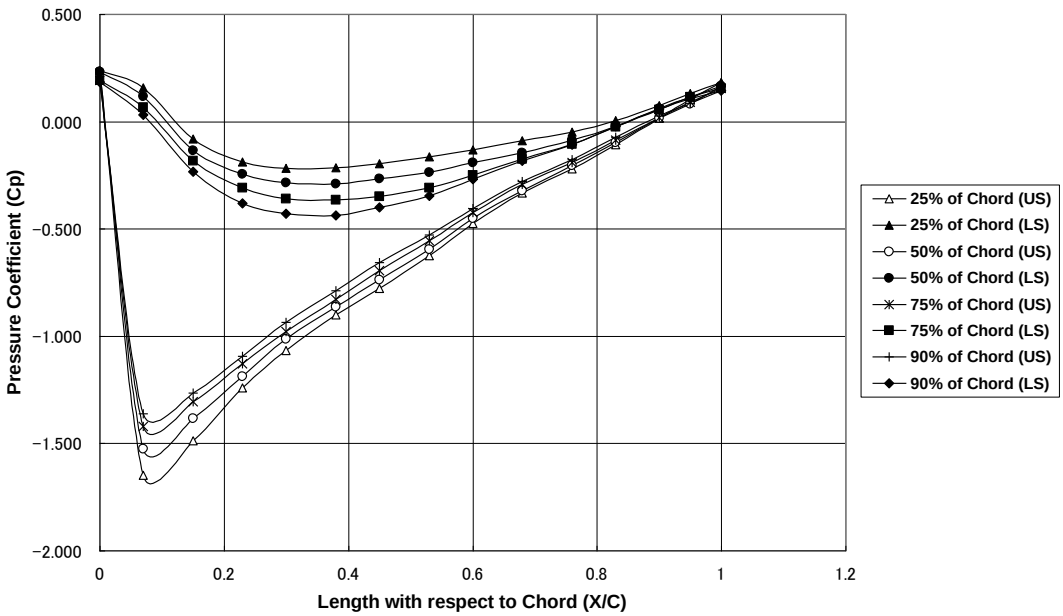

Figure 8.22: Surface Pressure at Different Percentage of Chord Length of Aerofoil Shaped Fuselage Model at 9° AOA and 20 m/s.

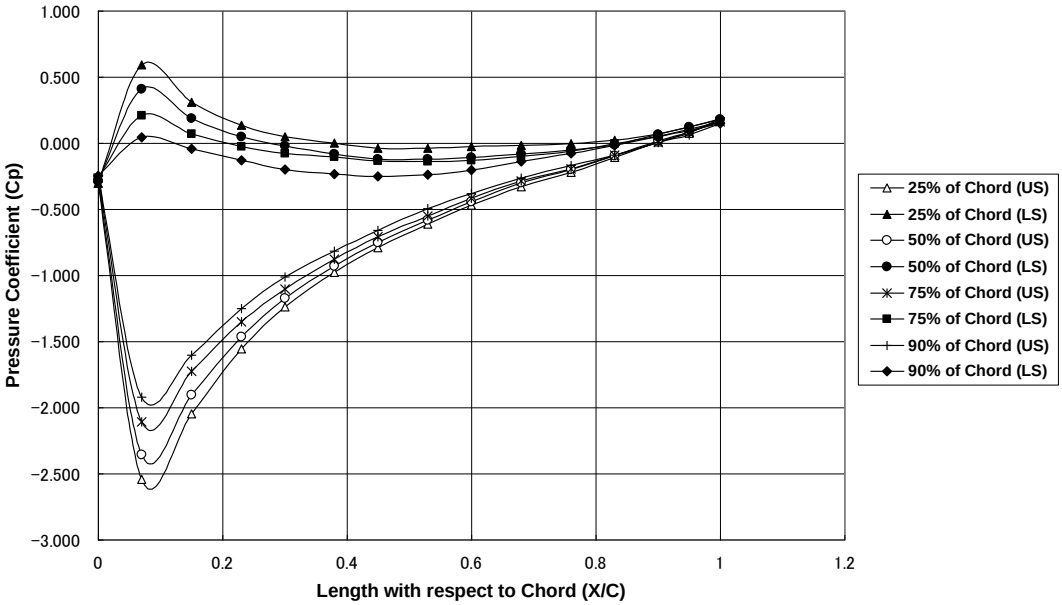

Figure 8.23: Surface Pressure at Different Percentage of Chord Length of Aerofoil Shaped Fuselage Model at 15° AOA and 20 m/s.

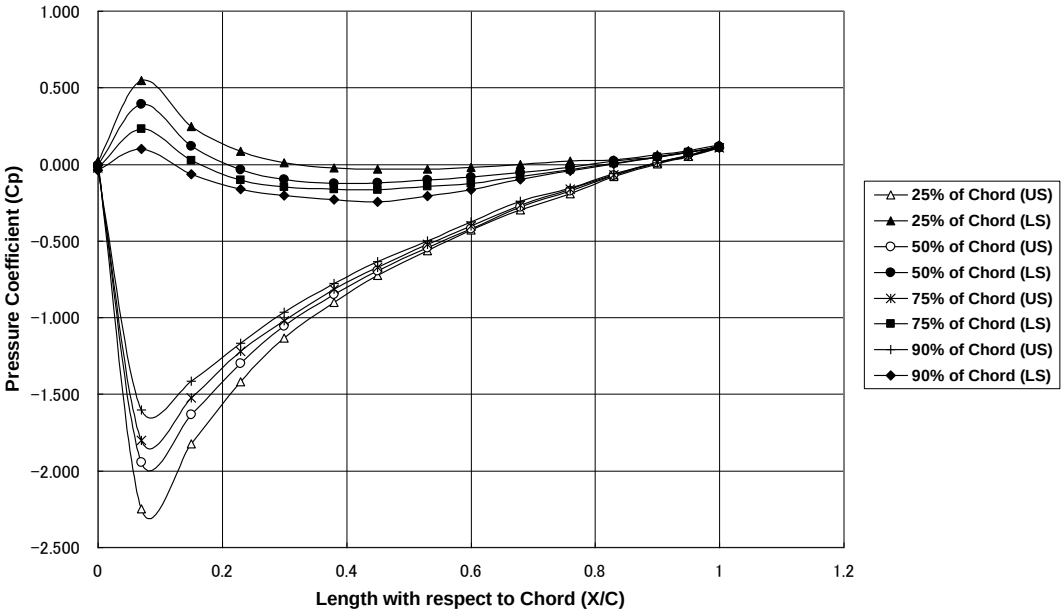

Figure 8.24: Surface Pressure at Different Percentage of Chord Length of Aerofoil Shaped Fuselage Model at 18°AOA and 20 m/s.

APPENDIX – 'P' TO FIGURE - 8.25 to 8.28

on *"Comparison of Pressure at Different Percentage from the Root of Conventional Cylindrical Shaped Fuselage UAV Model at 40 m/s"*

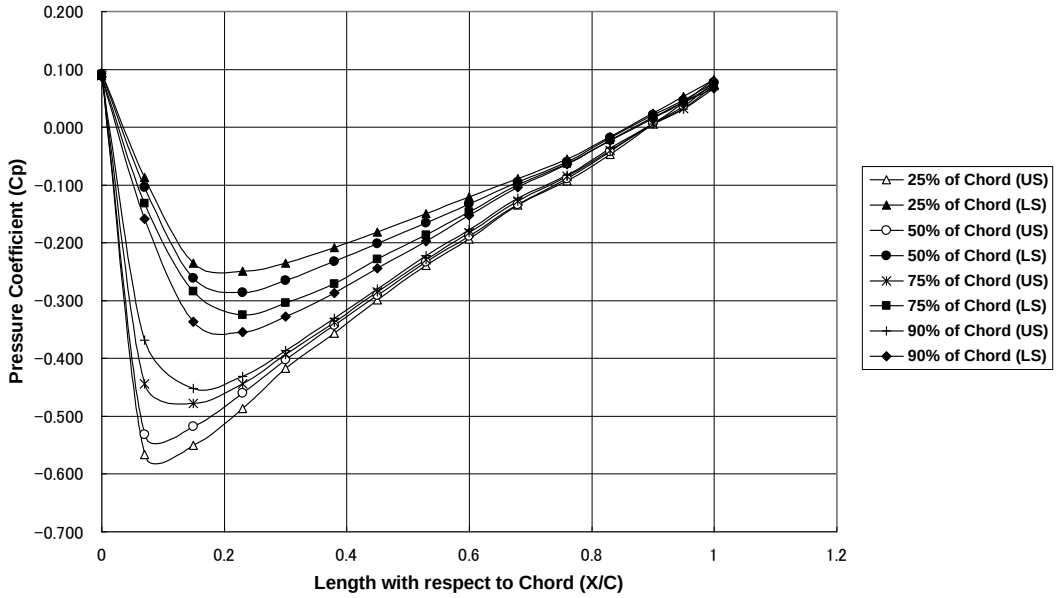

Figure 8.25: Surface Pressure at Different Percentage of Chord Length of Cylindrical Shaped Fuselage Model at 3° AOA and 40 m/s.

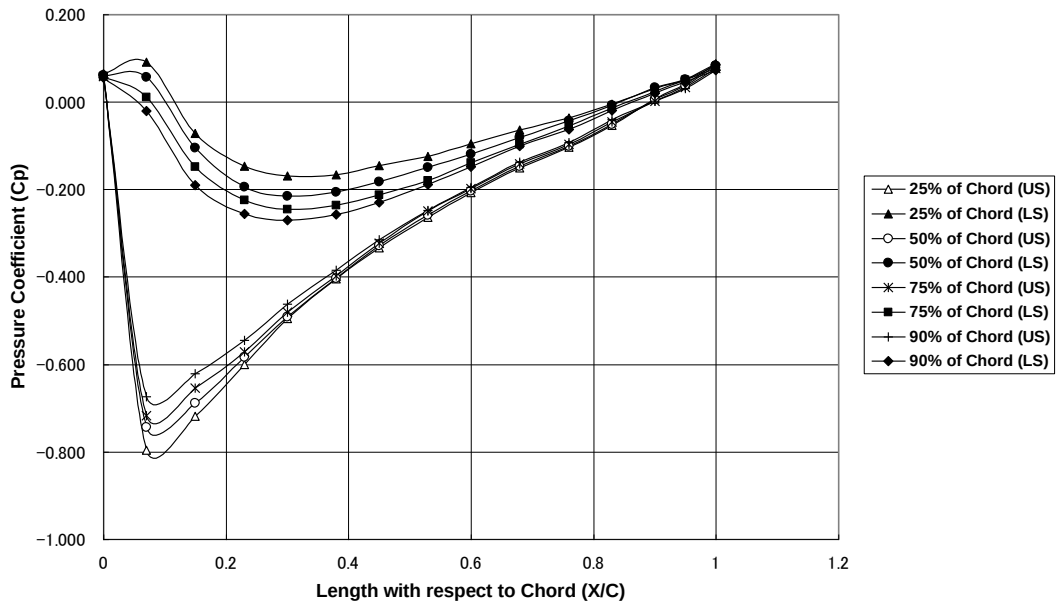

Figure 8.26: Surface Pressure at Different Percentage of Chord Length of Cylindrical Shaped Fuselage Model at 9° AOA and 40 m/s.

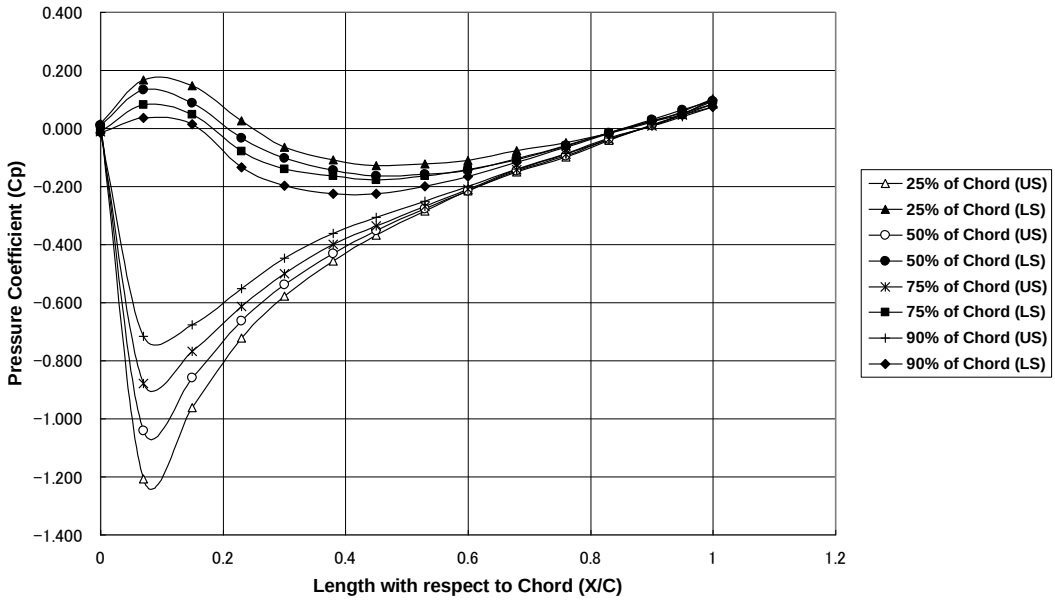

Figure 8.27: Surface Pressure at Different Percentage of Chord Length of Cylindrical Shaped Fuselage Model at 15° AOA and 40 m/s.

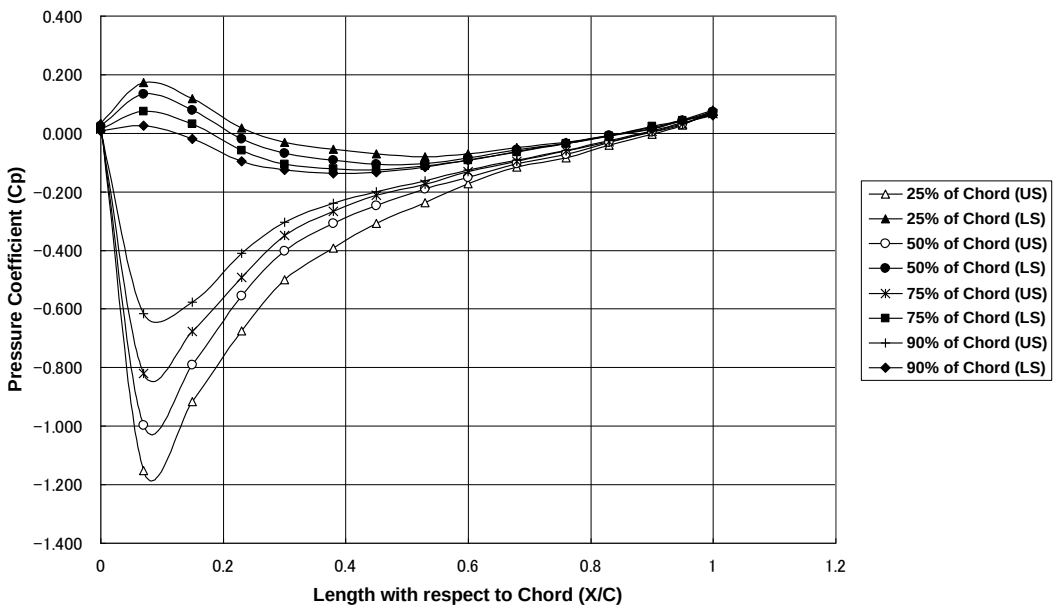

Figure 8.28: Surface Pressure at Different Percentage of Chord Length of Cylindrical Shaped Fuselage Model at 18°AOA and 20 m/s.

APPENDIX – 'Q' TO FIGURE – 8.29 to 8.32

on *"Comparison of Pressure at Different Percentage from the Root of Aerofoil Shaped Fuselage UAV Model at 40 m/s"*

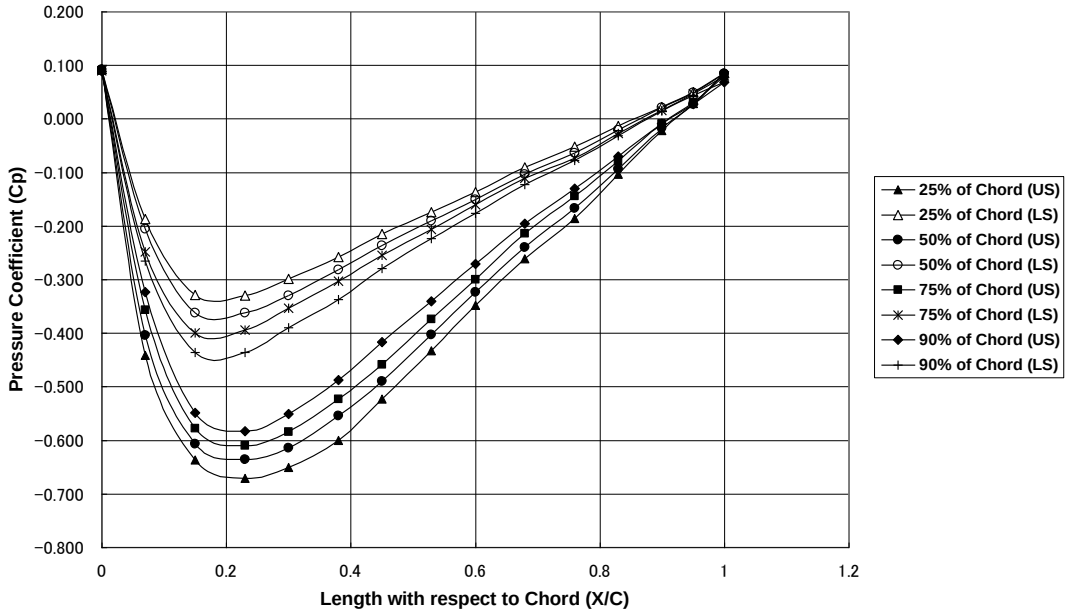

Figure 8.29: Surface Pressure at Different Percentage of Chord Length of Aerofoil Shaped Fuselage Model at 3° AOA and 40 m/s.

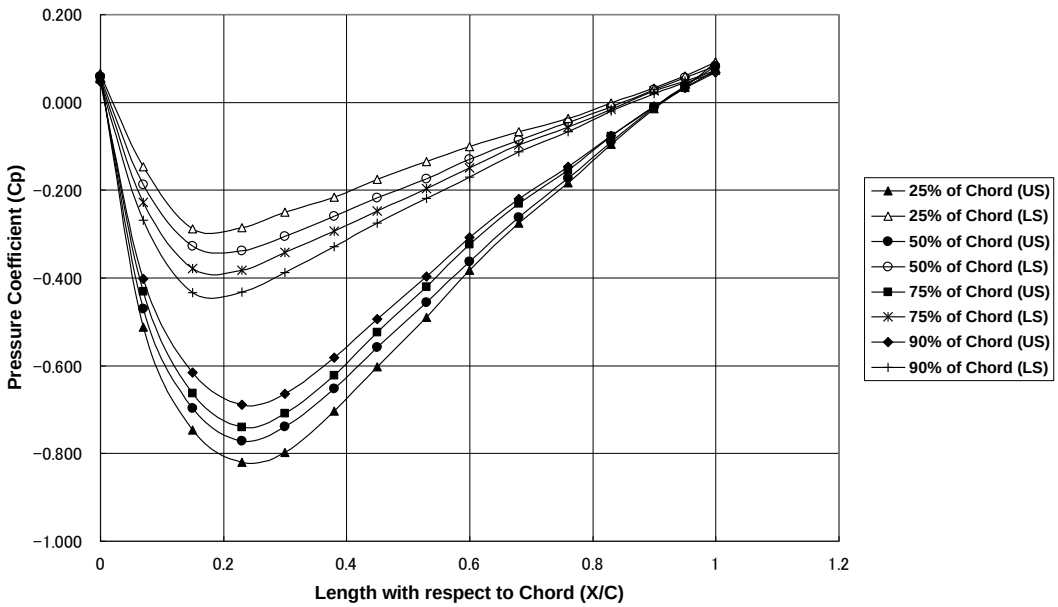

Figure 8.30: Surface Pressure at Different Percentage of Chord Length of Aerofoil Shaped Fuselage Model at 9° AOA and 40 m/s.

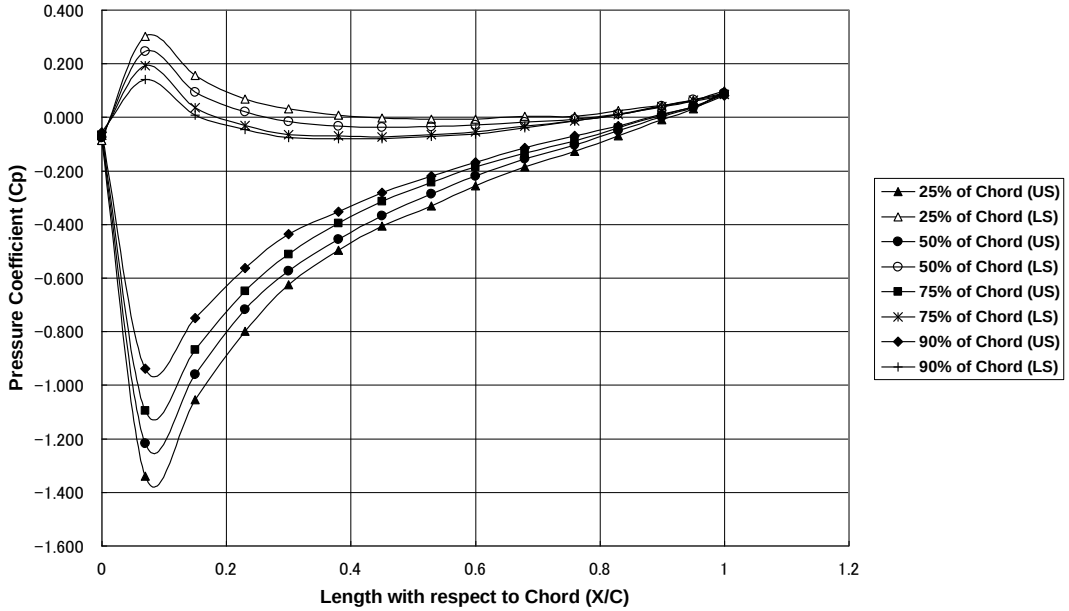

Figure 8.31: Surface Pressure at Different Percentage of Chord Length of Aerofoil Shaped Fuselage Model at 15° AOA and 40 m/s.

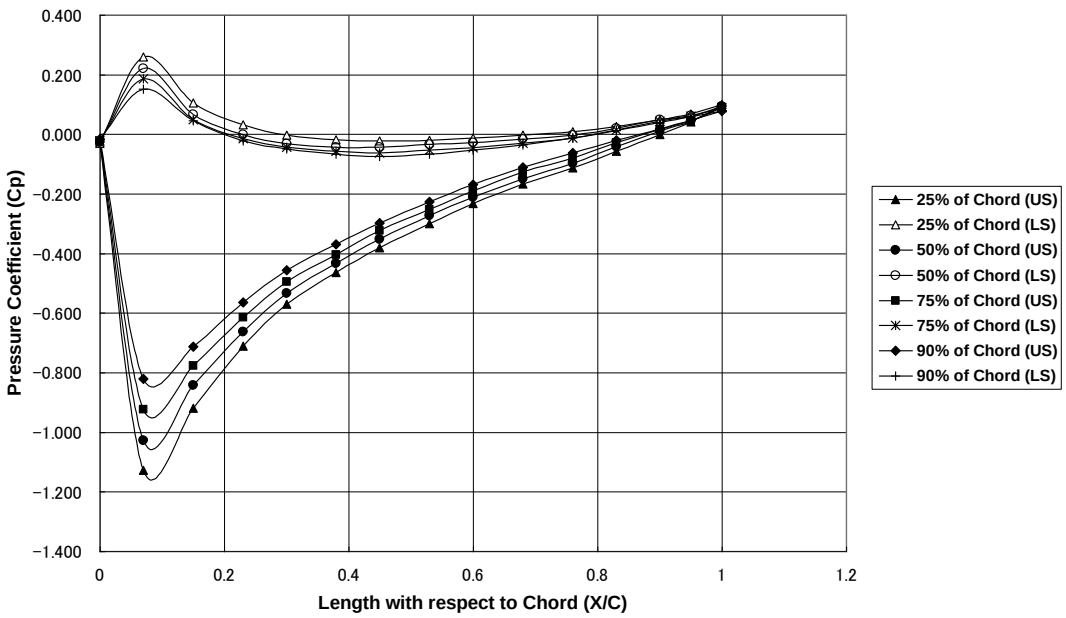

Figure 8.32: Surface Pressure at Different Percentage of Chord Length of Aerofoil Shaped Fuselage Model at 18°AOA and 40 m/s.

APPENDIX – 'R' TO FIGURE – 9.19 to 9.22

on *"Comparison of Pressure at Different Percentage from the Root of Conventional Cylindrical Shaped Fuselage UAV Model at 20 m/s"*

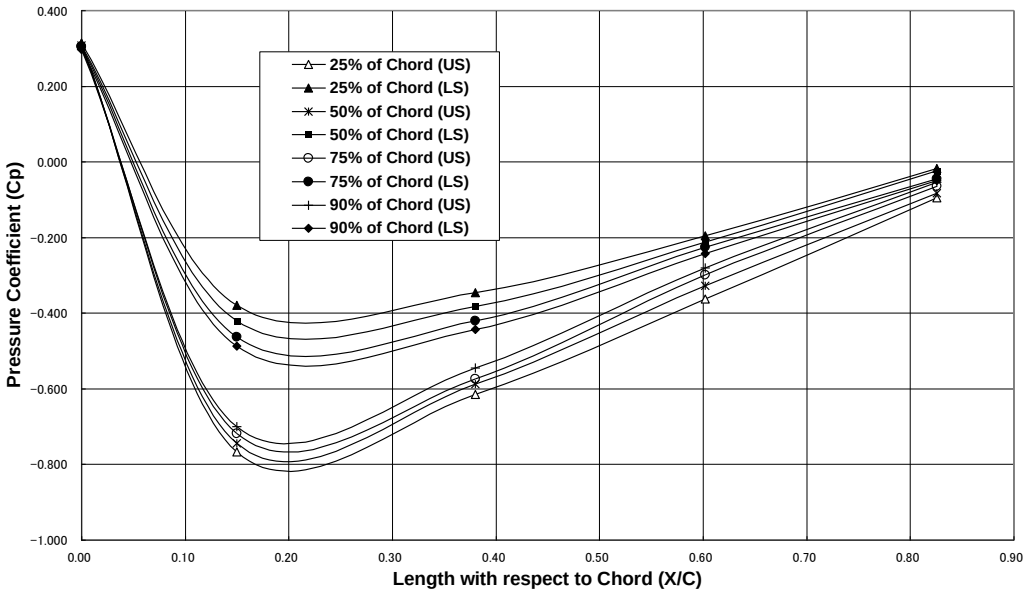

Figure 9.19: Surface Pressure at Different Percentage of Chord Length of Cylindrical Shaped Fuselage Model at 3° AOA and 20 m/s.

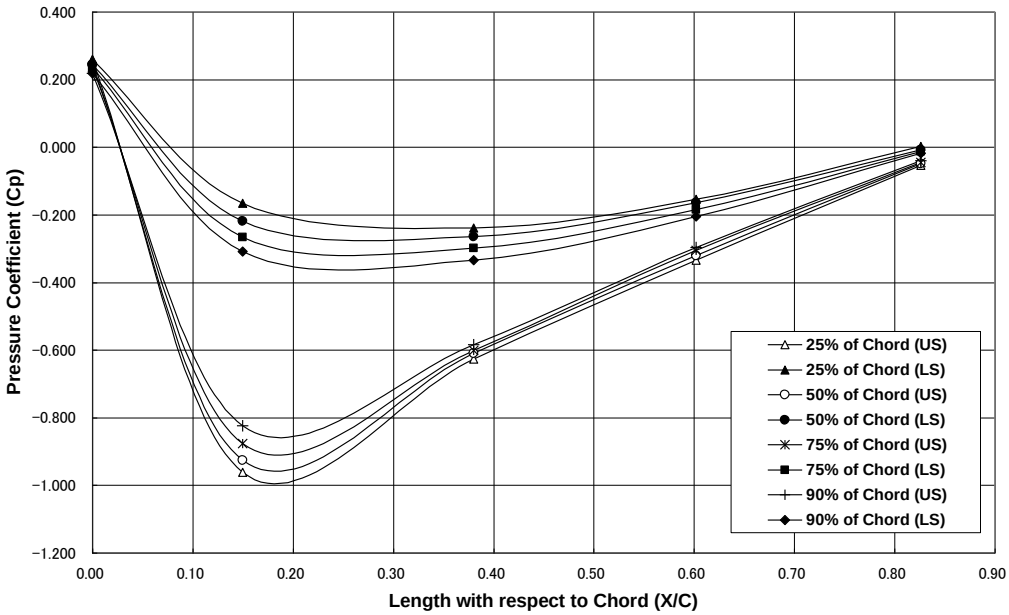

Figure 9.20: Surface Pressure at Different Percentage of Chord Length of Cylindrical Shaped Fuselage Model at 9° AOA and 20 m/s.

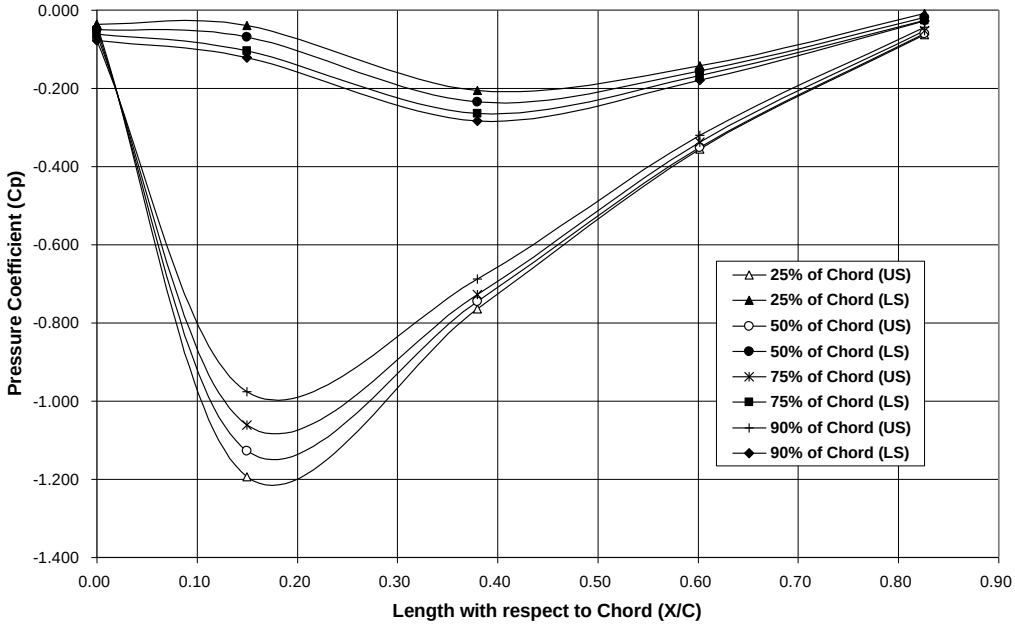

Figure 9.21: Surface Pressure at Different Percentage of Chord Length of Cylindrical Shaped Fuselage Model at 14° AOA and 20 m/s.

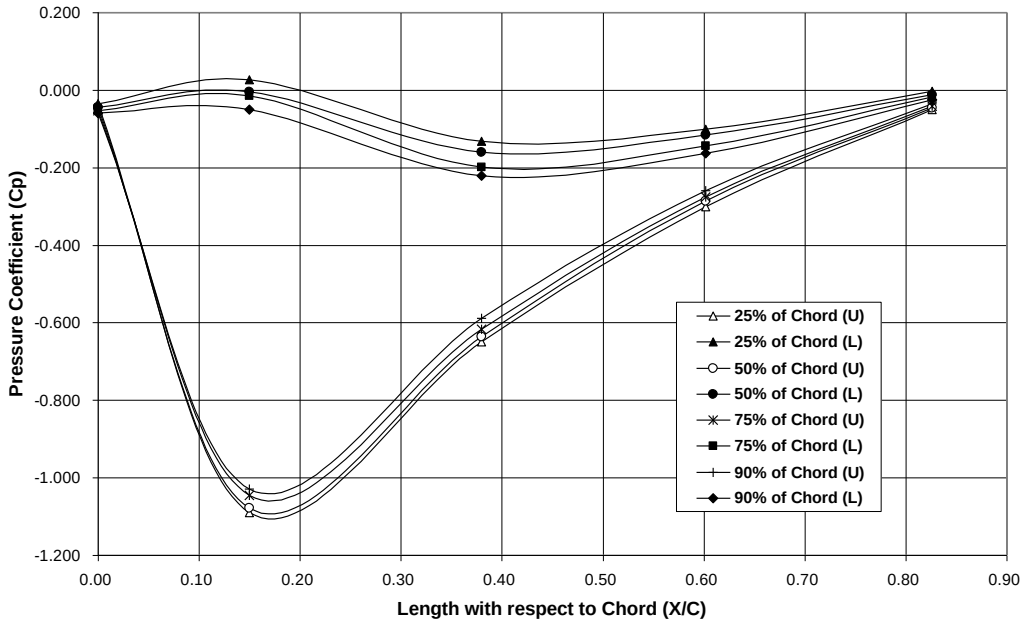

Figure 9.22: Surface Pressure at Different Percentage of Chord Length of Cylindrical Shaped Fuselage Model at 18°AOA and 20 m/s.

APPENDIX – 'S' TO FIGURE – 9.23 to 9.26

on *"Comparison of Pressure at Different Percentage from the Root of Aerofoil Shaped Fuselage UAV Model at 20 m/s"*

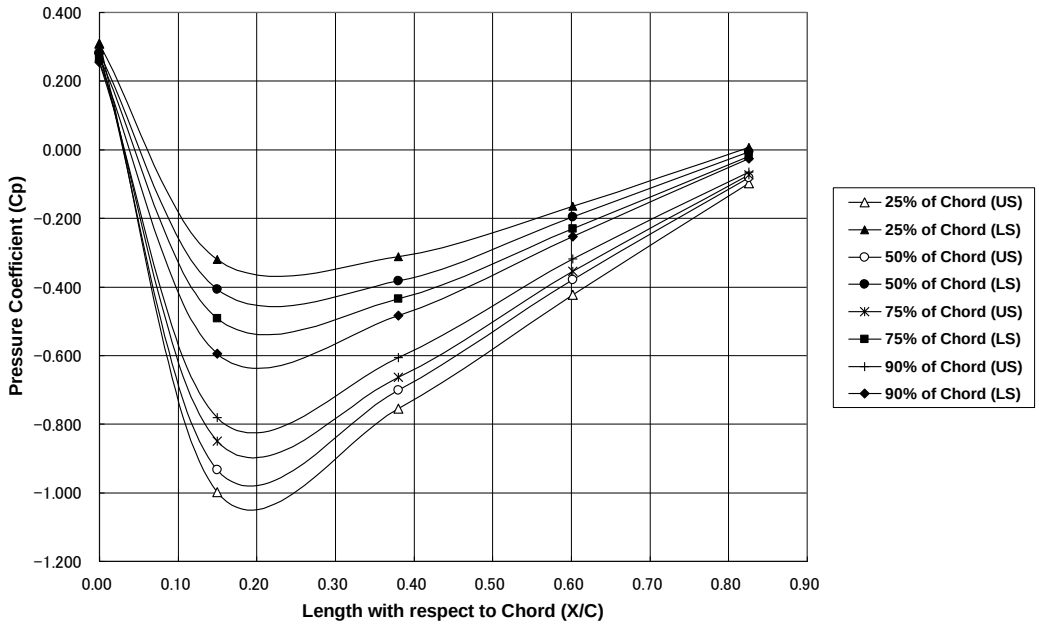

Figure 9.23: Surface Pressure at Different Percentage of Chord Length of Aerofoil Shaped Fuselage Model at 3° AOA and 20 m/s.

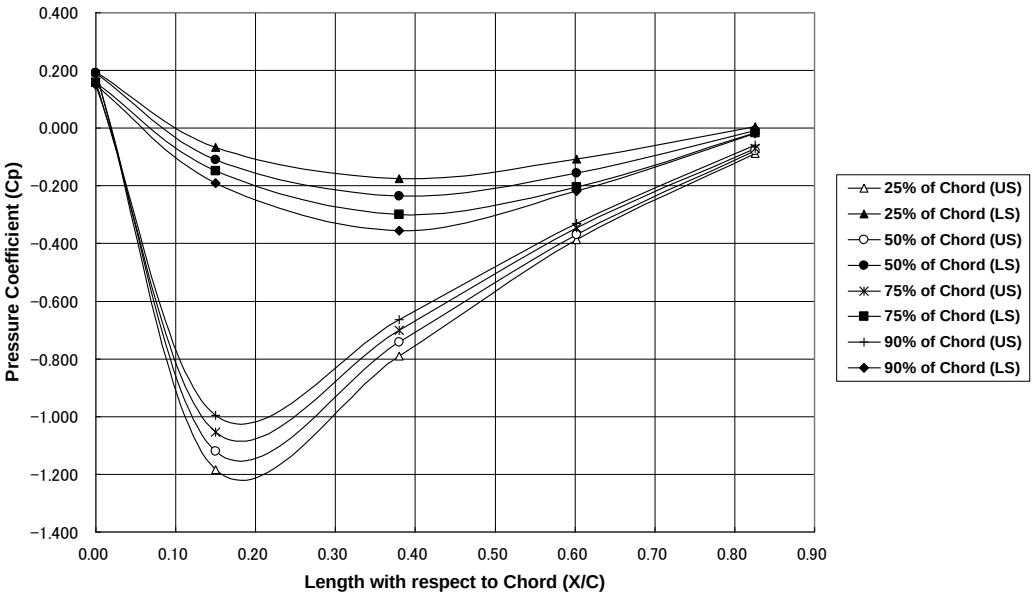

Figure 9.24: Surface Pressure at Different Percentage of Chord Length of Aerofoil Shaped Fuselage Model at 9° AOA and 20 m/s.

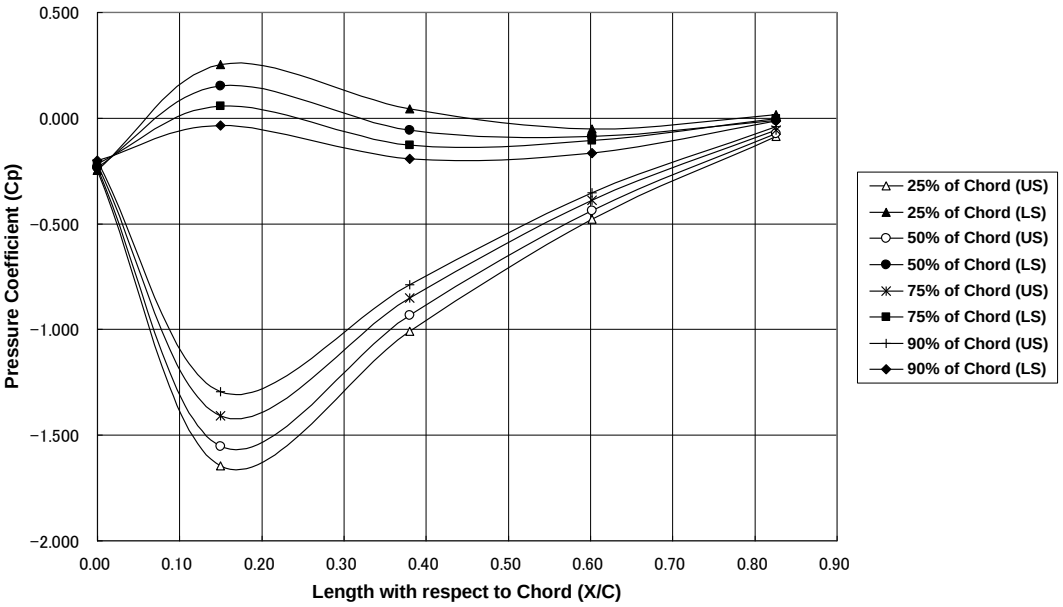

Figure 9.25: Surface Pressure at Different Percentage of Chord Length of Aerofoil Shaped Fuselage Model at 14° AOA and 20 m/s.

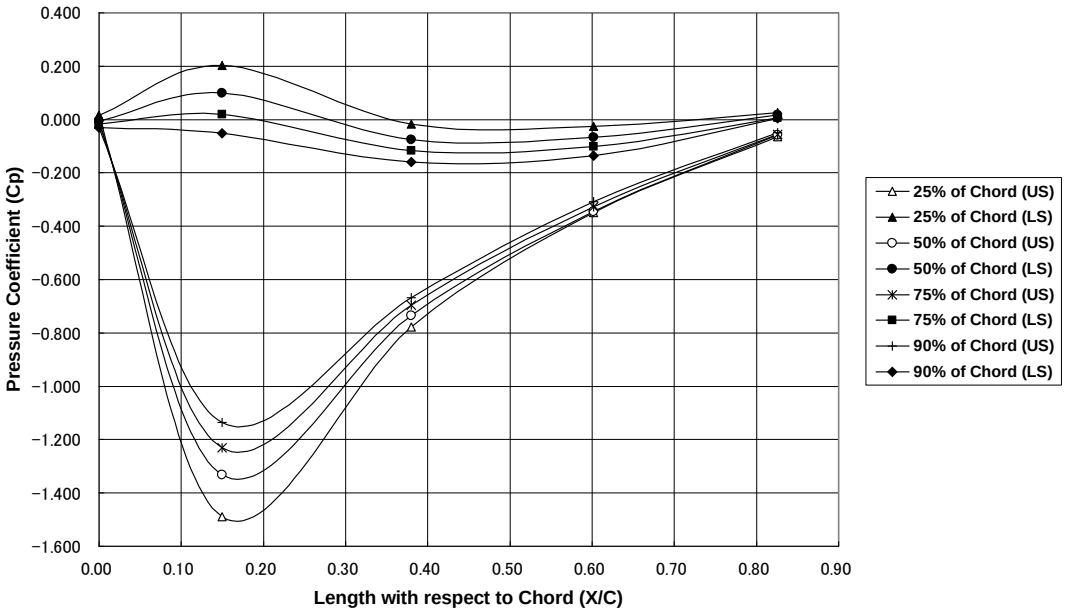

Figure 9.26: Surface Pressure at Different Percentage of Chord Length of Aerofoil Shaped Fuselage Model at 18°AOA and 20 m/s.

APPENDIX – 'T' TO FIGURE – 9.27 to 9.30

on *"Comparison of Pressure at Different Percentage from the Root of Conventional Cylindrical Shaped Fuselage UAV Model at 40 m/s"*

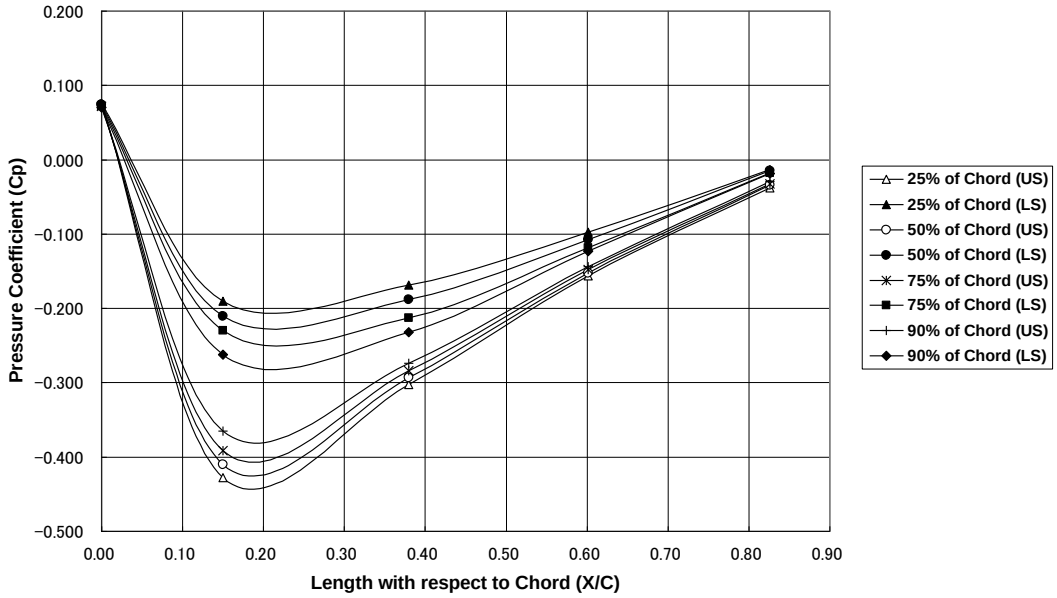

Figure 9.27: Surface Pressure at Different Percentage of Chord Length of Cylindrical Shaped Fuselage Model at 3° AOA and 40 m/s.

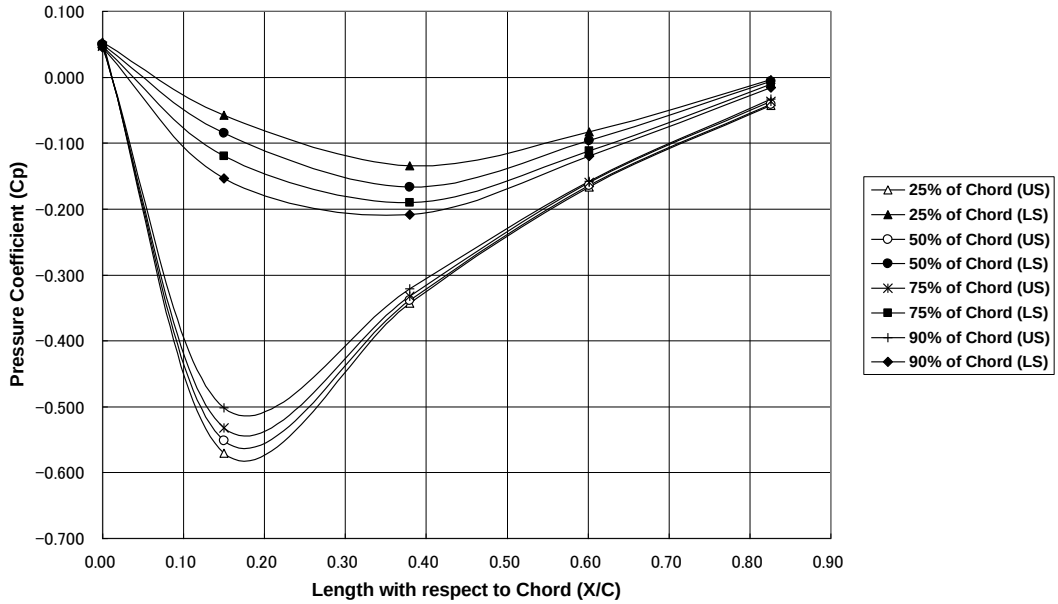

Figure 9.28: Surface Pressure at Different Percentage of Chord Length of Cylindrical Shaped Fuselage Model at 9° AOA and 40 m/s.

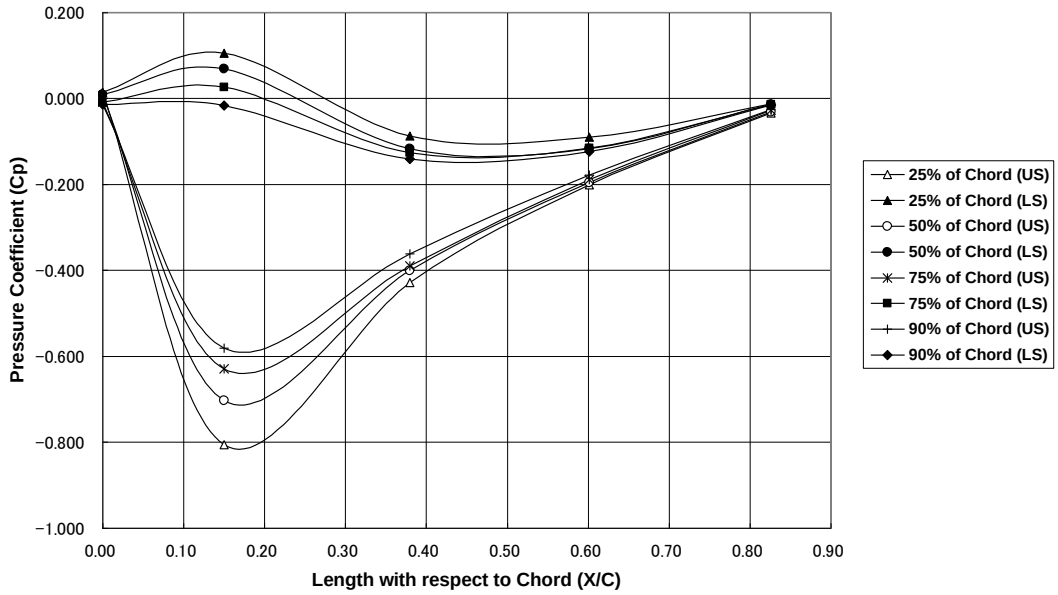

Figure 9.29: Surface Pressure at Different Percentage of Chord Length of Cylindrical Shaped Fuselage Model at 14° AOA and 40 m/s.

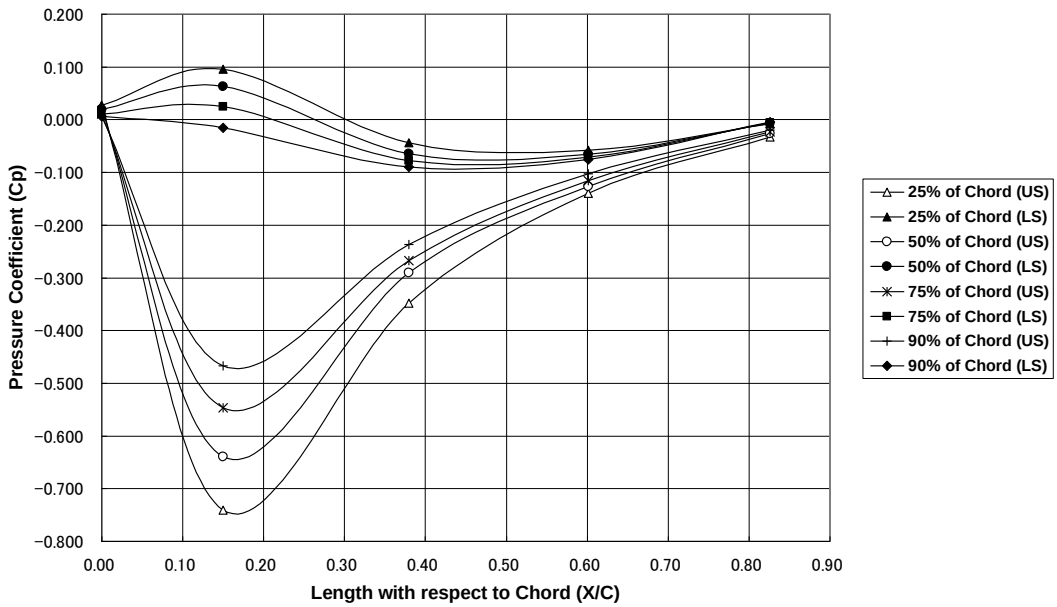

Figure 9.30: Surface Pressure at Different Percentage of Chord Length of Cylindrical Shaped Fuselage Model at 18°AOA and 20 m/s.

APPENDIX – 'U' TO FIGURE – 9.31 to 9.34

on *"Comparison of Pressure at Different Percentage from the Root of Aerofoil Shaped Fuselage UAV Model at 40 m/s"*

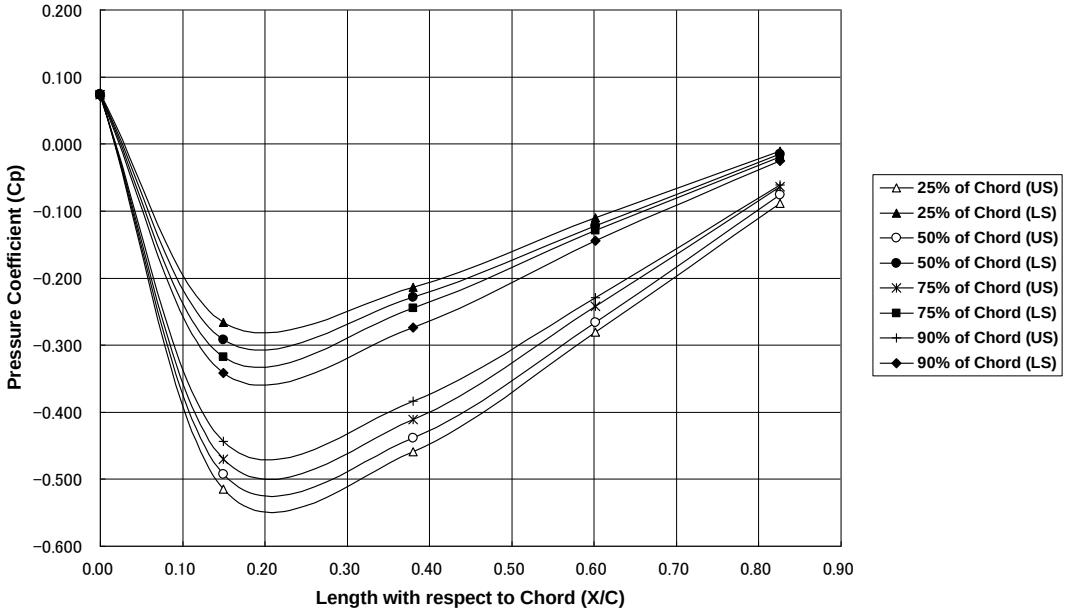

Figure 9.31: Surface Pressure at Different Percentage of Chord Length of Aerofoil Shaped Fuselage Model at 3° AOA and 40 m/s.

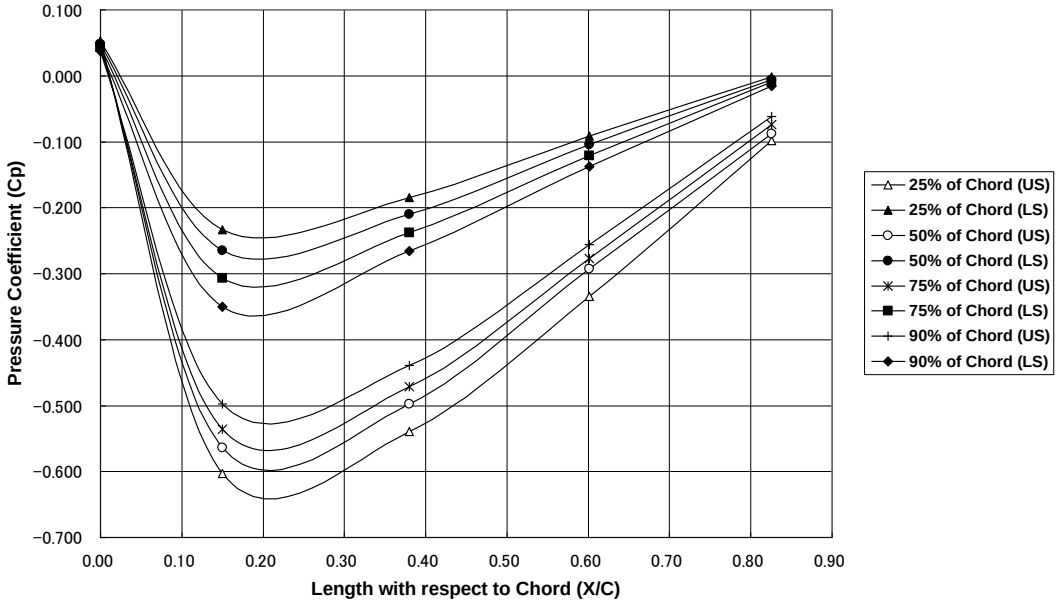

Figure 9.32: Surface Pressure at Different Percentage of Chord Length of Aerofoil Shaped Fuselage Model at 9° AOA and 40 m/s.

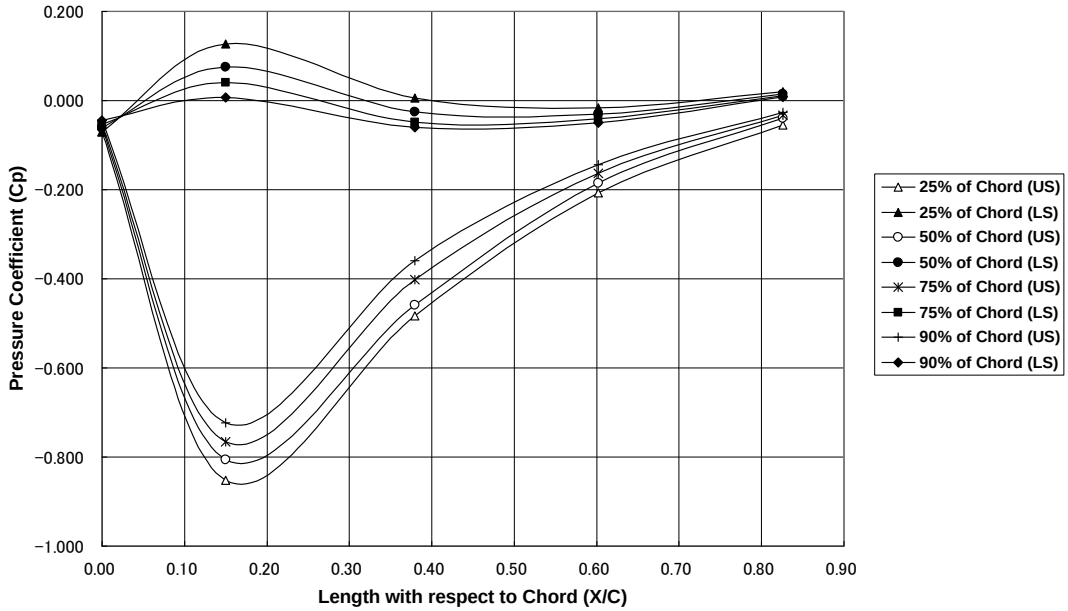

Figure 9.33: Surface Pressure at Different Percentage of Chord Length of Aerofoil Shaped Fuselage Model at 14°AOA and 40 m/s.

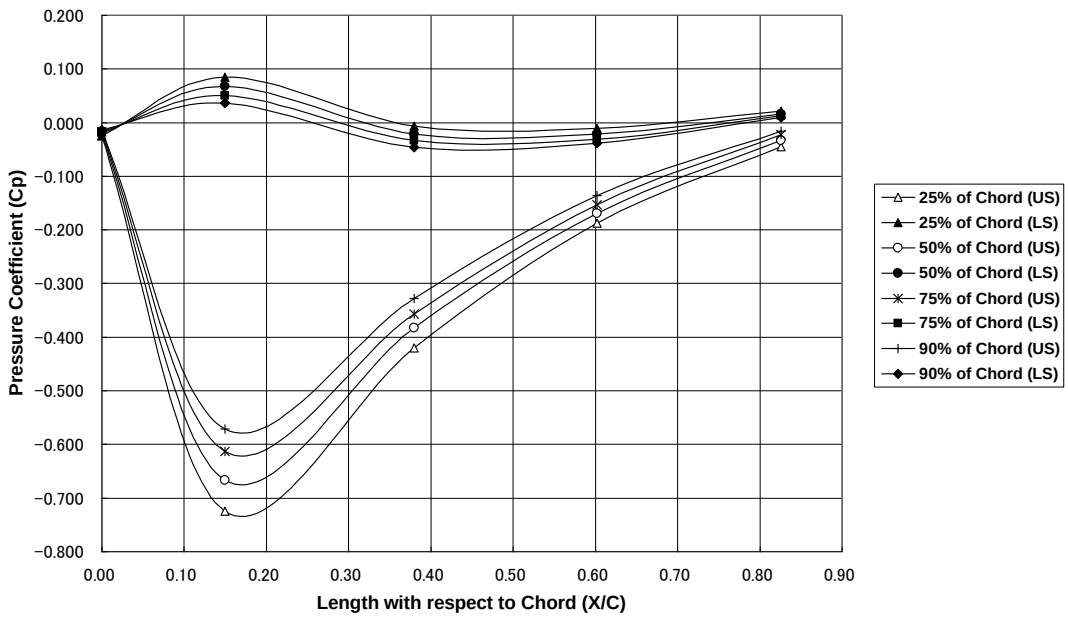

Figure 9.34: Surface Pressure at Different Percentage of Chord Length of Aerofoil Shaped Fuselage Model at 18° AOA and 40 m/s.

APPENDIX – 'F' TO FIGURE 4.40, 4.41, 4.42 and 4.43

on *"Surface Pressure of Aerofoil Shaped Fuselage at 40 m/s"*

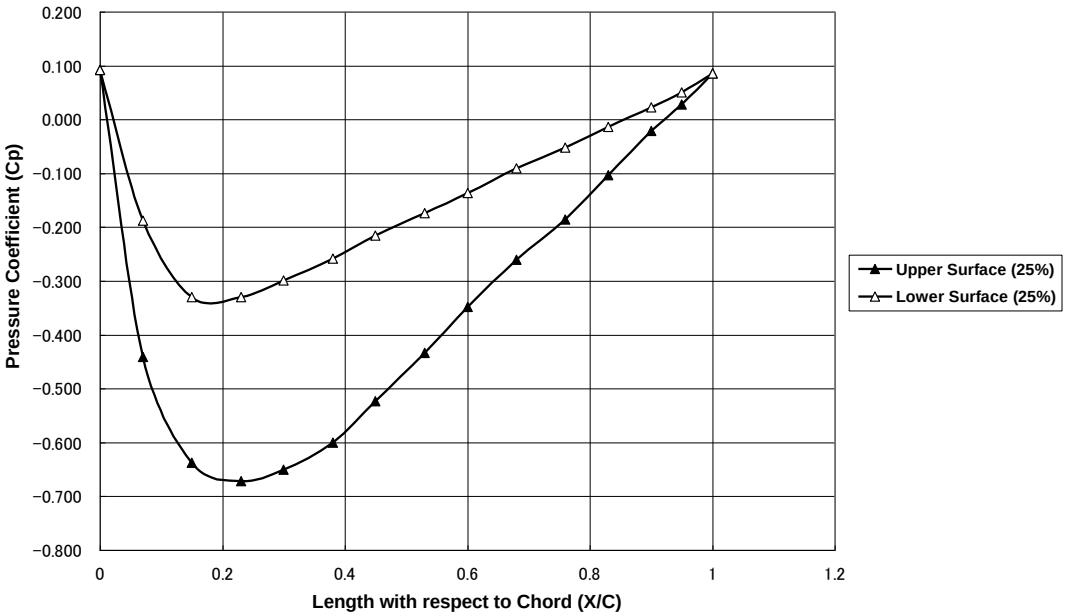

Figure 4.40a: Variation of Pressure with Chord Length for Aerofoil Shaped Fuselage UAV model at 25% from the root at 3° Angle of Attack.

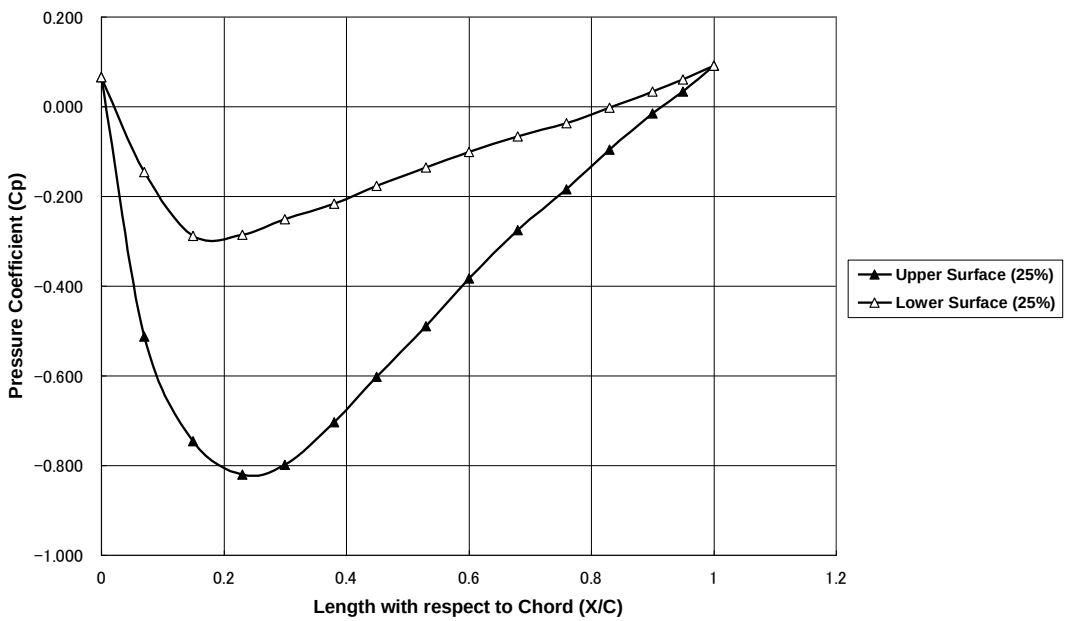

Figure 4.40b: Variation of Pressure with Chord Length for Aerofoil Shaped Fuselage UAV model at 25% from the root at 9° Angle of Attack.

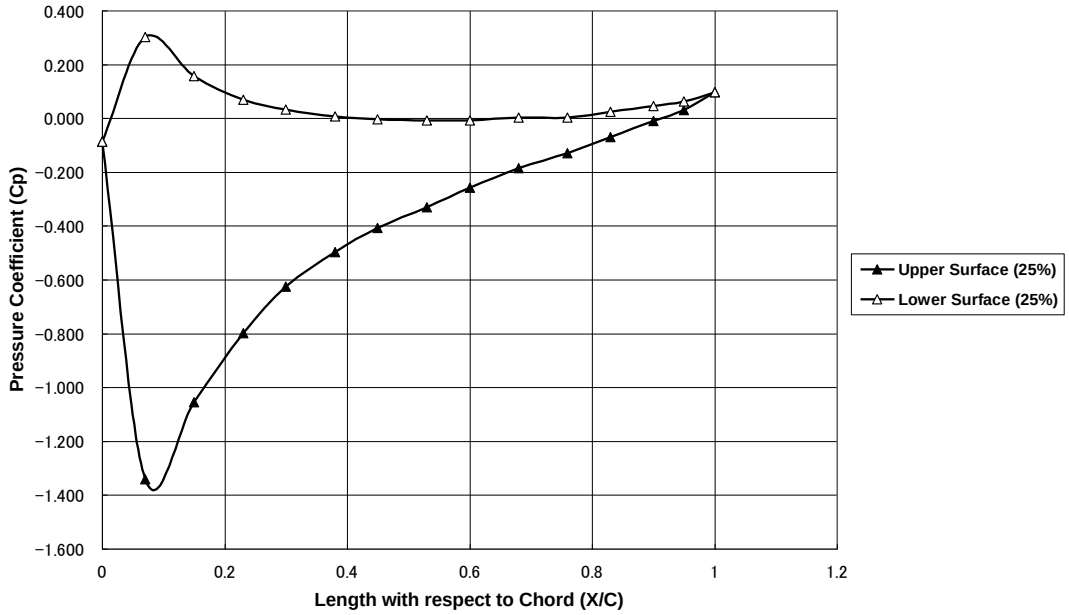

Figure 4.40c: Variation of Pressure with Chord Length for Aerofoil Shaped Fuselage UAV model at 25% from the root at 15° Angle of Attack.

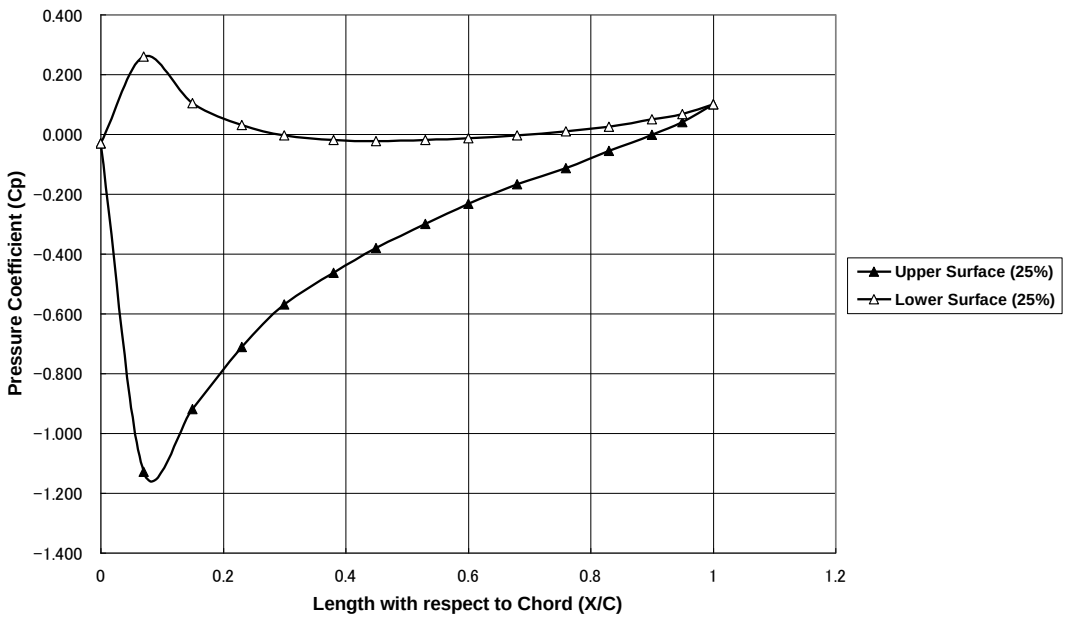

Figure 4.40d: Variation of Pressure with Chord Length for Aerofoil Shaped Fuselage UAV model at 25% from the root at 18° Angle of Attack.

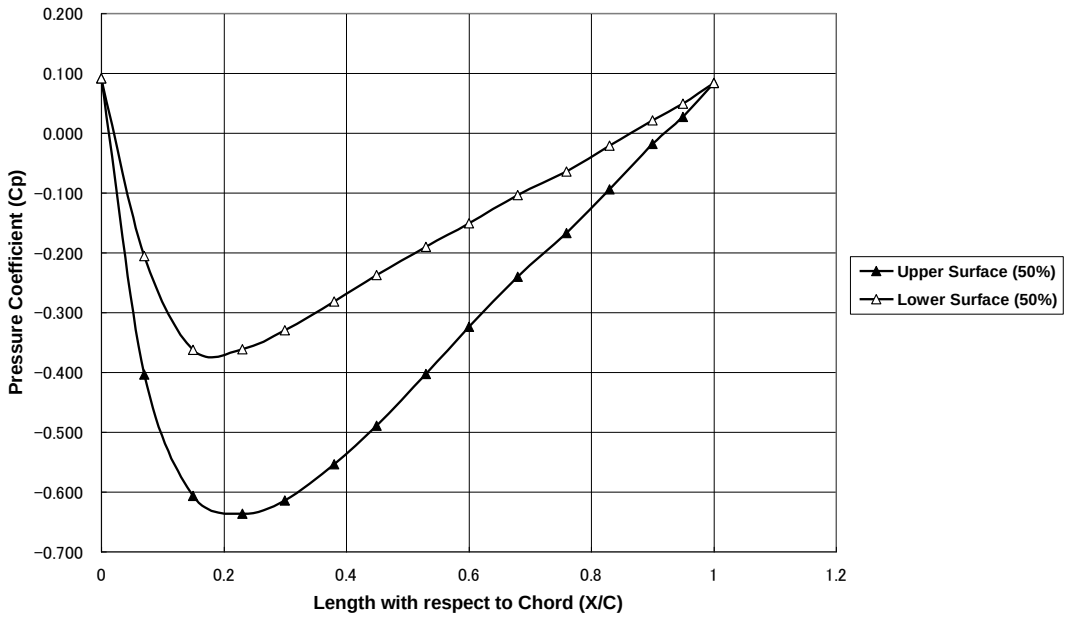

Figure 4.41a: Variation of Pressure with Chord Length for Aerofoil Shaped Fuselage UAV model at 50% from the root at 3° Angle of Attack.

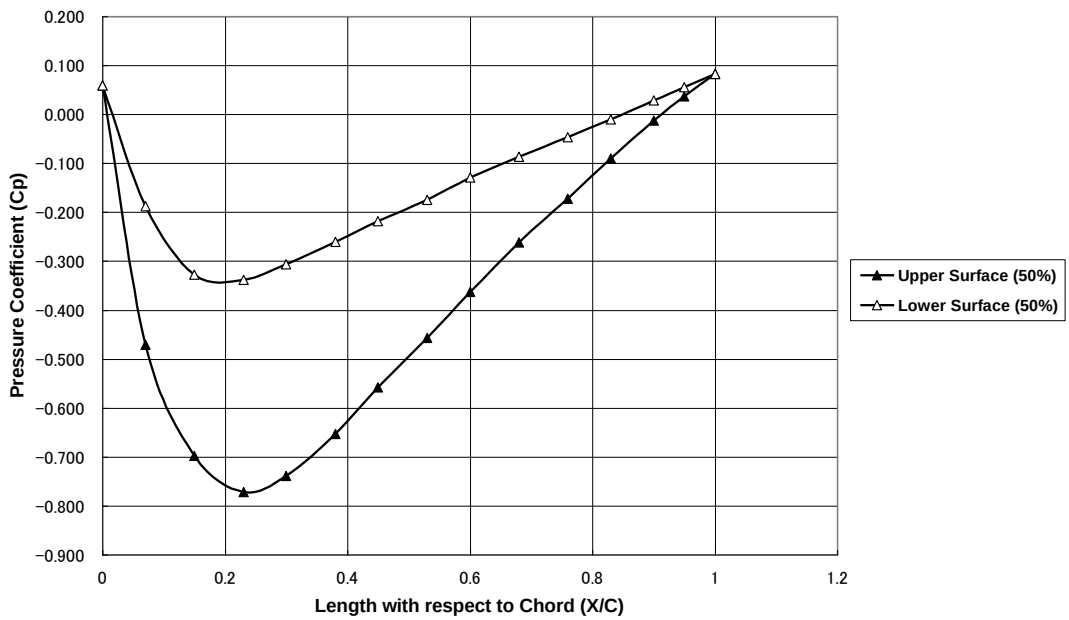

Figure 4.41b: Variation of Pressure with Chord Length for Aerofoil Shaped Fuselage UAV model at 50% from the root at 9° Angle of Attack.

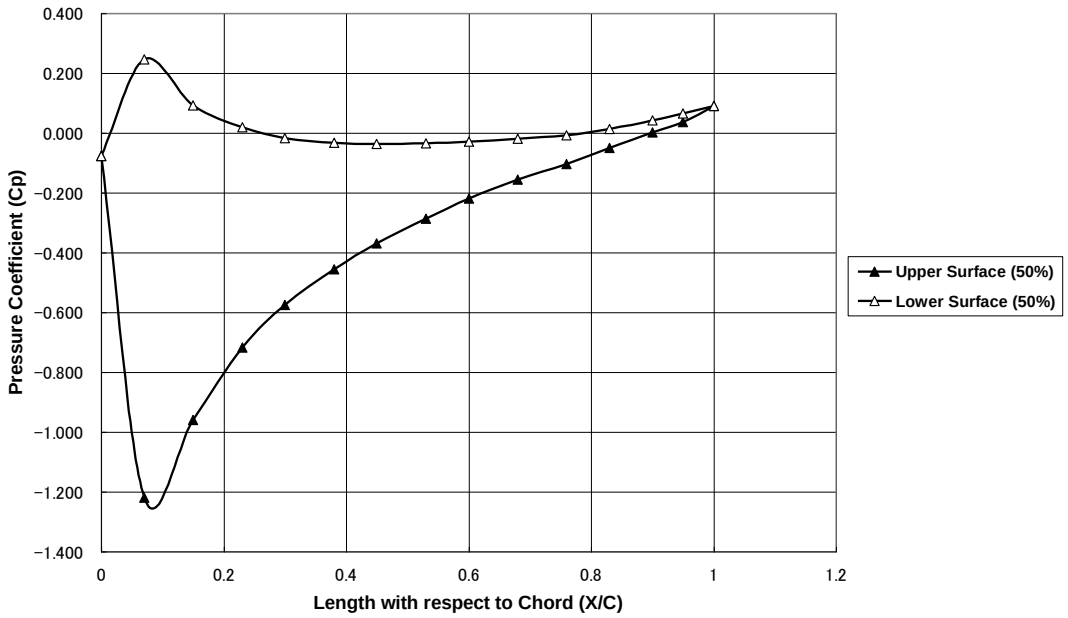

Figure 4.41c: Variation of Pressure with Chord Length for Aerofoil Shaped Fuselage UAV model at 50% from the root at 15° Angle of Attack.

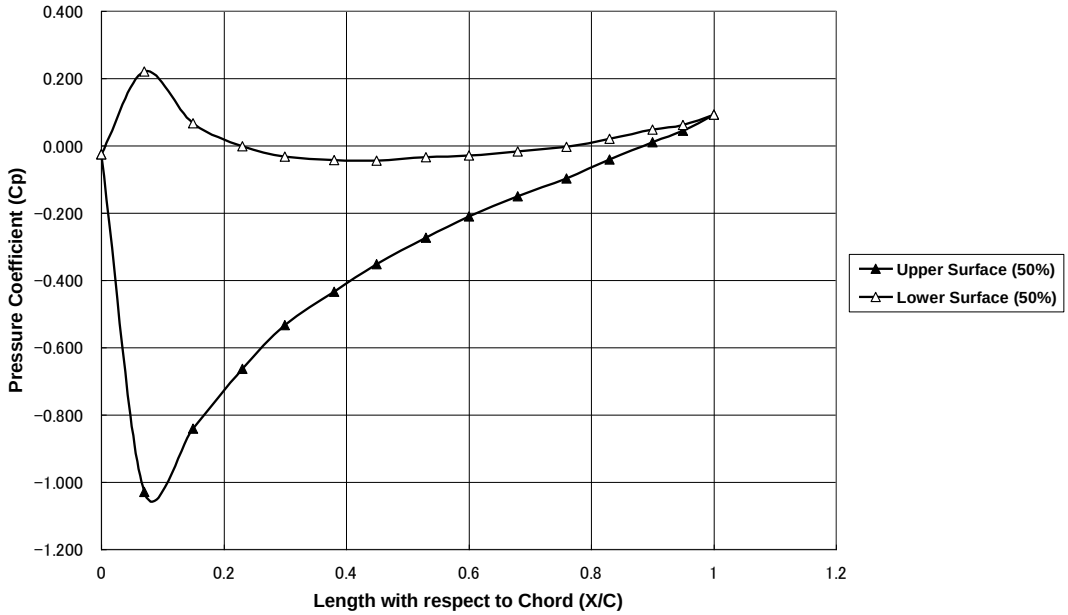

Figure 4.41d: Variation of Pressure with Chord Length for Aerofoil Shaped Fuselage UAV model at 50% from the root at 18° Angle of Attack.

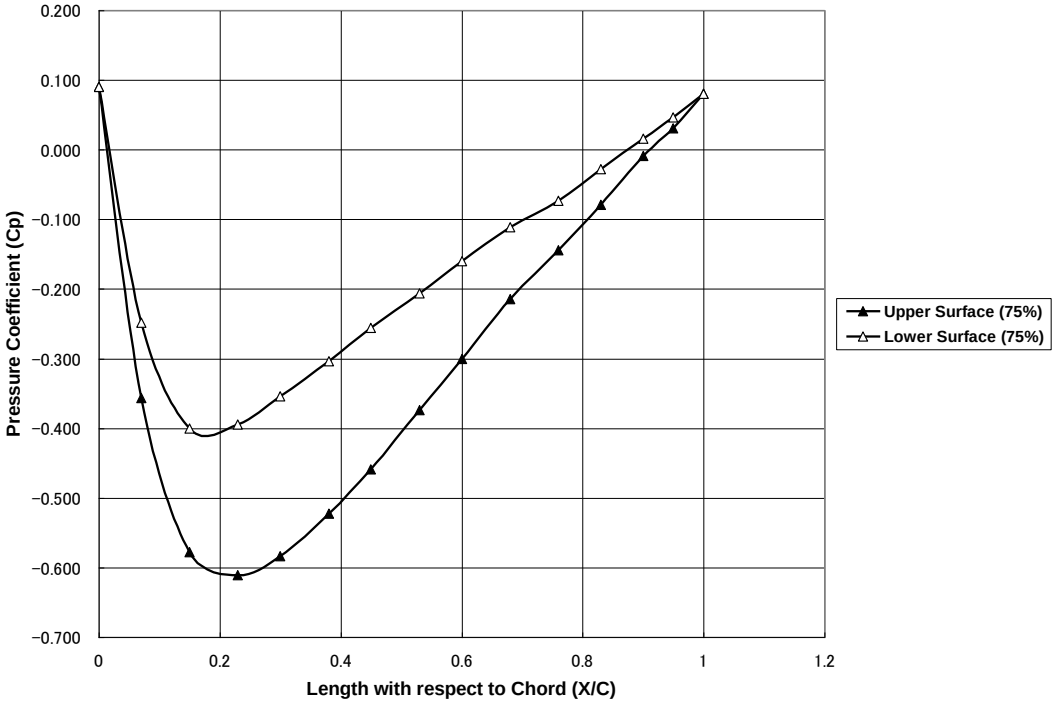

Figure 4.42a: Variation of Pressure with Chord Length for Aerofoil Shaped Fuselage UAV model at 75% from the root at 3° Angle of Attack.

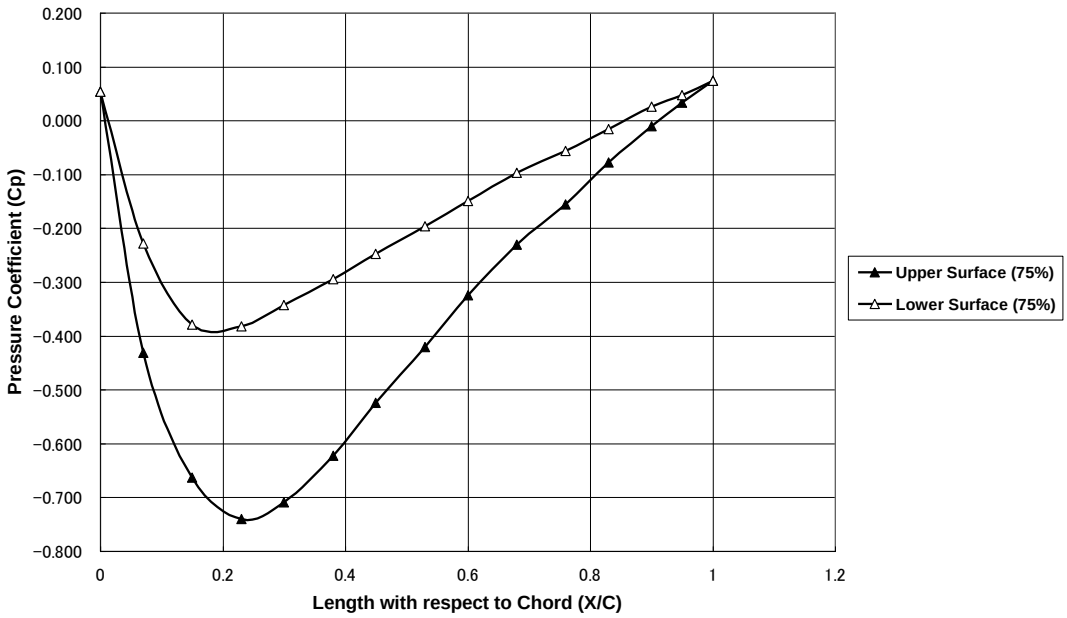

Figure 4.42b: Variation of Pressure with Chord Length for Aerofoil Shaped Fuselage UAV model at 75% from the root at 9° Angle of Attack.

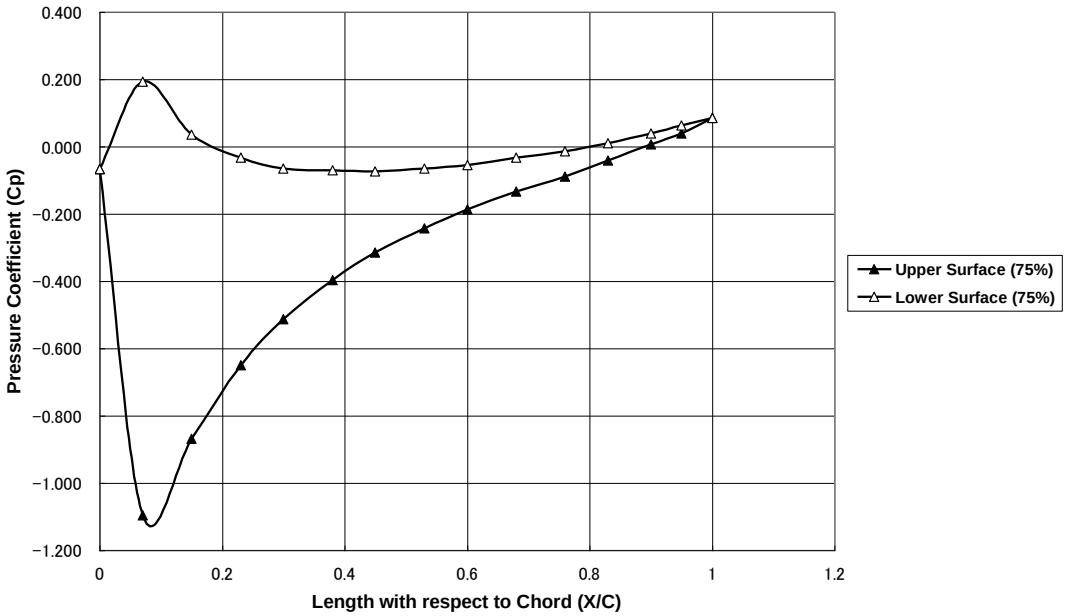

Figure 4.42c: Variation of Pressure with Chord Length for Aerofoil Shaped Fuselage UAV model at 75% from the root at 15° Angle of Attack.

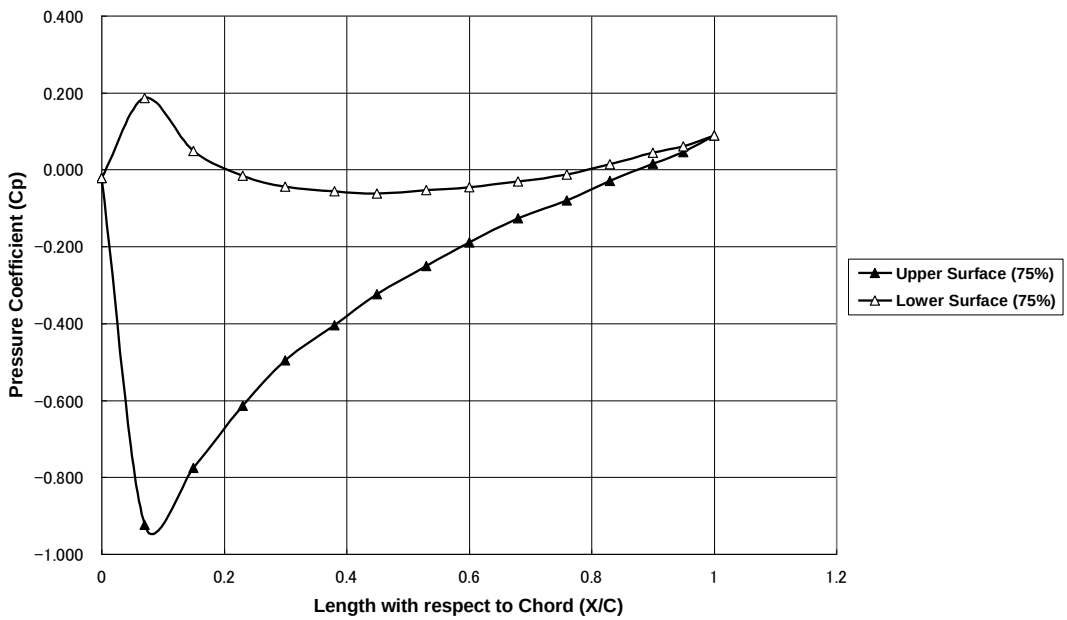

Figure 4.42d: Variation of Pressure with Chord Length for Aerofoil Shaped Fuselage UAV model at 75% from the root at 18° Angle of Attack.

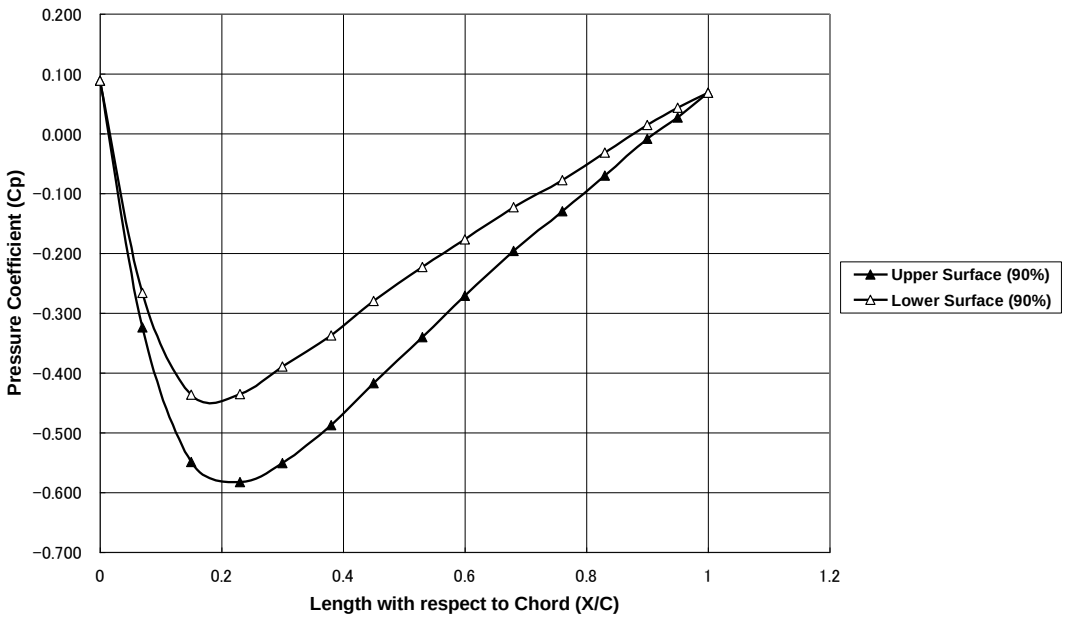

Figure 4.43a: Variation of Pressure with Chord Length for Aerofoil Shaped Fuselage UAV model at 90% from the root at 3° Angle of Attack.

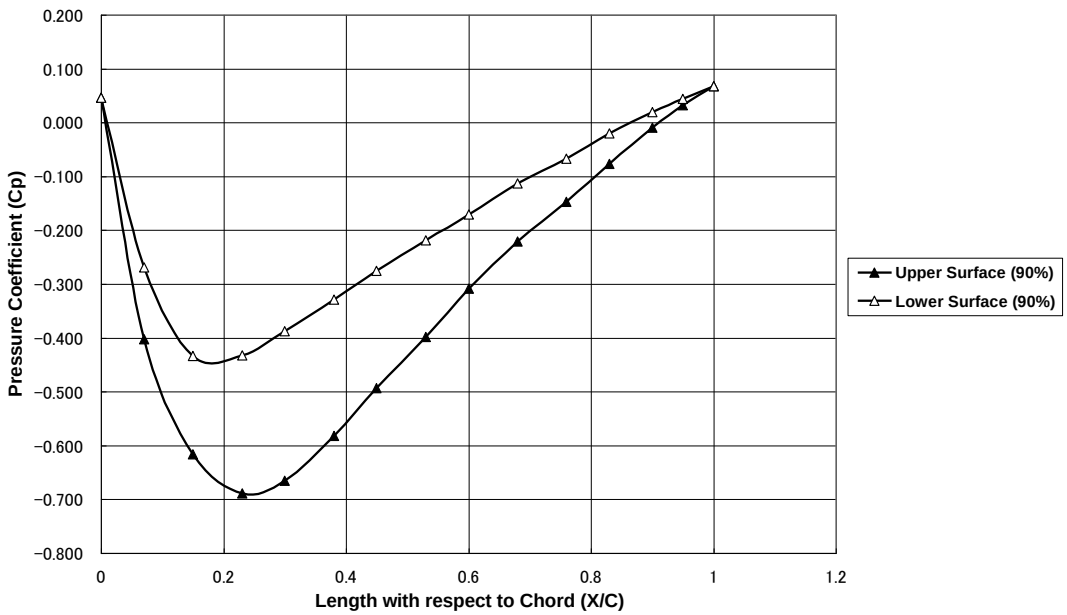

Figure 4.43b: Variation of Pressure with Chord Length for Aerofoil Shaped Fuselage UAV model at 90% from the root at 9° Angle of Attack.

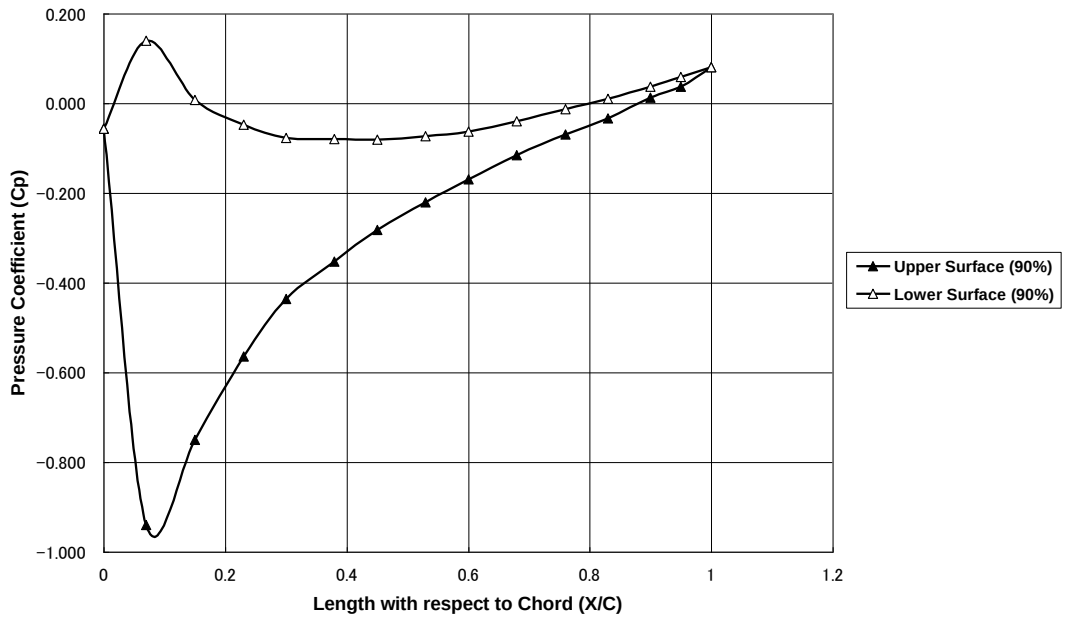

Figure 4.43c: Variation of Pressure with Chord Length for Aerofoil Shaped Fuselage UAV model at 90% from the root at 15° Angle of Attack.

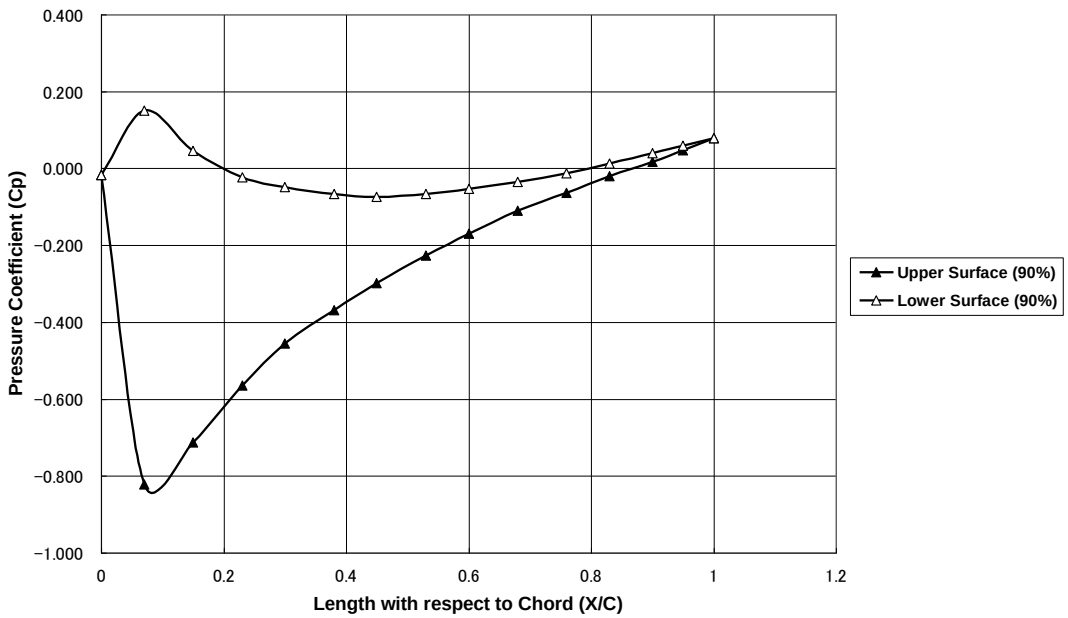

Figure 4.43d: Variation of Pressure with Chord Length for Aerofoil Shaped Fuselage UAV model at 90% from the root at 18° Angle of Attack.

APPENDIX – 'A' TO FIGURE 4.24
on *"Surface Pressure of NACA 4416 Profile at 20 m/s"*

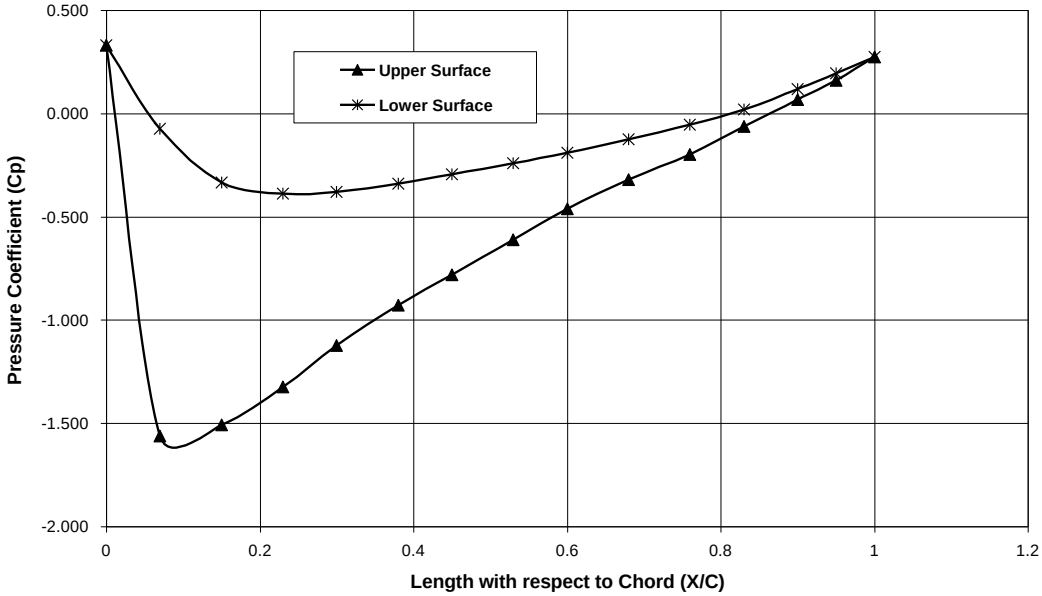

Figure 4.24a: Variation of Pressure with Chord Length for 2D NACA 4416 Aerofoil Profile at 3° Angle of Attack.

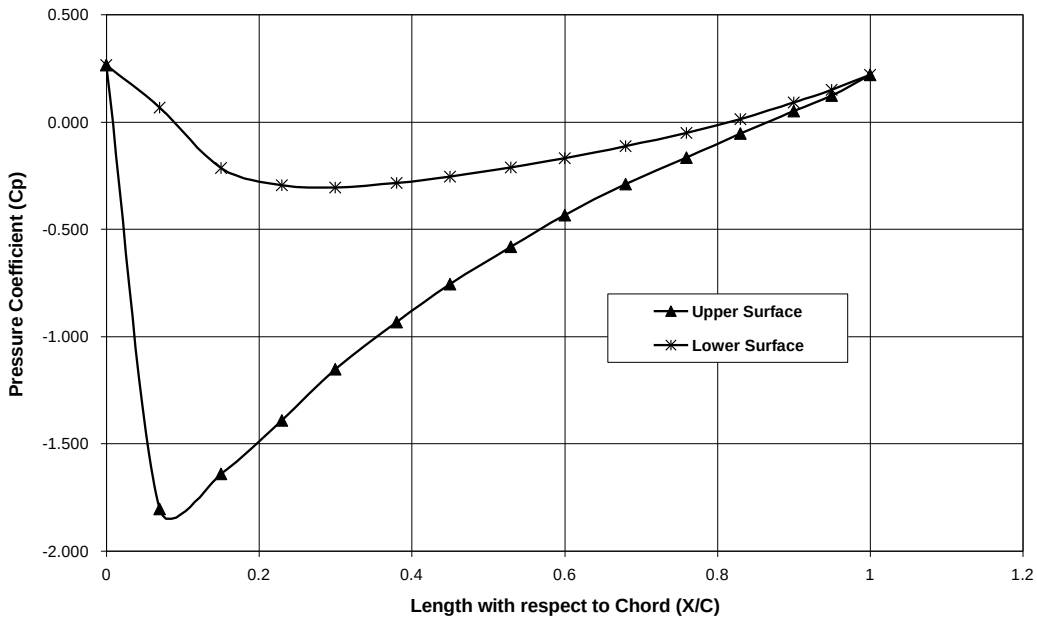

Figure 4.24b: Variation of Pressure with Chord Length for 2D NACA 4416 Aerofoil Profile at 9° Angle of Attack.

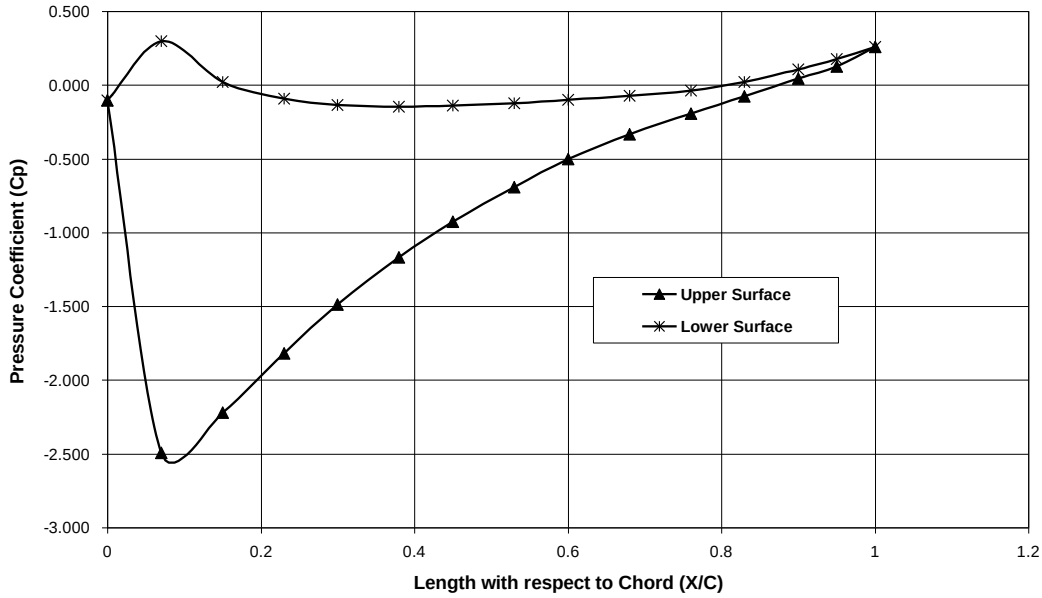

Figure 4.24c: Variation of Pressure with Chord Length for 2D NACA 4416 Aerofoil Profile at 15° Angle of Attack.

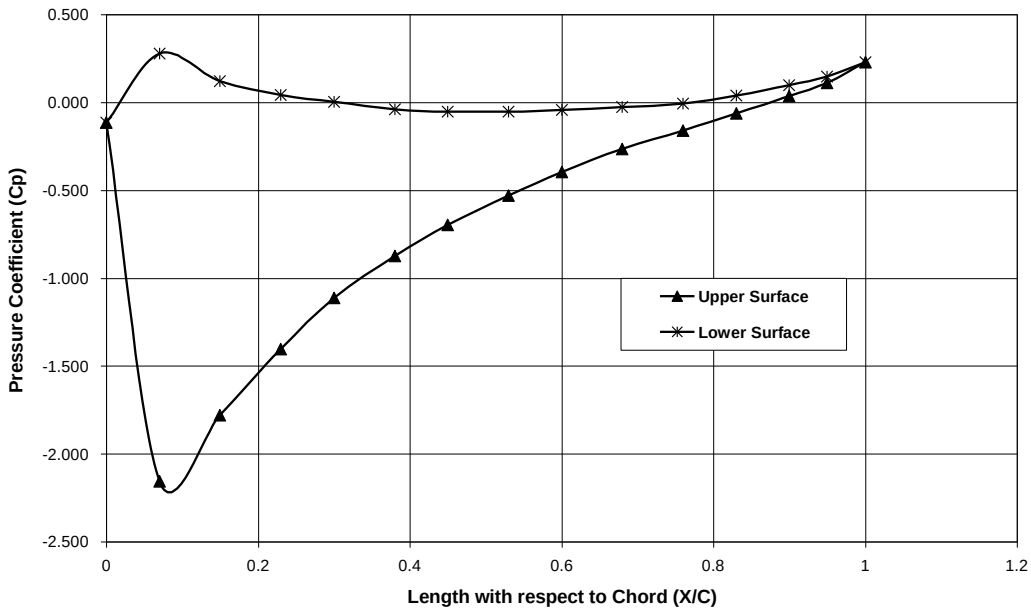

Figure 4.24d: Variation of Pressure with Chord Length for 2D NACA 4416 Aerofoil Profile at 18° Angle of Attack.

APPENDIX – 'B' TO FIGURE 4.26, 4.27, 4.28 and 4.29

on *"Surface Pressure of Conventional Cylindrical Shaped Fuselage at 20 m/s"*

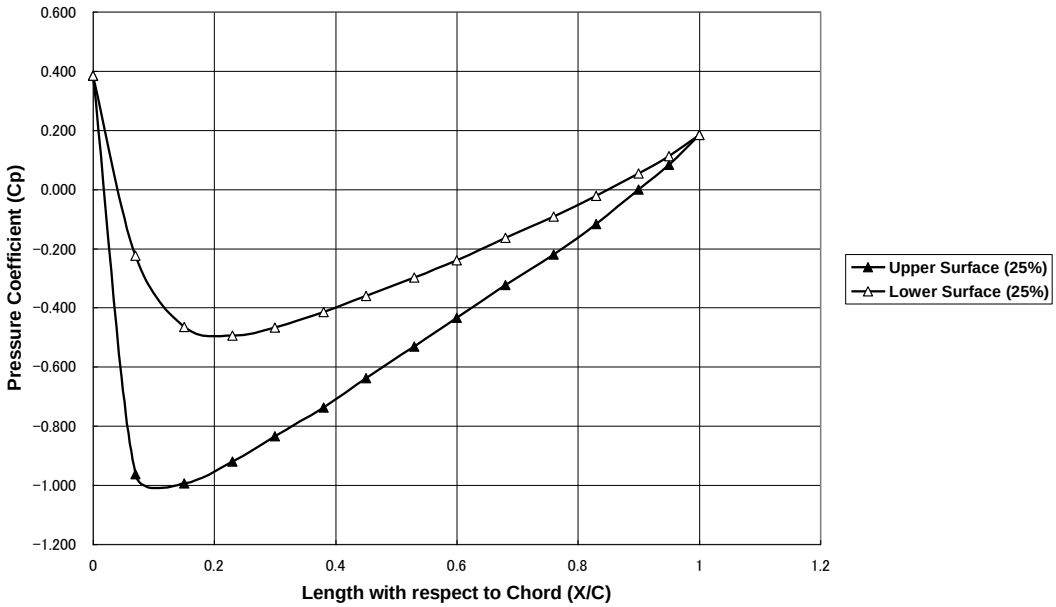

Figure 4.26a: Variation of Pressure with Chord Length for Conventional Cylindrical Shaped Fuselage UAV model at 25% from the root at 3° Angle of Attack.

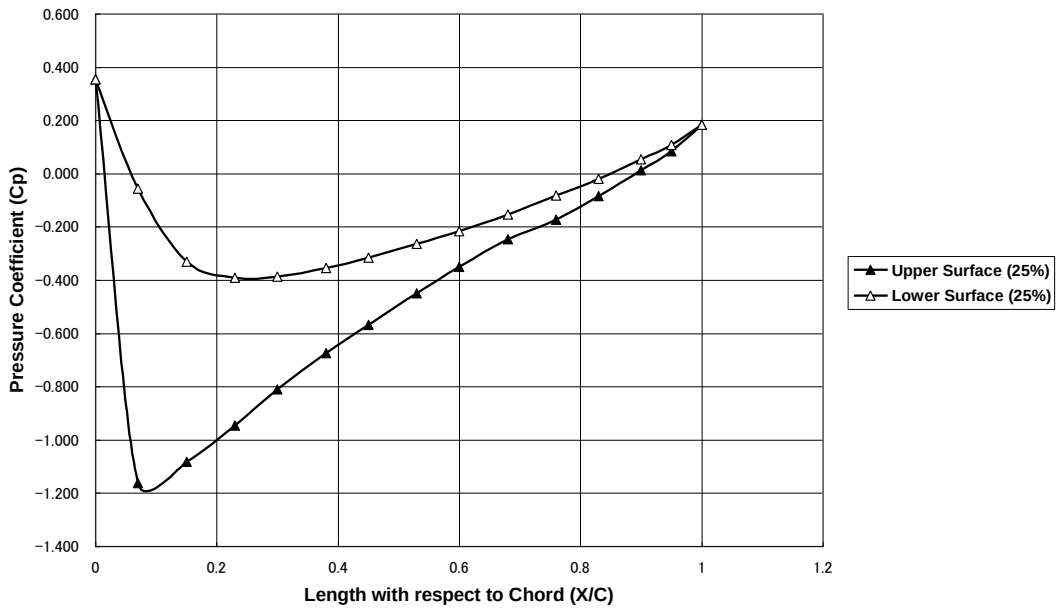

Figure 4.26b: Variation of Pressure with Chord Length for Conventional Cylindrical Shaped Fuselage UAV model at 25% from the root at 9° Angle of Attack.

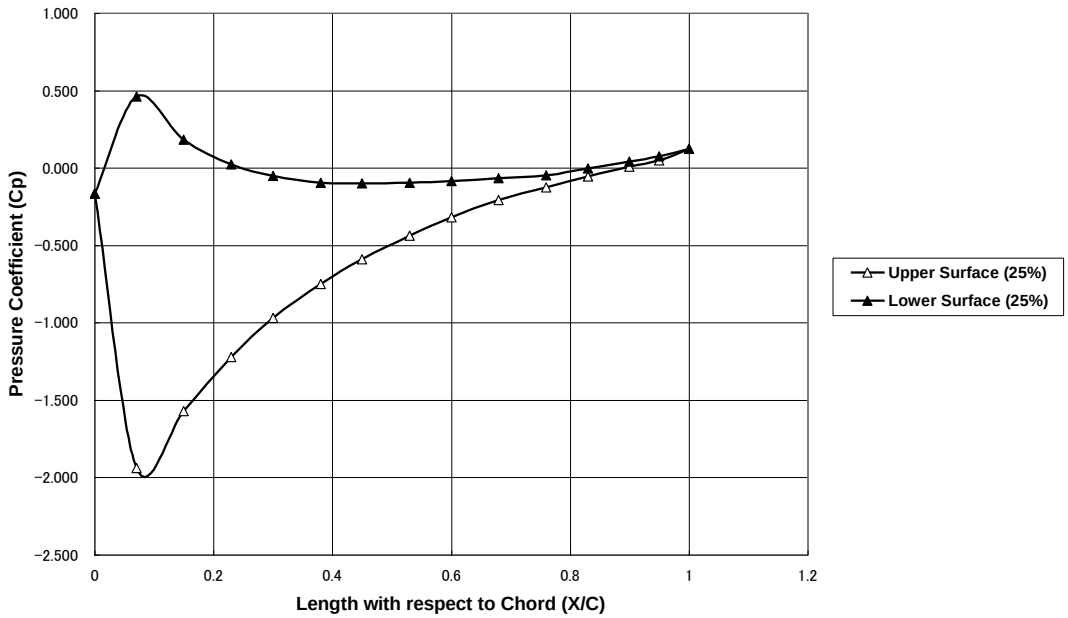

Figure 4.26c: Variation of Pressure with Chord Length for Conventional Cylindrical Shaped Fuselage UAV model at 25% from the root at 15° Angle of Attack.

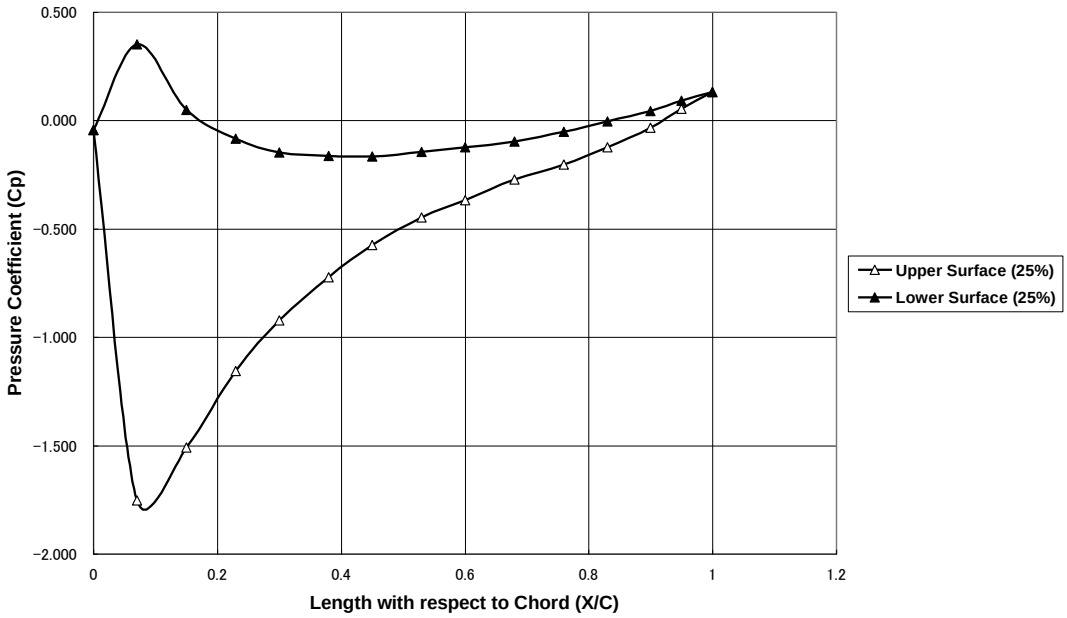

Figure 4.26d: Variation of Pressure with Chord Length for Conventional Cylindrical Shaped Fuselage UAV model at 25% from the root at 18° Angle of Attack.

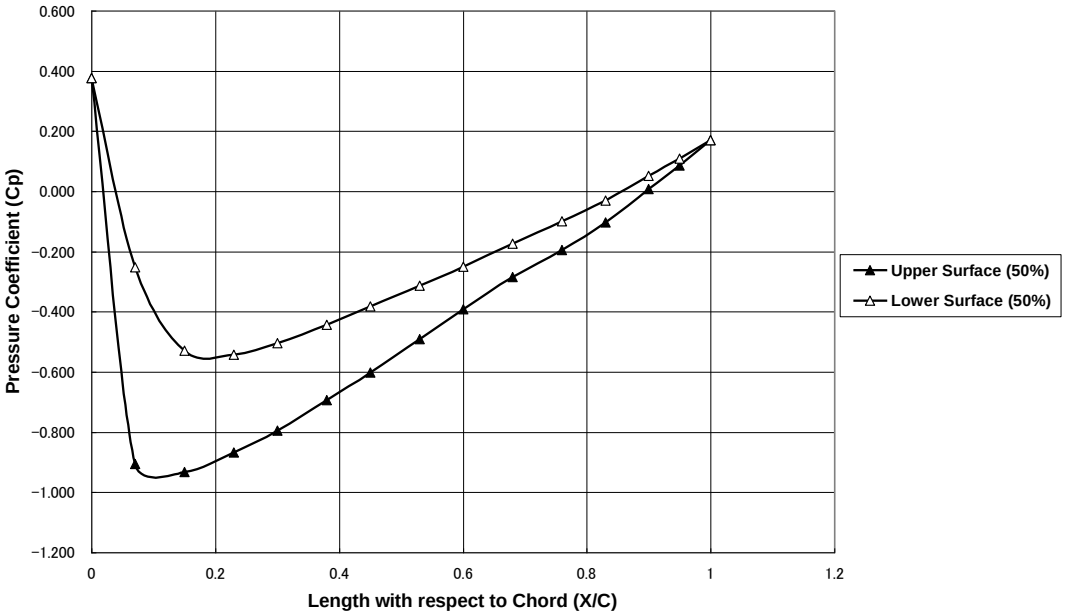

Figure 4.27a: Variation of Pressure with Chord Length for Conventional Cylindrical Shaped Fuselage UAV model at 50% from the root at 3° Angle of Attack.

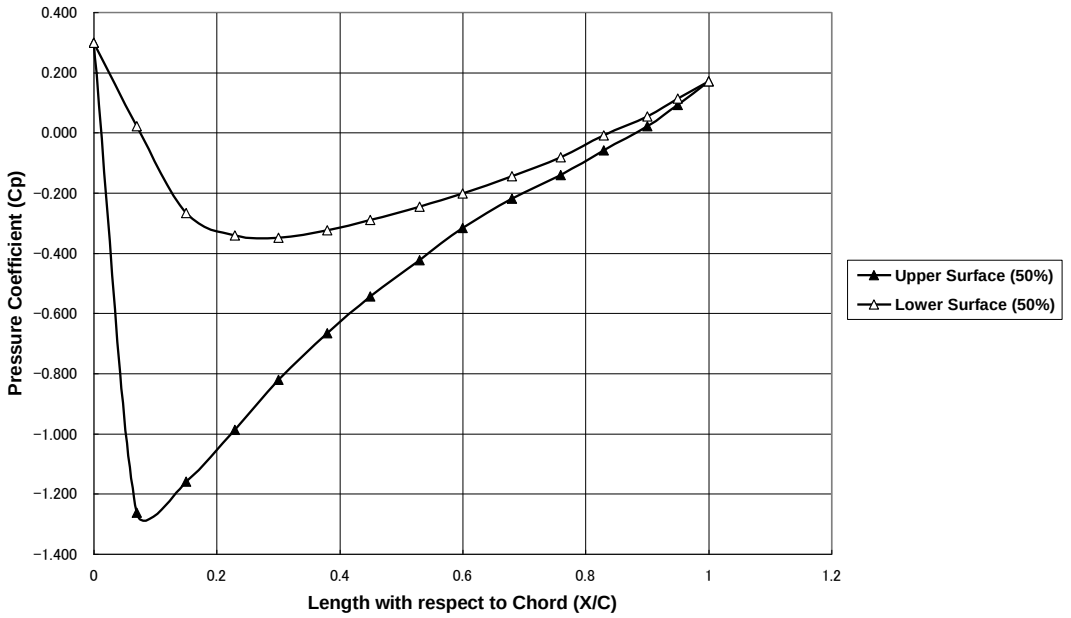

Figure 4.27b: Variation of Pressure with Chord Length for Conventional Cylindrical Shaped Fuselage UAV model at 50% from the root at 9° Angle of Attack.

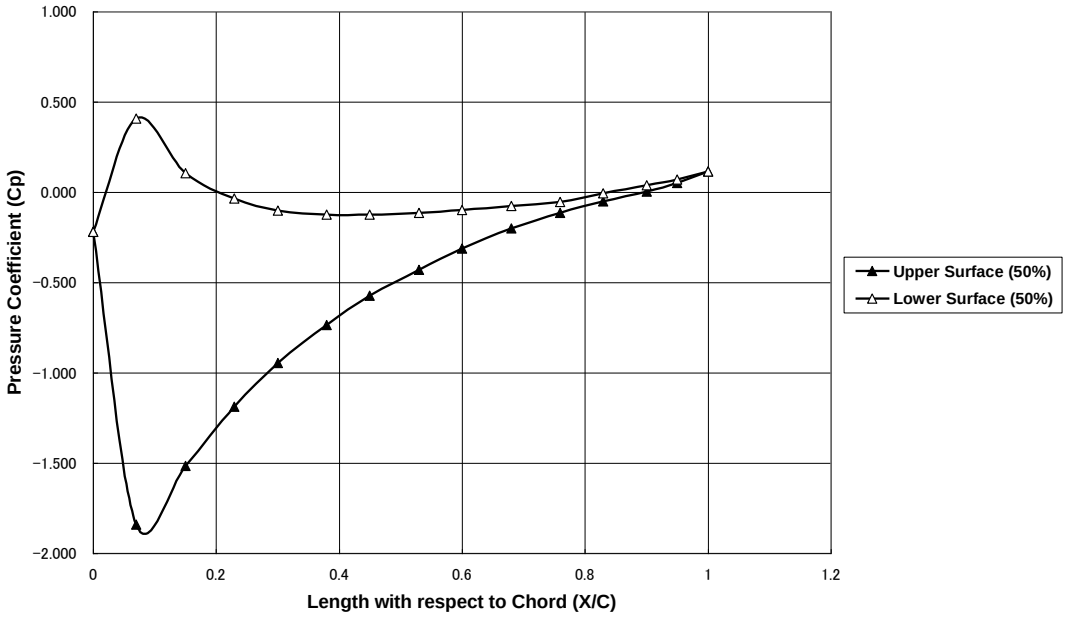

Figure 4.27c: Variation of Pressure with Chord Length for Conventional Cylindrical Shaped Fuselage UAV model at 50% from the root at 15° Angle of Attack.

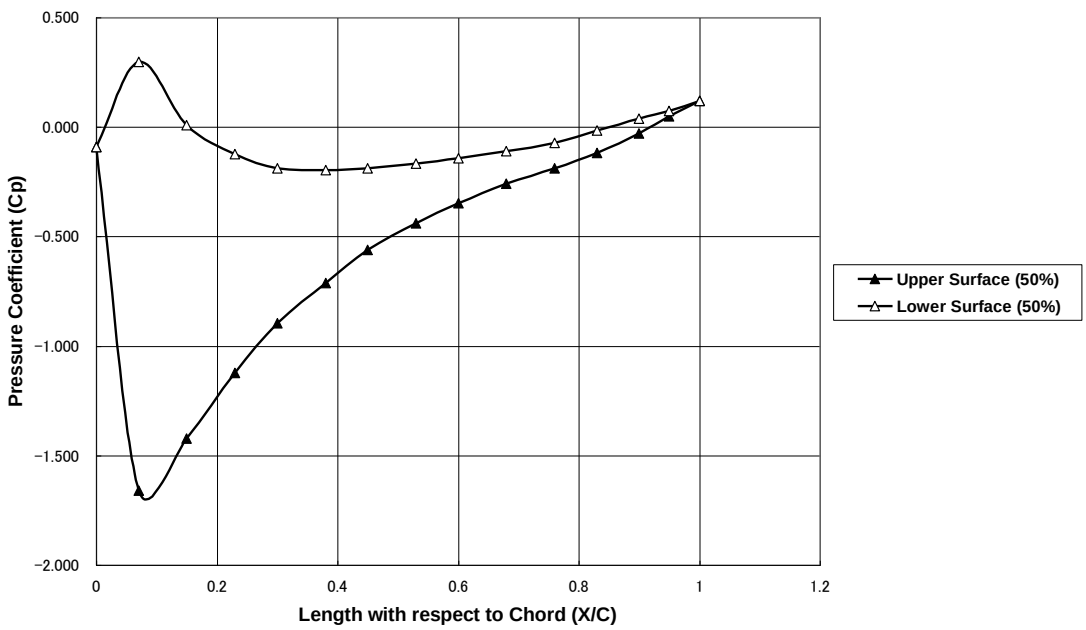

Figure 4.27d: Variation of Pressure with Chord Length for Conventional Cylindrical Shaped Fuselage UAV model at 50% from the root at 18° Angle of Attack.

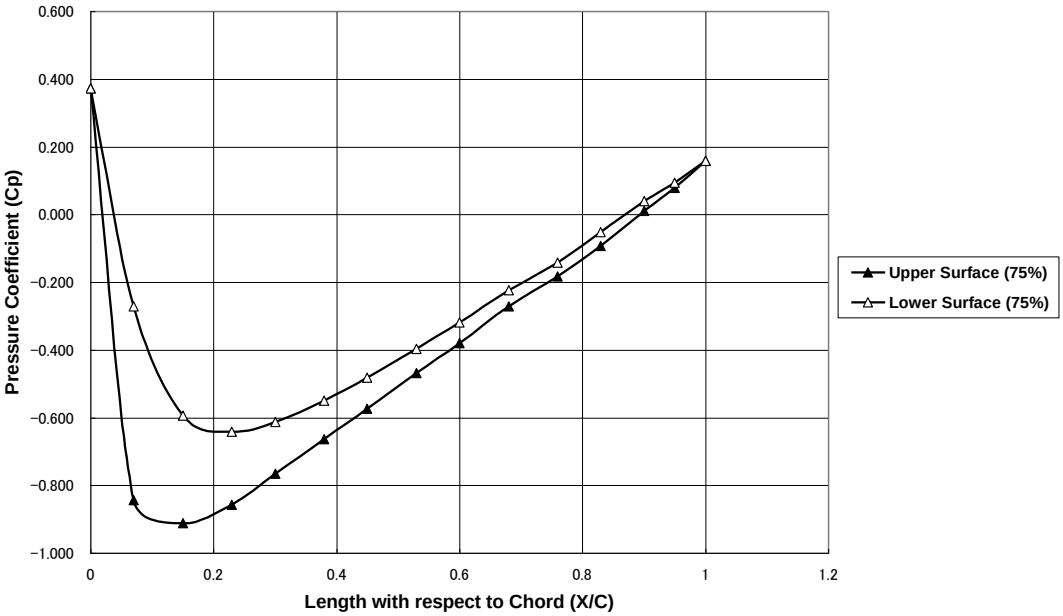

Figure 4.28a: Variation of Pressure with Chord Length for Conventional Cylindrical Shaped Fuselage UAV model at 75% from the root at 3° Angle of Attack.

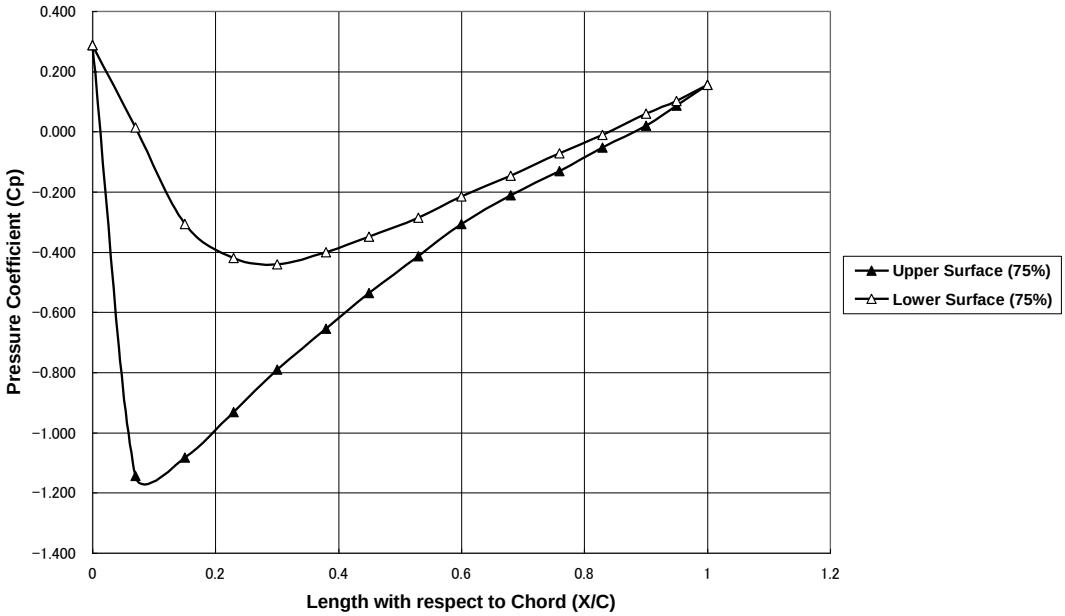

Figure 4.28b: Variation of Pressure with Chord Length for Conventional Cylindrical Shaped Fuselage UAV model at 75% from the root at 9° Angle of Attack.

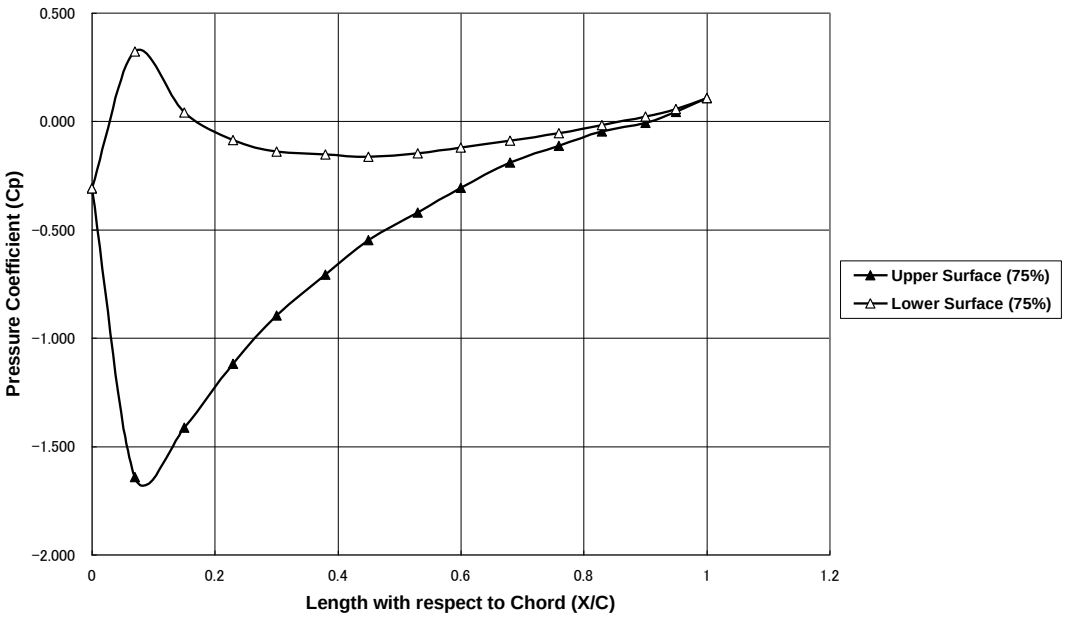

Figure 4.28c: Variation of Pressure with Chord Length for Conventional Cylindrical Shaped Fuselage UAV model at 75% from the root at 15° Angle of Attack.

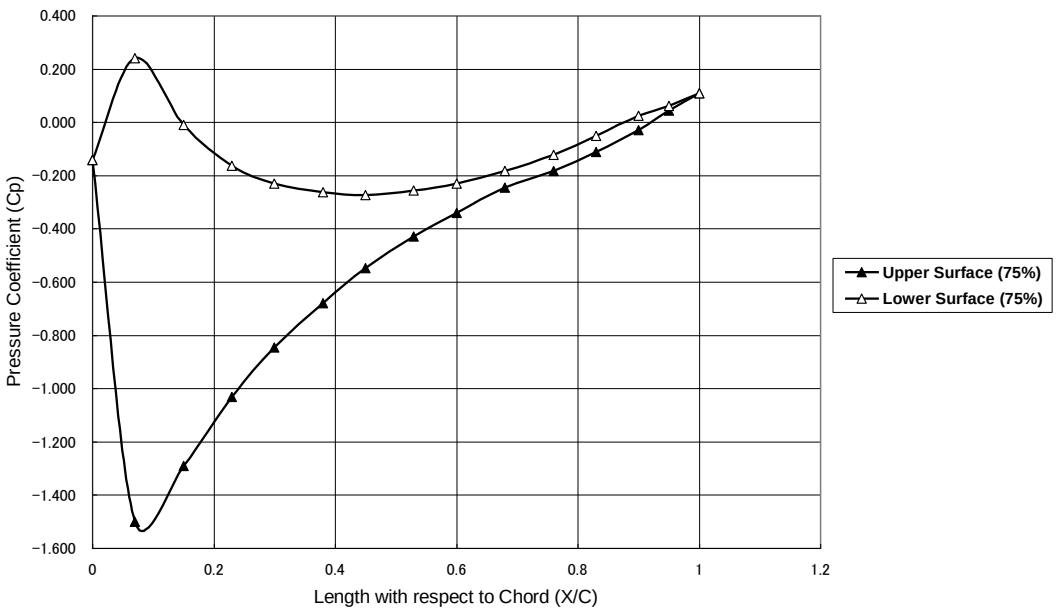

Figure 4.28d: Variation of Pressure with Chord Length for Conventional Cylindrical Shaped Fuselage UAV model at 75% from the root at 18° Angle of Attack.

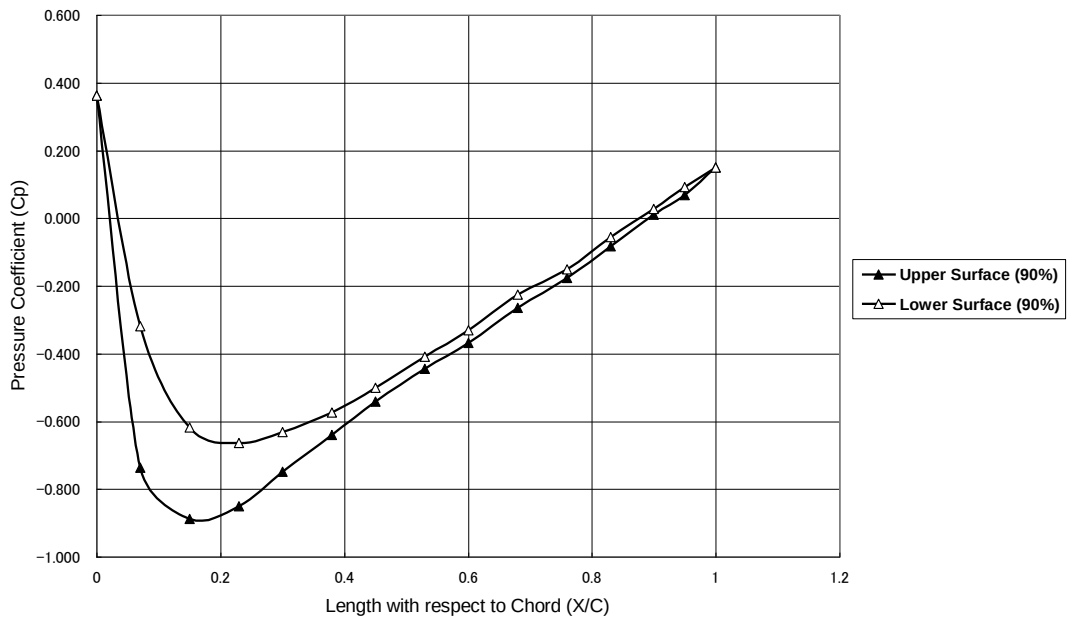

Figure 4.29a: Variation of Pressure with Chord Length for Conventional Cylindrical Shaped Fuselage UAV model at 90% from the root at 3° Angle of Attack.

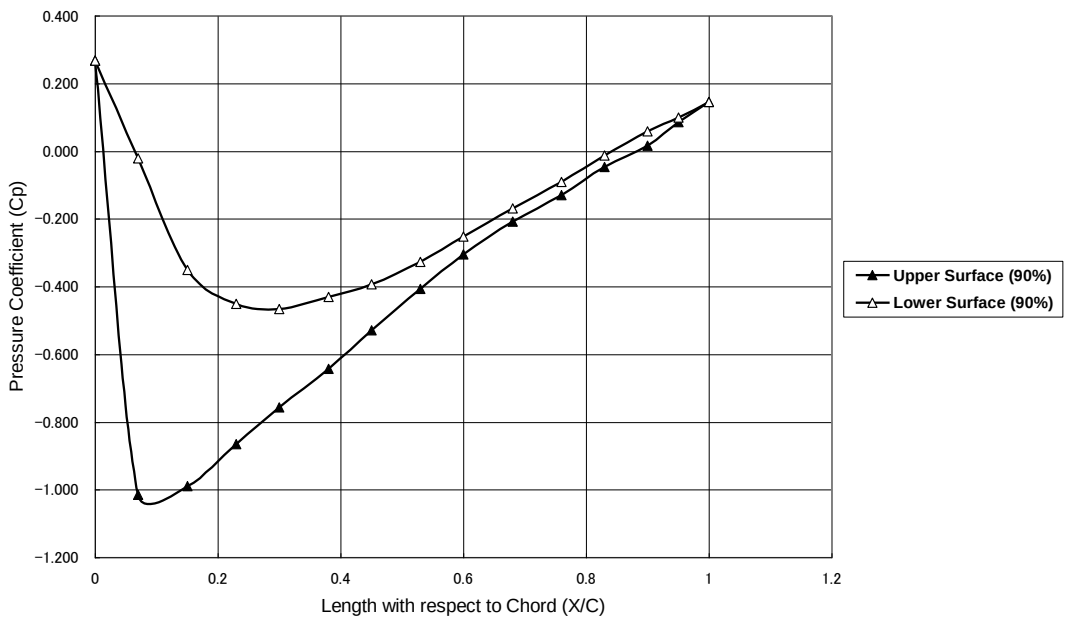

Figure 4.29b: Variation of Pressure with Chord Length for Conventional Cylindrical Shaped Fuselage UAV model at 90% from the root at 9° Angle of Attack.

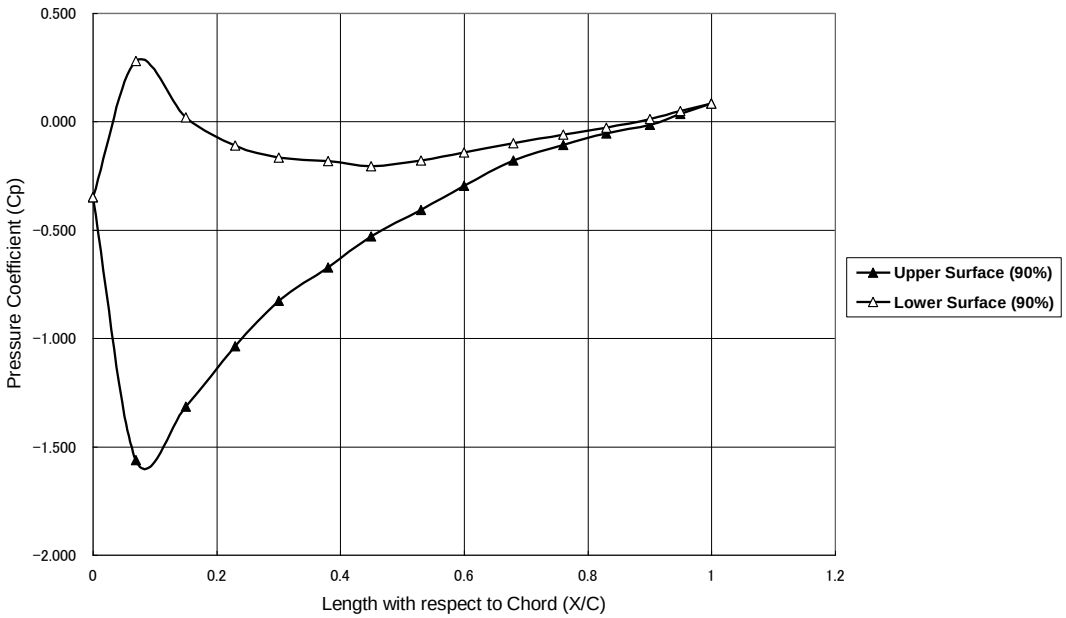

Figure 4.29c: Variation of Pressure with Chord Length for Conventional Cylindrical Shaped Fuselage UAV model at 90% from the root at 15° Angle of Attack.

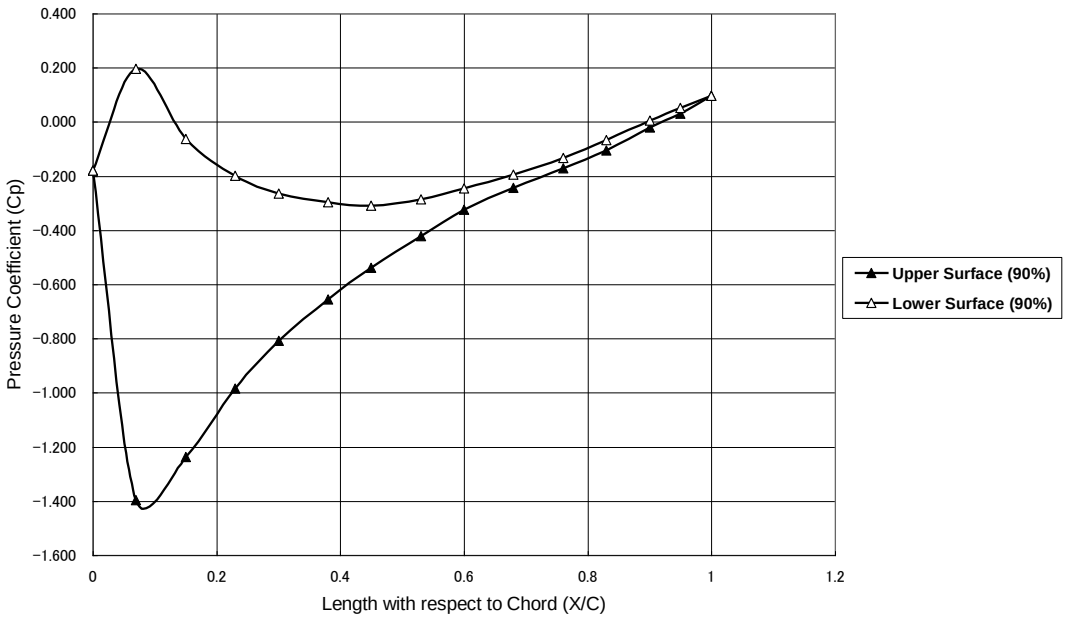

Figure 4.29d: Variation of Pressure with Chord Length for Conventional Cylindrical Shaped Fuselage UAV model at 90% from the root at 18° Angle of Attack.

APPENDIX – 'C' TO FIGURE 4.31, 4.32, 4.33 and 4.34

on *"Surface Pressure of Aerofoil Shaped Fuselage at 20 m/s"*

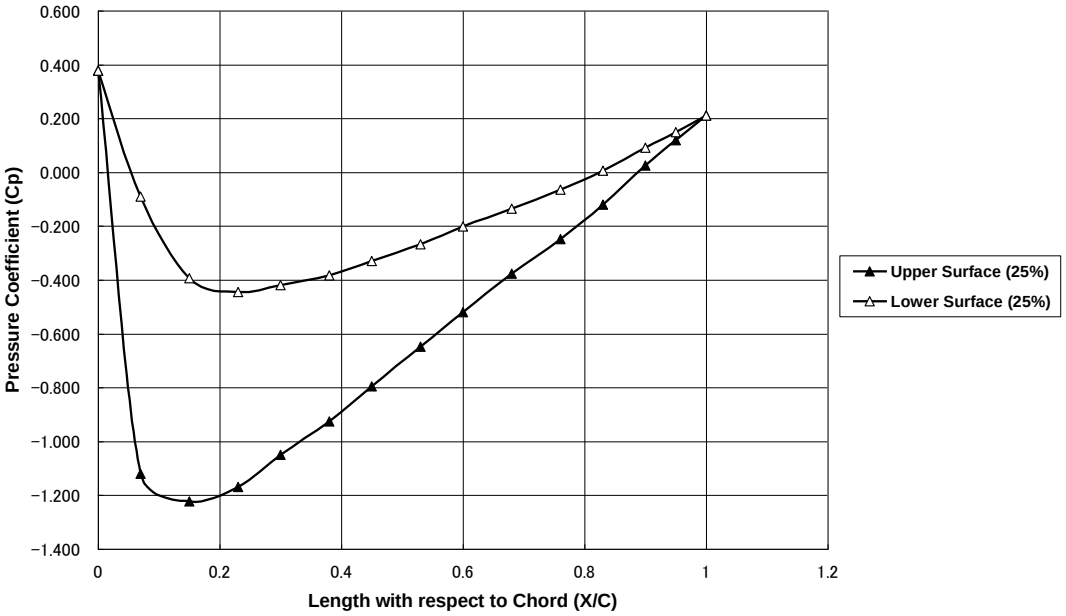

Figure 4.31a: Variation of Pressure with Chord Length for Aerofoil Shaped Fuselage UAV model at 25% from the root at 3° Angle of Attack.

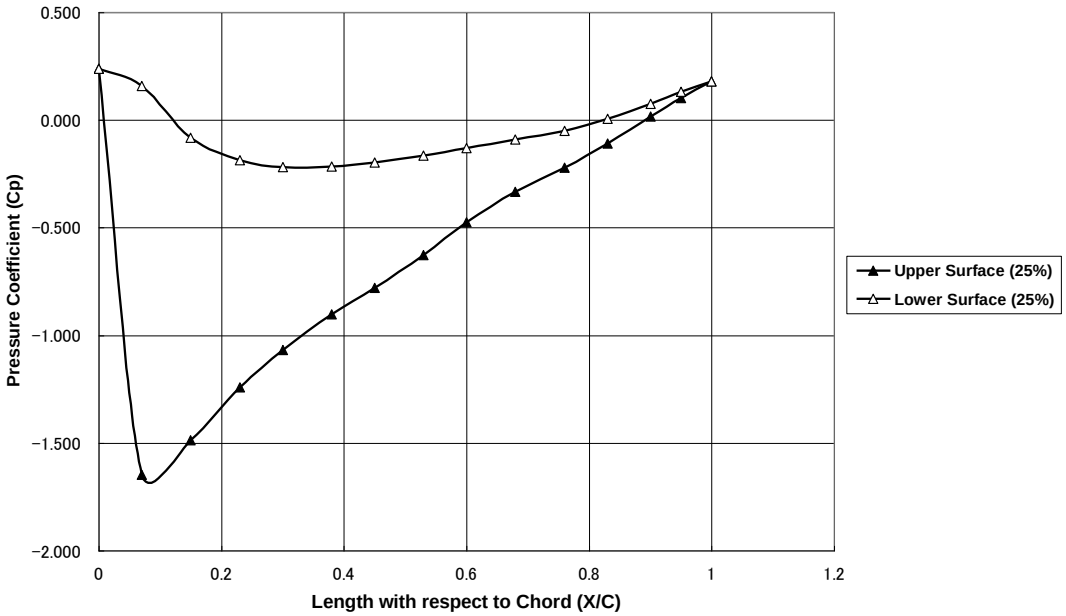

Figure 4.31b: Variation of Pressure with Chord Length for Aerofoil Shaped Fuselage UAV model at 25% from the root at 9° Angle of Attack.

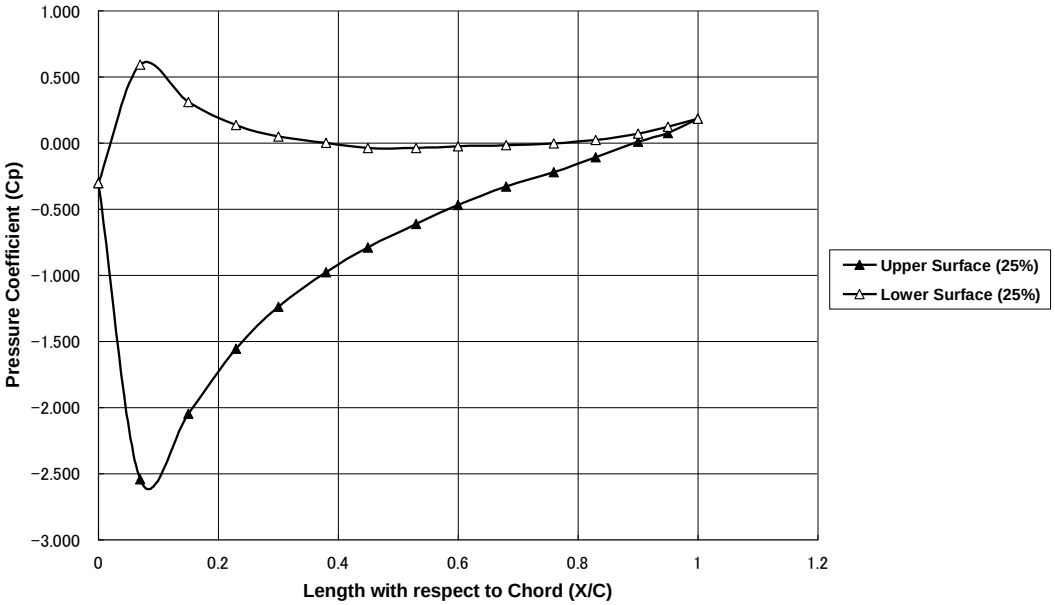

Figure 4.31c: Variation of Pressure with Chord Length for Aerofoil Shaped Fuselage UAV model at 25% from the root at 15° Angle of Attack.

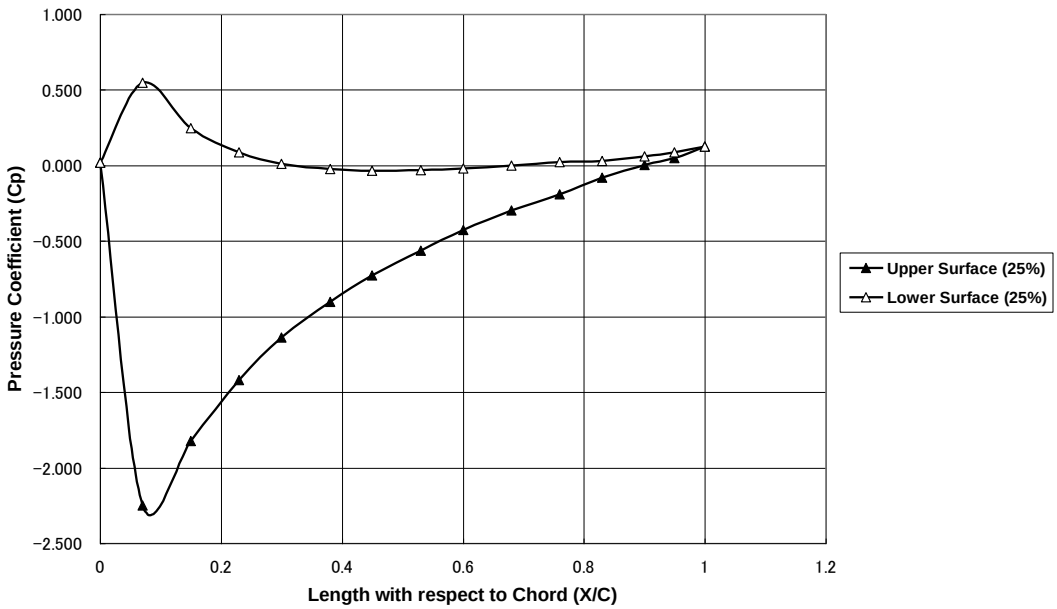

Figure 4.31d: Variation of Pressure with Chord Length for Aerofoil Shaped Fuselage UAV model at 25% from the root at 18° Angle of Attack.

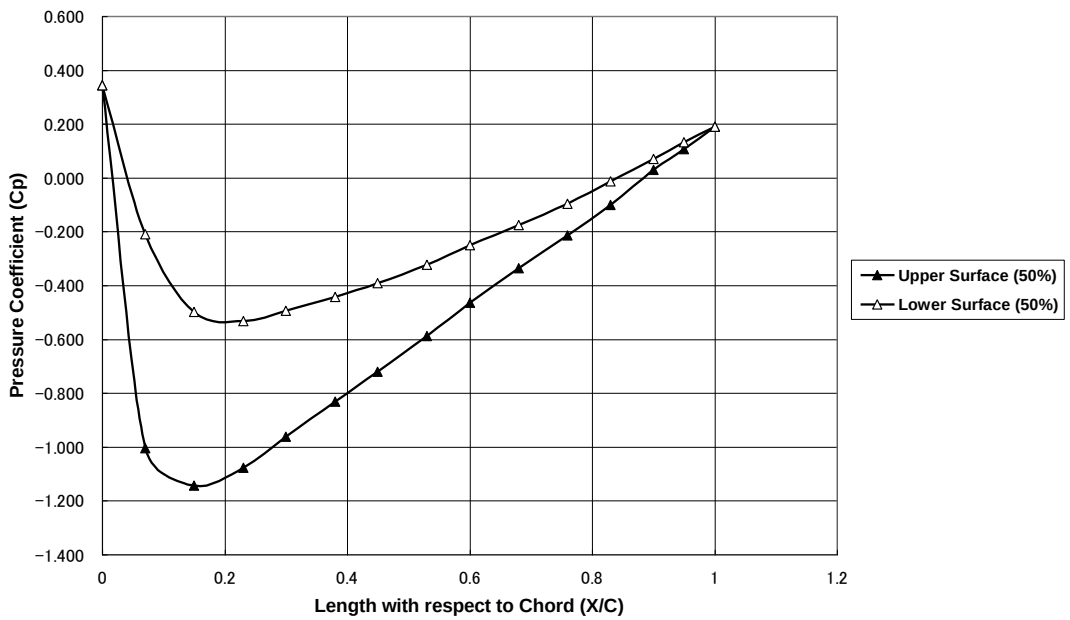

Figure 4.32a: Variation of Pressure with Chord Length for Aerofoil Shaped Fuselage UAV model at 50% from the root at 3° Angle of Attack.

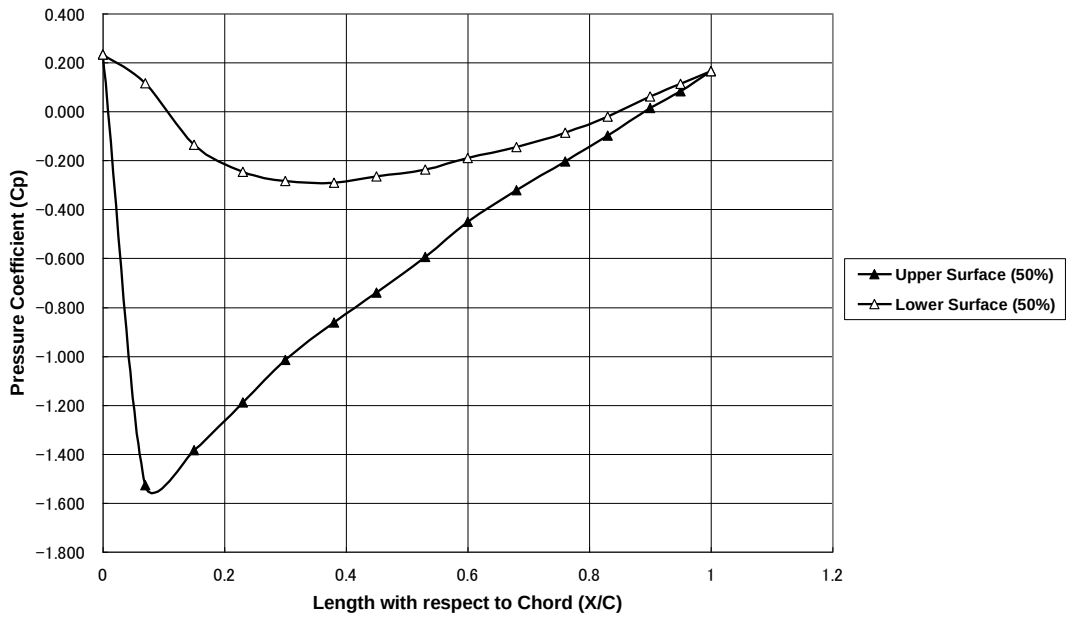

Figure 4.32b: Variation of Pressure with Chord Length for Aerofoil Shaped Fuselage UAV model at 50% from the root at 9° Angle of Attack.

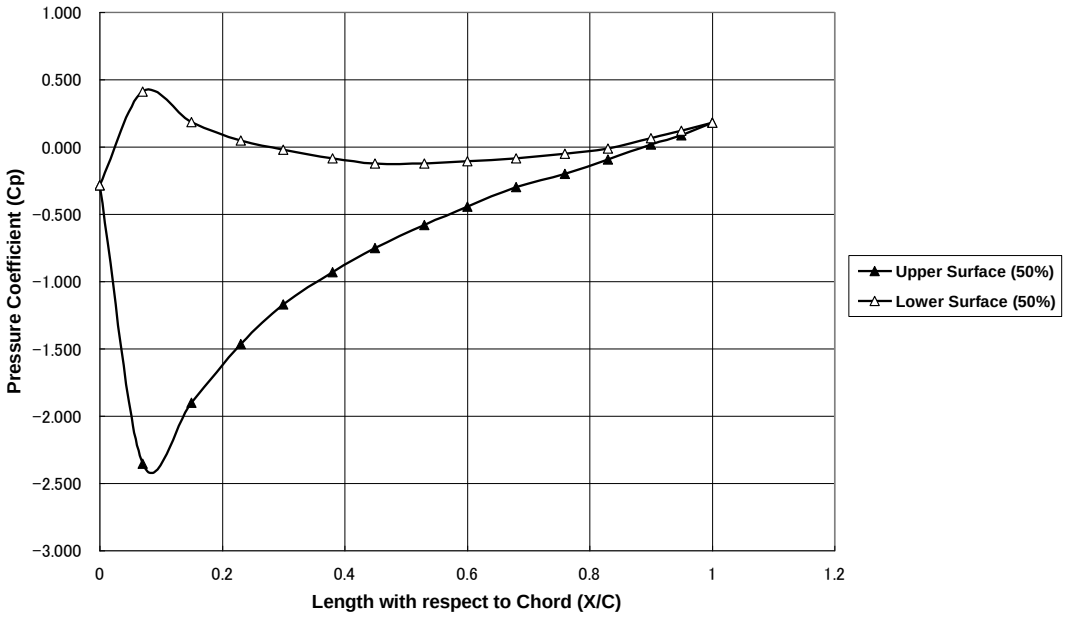

Figure 4.32c: Variation of Pressure with Chord Length for Aerofoil Shaped Fuselage UAV model at 50% from the root at 15° Angle of Attack.

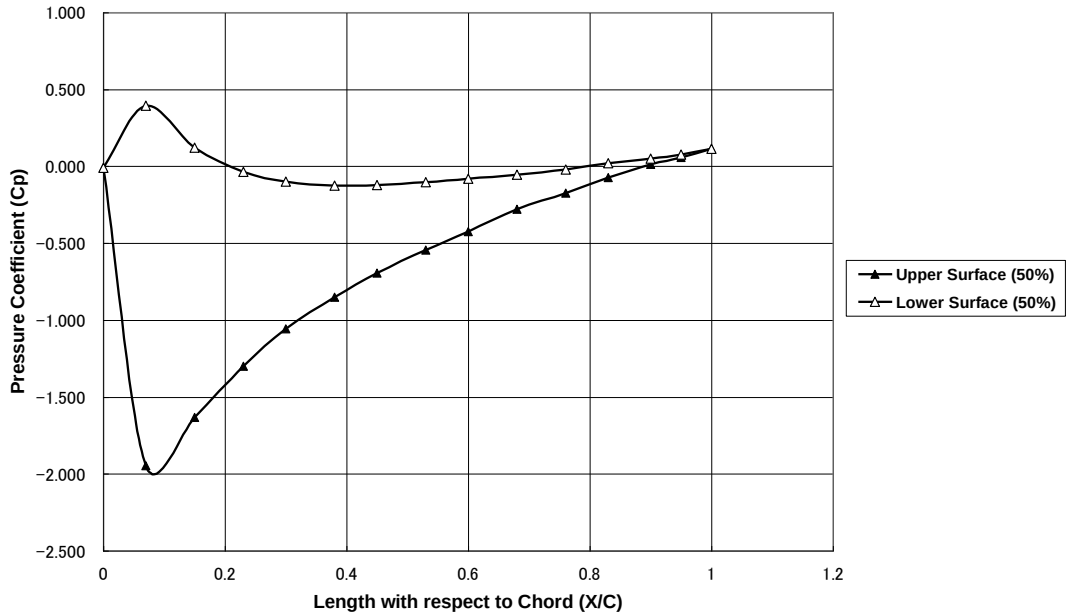

Figure 4.32d: Variation of Pressure with Chord Length for Aerofoil Shaped Fuselage UAV model at 50% from the root at 18° Angle of Attack.

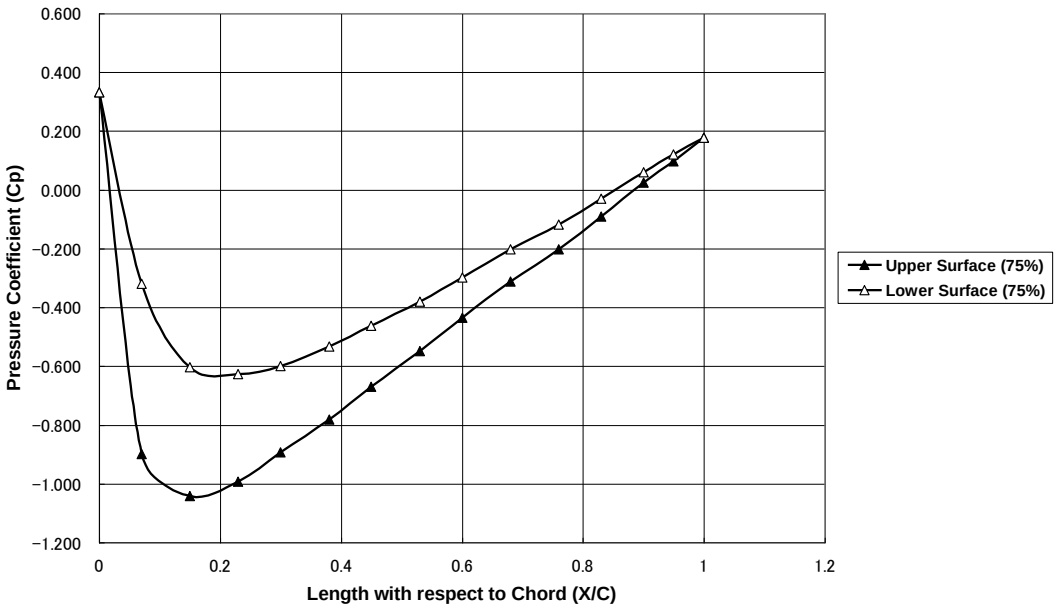

Figure 4.33a: Variation of Pressure with Chord Length for Aerofoil Shaped Fuselage UAV model at 75% from the root at 3° Angle of Attack.

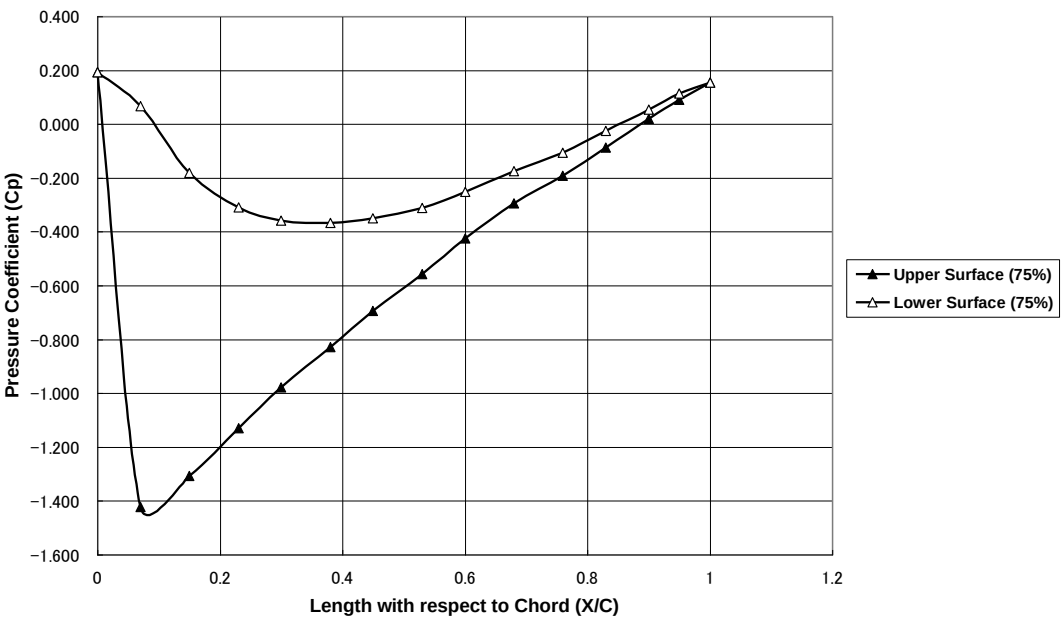

Figure 4.33b: Variation of Pressure with Chord Length for Aerofoil Shaped Fuselage UAV model at 75% from the root at 9° Angle of Attack.

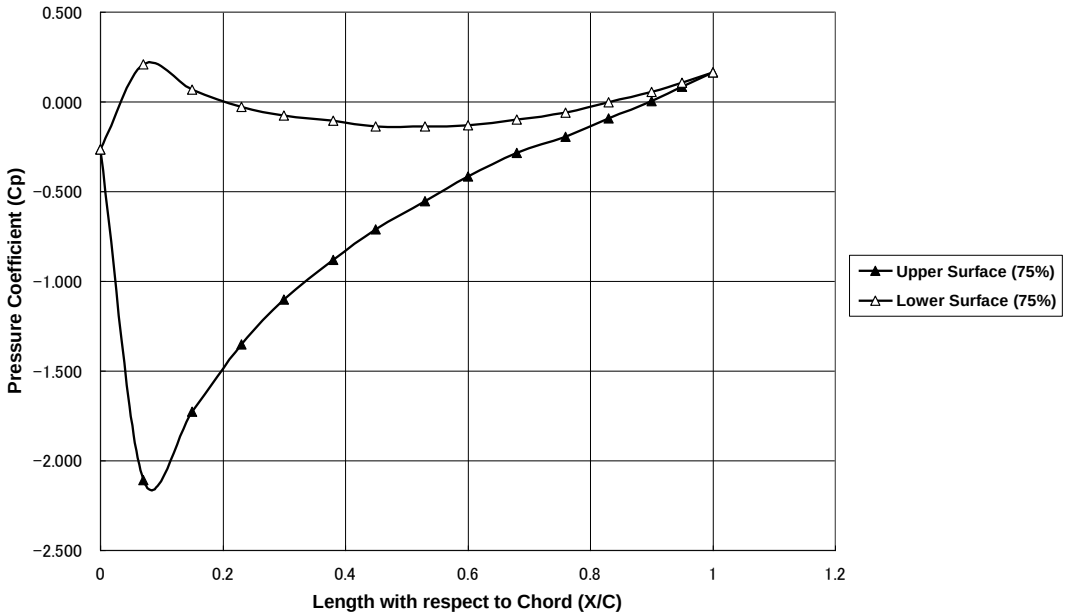

Figure 4.33c: Variation of Pressure with Chord Length for Aerofoil Shaped Fuselage UAV model at 75% from the root at 15° Angle of Attack.

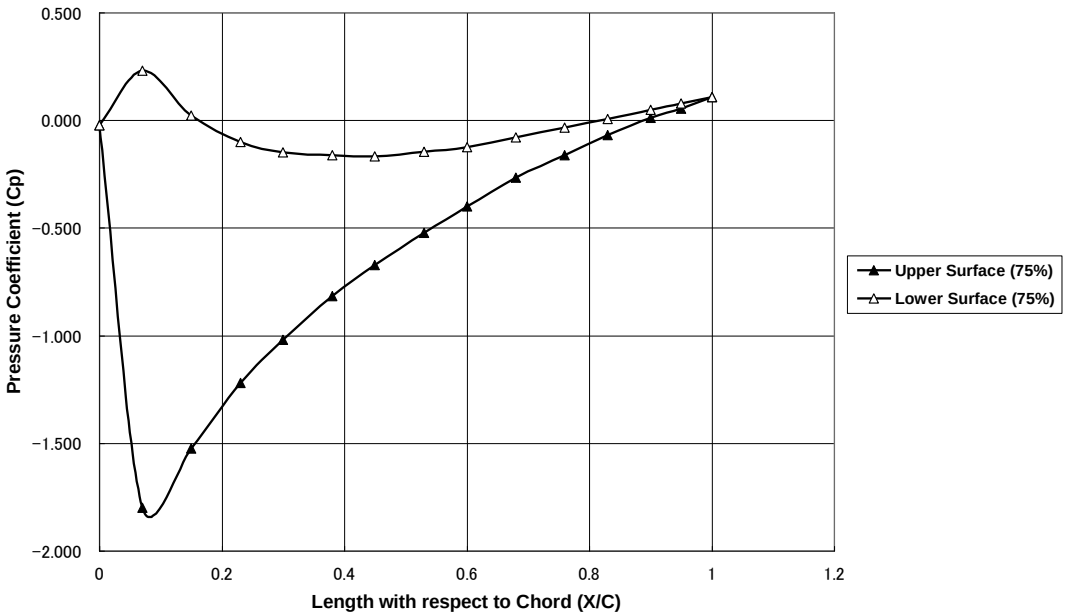

Figure 4.33d: Variation of Pressure with Chord Length for Aerofoil Shaped Fuselage UAV model at 75% from the root at 18° Angle of Attack.

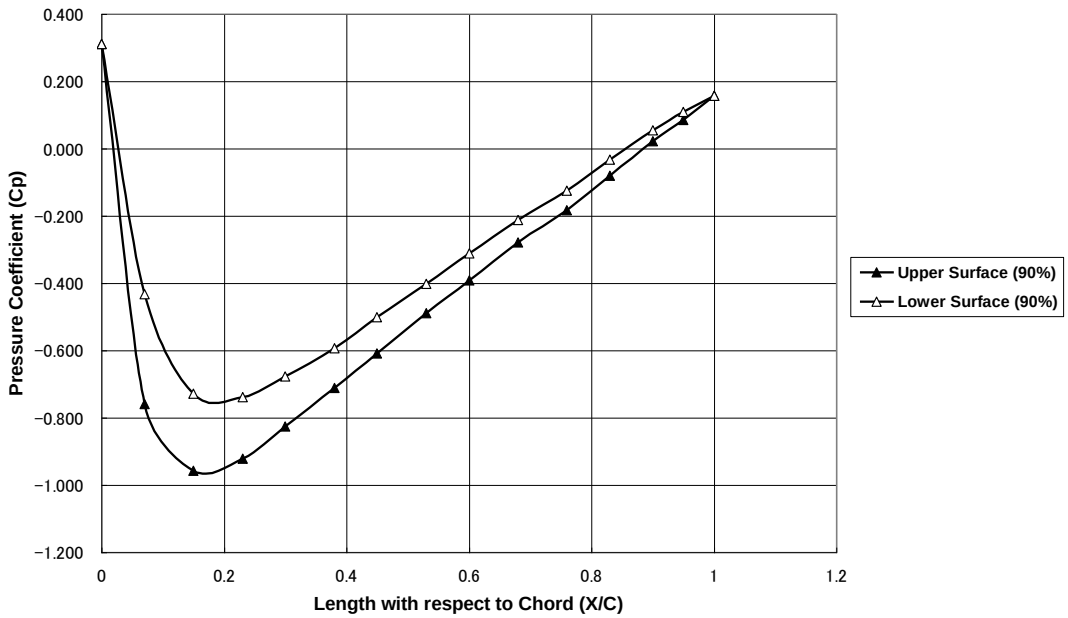

Figure 4.34a: Variation of Pressure with Chord Length for Aerofoil Shaped Fuselage UAV model at 90% from the root at 3° Angle of Attack.

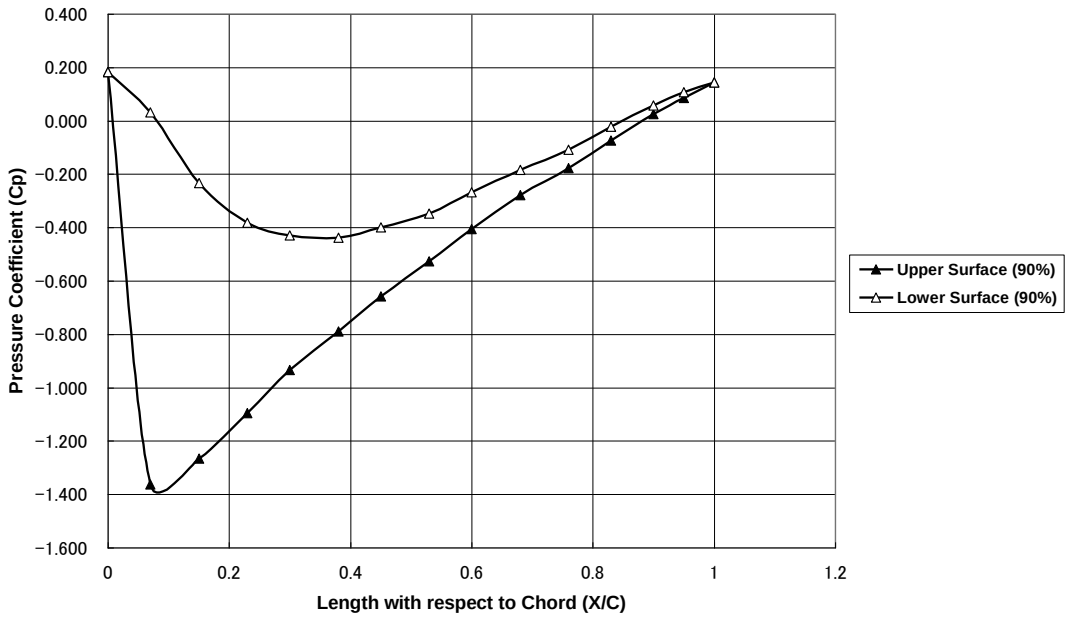

Figure 4.34b: Variation of Pressure with Chord Length for Aerofoil Shaped Fuselage UAV model at 90% from the root at 9° Angle of Attack.

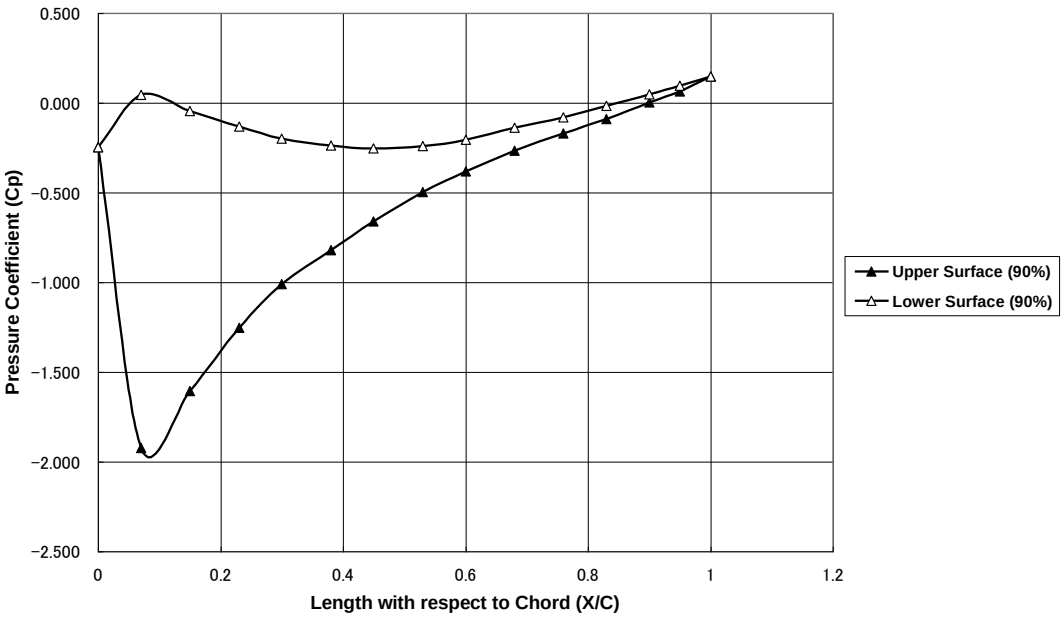

Figure 4.34c: Variation of Pressure with Chord Length for Aerofoil Shaped Fuselage UAV model at 90% from the root at 15° Angle of Attack.

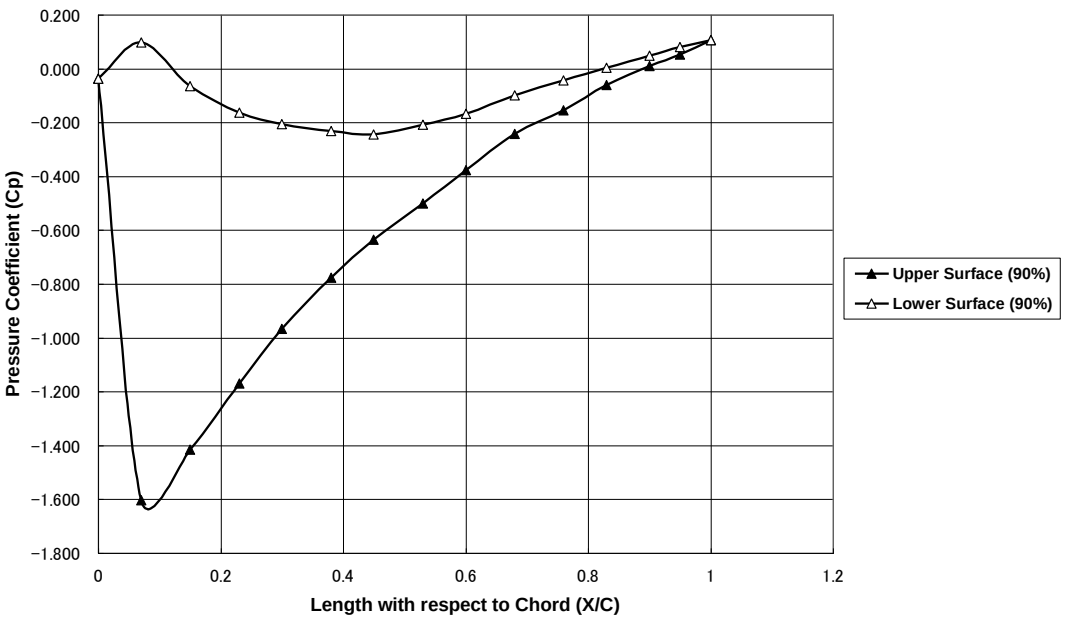

Figure 4.34d: Variation of Pressure with Chord Length for Aerofoil Shaped Fuselage UAV model at 90% from the root at 18° Angle of Attack.

APPENDIX – 'D' TO FIGURE 4.35

on *"Surface Pressure of 2D NACA 4416 Aerofoil Profile at 40 m/s"*

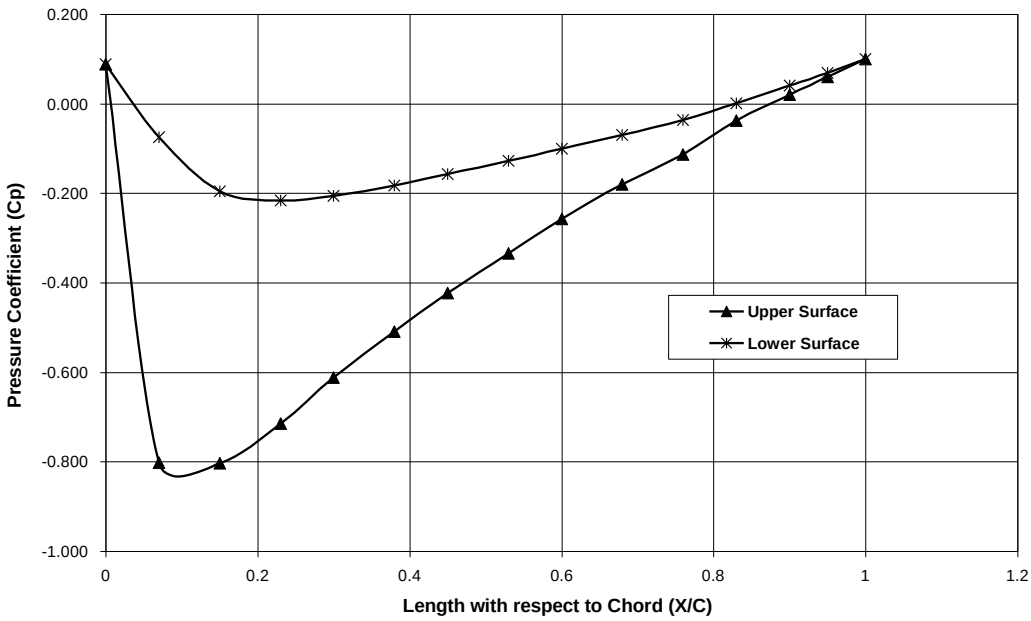

Figure 4.35a: Variation of Pressure with Chord Length for 2D NACA 4416 Aerofoil Profile at 3° Angle of Attack.

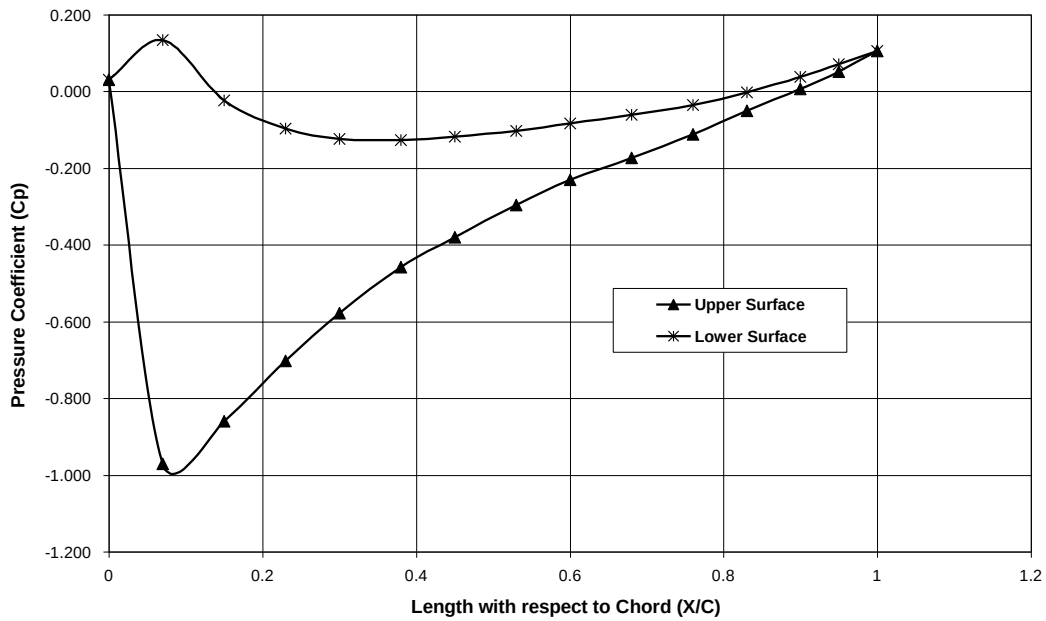

Figure 4.35b: Variation of Pressure with Chord Length for 2D NACA 4416 Aerofoil Profile at 9° Angle of Attack.

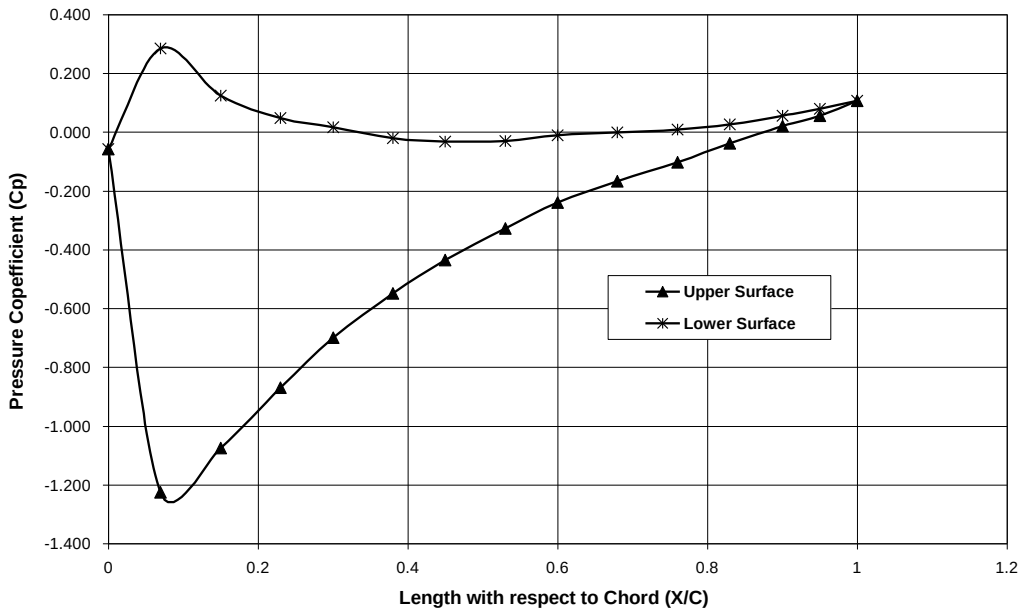

Figure 4.35c: Variation of Pressure with Chord Length for 2D NACA 4416 Aerofoil Profile at 15° Angle of Attack.

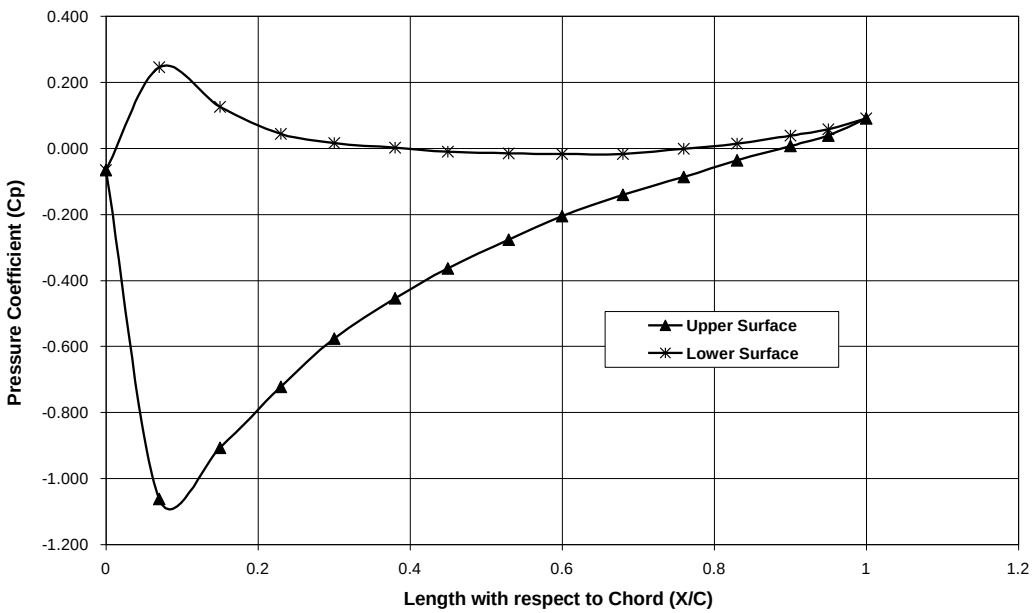

Figure 4.35d: Variation of Pressure with Chord Length for 2D NACA 4416 Aerofoil Profile at 18° Angle of Attack.

APPENDIX – 'E' TO FIGURE 4.36, 4.37, 4.38 and 4.39

on *"Surface Pressure of Conventional Cylindrical Shaped Fuselage at 40 m/s"*

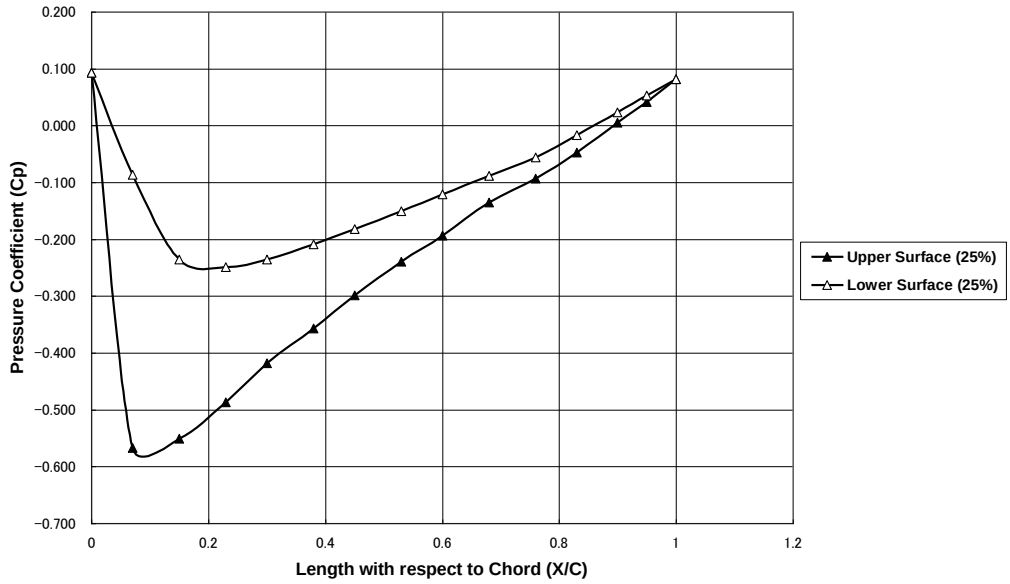

Figure 4.36a: Variation of Pressure with Chord Length for Conventional Cylindrical Shaped Fuselage UAV model at 25% from the root at 3° Angle of Attack.

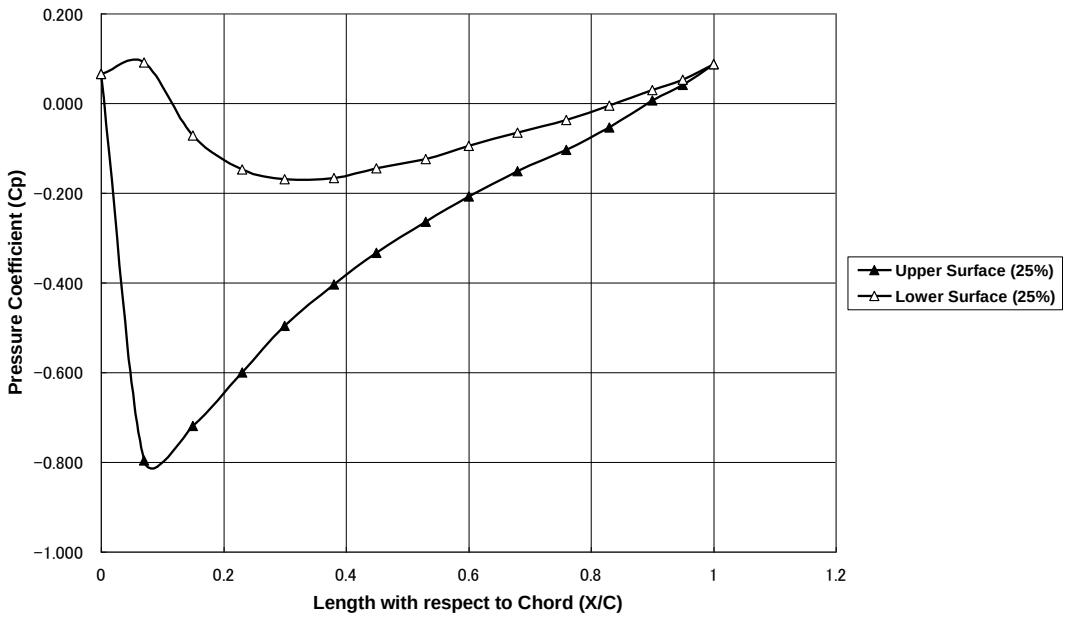

Figure 4.36b: Variation of Pressure with Chord Length for Conventional Cylindrical Shaped Fuselage UAV model at 25% from the root at 9° Angle of Attack.

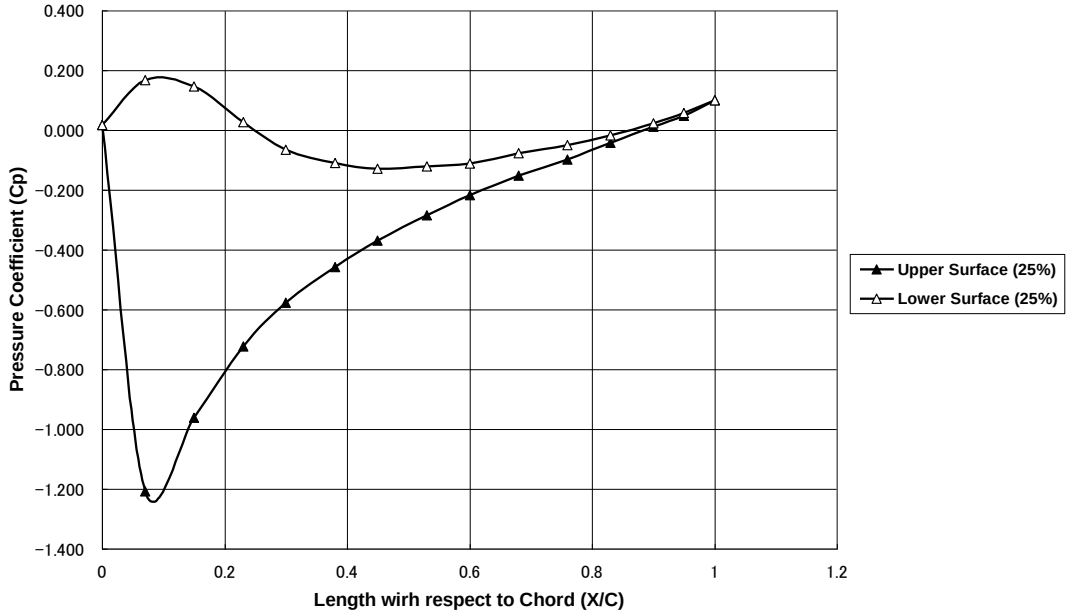

Figure 4.36c: Variation of Pressure with Chord Length for Conventional Cylindrical Shaped Fuselage UAV model at 25% from the root at 15° Angle of Attack.

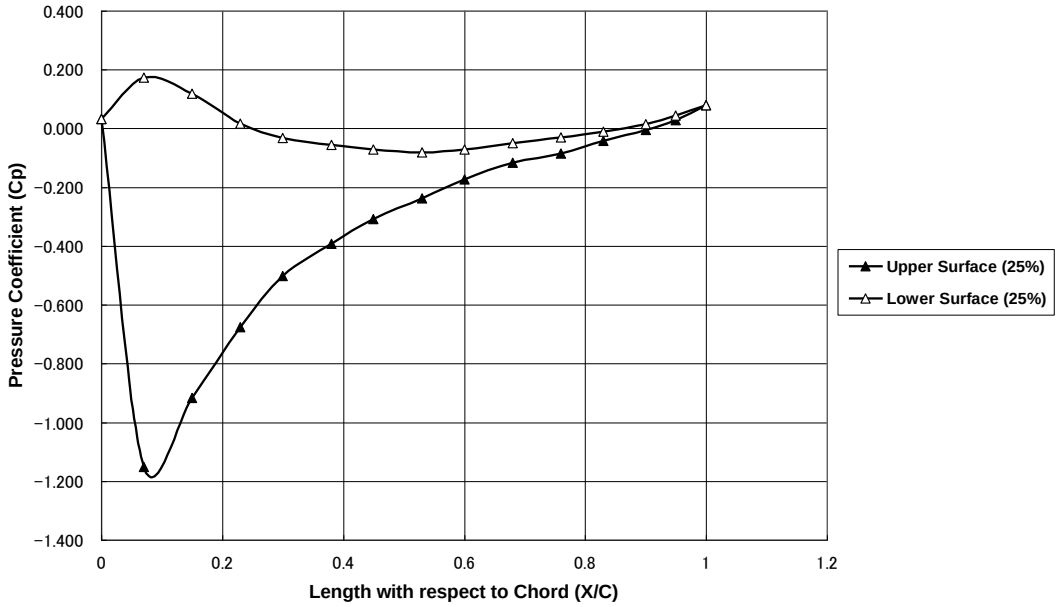

Figure 4.36d: Variation of Pressure with Chord Length for Conventional Cylindrical Shaped Fuselage UAV model at 25% from the root at 18° Angle of Attack.

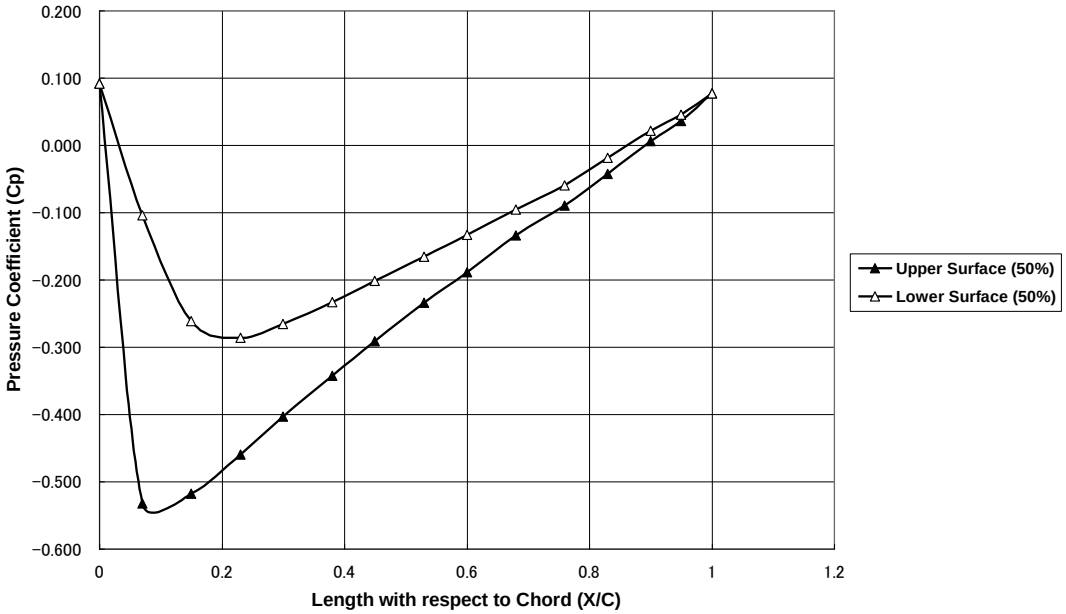

Figure 4.37a: Variation of Pressure with Chord Length for Conventional Cylindrical Shaped Fuselage UAV model at 50% from the root at 3° Angle of Attack.

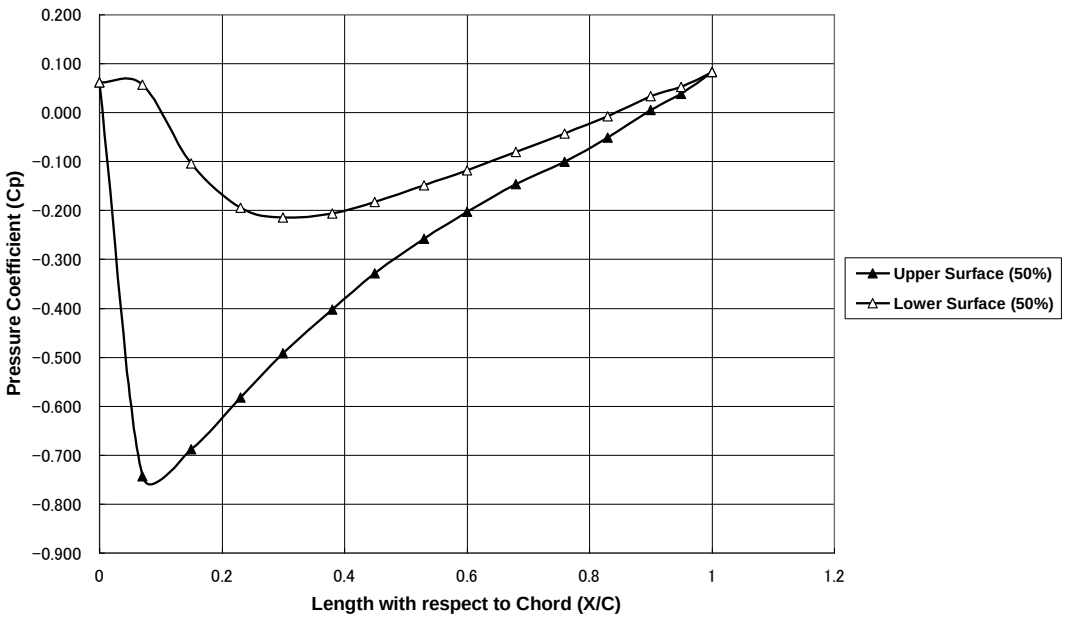

Figure 4.37b: Variation of Pressure with Chord Length for Conventional Cylindrical Shaped Fuselage UAV model at 50% from the root at 9° Angle of Attack.

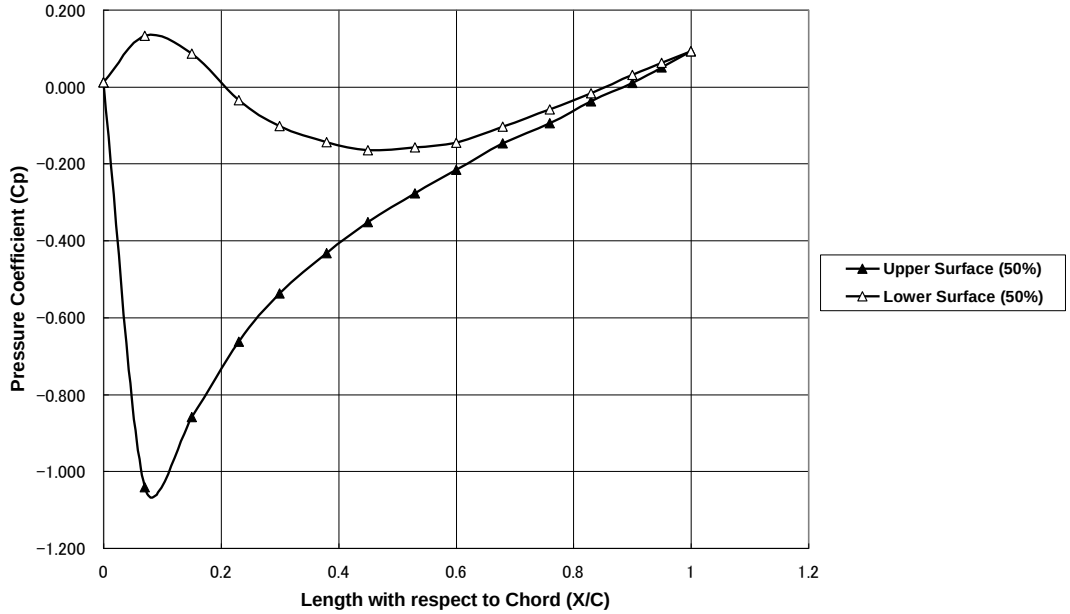

Figure 4.37c: Variation of Pressure with Chord Length for Conventional Cylindrical Shaped Fuselage UAV model at 50% from the root at 15° Angle of Attack.

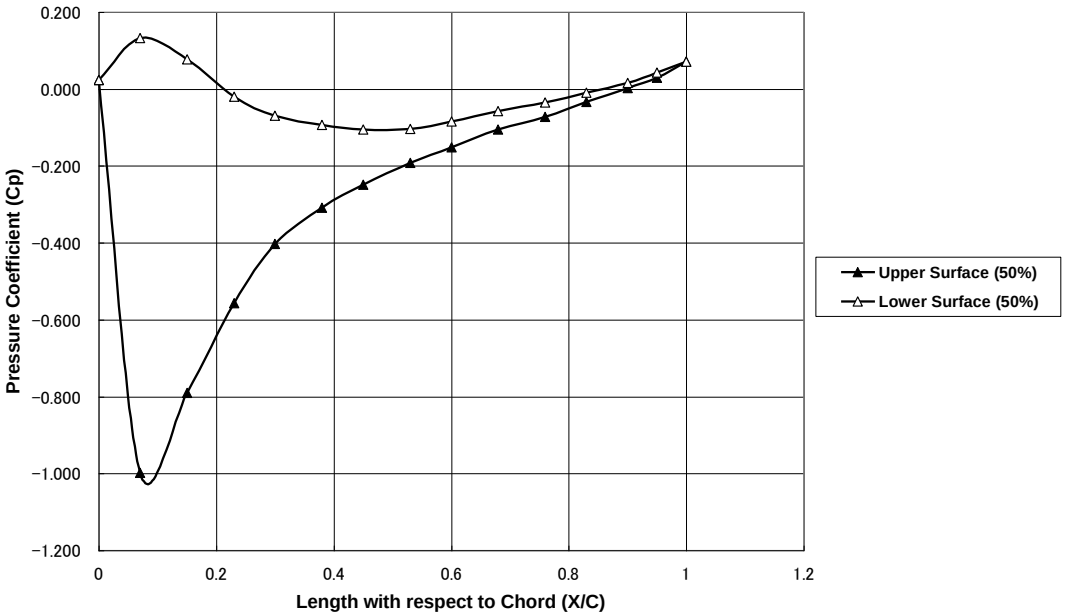

Figure 4.37d: Variation of Pressure with Chord Length for Conventional Cylindrical Shaped Fuselage UAV model at 50% from the root at 18° Angle of Attack.

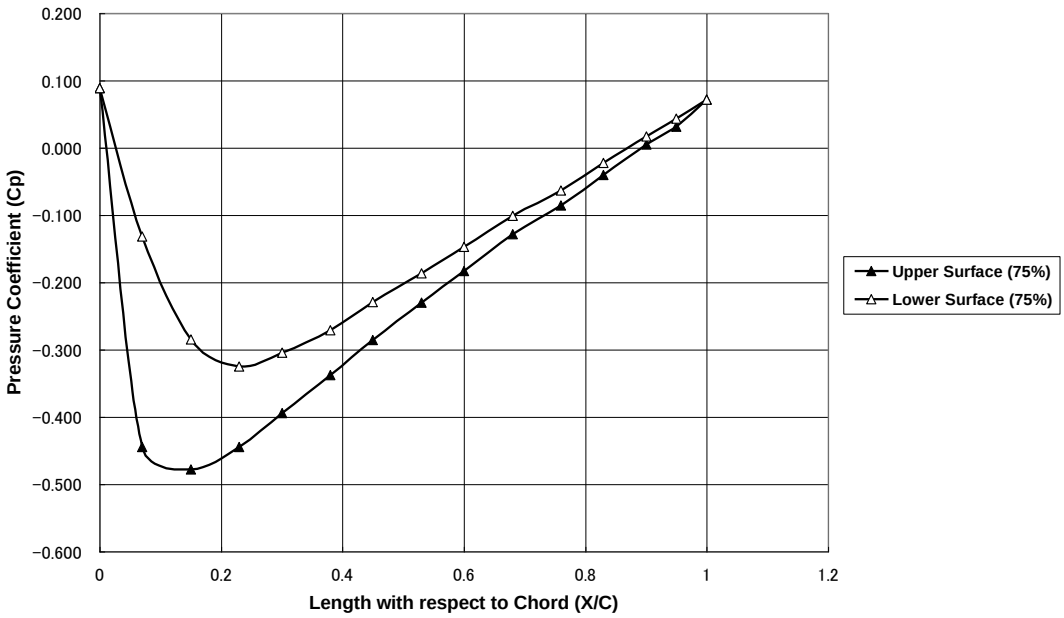

Figure 4.38a: Variation of Pressure with Chord Length for Conventional Cylindrical Shaped Fuselage UAV model at 75% from the root at 3° Angle of Attack.

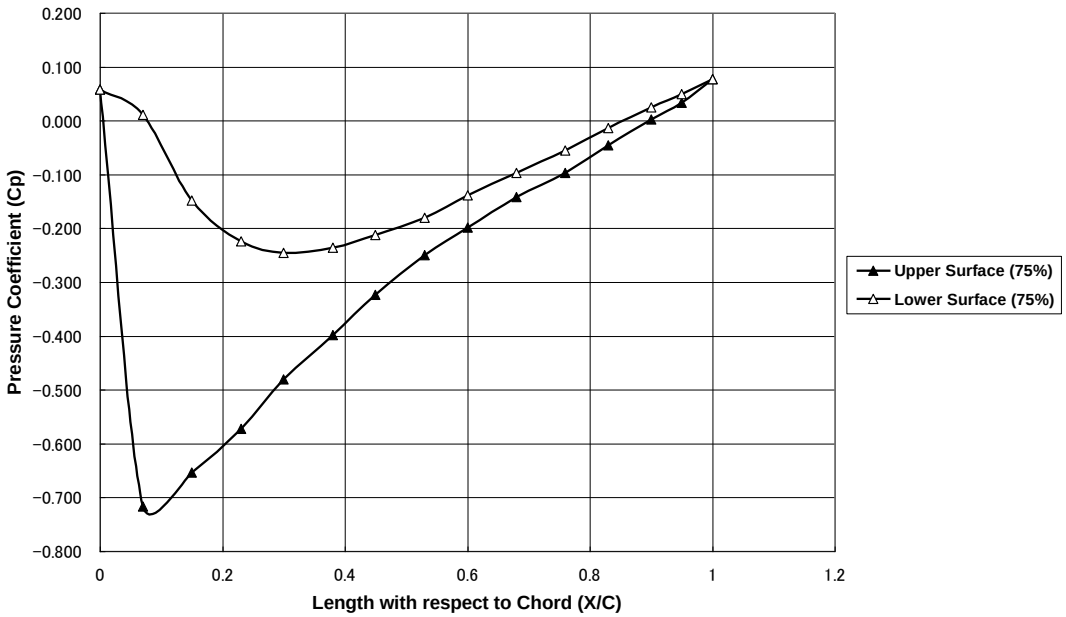

Figure 4.38b: Variation of Pressure with Chord Length for Conventional Cylindrical Shaped Fuselage UAV model at 75% from the root at 9° Angle of Attack.

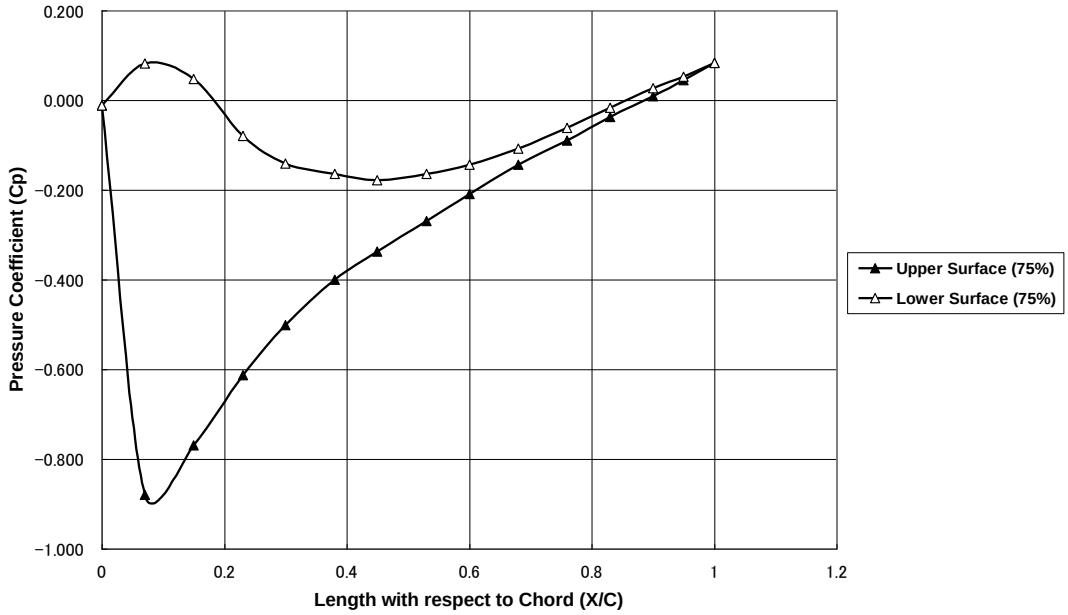

Figure 4.38c: Variation of Pressure with Chord Length for Conventional Cylindrical Shaped Fuselage UAV model at 75% from the root at 15° Angle of Attack.

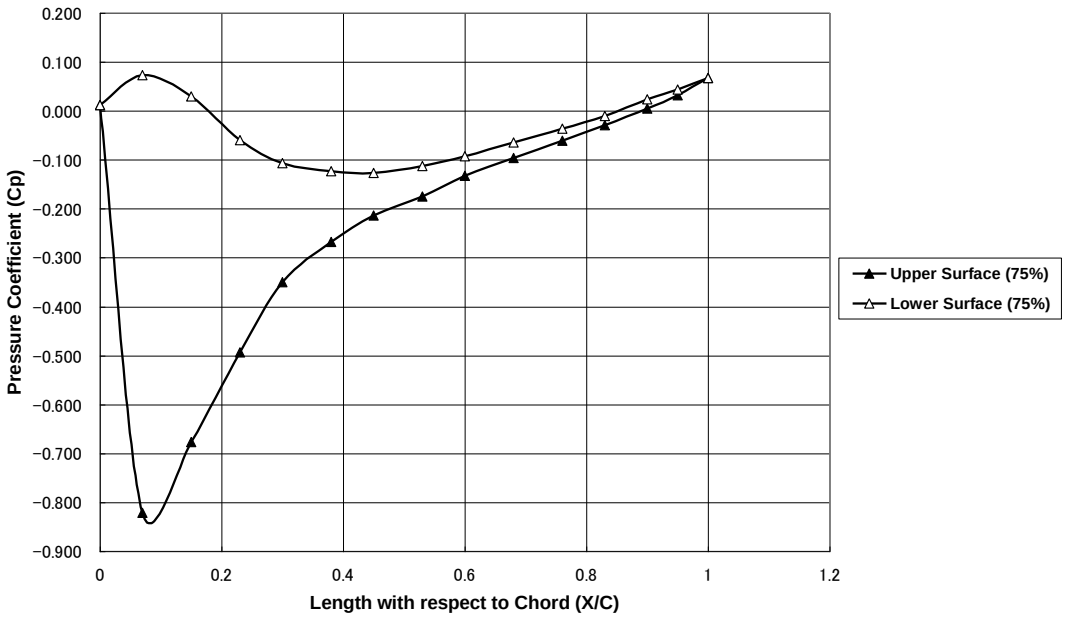

Figure 4.38d: Variation of Pressure with Chord Length for Conventional Cylindrical Shaped Fuselage UAV model at 75% from the root at 18° Angle of Attack.

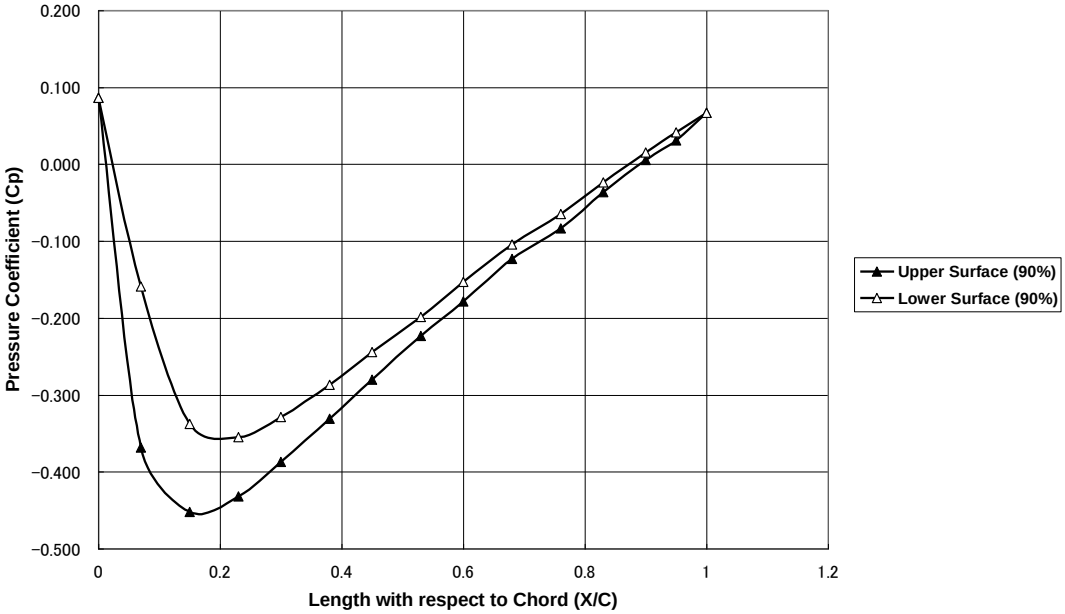

Figure 4.39a: Variation of Pressure with Chord Length for Conventional Cylindrical Shaped Fuselage UAV model at 90% from the root at 3° Angle of Attack.

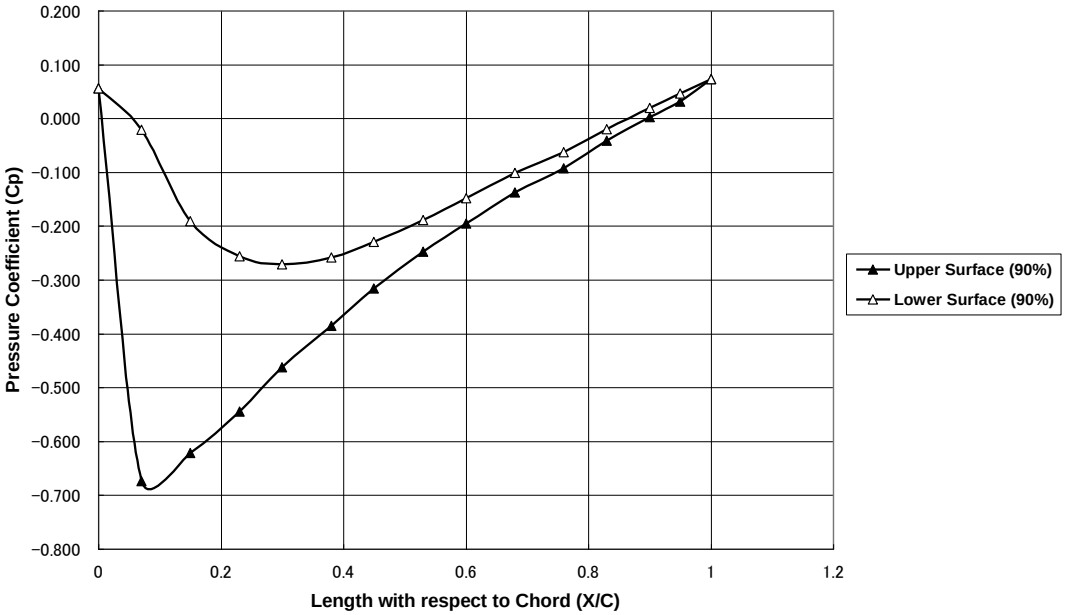

Figure 4.39b: Variation of Pressure with Chord Length for Conventional Cylindrical Shaped Fuselage UAV model at 90% from the root at 9° Angle of Attack.

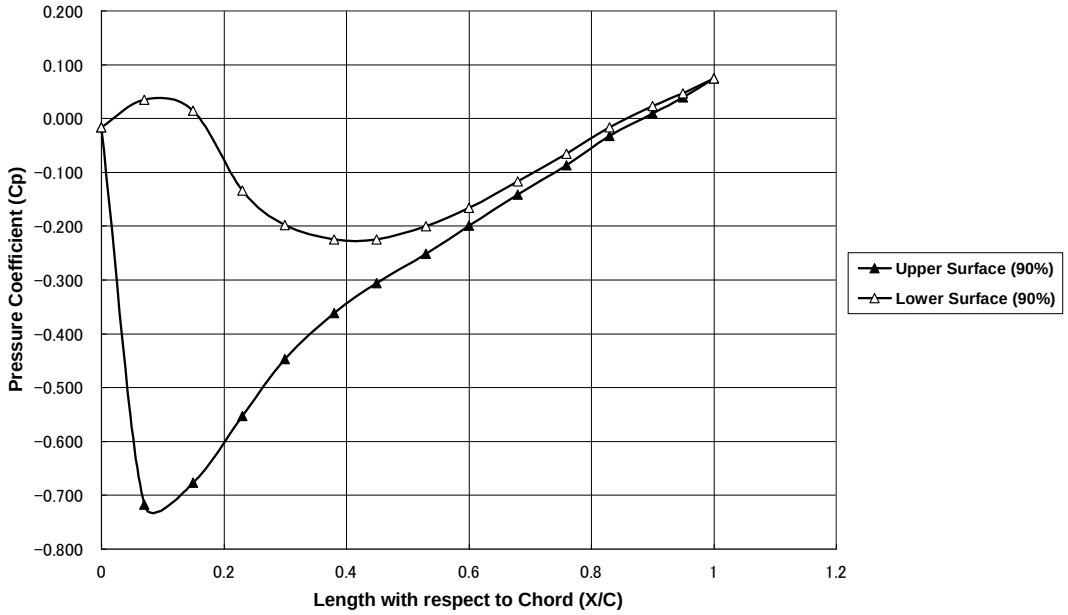

Figure 4.39c: Variation of Pressure with Chord Length for Conventional Cylindrical Shaped Fuselage UAV model at 90% from the root at 15° Angle of Attack.

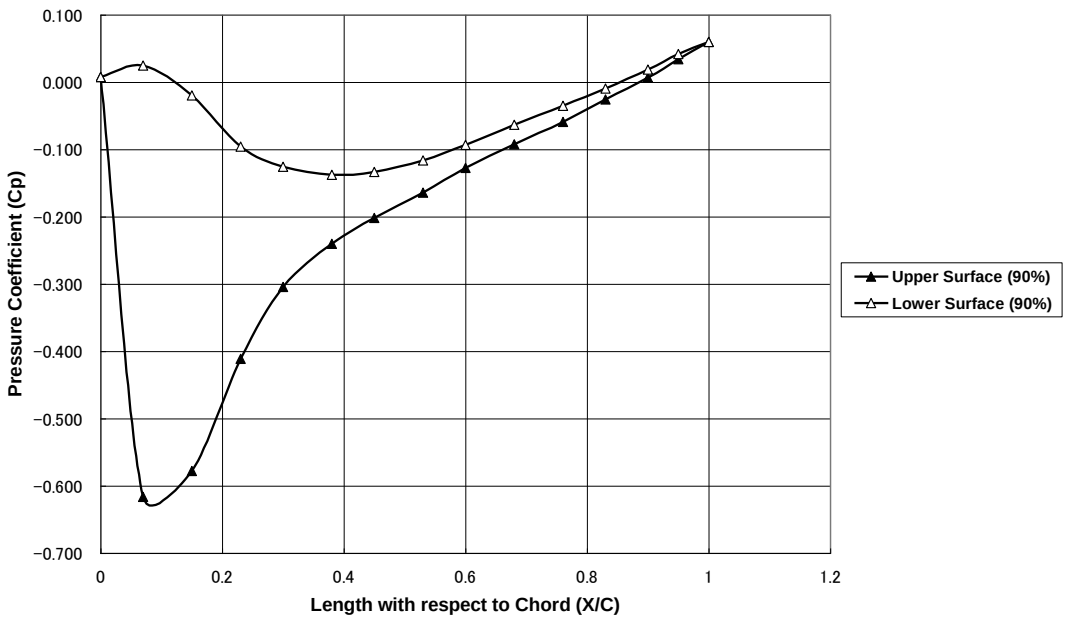

Figure 4.39d: Variation of Pressure with Chord Length for Conventional Cylindrical Shaped Fuselage UAV model at 90% from the root at 18° Angle of Attack.

APPENDIX – ‘A’ to ‘U’

APPENDIX – ‘A’

APPENDIX – ‘B’

APPENDIX – ‘C’

APPENDIX – ‘D’

APPENDIX – ‘E’

APPENDIX – ‘F’

APPENDIX – ‘G’

APPENDIX – ‘H’

APPENDIX – ‘J’

APPENDIX – ‘K’

APPENDIX – ‘L’

APPENDIX – ‘M’

APPENDIX – ‘N’

APPENDIX – ‘P’

APPENDIX – ‘Q’

APPENDIX – ‘R’

APPENDIX – ‘S’

APPENDIX – ‘T’

APPENDIX – ‘U’